Doctoral theses at NTNU, 2023:180

Knut Emil Ringstad

CFD Modelling for Improved Components in CO2 and Ammonia Vapour Compression Systems

Doctoral thesis

NTNU
Norwegian University of Science and Technology
Thesis for the Degree of
Philosophiae Doctor
Faculty of Engineering
Department of Energy and Process Engineering

NTNU
Norwegian University of
Science and Technology

Knut Emil Ringstad

CFD Modelling for Improved Components in CO2 and Ammonia Vapour Compression Systems

Thesis for the Degree of Philosophiae Doctor

Trondheim, June 2023

Norwegian University of Science and Technology
Faculty of Engineering
Department of Energy and Process Engineering

NTNU
Norwegian University of
Science and Technology

NTNU
Norwegian University of Science and Technology

Thesis for the Degree of Philosophiae Doctor

Faculty of Engineering
Department of Energy and Process Engineering

ISBN 978-82-326-7064-2 (printed ver.)
ISBN 978-82-326-7063-5 (electronic ver.)
ISSN 1503-8181 (printed ver.)
ISSN 2703-8084 (online ver.)

Doctoral theses at NTNU, 2023:180

Printed by NTNU Grafisk senter

Preface

This thesis is submitted in partial fulfillment of the requirements for the degree of philosophiae doctor (PhD) at the Norwegian University of Science and Technology (NTNU). The work presented in this thesis has been performed at the Department of Energy and Process Engineering, with professor Armin Hafner as main supervisor. Dr. Åsmund Ervik and Dr. Yosr Allouche were the candidate's co-supervisors. The research was conducted as part of the FME project HighEff - Center for an Energy Efficient and Competitive Industry for the future.

Abstract

Refrigeration and heat-pumping systems are shifting to natural, environmentally-friendly refrigerants like CO_2 to combat global warming. Ejectors are often used in these systems for expansion work recovery to enhance efficiency. However, ejector design is complex due to interdependent parameters and flow complexity, necessitating advanced models and tools. This thesis aims to improve CO_2 ejector modeling for robust design optimization and a better understanding of system operation.

To create a fundamental background for this work, key knowledge gaps on this topic are reported in an exhaustive review of CO_2 two-phase ejector flow modeling. An overview of different available ejector models is reported and highlights the strengths and weaknesses of the different approaches. Other aspects, such as turbulence, non-equilibrium conditions, experimental data, and model applications are thoroughly reviewed. Different models are implemented into the ANSYS Fluent computational fluid dynamics(CFD) framework, and a comparative study of these models is performed. An experimental test campaign is conducted to validate models implemented in this work. To explore novel ejector concepts and develop improved ejector design methodologies, an algorithm for automated CFD model setup was developed to generate a database of CFD results. The Gaussian Process Regression (GPR) machine learning model is applied for modeling ejector performance trained on this database. Additionally, a numerical investigation of a novel swirl bypass concept for performance improvements of ejectors at off-design conditions is conducted.

Based on the review of current CO_2 ejector models, it is found that significant discrepancies between experiments and model prediction are still found. These are typically attributed to non-equilibrium thermodynamics and turbulence modeling. Based on CFD model comparisons, it was found that stable and accurate modeling of CO_2 ejectors with a numerically efficient CFD method is challenging and

requires further development, especially for low motive-pressure conditions. The novel two-fluid model presented in this work can predict CO_2 ejector performance with appropriate parameter selection, but potential challenges for further studies include the complexity of experimental tuning and numerical instabilities. The homogeneous equilibrium CFD model was experimentally validated and reproduced mass flow rates within 2-12% and 3-50% error for the motive and suction flow rates, respectively.

The GPR machine learning model algorithm was applied for modeling ejector performance with various ejector geometries and at various operating conditions with mean errors in entrainment ratio below 0.1 [-]. The algorithm was able to map ejector performance for off-design conditions, explore and optimize ejector designs, and predict local flow structures. The numerical investigation of the swirl bypass ejector indicated that designing such a concept is sensitive to the specific ejector design and operating conditions. A reduction in entrainment ratio of 2-20% is obtained when operating with a swirl bypass inlet. The flow structure inside the ejector with a swirl bypass is also investigated in detail.

In conclusion, it is found that CO_2 ejector modeling using CFD is a valuable tool for their design. These models in combination with machine learning have been shown to be applicable for ejector design algorithms and performance mapping. Exploration of the novel ejector concepts using CFD is considered a key way to discover novel ejector improvements. Improved modeling approaches have a direct impact on design tool accuracy, and further experimental studies and numerical developments are valuable to enhance CO_2 ejector models in terms of accuracy, speed, and stability.

Acknowledgments

First I would like to acknowledge Prof. Armin Hafner for his supervision and support throughout these years. Special thanks also go to my co-supervisors Åsmund Ervik and Yosr Allouche for your feedback and support, and for guiding me to pursue very interesting research paths. Furthermore, my sincerest gratitude goes to Krzysztof Banasiak, for all the help, great discussions, and suggestions for research directions.

I would like to extend my thanks to the ejector simulation research team at the Silesian University of Technology (SUT) and at the University of Florence (UNIFI) for helping me understand and develop the CFD codes used in this work.

To my office mates and fellow researchers in the refrigeration group at NTNU, thank you for all the great times and the fantastic memories.

Lastly, I would like to thank my family and friends for your unending support and encouragement. Without you, this work would not have been possible.

Table of contents

List of tables

List of Algorithms

List of figures

Nomenclature

Abbreviations

ANN	Artificial Neural Network
CFC	Chlorofluorocarbons
CFD	Computational Fluid Dynamics
CO_2 / R744	Carbon dioxide
COP	Coefficient of performance
DNS	Direct numerical simulation
EoS	Equation of state
GP	Gaussian Process
GPR	Gaussian process regression
GWP	Global warming potential
HCFC	Hydrochlorofluorocarbons
HEM	Homogeneous equilibrium model
HFC	Hydro fluoro carbon
HFO	Hydro fluoro olefins
HNB	Homogeneous nucleation boiling model
HNL	Homogeneous nucleation line

HRM Homogeneous relaxation model

HVAC Heating, ventilation, air-conditioning, and refrigeration

IPCC Intergovernmental Panel on Climate Change

KPI Key performance index

LES Large eddy simulation

LHC Latin hyper cube

LRN Low Reynolds number

MFR Mass flow rate

ML Machine learning

PIV Particle Image Velocimetry

PWM Pulse width modulation

SW Span-Wagner equation of state

TFA Tri Fuoro acetic acid

TFM Two fluid model

UDF User defined function

UDRGMM User defined real gas mixture model

UDS User defined scalar

Symbols

α Volume fraction [-]

$\bar{E}$ Expectation value

β Mass fraction [-]

χ Scaled sampling variable

ΔH Latent heat [J]

$\dot{m}$ Mass flow rate [kg/s]

$\dot{S}_{h1,2,3}$ Enthalpy equation source term [J/s]

ϵ	Turbulent kinetic energy dissipation [m^2/s^3]
η	Ejector efficiency [-]
Γ	Phase change source term [kg/(m^3 s)]
γ	Flow uniformity index
$\hat{\Lambda}$	Phase change coefficient - HNB [-]
κ	Karman constant [-]
Λ	Phase change coefficient - UDRGMM [1/s]
λ	Thermal conductivity [J/(s K)]
μ	Dynamic viscosity [kg/m s]
ν	Kinematic viscosity [m^2/s]
ω	Entrainment ratio [-]
ϕ	Flow variable
Π	Pressure ratio [-]
ψ	Volume averaged property
ρ	Density [kg/m^3]
Σ	Diffusion coefficient [kg/m s]
σ	Data variance
τ	Stress tensor [kg/m s^2]
τ_{qij}	Phase stress tensor [kg/m s^2]
θ	Angle [°]
Υ	Interfacial multiphase turbulence term [J/(kg s)]
$\vec{u}$	Velocity vector [m/s]
ξ	Mass averaged property
ζ	Hyperparameter
B	Law of the wall constant [-]

C	Equation constants
c	Speed of sound [m/s]
C_D	Drag coefficient [-]
c_p	Heat capacity [J/K]
d	Diameter [m]
D_{diff}	Diffuser outlet diameter [mm]
$D_{\text{m-out}}$	Motive outlet diameter [mm]
D_{mix}	Mixing chamber diameter [mm]
E	Total energy [J]
f^{mom}	Friction factor [-]
F_{qp}^{mom}	Momentum exchange coefficient [N]
G	Turbulent strain rate production [J/(kg s)]
H	Wall roughness heigth [m]
k	Turbulent kinetic energy [J/kg]
L	Latent heat [J]
L	Length [m]
L_{mix}	Mixing chamber length [mm]
m_M	Molar mass [kg/kmol]
P	Pressure [Pa]
R	Momentum exchange [N]
r	Mesh refinement ratio
s	Entropy [J/K]
T	Temperature [K]
t	Time [s]
U^+	Turbulent dimensionless wall velocity [-]

u_τ	Turbulent wall friction velocity [-]
V	Volume [m^3]
$v_{q,p}$	Slip velocity [m/s]
y^+	Turbulent dimensionless wall distance [-]
N	Normal distribution
a	Sampling range
f	Underlying unobservable function
G	Learning rate
g	Specific Gibbs free energy [J/kg]
h	Enthalpy [J/kg]
i	Specifc internal energy [J/kg]
K	Covariance function - kernel
l	Characteristic length scale
M	Data mean
Ma	Mach number [-]
N	Number of points
n	Noise
p	Probabilty
Pr	Prandtl number [-]
Q	Heat flux [W/s]
Re	Reynolds number [-]
W	Work [J/s]
x	Direction vector [m]
X,y	Data in dataset

Subscripts

b	Particulate
c	Condensation
e	Evaporation
eff	Effective
i,j	Notation indices
l	Liquid
m	Motive
m	Pseudo-fluid mixture property
o	Outlet
p,q,k	Phase index
s	Suction
t	Turbulent
v	Vapor

1 Introduction

"It's not worth doing something unless someone, somewhere, would much rather you weren't doing it."

— Terry Pratchett

1.1 Motivation

In 2015, the 193 countries in the United Nations general assembly presented 17 sustainable goals for 2030. This agreement presents common global goals for our future, with focus areas such as (1) poverty, (2) world hunger, (13) climate change, and (16) world peace. Immense efforts will be required from people, industries, and policymakers worldwide to achieve these goals. The Heating, Ventilation, Air-conditioning, and Cooling (HVAC) industry is in an opportune position to take on several of these challenges. Environmentally friendly, affordable, and efficient developments within this field can target the goals of (2) world hunger, (8) green employment and economic growth, (9) innovation of industries, (11) sustainable cities and transport, (12) improved cycles for consumption of goods and (13) climate-friendly and sustainability, shown in Figure 1.1.

Global warming is one of the most pressing issues humanity has faced in the last decades urging the need for immediate and disruptive changes to our societies to adopt clean, robust, and resilient technological and behavioral solutions. Large-scale restructuring of industries will be required if the Intergovernmental Panel on Climate Change (IPCC) goal of less than 1.5-degree warming compared to pre-industrial levels is to be met [1]. The growing concern about climate change

Figure 1.1: UN sustainable goals

has incited a shift in the HVAC sector, towards adopting more efficient and clean technologies to help deliver societal, economic, and health goals as defined by the UN sustainable development goals.

Historically, the first refrigeration systems (1830-1930) were operated with working fluids that appear naturally in the environment, such as CO_2 and ammonia. Due to safety and durability concerns, new synthetic refrigerants - chloro-fluoro-carbon (CFC) and hydro-chloro-fluoro-carbons (HCFC) - were introduced in the 1930s [2]. In the 1980's it was revealed that these refrigerants caused a breakdown of the ozone layer. Emphasis was put on reducing the usage of ozone-depleting refrigerants with the introduction of the Montreal Protocol. This shifted refrigerant usage from CFCs and HCFCs to the new synthetic refrigerant hydro-fluoro-carbons (HFC). HFCs have no ozone depletion effect, however, several of the HFC working fluids have a large GWP when released into the atmosphere. As an example, the HFCs R22 and R404A have GWP values of 1760 $kg_{CO2\ eqv}$ / $kg_{Refrigerant}$ and 3943 $kg_{CO2\ eqv}$ / $kg_{Refrigerant}$, respectively. According to Gullo et al. [3], yearly leakages of the total charge can range from 15-20% in modern systems and up to 30% in lower-quality systems. This amounts to large yearly emissions of greenhouse gases. Furthermore, such synthetic gases have unknown consequences for the natural environment, similar to the then-unknown ozone depletion effects of synthetic CFC gases. To combat these emissions, significant legislative action has been ratified, such as the Kigali amendments to the Montreal Protocol and the EU F-gas Regulation [4], to remove high GWP working fluids and replace them with low GWP alternatives.

In recent years, hydro-fluoro-olefins (HFOs) have been presented as an alternative synthetic working fluid replacement for the current generation of HFCs. HFOs are characterized by a lower GWP than the previous HFCs, however, are also found to be less chemically stable and therefore decompose more rapidly in the atmosphere [5]. Recent studies [5, 6] indicate that the decomposition of some common HFOs and HFCs can result in Tri Fluoro acetic acid (TFA). These substances are reported to contaminate drinking water through rainfall and their further decomposition in the atmosphere is hypothesized to result in aerosols that have a large impact on climate change.

The alternative to synthetic refrigerants is natural working fluids, such as ammonia, hydrocarbons, water, and CO_2. As they are found abundantly in nature, natural refrigerants have fewer unknown effects on the environment. These natural alternatives are affordable, widely available, clean, and sustainable which contributes towards achieving society's goals for greenhouse gas (GHG) emissions reduction. A large number of works have been published during the last decades on the design of high-performance natural refrigeration systems operating under different ambient conditions. Within this context, CO_2 (R744) is considered a low GWP working fluid offering a long-term solution to reduce the climate impact of refrigeration. The proven technological performance and low climate impact of CO_2 refrigeration systems have allowed CO_2 refrigeration to take a central role in the European supermarket segment [7]

The demand for refrigeration and air-conditioning uses today about 17% of the world's current electricity consumption. Energy consumption accounts for 80% of the total emissions of the refrigeration sector [8]. Therefore, significant efforts must be put toward the development of energy-efficient and sustainable systems that can be economically viable, technically implemented, and applied globally. To this end, the European Union has committed to cut greenhouse gas emissions by more than 40% compared to 1990 levels by 2030, and achieve at least a 32.5% improvement in energy efficiency by 2030 [9]. To reach these energy efficiency targets, significant improvements in all sectors and industries are required. Further research into improved refrigeration cycles and their components is therefore motivated, as a step toward these goals.

A conventional vapor compression refrigeration system is comprised of a loop of circulating refrigerant (working fluid) that absorbs heat at a low temperature and releases heat at a high temperature. This is done by compressing and expanding the working fluid to appropriate temperatures compared to the required cooling and ambient temperature. This refrigeration cycle is comprised of four components; a compressor, a condenser or gas cooler, an expansion device (typically an expansion valve), and an evaporator. The compressor compresses the working fluid, increasing its temperature and pressure. At this high temperature, heat is released to ambient

air through a condenser or gas cooler. After the condenser, an expansion device is used to reduce the pressure and temperature. At the lower temperature, the working fluid absorbs heat in the evaporator. In the standard refrigeration cycle, a simple expansion valve is used as the expansion device. However, this throttling process causes expansion loss that may be significant for refrigeration cycles.

The limited performance of CO_2 refrigeration systems in high ambient temperatures has been widely reported in previous studies [3]. This is largely attributed to expansion losses when the system operates above the critical temperature of CO_2 ($31.1°C$). Considerable efforts have been put in by researchers to support the global adoption of natural refrigerants to assure available low-emission solutions in all climates. Advanced technological solutions are demonstrated in order to improve the efficiency of these systems also in warm countries, achieving promising results. For a complete overview of these technologies, the reader is referred to the work by Gullo et al. [10, 7]. Currently, the most up-to-date solution is systems supported by two-phase ejectors.

Ejectors are simple and affordable devices that can recover lost expansion work, improving efficiency, mainly when operating under high ambient temperatures. A number of studies indicate that the adoption of the ejector technology could achieve improvements in the system efficiency in the range of 10-30% for trans-critical operation [11, 12]. Furthermore, CO_2 ejector refrigeration systems were found to consume 25% less energy when compared to HFC-based systems [7]. This shows the potential of the technology to be adopted by low-income economies in order to meet simultaneously their economical, societal, and health development goals.

Reaching the previously mentioned sustainable goals is dependent on the adaptation of environmentally friendly and efficient cooling systems in developing countries. Many of these countries are situated in warm climates, which further motivates research into technologies that can provide better efficiency, lower cost, and more reliability such as ejector-supported CO_2 systems.

Over the last decade, intensive research has been put toward the design of efficient CO_2 ejector systems. Novel devices have been proposed, such as the multiblock ejector [13], the needle-controlled ejector [14, 15] and the suction bypass ejector [16]. Many of these devices have also seen significant commercial interest, and have been successfully commercialized. Ejectors for R744 refrigeration are still a very actively researched topic to achieve improved CO_2 system efficiency. It should be noted that ejector efficiency is sensitive to the specific ejector design and operating conditions. Nakagawa et al. [12] found that a 34 to 82% reduction in system coefficient of performance (COP) can occur when operating an ejector system at off-design conditions. Consequently, standardized ejectors which are not

designed to operate for that specific application may limit system performance. The availability of accurate tools and methodologies will help in providing ejector design for each specific application. The development of ejector performance maps would describe the optimal operation of the device under different operating conditions. This will consequently lead to the improvement of the system's performance and be useful to optimize its operation.

Accurate numerical modeling is essential for high-performing CO_2 ejector design. Small changes in the ejector geometry or operating condition can have significant impacts on the ejector performance. Therefore, a reliable model is a cost-effective way to run experiments that may involve expensive components and measurement devices. This will also overcome the technical and financial challenges associated with testing different ejectors with specific optimal design conditions for various applications [17, 18]. This has prompted research efforts to be placed towards the development of advanced models for CO_2 ejectors, such as the 0D and 1D models [19, 20, 21, 15, 22, 23], which have been applied for system-level calculations and ejector design. The main limitation associated with numerical modeling using the thermodynamic or 1D approaches is their inability to predict multidimensional phenomena such as flow separation or shock-wave patterns. Furthermore, transport and interaction between the suction and motive flow are explicitly handled which typically involves simplified modeling of mixing and turbulence which may limit model accuracy, especially outside the range of designs and operating conditions where the model was tuned. This problem becomes important when exploring novel ejector designs. Furthermore, new geometric ejector designs that are not within conventional ejector design space are not possible to investigate with such approaches. In recent years, emphasis has therefore been put toward developing accurate and fast multiphase computational fluid dynamics (CFD) models for CO_2 ejectors, where the full 2D or 3D ejector physics are resolved, allowing for more exploratory investigations of ejector designs. CFD modeling has the added benefit of allowing detailed insights into ejector physics as all flow variables are available. However, CFD models are, in general, more complex and more computationally costly, and their limitations and underlying assumptions must be considered when applied to a large range of flow conditions. Both numerical modeling and experimental validation data are required to achieve better next-generation ejectors.

This thesis is a part of the HighEFF - Centre for an Energy-Efficient and Competitive Industry for the Future, an 8-year Research Centre under the FME-scheme (Centre for Environment-friendly Energy Research,257632/E20). HighEff focuses on technologies and processes with the potential for a large reduction in specific energy use. This work will focus on research into improved components for natural refrigeration systems, with special emphasis on CO_2 ejectors.

1.2 Aim of study

The aim of this work is to contribute to the improvement of natural refrigeration systems by investigating the design of CO_2 ejectors. This is to be done through the exploration and validation of numerical models, investigations into novel ejector concepts, and the development of new methodologies for component design. The objectives of the work are summarized as follows:

- Investigate and identify current state-of-the-art approaches to numerical modeling of CO_2 ejectors and relevant experimental methods for model validation.
- Implement and compare available CO_2 ejector models in terms of accuracy and speed.
- Investigate and implement novel ejector models for improved speed and accuracy.
- Conduct experimental measurements on CO_2 ejectors and validate the results against numerical models.
- Investigate novel ejector concepts for efficiency improvements using numerical modeling
- Develop improved ejector design methodologies using automated model approaches and data analysis.

1.3 Contributions

The main novel contributions of this thesis can be summarized:

- Presented a review of CO_2 ejector modeling and its specific modeling challenges filling a significant knowledge gap in the research field.
- Experimental measurement data of a novel CO_2 ejector geometry collected at varied operating conditions and made openly available.
- Development of a novel Eulerian two-fluid model for CO_2 ejectors, which was, to the best of the author's knowledge, the first presented in the open literature.
- Development of an automated ejector meshing and CFD database generation tool for ejectors, which was among the first made openly available.

- Implementation of machine learning Gaussian Process Regression model for ejector performance prediction. To the best of the author's knowledge, this was the first use of the GPR machine learning approach for CO_2 ejectors.
- Development of an optimization tool using machine learning for CO_2 ejectors, to the best of the author's knowledge, among the first tools of its type implemented for CO_2 ejector optimization.
- Designed a new ejector for an industry client, implemented in new CO_2 heat pumps.
- Presented first numerical investigation of a novel swirl bypass ejector concept for CO_2 ejectors.

1.4 Structure of thesis

The structure of the thesis is comprised of eight chapters and a collection of three journal publications. The main content is described as follows:

- Chapter 1 contains the introduction to the main topics and motivation for the thesis work. The objective and scope of the research work are presented, followed by a list of the scientific publications
- Chapter 2 gives the technical background information on ejectors within refrigeration and their design, control, and history.
- Chapter 3 summarizes the background information and the details of the different models discussed in this thesis. Furthermore, experimental validation and verification (mesh refinement study, equation of state refinement study) are presented.
- Chapter 4 gives the details and results of the experimental test campaign conducted during the thesis work.
- Chapter 5 contains the details of the ejector design tool that has been developed in this thesis work. Relevant background information regarding the machine learning model employed is also given.
- Chapter 6 summarizes the research articles presented in this thesis work. The chapter is organized into sections where each journal publication is summarized.
- Chapter 7 contains the conclusions and main results from the doctoral work.

- Chapter 8 presents suggestions for further work within CO_2 ejectors, and their modeling and design methodologies and discusses the thesis in a wider context.

1.5 List of publications

The author of this thesis contributed to three journal articles and five conference papers on the subject of ejector modeling and design. All papers are attached in the appendix.

1.5.1 Journal publications

Article I

Ringstad, Knut Emil; Allouche, Yosr; Gullo, Paride; Ervik, Åsmund; Banasiak, Krzysztof; Hafner, Armin. (2020) A detailed review on CO2 two-phase ejector flow modeling. *Thermal Science and Engineering Progress.* vol. 20.

Author Contributions: Conceptualization, **K.E.R.**, A.H., Å.E., Y.A., P.G. and K.B.; Methodology, **K.E.R.**, A.H., Å.E., Y.A., P.G. and K.B. ; Investigation, **K.E.R.**, A.H., Å.E., Y.A., P.G. and K.B.; Data curation, **K.E.R.**; Writing - Original draft preparation, **K.E.R.**; Writing - Review and editing, **K.E.R.**, A.H., Å.E., Y.A., P.G. and K.B.; Visualization, **K.E.R.**, Å.E.; Supervision, A.H., Å.E., Y.A., P.G. and K.B.; Project administration, A.H.; Funding acquisition, A.H.

Article II

Ringstad, Knut Emil; Ervik, Åsmund; Banasiak, Krzysztof; Hafner, Armin. (2021) Machine learning and CFD for mapping and optimization of CO2 ejectors. *Applied Thermal Engineering.*

Author Contributions: Conceptualization, **K.E.R.**, A.H., Å.E. and K.B.; Methodology, **K.E.R.**,Å.E.; Software, **K.E.R.**; Validation, **K.E.R.**; Investigation, **K.E.R.**; Data curation, **K.E.R.**; Writing - Original draft preparation, **K.E.R.**; Writing - Review and editing, **K.E.R.**, A.H., Å.E. and K.B.; Visualization, **K.E.R.**; Supervision, A.H., Å.E. and K.B.; Project administration, A.H.; Funding acquisition, A.H.

Article III

Ringstad, Knut Emil; Ervik, Åsmund; Banasiak, Krzysztof; Hafner, Armin. (2022) Swirl-Bypass Nozzle for CO_2 Two-Phase Ejectors: Numerical Design Exploration *Energies.*

Author Contributions: Conceptualization, **K.E.R.**, A.H., Å.E. and K.B.; Methodology, **K.E.R.**,Å.E. and K.B.; Software, **K.E.R.** and Å.E.; Validation, **K.E.R.** and K.B.; Investigation, **K.E.R.**, A.H., Å.E. and K.B.; Data curation, **K.E.R.** and K.B.; Writing - Original draft preparation, **K.E.R**., A.H., Å.E. and K.B.; Writing - Review and editing, **K.E.R.**, A.H., Å.E. and K.B.; Visualization, **K.E.R.**; Supervision, A.H., Å.E. and K.B.; Project administration, A.H.; Funding acquisition, A.H.

1.5.2 Conference articles

Conference article I

Ringstad, Knut Emil; Hafner, Armin; Allouche, Yosr. (2019) Investigation of CFD models for ammonia ejector design. *8th Conference on Ammonia and CO2 Refrigeration Technologies, Proceedings.*

Conference article II

Ringstad, Knut Emil; Allouche, Yosr; Gullo, Paride; Banasiak, Krzysztof; Hafner, Armin. (2019) CO2 ejector modeling using CFD: current status. *Proceedings of the 25th IIR International Congress of Refrigeration. Montréal, Canada, August 24-30, 2019.*

Conference article III

Ringstad, Knut Emil; Hafner, Armin. (2020) Two-fluid CFD model for 2 two-phase ejectors. *Proceedings of the 14th IIR-Gustav Lorentzen Conference on Natural Refrigerants - GL2020.*

Conference article IV

Ringstad, Knut Emil; Hafner, Armin. (2021) Comparative study of R744 ejector CFD models. Proceedings of the IIR - 10th International Conference on Compressors and Coolants.

Conference article V

Ringstad, Knut Emil; Banasiak, Krzysztof; Hafner, Armin. (2021) CFD-based design algorithm for CO2 ejectors. 9th Conference on Ammonia and CO2 Refrigeration Technologies, Proceedings.

1.6 Open access

The sharing of research data and research methods is considered a key part of the furthering of science. To this end, all software and data that are not proprietary to other research groups or companies are shared open access. All journal publications that have been developed in this thesis work are openly available.

The ejector design tool, ***EjectorDesigner***, is made available with open access, and the documentation is added as an appendix to this thesis. The code for 2D and 3D ejector meshing in ANSYS ICEM, the scripts for full automation of CFD database generation, post-processing, and the data results from the ejector design algorithm are all made available open access at the *github* depository:

`https://github.com/knutringstad/EjectorDesigner`

Data from the experimental test campaign and scripts for analysis of the swirl-bypass ejector modeling are available at the *github* depository:

`https://github.com/knutringstad/Swirl_bypass_ejector`

2 Background

"Wisdom comes from experience. Experience is often a result of lack of wisdom."

— T. Pratchett

2.1 CO2 refrigeration

The first CO_2 based refrigeration system was invented by Alexander Twinning in 1850. As one of the first working fluids used in refrigeration systems, CO_2 as a refrigerant was very popular. Later, with the growth of CFC gas-based refrigeration in the 1950s-60s, CO_2 was slowly phased out as a refrigerant [24]. CO_2 refrigeration was still considered a niche solution up until the 1990s when the significant greenhouse effects of HFCs were emphasized [24]. Consequently, the interest in environmentally friendly and natural refrigerants has increased, and CO_2 has been reintroduced as a clean and sustainable alternative refrigerant, largely promoted by Gustav Lorentzen [25, 26, 27, 28]. Early investigations on CO_2 systems were focused on automobile air conditioning [26, 27] and heat pumps for water heating [27, 28, 29]. Over the last decades focus on environmental impact has increased. Legislative agreements aiming at the phase-out of high GWP working fluids, such as the Kigali Amendment to the Montreal Protocol and the EU F-gas Regulation 517/2014 [4], have been in force since 2015. This increase in the policymakers and public awareness about the environmental impact of the commonly applied refrigerants at that time was the main driver for the uptake of deep investigations on CO_2 refrigeration solutions. This has allowed CO_2 to take a leading role in the

refrigeration and heat-pumping sector.

The favorable thermo-physical properties of CO_2 as a refrigerant have largely contributed to its popularity. CO_2 is often referred to as a "near-ideal" working fluid [27]. It is characterized by negligible GWP (GWP of 1), non-flammability, non-toxicity, low cost, availability, and favorable thermophysical properties for efficient heat transfer [30]. Additionally, the higher operating pressures than other working fluids yield a higher volumetric heating capacity which allows CO_2 systems to be built more compactly, useful when subjected to space constraints [24]. Compared to most other working fluids, CO_2 has a low critical temperature of 31.1 °C and high critical pressure of 73.8 bar. Therefore CO_2 systems are designed and operated differently from most other working fluids. Their associated cycles are often operated at super-critical conditions. In these cycles, the condenser is exchanged with a gas cooler. When operating at sub-critical conditions, the gas cooler operates as a condenser and has a constant condensation temperature. However, at super-critical conditions, the CO_2 behaves similarly to a gas and is cooled at a gliding temperature.

CO_2 based refrigeration and heat-pumping systems have been used for many applications, such as supermarkets [3, 31], heat pump units [32, 33, 34], vehicles [35, 36, 37], light commercial refrigeration [38, 39], tumble dryers [40, 41], chillers [42], air-conditioners [43], and integrated systems for hotels [44]. However, due to the fluid's thermodynamic properties, expansion losses in super-critical CO_2 refrigeration systems are higher than those occurring in conventional refrigeration cycles. This is considered to be the main limitation of CO_2 refrigeration cycles, and would consequently reduce CO_2 system efficiency significantly, especially when the system is operating at high ambient temperatures leading to supercritical conditions. The limitation of CO_2 high-temperature coined the term "the CO_2 equator", being a theoretical geographical line crossing central Europe, south of which CO_2 systems could not compete with HFC-based systems [45, 10].

Several research works have addressed the expansion loss challenges aiming to improve system efficiency mainly when operated under higher ambient temperatures [46, 47]. Some of the developed solutions are the implementation of parallel compression [46], mechanical subcooling [48] and overfed evaporators [49]. Other alternatives are using expanders and ejectors (discussed further in Chapter 2.2) for work recovery. The potential of expanders has been investigated for CO_2 systems in several studies [50, 51, 52], however, these are currently considered not economically competitive in comparison to ejectors, when integrated into CO_2 systems applied to, for example, supermarkets [3]. Compared to the expanders, ejectors are financially affordable, have no moving parts (i.e. improved reliability), and have the ability to handle two-phase flows without risks of damage. Consequently, Lawrence and Elbel [11] claimed that the adoption of an ejector should be favorable

to use for HVAC&R units. Considering these advantages, the adoption of ejectors to improve the efficiency of CO_2 refrigeration cycles has become a hot research topic over the last decade. Because of these technological improvements, it is now possible for CO_2 refrigeration systems to compete with those using HFCs even in central Africa [3], removing the "CO_2 equator.

2.2 Ejectors

The use of ejectors dates back to its invention by Henry Giffard in 1858, as shown in Figure 2.1. The first design was a condensing steam ejector (called injector) applied for pumping liquid water to steam-engine reservoirs [53, 54]. Since then, the device has been regarded with much interest due to its simple design and, previously considered, paradoxical physics.

> *"Seldom has an invention caused so much astonishment and wild speculation among mechanics, and even among scientists, as the injector did... It was regarded as a case of perpetual motion-the means of doing work without power, or, as the Americans expressed it, by the same means a man could raise himself by pulling on his bootstraps." - Angus Sinclair, Locomotive Engine Running and Management, 7th ed. (New York, 1887)*

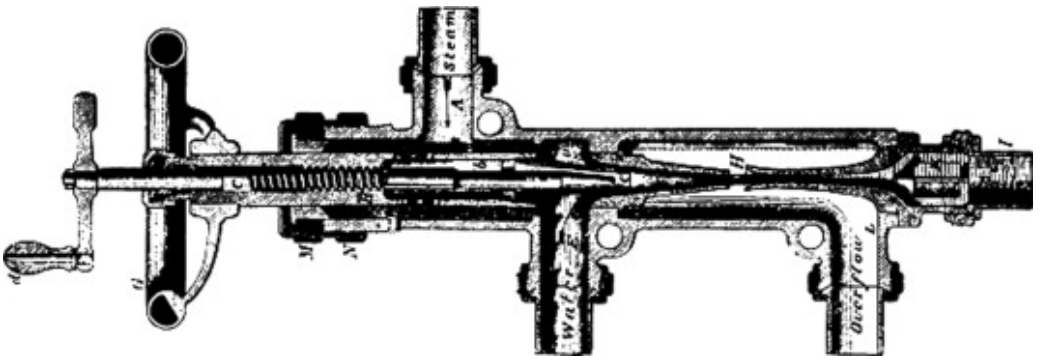

Figure 2.1: The injector design by Henry Giffard [53]

Over the years, the ejector has been used for many applications, such as nuclear and chemical engineering, where reliability and low maintenance are a priority [53]. In recent years, ejectors have been applied to new systems such as hydrogen fuel cells [55], and boil of gas pumping for liquefaction [56]. A key application of ejectors has been for refrigeration purposes. It was first introduced for expansion work recovery in refrigeration by Gay [57] and studied in detail by Kornhauser [58]. Since then, extensive research has been put toward ejectors in refrigeration systems for different working fluids such as air, steam, CO_2, hydrocarbons, ammonia, HFCs, HCFC, and HFOs [59]. The topic of ejectors in vapor compression systems has been extensively reviewed in terms of cycles and applications [7, 11, 60, 61, 62, 59], thermodynamic modeling [11, 63, 64, 62, 61, 53] geometric design [62, 59] and historic developments [59, 53, 65].

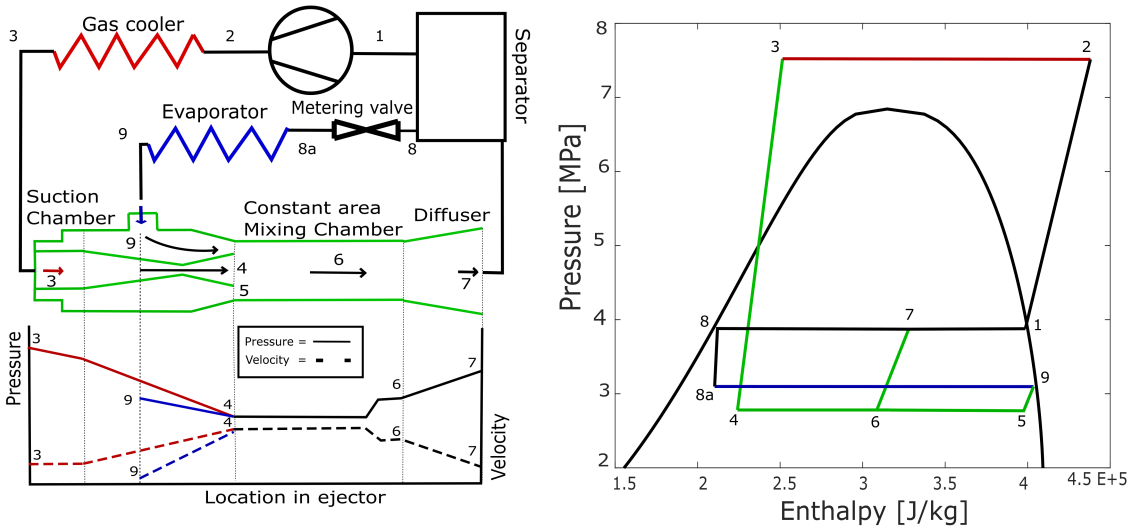

Figure 2.2: (a) Schematic of a standard transcritical ejector cycle (b) Pressure-enthalpy diagram of the transcritical ejector cycle [71].

Special emphasis has been given to ejector applications in super-critical CO_2 refrigeration and heat pump systems. The large expansion losses discussed in the previous section (Section 2.1) can then be partially recovered, reducing compressor power consumption. Ejectors for CO_2 refrigeration systems have been extensively reviewed in previous works [53, 11, 3, 66], high potential of ejectors to improve the system efficiency has been demonstrated. Elbel et al. [11] summarized that for super-critical CO_2 cycles, system COP improvements with ejector support ranged from 15-30% [67, 68, 69, 12, 15, 70], while also emphasizing some important challenges involved in ejector cycles that need to be carefully addressed, such as high-side pressure control, liquid-vapor separator design, and compressor oil return.

2.2.1 The CO_2 ejector working principle and the efficiency definition

The following section is based on the review article by the author [71]. The ejector is a device that has two inlets, named the motive (or primary) and suction (or secondary) inlets, and one outlet. The main objective of an ejector is to expand a high-pressure flow and to recover that work in the form of compressing a lower-pressure suction flow. The conventional trans-critical CO_2 cycle with ejector and its idealized pressure-enthalpy (P-h) diagram is shown in Figure 2.2a and Figure 2.2b, respectively. The refrigerant flow and an idealized pressure and velocity profile are presented in Figure 2.2 (a).

Assuming thermodynamic equilibrium, the high pressure at the motive inlet accelerates the flow in the motive nozzle converging section to sonic conditions (Ma=1)

at the throat of the nozzle. The flow accelerates further in the motive nozzle diverging section to a super-sonic flow (Ma>1). As the flow is accelerated, the pressure is reduced, which initiates a phase change process from liquid to gas in the nozzle, called flashing, when entering into the two-phase dome [72]. The motive flow continues from the divergent part of the nozzle into a low-pressure region (thermodynamic state 4) which drives the CO_2 from the secondary inlet (thermodynamic state 9) into the suction chamber (thermodynamic state 5). The primary and secondary streams are then mixed in the mixing chamber (thermodynamic state 6). The flow is then decelerated in the diffuser, converting a part of the kinetic energy into a pressure increase (thermodynamic state 7, identifying the intermediate pressure). In total, parts of the energy losses in the expansion process of the motive flow are recovered and used to compress the suction flow to produce the desired pressure lift.

Two advantages of equipping a vapor compression system with an ejector when compared to the conventional CO_2 cycle are: (I) the compressor energy consumption is reduced as a consequence of pre-compression of the flow from the low evaporator pressure (thermodynamic state 9) to the intermediate one (thermodynamic state 1); (II) increased refrigerating capacity since vapor quality and enthalpy of the flow entering the evaporator is lowered. Two-phase ejector performance is generally evaluated using the following indicators: the mass entrainment ratio (ω), the suction pressure ratio (Π), the pressure lift (P_{lift}), and the ejector isentropic efficiency (η). The mass entrainment ratio (ω) is defined as the ratio of the suction (or entrained) mass flow rate ($\dot{m}_9$) to the motive mass flow rate ($\dot{m}_3$):

$$\omega = \frac{\dot{m}_9}{\dot{m}_3} \tag{2.1}$$

where the subscript indicates the thermodynamic state referred to in Figure 2.2.

The suction pressure ratio (Π) is used to evaluate the compression ratio between the ejector outlet pressure and the ejector suction pressure. The pressure lift (P_{lift}) is used to evaluate the difference between the ejector outlet pressure and the ejector suction pressure:

$$\Pi = \frac{P_7}{P_5} \tag{2.2}$$

$$P_{\text{lift}} = P_7 - P_5 \tag{2.3}$$

Lastly, the ejector efficiency (η_{Elbel}) according to Elbel [15] is the ratio between the actual amount of work recovered by the ejector ($\dot{W}_{\text{r}}$) and the total work recovery potential for an isentropic process ($\dot{W}_{\text{r, max}}$) [15]:

$$\eta_{\text{Elbel}} = \frac{\dot{W}_{\text{r}}}{\dot{W}_{\text{r,max}}} = \omega \cdot \frac{h(P_7, s_9) - h_9}{h_3 - h(P_7, s_3)} \tag{2.4}$$

h is the specific enthalpy.

The efficiency according to Elbel [15] has become a commonly used indicator to compare CO_2 ejector performance. However, there are several other performance metrics available in the literature. Lawrence et al. [73] compared different two-phase ejector efficiency metrics and discussed their advantages and limitations. The study covered the proposed efficiencies by Nakagawa and Takeuchi [74], Butrymowicz et al. [75], Elbel and Hrnjak [15], and Ozaki et al. [76], given by:

$$\eta_{\text{Takeuchi}} = \frac{(\dot{m}_3 + \dot{m}_9)\frac{P_7 - P_9}{\rho_9} - \dot{m}_9 \frac{u_9^2}{2}}{\dot{m}_3(h_3 - h(P_7, s_3))} \tag{2.5}$$

$$\eta_{\text{Butrymowicz}} = \omega \cdot \frac{\frac{P_9}{\rho_9} \ln\left(\frac{P_7}{P_9}\right)}{\frac{P_3 - P_7}{\rho_3} + \frac{1}{2}u_4^2} \tag{2.6}$$

$$\eta_{\text{Ozaki}} = \omega \cdot \frac{h(P_7, s_9) - h_9}{h_3 - h(P_6, s_3)} \tag{2.7}$$

$$\eta_{\text{Haider}} = \frac{\dot{m}_9(h_7 - h(P_9, s_7))}{\dot{m}_3(h_3 - h(P_9, s_9))} \tag{2.8}$$

Here, u is the local velocity, ρ is the density and s is the specific entropy. The efficiencies of Nakagawa, Butrymowicz, and Ozaki require knowledge of the internal mixing pressure (P_6) for the evaluation of the ejector efficiency. This parameter is often difficult to obtain for experimental studies where the mixing pressure is not readily available. They are therefore mostly used to compare ejectors in analytical models. In comparison, the Elbel efficiency only depends on inlet and outlet parameters (suction and motive inlet enthalpy and mass flow rates) that are often easy to obtain. However, some limitations to this efficiency metric are highlighted by Lawrence et al. [73], where the Elbel efficiency calculation assumes isentropic compression, corresponding to the maximum possible work recovery. Consequently, the Elbel efficiency metric was concluded to underpredict the actual ejector recovery efficiency.

Recently, Haider et al. [77] presented an efficiency-based assumption for a separate expansion of suction and motive streams, Eqn. (2.8). The motive stream is here expanded down to suction conditions, and the suction stream is assumed to be

isentropically compressed to the outlet pressure. They found that this efficiency definition balances pressure recovery and entrainment ratio for liquid pumping.

Alternative methods for predicting efficiency can be based on entropy generation or exergy destruction in suction flow. Lawrence et al. [73] found large differences in calculated efficiencies for the same operating condition. This makes performance comparison difficult to perform as long as no consistent and validated efficiency metric yet exists. Therefore in this thesis, because of the non-availability of the pressure data at different locations of the mixing chamber, and because the efficiency definition by Elbel is commonly applied to evaluate ejector performance in previous literature [78, 3, 79], the Elbel efficiency is used to calculate ejector efficiency. The Haider efficiency was not considered for this thesis, as the study [77] was published after the main work was completed.

2.3 Ejector design

An ejector is commonly comprised of four sections; the motive nozzle, the mixing chamber, the diffuser, and the suction nozzle. The different ejector design parameters are illustrated in Figure 2.3.

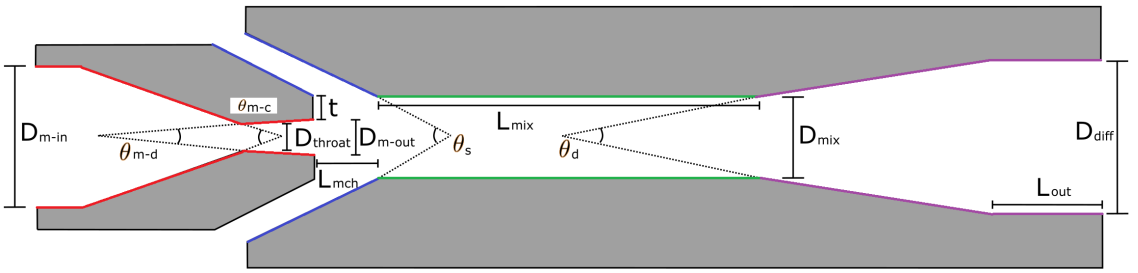

Figure 2.3: Sketch of the different ejector design parameters. The ejector's inner walls are colored according to the different ejector sections. Red: Motive nozzle, green: mixing chamber, purple: diffuser, blue: suction nozzle. Illustration based on the image from Ringstad et al. [80].

The motive nozzle is typically designed as a converging-diverging nozzle, to produce a supersonic flow towards the outlet. The motive flow is determined both by the nozzle operating conditions and the throat diameter (D_{throat}). The nozzle diverging section is designed such that it further accelerates the motive flow beyond sonic velocities. The nozzle outlet diameter ($D_{\text{m-out}}$) therefore impacts the potential expansion of the motive flow. The nozzle outlet ($D_{\text{m-out}}$) should be precisely designed in order to avoid the under- and overexpansion of the motive flow at the ejector design conditions so as to avoid irreversible losses in the jet. The mixing

chamber should be designed long enough to accommodate the mixing process of the motive and suction streams, but the length should be optimally designed in order to avoid unnecessary losses associated with shock waves and wall friction. Furthermore, the mixing chamber diameter must also be optimized such that the available flow area after the expansion of the motive flow is large enough to entrain a maximum amount of suction flow, discussed in more detail in Ringstad et al. [18]. Several studies on ejector geometry design have reported that an appropriate mixing chamber design is critical to achieving high ejector performance [17, 69, 12, 80]. In fact, improper sizing of the ejector mixing chamber has been reported to reduce the COP of ejector-based refrigeration systems by up to 10% [12]. The diffuser must be designed to recover as much pressure as possible and reduce the mixture velocity. Here, the outlet diameter (D_{diff}) must be optimized for the appropriate pressure range and the diffuser angle should be designed to avoid flow separation and shock trains. For more details on ejector design, the reader is referred to the book by Grazzini et al. [81].

2.3.1 Ejector operation control

The need for improved ejector control devices and strategies was reported by Elbel et al. [11]. A static ejector design quickly drops off in efficiency as soon as the operating conditions are different from the design point. This is generally associated with the motive nozzle and mixing chamber geometry design. First, the motive nozzle throat diameter is not variable for conventional designs, this means that for a supersonic ejector, the motive flow is choked, and the mass flow rate is primarily defined by the upstream pressure. The flow expansion process inside the nozzle is primarily determined by the nozzle outlet diameter. The relationship between the nozzle inlet and outlet diameter must therefore be established for a specific pressure design point in the mixing chamber. Consequently, at off-design conditions, the motive nozzle outlet pressure and mixing chamber pressure do not coincide, leading to losses due to the under-expansion or over-expansion of the motive flow. Second, the mixing chamber geometry has a fixed design. It is reported that both the mixing chamber length and diameter would have a significant impact on the ejector performance as it defines the suction flow behavior [69, 12, 80]. Incorrect engineering of the mixing chamber at off-design conditions was found to significantly reduce the ejector entrainment ratio [80].

For applications such as commercial transcritical CO_2 systems, ejectors typically operate under different pressure and mass flow rate operating conditions for both motive and suction flows. For a static ejector design without active control, these two variables are not possible independently control due to the flow being choked. Hence, consistent control strategies should be implemented for capacity control. Different capacity control techniques with ejectors have recently been reviewed by Gullo et al. [66], for more details see their review article.

To the best of the authors' current knowledge, four capacity control solutions for CO_2 ejectors have been reported in the literature: the needle-controlled ejector [15], the multi-block ejector [13], the swirl-controlled ejector [82], and the pulse width modulation (PWM) ejector [47]. These approaches are typically compared to a baseline system with a static ejector and a parallel expansion valve to control the flow rate and high side pressure. The different ejector capacity control solutions are illustrated in Figure 2.4.

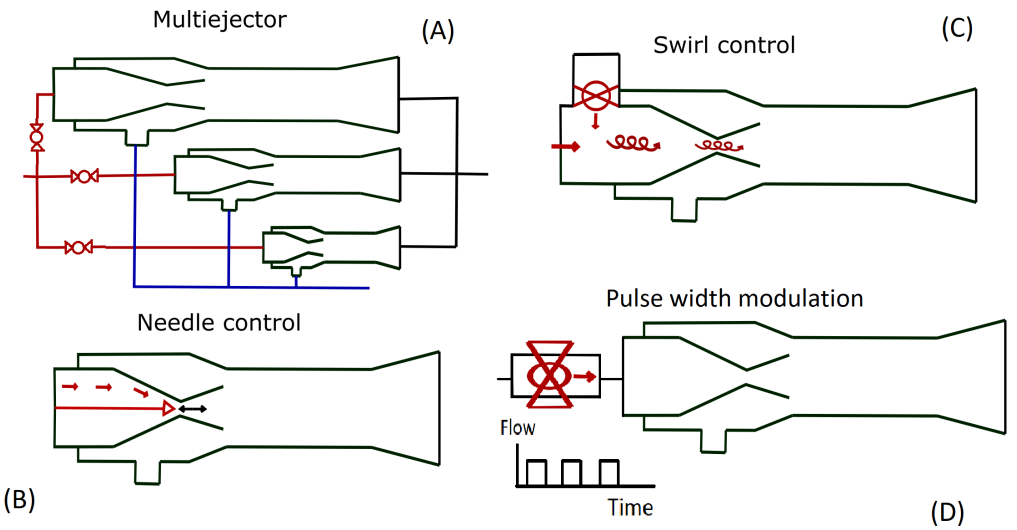

Figure 2.4: Illustrations of the ejector concepts for three ejector control solutions [71].

As can be seen in Figure 2.4 (B), the needle-controlled ejector is controlled by moving a needle towards and out from the motive nozzle throat to change the flow area of the motive nozzle and consequently the flow rate. Elbel and Hrnjak [15] investigated this approach and found that the needle-controlled ejector can be implemented to control the high-side pressure and improve COP by up to 7%. However, the authors have reported some limitations associated with this control strategy [11], such as the increased friction induced by the needle and the high precision of the needle positioning needed for accurate control and high performance. Gullo et al [66] reported the importance of an accurate design of the needle for capacity control. Liu et al. [83, 14] studied the performance of a CO_2 air-conditioner with a needle-controlled ejector and reported a maximum improvement in COP of up to 147%.

Figure 2.4 (A) shows the multi-ejector concept which consists of several ejectors of different sizes arranged in parallel (typically 4-6 ejectors). The ejectors are activated using solenoid valves. The ejector sizes are activated and combined in such a way

as to control the ejector motive mass flow rate. The concept was initially proposed and investigated by Hafner et al. [13] and has since then been thoroughly studied for supermarket and heat pump applications [84, 7]. The device has also been implemented commercially in the Danfoss Multiejector block [85]. The application of the multi-ejector concept to control the motive flow rate has shown a COP improvement of up to 7% [86]. However, as for the needle-controlled ejector, the control strategy of the multi-ejector block is quite complex to quickly control the different solenoid valves to achieve the intended flow rate and the multi-ejector block is obviously more expensive than using a single ejector [66].

The swirl-controlled ejector (also referred to as a vortex ejector) is shown in Figure 2.4 (C) and the ejector control is performed by adjusting the swirl component of the motive flow before the nozzle. The control strategy is based on the swirl intensity limiting the maximum flow rate through the nozzle. The motive flow is split into two flows, one flow entering the motive nozzle in the normal direction, and the second flow entering in a tangential direction to generate swirl motion. The motive swirl intensity is then controlled by a valve (shown at the top of the nozzle in Figure 2.4 (c)) which regulates the tangential component of the motive flow. The swirl-controlled ejectors are often preferred to the needle-controlled ejectors as it offers a reduced risk of clogging, less maintenance as it includes no moving parts, and lower cost [66]. This design was initially suggested for an R134a ejector by Zhu and Elbel [82], who claimed that the swirl component could be used to limit the motive flow by up to 36% compared to a no swirl ejector. Later on, Zhu et al [19] studied the influence of various geometry parameters on swirl ejector performance. Their findings have shown that the length of the nozzle diverging section is critical for the swirl control mechanism to function [19]. The vortex-controlled ejector has been further investigated by Zhu and Elbel [87] for CO_2 refrigeration systems achieving a COP improvement of 8.1%. The achieved COP improvements were found to be very similar (0.2% lower COP for swirl controlled) to those obtained by needle-controlled ejectors. The swirl-controlled ejector is still undergoing experiments at a laboratory scale [66].

A pulse-width modulation (PWM) controlled device was proposed by Gullo et al. [47]. This concept modulates the ejector capacity by opening and closing the motive nozzle for a specified period of time corresponding to a specified capacity requirement. E.g. if 70% ejector capacity is required, the motive nozzle of the PWM ejector will be opened for 70% of a given time window. This concept is illustrated in Figure 2.4 (D). PWM ejectors were found to achieve up to 5% improvement in COP compared to a passive ejector system, which is higher than the 2-4% improvement found for needle and vortex ejectors. However, this solution requires that the evaporator flow is stopped intermittently with the pulse frequency, which may reduce system efficiency. Similarly to the swirl-controlled ejectors, the PWM

control design technology is still in early-stage investigations, and further work is needed to qualify it as a competitive solution.

Another potential concept for ejector control is variable-area radial ejectors. Such ejectors have the motive nozzle in a radial configuration, which allows the motive flow area to be controlled by increasing or decreasing the separation of the two discs that define the motive flow duct. The concept has been numerically investigated for air ejectors by Rahimi et al. [88]. They found that increases in entrainment ratio up to 30% are possible by controlling the separation between the motive nozzle discs. Radial ejectors are still in the early stages of research and further work is needed to further verify the concept. Further investigation into its application for CO_2 ejectors and comparison with other variable area flow control mechanisms are suggested.

2.3.2 Suction bypass ejectors

Another way to improve the ejector performance is the active control of the suction flow. One device based on such a design is the suction bypass design [79], shown in Figure 2.5. This ejector has an additional inlet connected to the suction line placed along the mixing section. The functionality of this additional inlet is to entrain additional suction flow when the system operates at off-design conditions. At off-design operating conditions, the pressure distribution in the mixing section of the ejector is so that a low-pressure zone typically occurs near the end of the ejector. This bypass inlet is then placed near this low-pressure zone such that additional suction flow enters the ejector, consequently increasing the entrainment ratio. The bypass concept was found to improve ejector performance as it reduces entropy production caused by supersonic shocks and increases entrainment ratio [79]. Suction bypass ejectors have been explored for CO_2 ejectors by Bodys et al. [16, 79]. Bodys et al. [16] have further discussed the possibility of exploring bypass swirl to further improve the ejector efficiency. The optimal axial placement of the bypass inlet for the highest efficiency at varied operating conditions is still a challenge with such concepts that need further exploration.

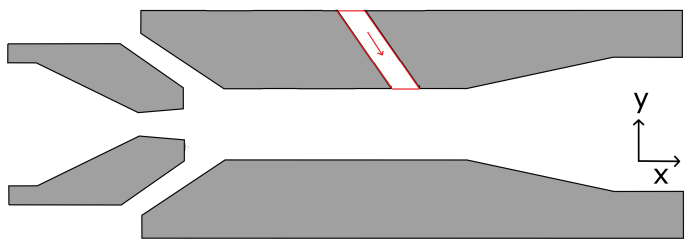

Figure 2.5: Illustration of an ejector with an installed bypass inlet colored in red.

The swirl flow component has a theoretical benefit for flow mixing, as the motive- and suction flows exchange momentum over a longer path. Moreover, the increased turbulence induced by the swirl may improve mixing. Bodys et al. [89] numerically investigated the effects of the swirl component in both the motive and suction nozzle inlet conditions of a two-phase CO_2 ejector. It was concluded that a 3% increase in the entrainment ratio could be achieved when including an inlet swirl component at the motive nozzle inlet. However, including a swirl component in the suction flow was found to negatively affect the suction flow rate and consequently reduced the entrainment ratio. A novel concept combining swirl flow generation with the bypass concept is further presented in this thesis based on numerical simulation. This design could be applied both for increasing off-design operation with suction flow bypass or for control of motive mass flow rate, illustrated in Figure 2.6 (A) and (B), respectively. For detailed information, the reader is directed to Ringstad et al. [18].

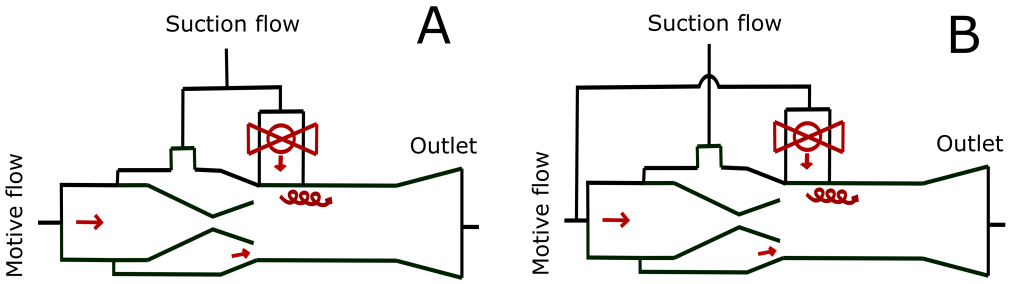

Figure 2.6: Illustration of the two swirl-bypass concepts (A) and (B). Concept (A) is a suction swirl bypass ejector. Concept (B) is a motive swirl bypass ejector.

3 Thermo-fluid dynamic models

"It's still magic even if you know how it's done."

— T. Pratchett, *Wee Free Men*

This chapter presents background theories for the methodologies applied in the Thesis. Multiphase fluid dynamics, thermodynamics of CO_2, turbulence, and numerical modeling are here discussed. The models used in this work are presented in detail in Section 3.2. The model validation and mesh independence studies are also presented in Section 3.4.

For a complete review of two-phase CO_2 ejector modeling the reader is referred to Ringstad et al. [71].

3.1 Background theory

3.1.1 Multiphase fluid dynamics

Fluid dynamics involves empirical and semi-empirical laws describing the flow of fluids in order to understand their behavior under applied forces. The field is comprised of several challenging problems that are actively studied. Some of the more investigated topics are super-sonic and compressible flows, turbulence, fluid-structure interactions, multiphase flows, and reacting flows. The underlying assumption of fluid dynamics is that fluids are continuous, disregarding molecular dynamics. From this, a set of fundamental conservation equations for mass, momentum, and energy, which collectively are referred to as the Navier-Stokes equa-

tions, can be derived. The Navier-Stokes equations are, however, defined within a single continuous fluid and are therefore ill-posed at the discontinuous interface between two phases, such as liquid and gas. Therefore special attention must be dedicated to defining models that handle the conservation equations with moving interfaces at various length scales. The most commonly used models for multiphase flows are derived from integral averaging, to reduce the interface discontinuities to source terms, in an averaged set of the continuum equations [90].

Flows where more than one phase exists, such as liquid-gas or gas-solid, are referred to as multiphase flows. Multiphase flows are characterized by the regime (flow pattern) that develops in the flow. These flow regimes are classified according to how the different phases are distributed and flow. Common classifications that are referred to in the literature are shown in Figure 3.1.

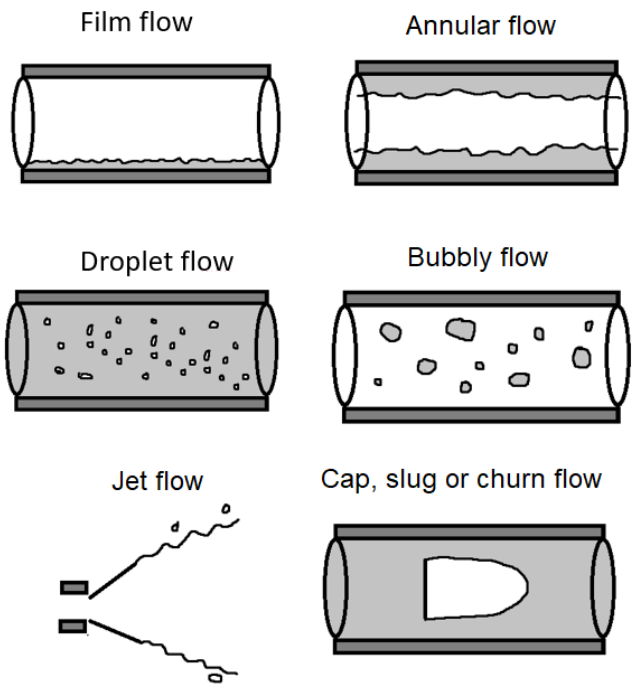

Figure 3.1: Illustration of different two-phase flow regime classifications, based on more detailed classifications by Ishii and Hibiki [90]

Modeling of the CO_2 two-phase ejector is highly challenging due to the coupled flow dynamics, two-phase flow with different types of flow regimes (atomization jet flow, bubbly flow, droplet flow), nucleation and phase change, super-sonic and compressible flow, turbulence in a two-phase system, and complex thermodynamics

(super-critical and non-equilibrium conditions). The limited availability of experimental data is another challenge, as this makes the results difficult to assess. The challenges associated with the CO_2 two-phase ejector modeling are described in the following sections. For further details the reader is referred to Ringstad et al. [71].

3.1.1.1 Models of two-phase flow

The large variation of flow phenomena in two-phase flows requires different models to be employed. To this end, several multiphase models have been described in the literature with different levels of complexity and underlying assumptions. These models are based on an averaging procedure, such as over space or time, of the single-phase Navier-Stokes fluid flow equations:

$$\frac{\partial}{\partial t}\rho_k + \nabla \cdot (\rho_k \vec{u}_k) = 0, \tag{3.1}$$

$$\frac{\partial}{\partial t}\rho_k \vec{u}_k + \nabla \cdot (\rho_k \vec{u}_k \vec{u}_k) = -\nabla \cdot P_k + \nabla \cdot \tau, \tag{3.2}$$

$$\frac{\partial}{\partial t}\rho_k (i_k + \frac{u_k^2}{2}) + \nabla \cdot (\rho_k \vec{u}_k (i_k + \frac{u_k^2}{2})) = -\nabla \cdot Q_k + \nabla \cdot (T_k \cdot \vec{u}_k) \tag{3.3}$$

One way of classifying the different models is proposed by Linga et al. [91]. Following this classification, the multiphase models are organized according to the degree of non-equilibrium between the phases accounted for by the model. Physically, the phases exist at different pressures (P_k), temperatures (T_k), velocities ($\vec{u}_k$), and Gibbs free energy (g_k). These non-equilibriums are typically simplified for the sake of tractability and reduced complexity. The different models can then be classified according to the combination of variables in disequilibrium that are accounted for. The most simplified models are the 3-equation homogeneous equilibrium models that assume full equilibrium for all variables. By accounting for chemical disequilibrium in the Gibbs free energy, g_k, the 4-equation homogeneous models are obtained. These models can account for meta-stable thermodynamic states, which is a preferred property for applications with rapid depressurization such as ejectors. Two-fluid models (or Eulerian-Eulerian models) allow for non-equilibrium in velocity, temperature, and chemical potential, where the phases are considered co-existing interpenetrating flows with their own set of flow equations that are coupled by several sub-models. Table 3.1 presents an overview of current R744 models and which non-equilibrium states are considered in each model.

Each disequilibrium included increases complexity and, consequently, requires additional sub-models. To account for chemical disequilibrium, model equations for the phase change process must be supplied. Similarly, to account for the velocity disequilibrium of the phases, appropriate models for the velocity slip are needed.

Table 3.1: Overview of the considered disequilibrium of different models

Non-equilibrium	Chem	Mom	Temp	Press
HEM [92],[93],[94]	×	×	×	×
HRM [95],[96]	✓	×	×	×
Mixture [97]	✓	×	×	×
Mixture [98]	✓	✓	×	×
Two-Fluid [99]	✓	✓	✓	×

The main challenges with increasing model complexity are the increased model uncertainties and the introduction of additional parameters which often require experimental tuning.

3.1.1.2 Phase change models

For CO_2 two-phase liquid-gas ejectors, the primary flow is subject to a rapid acceleration in the motive nozzle. Typically, the pressure drops below the saturation pressure near the nozzle throat or in the nozzle diverging section (see Figure 2.2). This process initiates a phase change from liquid to gas. The phase change process occurs in two stages: bubble nucleation and bubble growth. Bubble nucleation is the process where the first bubbles are nucleated in the liquid, and bubble growth is a phase change occurring on the bubble-liquid interface. Due to the rapid pressure drop, the timescales where the liquid CO_2 is in a metastable superheated state become comparable to the flow time-scale, discussed below.

To nucleate a stable bubble, energy is required to overcome the necessary surface tension- and expansion energy of the bubble. By analyzing the work required to nucleate a bubble as a function of bubble size, it can be shown that any bubble below a certain size will spontaneously collapse. Similarly, any bubble larger than this size will spontaneously grow and remain stable [81]. This size scale is referred to as the critical radius, r_c, and is reduced with increased superheat. The larger the bubble, the higher the required work necessary to generate the bubble. The work required to produce such a bubble is also higher for larger bubbles. The nucleation of a stable bubble will therefore occur if a random fluctuation of energy is larger than this required work. The models used to predict nucleation are therefore often stochastic and based on kinetic theory. Another factor for nucleation is the presence of surfactants and nucleation sites, such as on walls, which can reduce the required work [81]. After nucleation, bubble growth is typically analyzed with bubble dynamic equations, such as the Rayleigh-Plesset equations [100]. Here, heat, mass, and momentum exchange between the bubbles and the surrounding liquid are important to predict. In literature, simplified models accounting for the phase change in CO_2 ejectors simplified models for phase change are often reported.

These models are popular because of the high complexity of the problem.

3.1.2 Thermodynamic equation of state

Appropriate prediction of the thermodynamic properties is important for simulation accuracy. This is especially applicable for CO_2 two-phase ejectors that typically operate at supercritical and near-critical conditions. To close the equation set of thermo-fluid flow an equation of state is needed that relates the thermodynamic states, such as temperature and pressure, to the thermodynamic properties, such as density, speed of sound, or thermal conductivity. An equation of state (EoS) is an equation of the form:

$$f(P, V, T) = 0. \tag{3.4}$$

The Span-Wagner EoS (SW-EoS) [101] is considered the most accurate and reliable equation of state for CO_2 [102]. Due to the high computational costs of the Span-Wagner method [101], pre-calculated look-up tables for thermodynamic properties have been applied in the literature to provide simulation models with lower computational cost [103, 94, 92, 97]. The thermodynamic properties are interpolated based on the look-up tables, which introduces an error. Using more points in the pre-calculated look-up table will increase the accuracy of the method, however, will also increase the computation time and required computational storage capacity of the method. As an example, Giacomelli et al. [97] found errors in the properties estimates up to 1.6% in their coarse lookup table. However, the smaller-sized look-up table was preferred to reduce computation time. Alternatively, look-up tables based on variable step size are preferred, such as those implemented by Fang et al.[103]. This is especially important near the critical point of CO_2, where large variations in properties occur. Following the work by Span and Wagner [101], further efforts have been put toward improving the modeling of CO_2 properties. The modeling of e.g. the liquid phase and near-critical viscosity has been improved by more accurate experimental measurements [104, 105, 106], however, uncertainties up to 3-4% in liquid viscosity are still observed in the latest correlations. The effect of bulk viscosity (volume viscosity) can be significant for compressible flow with poly-atomic gases. Fang et al. [94] studied the effect of bulk viscosity on a converging-diverging nozzle with CO_2 using CFD. It was concluded that the bulk viscosity had no noticeable effect on the flow. Furthermore, it has been reported by Awad et al. [107] that appropriate averaging laws should be considered for mixture properties. The EoS used in this work is further discussed in Section 3.3.4

3.1.2.1 Non-equilibrium effects

Knowledge of non-equilibrium effects is critical for a proper understanding of two-phase ejectors. In a two-phase flow, non-equilibrium states can be divided into thermodynamic and transport non-equilibriums. Thermodynamic non-equilibrium

corresponds to the superheated or subcooled state of a liquid or gas, respectively. Transport non-equilibrium corresponds to differing temperatures, pressures, or velocities of the phases [91].

During rapid depressurization, as in the motive nozzle of a CO_2 ejector (see Figure 2.2), the saturation temperature will drop below the liquid temperature, superheating the liquid. The liquid starts to evaporate until the equilibrium state is reached. The degree of superheat is therefore limited by the phase change mechanism. Beyond the homogeneous nucleation line (HNL), shown in Figure 3.2, any perturbation will rapidly induce a phase change, imposing the upper limit on superheating. Even so, the speed of this phase change can be non-negligible in comparison to the rate of transport at high velocities in ejector motive flows. Three cases of ejector motive conditions are plotted with an illustrated isenthalpic expansion process in Figure 3.2, which corresponds to the expansion process in the motive nozzle. Case 1 is a near-critical expansion, and cases 2 and 3 are off-critical expansions, in terms of the notions established in Ringstad et al. [99]. From Figure 3.2 one may note that as the degree of sub-cooling at the motive nozzle inlet increases (lower enthalpy) and moves towards off-critical expansion, the theoretically achievable superheat increases, and so do the relevance of Gibbs free energy non-equilibrium. It is clear that for near-critical expansion the possible thermodynamic non-equilibrium is very small as the path almost immediately crosses the HNL, and therefore the phase change occurs rapidly. The figure is generated based on the framework established by Wilhelmsen et al.[108] and Aursand et al. [109].

3.1.2.2 Speed of sound

The speed of sound through a fluid is the speed at which a pressure disturbance can propagate and is defined as:

$$c = \left(\frac{\partial P}{\partial \rho} \right)_s^{1/2}, \tag{3.5}$$

This property is a well-defined thermodynamic property in single-phase flows. For multiphase flows, the speed of sound will depend on the flow characteristics and mathematically on the chosen model assumptions. In general, the speed of sound is lower for a two-phase mixture than the speed of sound for either phase in isolation. Each equilibrium condition enforced in the modeling assumptions reduces the two-phase speed of sound [110]. When assuming full equilibrium between the two phases, the speed of sound drops significantly and is discontinuous as a function of vapor fraction. As discussed by Brennen [111], the calculation of the two-phase speed of sound increases rapidly in complexity as more multiphase effects are included. The choice of two-phase speed of sound for CO_2 two-phase ejectors is

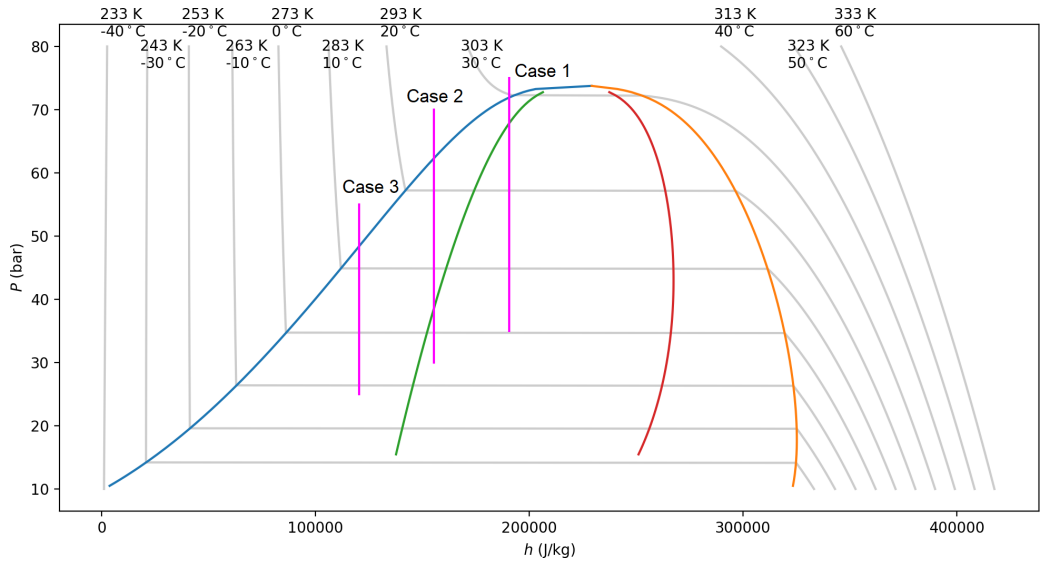

Figure 3.2: P-h plot of the saturation- and homogeneous nucleation lines based on the framework by Wilhelmsen et al. [108] and Aursand et al. [109]. The phase envelope is shown as blue and orange lines indicating the liquid and vapor sides, respectively. These lines meet at the critical point. The red and green lines are the limits where homogeneous nucleation will occur, of bubbles in the liquid phase (crossing the green line from the left) or droplets in the vapor phase (crossing the red line from the right). The magenta lines indicate isenthalpic expansion for three different initial state points with near-critical and off-critical expansion. The grey lines are isotherms, as labeled at the top.

further discussed by Giacomelli et al. [112] and De Lorenzo [113]. In this work, the speed of sound model is calculated from interpolation between points in the equation of state.

3.1.3 Turbulence

An accurate description of the mixing phenomenon and the flow structure inside the ejector is highly dependent on accurate modeling of the turbulent flow. Due to the complexity and lack of insight into multiphase turbulence, accurate turbulence modeling in CO_2 two-phase ejectors is more complex than for single-phase ejectors. Multiphase turbulence has therefore often been ignored in current CO_2 ejector models.

To model compressible multiphase turbulence, fluctuations in velocity, density, and mass fraction, as well as interface effects must be considered. Different averaging procedures are therefore considered to reduce the need for excessive sub-modeling. A common approach is to use ensemble- and phase averaging. Model complexity can then be reduced to modeling a few additional terms in the momentum and

energy equations. Most prominent is the non-linear momentum fluctuation $u_i'u_j'$, typically modeled by a Boussinesq approximation, Eqn. (3.6), where turbulent fluctuations are treated as a diffusive turbulent viscosity.

$$\overline{u_i'u_j'} = \nu_t(\frac{\partial u_i}{\partial x_j} + \frac{\partial u_j}{\partial x_i}) - \frac{2}{3}k\delta_{ij} \tag{3.6}$$

Where, u' is a turbulent fluctuation in the velocity field, and ν_t is the turbulent viscosity. Commonly, a set of transport equations for turbulent kinetic energy, k, Eqn. (3.7), and the turbulent energy dissipation ϵ Eqn. (3.7), is solved to close the relation for turbulent viscosity relation, according to $\nu_t = C_\nu \frac{k^2}{\epsilon}$.

$$\frac{\partial(\rho_m k)}{\partial t} + \frac{\partial(\rho_m k u_i)}{\partial x_i} = \frac{\partial}{\partial x_j}\left[\frac{\mu_t}{C_k}\frac{\partial k}{\partial x_j}\right] + G_{k,m} - \rho_m\epsilon + \Upsilon_{\epsilon,m} \tag{3.7}$$

$$\frac{\partial(\rho_m \epsilon)}{\partial t} + \frac{\partial(\rho_m \epsilon u_i)}{\partial x_i} = \frac{\partial}{\partial x_j}\left[\frac{\mu_t}{C_\epsilon}\frac{\partial \epsilon}{\partial x_j}\right] + \frac{\epsilon}{k}\left[C_{1\epsilon}G_{k,m} - C_{2,\epsilon}\rho_m\right] + \Upsilon_{k,m} \tag{3.8}$$

where the subscript, m, indicates mixture properties based on mass or volume-weighted averaging. $G_{k,m}$ is the strain rate production of k, $G_{k,m} = \mu_t(\partial u_j/\partial x_i + \partial u_i/\partial x_j)^2$. Interfacial turbulence interactions are included in the terms $\Upsilon_{k,m}$ and $\Upsilon_{\epsilon,m}$, which are further sub-modeled [114]. Additional multiphase effects, such as bubble-induced turbulence, dispersion forces, and the influence of other neglected terms have so far not been discussed in any of the current CO_2 ejector models.

Multiphase turbulence modeling is made challenging for ejectors due to the variation of operating conditions and geometry. As one ejector can have different turbulent characteristics and length scales, flow regimes, and velocities, multiphase turbulence models will have to make assumptions that may improve prediction accuracy for only a subset of ejectors. In addition, these interactions will then depend on the multiphase formulation used. Lastly, validating these models with local measurements is highly challenging due to the difficulties in obtaining and analyzing the data in terms of multiphase turbulence. For further details on multiphase turbulence see the texts by Ishii and Hibiki [90], Coutier-Delogosha et al.[115], and Morel [116].

3.1.3.1 Turbulence models

The commonly used CO_2 ejector models consider pseudo-fluid turbulence, i.e. assuming that the turbulent structures behave similarly to single-phase turbulence. Already, a large set of turbulence models have been studied for CO_2 ejector modeling, as shown in Table 3.2. The latest research articles recommend the use of the k-ω SST model due to its better predictions of local and global flow parameters for single-phase flows [117, 118, 119]. A comparison of turbulence model performance

for CO_2 ejectors was conducted by Haida et al. [78]. In this work, the authors compared four commonly used turbulence models, namely the k-ϵ Realizable model, the k-ω SST model, the Transition SST model, and the Reynolds stress model. It was found that the Transition SST model and the Reynold stress model were best at predicting the local wall temperatures. Furthermore, the global entrainment ratio was found to be best predicted by the k-ϵ Realizable and the Transition SST. The authors noted a significant dependence on the near-wall turbulence formulations for the Reynolds stress model and the k-ϵ Realizable model. Recently, Bodys et al. [120] investigated the effect of turbulence models on a CO_2 ejector performance. They concluded that the most accurate formulations were the k-ω standard and the transition k-kl-ω model.

The disagreements in the literature indicate that further research is needed into appropriate turbulence models for two-phase ejector flow. Two-phase turbulence effects have largely been neglected in current literature and will require detailed investigations. Furthermore, it is highlighted that the interaction between the specific two-phase and turbulence model is important. This implies that the most accurate turbulence model may be different for different two-phase models.

Table 3.2: Presentation of the different turbulence models used for CO_2 ejector modeling and the corresponding multiphase model.

Study	Turbulence model	Model
[95]	$k-\epsilon$	HRM
[98]	$k-\omega$ SST	Mixture
[92]	$k-\epsilon$ RNG	HEM
[121]	$k-\epsilon$ RNG	HEM
[93]	$k-\omega$ SST	HEM
[122]	$k-\epsilon$ Realizable	HEM
[17]	$k-\epsilon$ Realizable	HEM & HRM
[123]	$k-\epsilon$ RNG	HEM
[124]	$k-\omega$ SST	HRM
[125]	$k-\epsilon$ Realizable	HEM
[97]	$k-\omega$ SST	Mixture & HEM
[78]	Comparative (4 models)	HRM
[94]	Comparative (2 models)	HEM
[120]	Comparative (5 models)	HNB

3.1.3.2 Wall models

The near-wall flow structures occur on different length scales in a boundary layer. By non-dimensionalizing the boundary layer velocity profile by the wall shear pa-

rameters, Eqns. (3.9-3.11), the turbulent boundary layer can be characterized according to the mechanisms that dominate at that length scale.

$$u_\tau = \sqrt{\frac{\tau_w}{\rho}} \tag{3.9}$$

$$y^+ = \frac{y u_\tau}{\nu} \tag{3.10}$$

$$U^+ = \frac{U}{\tau} \tag{3.11}$$

Close to the wall (y+<5) the viscous forces dominate, this region is referred to as the viscous sublayer. In this region, the velocity increases linearly with wall distance and the following relation holds:

$$U^+ = y^+ \tag{3.12}$$

Further from the wall ($5<y^+<30$), the flow structures transition into a turbulence-dominated region referred to as the buffer region. Beyond this ($y^+ > 30$) turbulence dominates the boundary layer. This region is referred to as the logarithmic sublayer as the velocity varies logarithmically with wall distance according to the relationship:

$$U^+ = \frac{1}{\kappa}\ln(y^+) + B, \tag{3.13}$$

where κ is the Karman constant, and B is a constant typically set to 5.2.

To solve the flow in this region, two approaches are commonly used; the Low Reynolds Number (LRN) approach and the wall model approach [126, 99]. The LRN method involves resolving the local structures to the wall. This necessitates the use of high-resolution meshes that resolve the turbulent length scales down to $y^+ \approx 1$. Alternatively, wall models such as Eqn. (3.13) can be used if the mesh is resolved down to the logarithmic sublayer ($y^+ \approx 30$). In most commercial software there are scalable wall functions available. These wall functions will use the LRN and wall models were applicable based on the local y^+ value of the mesh. These approaches are best applied to industrial cases or for CFD simulations where detailed knowledge of the flow structure is not available prior to meshing.

The effect of two-phase flows and nucleation is not considered in any of the turbulence models currently implemented, though several are available in the literature [127, 128]. However, their associated effects can be significant. Further work is then needed for further model improvements.

3.2 CO_2 ejector models and model development

As a part of this work, several models were developed and tested. Some of these models are also compared by Ringstad et al .[129]. Several of the models used and developed in this work are based on previous work at international research laboratories at the Silesian University of Technology - SUT and the Università Degli Studi di Firenze - UniFI.

3.2.1 Homogeneous Equilibrium Model

A homogeneous equilibrium model (HEM) based on the formulation by Smolka et al. [92] was developed and tested in this work. The version used in this work was developed with the guidance of the research group at SUT, adopting the same mathematical structure and numerical implementation [92, 122, 79].

The HEM assumes that both phases are at full mechanical, thermal, and thermodynamic equilibrium, hence the flow can be described using a single velocity-($\vec{u}$), temperature- (T), and pressure-field (P). The HEM is therefore classified as a pseudo-fluid or single-fluid approach where a single set of transport equations are solved for the mixture mass and momentum, respectively:

$$\frac{\partial}{\partial t}\rho_m + \nabla \cdot (\rho_m \vec{u}) = 0, \tag{3.14}$$

$$\frac{\partial}{\partial t}\rho_m \vec{u} + \nabla \cdot (\rho \vec{u}\vec{u}) = -\nabla \cdot P + \nabla \cdot \tau, \tag{3.15}$$

In this model, the mixture energy equation is reformulated to an equivalent enthalpy formulation:

$$\frac{\partial}{\partial t}\rho_m h_m + \nabla \cdot (\rho \vec{u} h_m) = \nabla \cdot (\Sigma_{\text{eff}} \nabla h_m) + \dot{S}_{h1} + \dot{S}_{h2} + \dot{S}_{h3} \tag{3.16}$$

Here, the subscript m indicates the pseudo-fluid mixture properties: ρ, $\vec{u}$, p, h, q refer to the density, velocity, pressure, enthalpy and heat flux, respectively. The effective stress tensor $\tau_{ij,\text{eff}}$ is the laminar (Newtonian) and turbulent stress tensors combined, $\tau_{ij,\text{eff}} = \tau_{ij} + \tau_{ij,\text{turb}}$. In this equation, Σ_{eff} is the effective diffusion coefficient, defined as:

$$\Sigma_{\text{eff}} = \frac{\mu_t}{Pr} + \frac{\lambda}{c_p}, \tag{3.17}$$

where μ_t is the turbulent viscosity, Pr is the Prandtl number, c_p is the mixture specific heat capacity, and λ is the thermal conductivity. The source terms $\dot{S}_{h1,2,3}$ in Eqn. (3.16) describe the mechanical energy (Eqn. 3.18), the irreversible dissipation

of the kinetic energy variations (Eqn. 3.19), and the dissipation of the turbulent kinetic energy (Eqn. 3.20), respectively [92].

$$\dot{S}_{h1} = u_i \frac{\partial P}{\partial x_i} \tag{3.18}$$

$$\dot{S}_{h2} = (\mu + \mu_T) \left[\frac{\partial u_i}{\partial x_j} + \frac{\partial u_j}{\partial x_i} - \frac{2}{3} \delta_{ij} \frac{\partial u_k}{\partial x_k} \right] - \frac{2}{3} \rho k \tag{3.19}$$

$$\dot{S}_{h3} = -\rho u_i \frac{\partial k}{\partial x_i} \tag{3.20}$$

The enthalpy and pressure can then be used to uniquely identify the thermodynamic equilibrium state, from which the thermodynamic properties can be calculated. Properties are typically divided into thermophysical (Eqn. 3.21) and transport (Eqn. 3.22) properties.

$$\begin{bmatrix} \rho \\ c_p \\ \alpha \\ T \\ s \end{bmatrix} = f(p, h), \tag{3.21}$$

$$\begin{bmatrix} \mu \\ \lambda \end{bmatrix} = g(P, h), \tag{3.22}$$

where $\rho, \alpha, \mu, \lambda, c_p, s$ are the pseudo-fluid density, vapor volume fraction, kinematic viscosity, thermal conductivity, heat capacity, and entropy, respectively.

The properties of liquid and gas are evaluated by the pressure and enthalpy, interpolated from a look-up table. The CoolPack library [130] for CO_2 is based on the Span-Wagner equation of state.

This CFD model was implemented into Fluent 2020 R1. The model was developed using user-defined functions for energy equation source terms and thermophysical properties, in addition to user-defined scalars for the mixture enthalpy.

3.2.2 User-Defined Real Gas - Mixture Model

The user-defined real-gas mixture model (UDRGMM) was developed in a previous work by Giacomelli et al. [112].

The mixture model is based on the standard formulations of pseudo fluid mixture models, with the mixture continuity and momentum equations as defined in Eqns. (3.14 - 3.15) and the energy equation is formulated as:

$$\frac{\partial}{\partial t}\left(\rho_m E_m\right) + \frac{\partial}{\partial x_j}\left[\rho_m u_{mj} E_m + u_{mj} P_m + Q_{mj} - u_{mi}\tau_{mij}\right] = 0, \tag{3.23}$$

At equilibrium, the pressure and enthalpy define the vapor quality of the flow. However, at non-equilibrium, an additional transport equation for the vapor fraction with a phase change model is needed, defined as:

$$\frac{\partial \rho\alpha}{\partial t} + u_j \frac{\partial \rho\alpha}{\partial x_j} = \Gamma, \tag{3.24}$$

where Γ is a phase source term modeling the phase change. The transport equation for the volume fraction (Eqn. 3.24) is solved with the mass transfer terms for evaporation and condensation explicitly included:

$$\Gamma = \Gamma_e - \Gamma_c, \tag{3.25}$$

where Γ_e and Γ_c are the mass transfer sources due to evaporation and condensation, respectively. Such an improved estimation of the phase composition allows for a more accurate estimate of the mixture properties. The properties are calculated based on mass-weighted averaging (Eqn. 3.26) for the thermodynamic variables, e.g. enthalpy or total energy, or volume-weighted average (Eqn. 3.27) for the variables mixture density, molecular viscosity, or thermal conductivity :

$$\xi_m = \beta_l \xi_l + (1 - \beta_l)\xi_v, \tag{3.26}$$

$$\psi_m = \alpha_l \chi_l + (1 - \alpha_l)\chi_v, \tag{3.27}$$

where ξ, and ψ are generic properties, α and β are the volume and mass fractions respectively. The subscripts l, v, and m correspond to the liquid, vapor, and mixture properties, respectively.

Giacomelli [97] considered a mass transfer model based on the Clausius-Clapeyron and Hertz-Knudsen equations, referred to as the Lee model [114]:

$$\Gamma_e = \Lambda_e \alpha_l \rho_l \frac{T - T_{sat}}{T_{sat}}, \tag{3.28}$$

$$\Gamma_c = \Lambda_c \alpha_v \rho_v \frac{T - T_{sat}}{T_{sat}}. \tag{3.29}$$

The main novelty in this approach is that the thermodynamic look-up tables are included for all variables and their derivatives through the ANSYS Fluent user-defined Real Gas Model. This allows more accurately calculated thermodynamic properties at the cost of additional computation time.

3.2.3 Two fluid model

Based on a combination of code from both the UDRGMM and the HEM approaches, a two-fluid model was implemented into the ANSYS Fluent Eulerian model. In comparison to previous pseudo-fluid approaches, a two-fluid model (TFM) allows for the full disequilibrium of velocity, temperature, and phase fraction (thermodynamic state). The two-fluid model solves one set of transport equations for each phase, q, with the surrounding phase, p. An equation for the mass (Eqn. 3.30), momentum (Eqn. 3.31), and energy (Eqn. 3.32) is solved for each of the two phases, liquid, and gas. Thus, 6 transport equations are solved, not including turbulence models. The pressure, P_m is assumed to be equal for both phases.

$$\frac{\partial \alpha_q \rho_q}{\partial t} + \frac{\partial}{\partial x_j}\left[\alpha_q \rho_q u_{qj}\right] + \Gamma_{qp} = 0, \tag{3.30}$$

$$\begin{aligned}\frac{\partial}{\partial t}\left(\alpha_q \rho_q u_{qi}\right) + \frac{\partial}{\partial x_j}\left[\alpha_q \rho_q u_{qi} u_{qj} - \tau_{qij}\right] + R_{pq,i} \\ -v_{pq,i}\Gamma_{qp} + \alpha_q \frac{\partial P_m}{\partial x_j}\delta_{ij} - F_{dispersed,i} = 0,\end{aligned} \tag{3.31}$$

$$\begin{aligned}\frac{\partial}{\partial t}\left(\alpha_q \rho_q h_q\right) + \frac{\partial}{\partial x_j}\left[\rho_q u_{qj} h_q + Q_{qj} - u_{qi}\tau_{qij}\right] \\ +Q_{pq} - H_{qp}\Gamma_{qp} + \alpha_q \frac{\partial P_m}{\partial t} = 0,\end{aligned} \tag{3.32}$$

The phase strain tensor is defined as:

$$\tau_{qij} = \alpha_q \mu_q \left(\frac{\partial u_{qi}}{\partial x_j} + \frac{\partial u_{qj}}{\partial x_i}\right) \tag{3.33}$$

The heat flux in each phase, q, and interfacial heat transfer Q_{pq}, need special treatment as discussed below. Several phase interaction terms are included in this model. $R_{pq,i}$ is the momentum interaction term. Phase change models for the interfacial mass transfer Γ_{pq} are discussed in Section 3.2.3.1. Phase change will also introduce additional transfer of energy, H_{qp}, and momentum, v_{qp}, which are the latent heat and drift velocity. Here, v_{qp} is the velocity if phase q for $\Gamma_{qp} > 0$, and velocity of phase p for $\Gamma_{qp} < 0$. Similarly, H_{qp} is defined depending on the direction of mass transfer:

$$H_{qp} = \Delta H_{lv} = -\Delta H_{vl} = \begin{cases} h_l + L, & \text{if } \Gamma_{qp} > 0 \\ h_v + L, & \text{if } \Gamma_{qp} < 0 \end{cases} \tag{3.34}$$

where L is the latent heat.

In this work, the Span-Wagner EoS was used by a look-up table, generated based on REFPROP software [112]. Different available phase interactions were not included in this model setup for the sake of simplicity. However, further work should investigate other interactions such as particle lift, wall lubrication, and virtual mass forces.

For a successful implementation of this model into ANSYS Fluent, some simplifying limitations of the software had to be overcome using *user-defined functions* (UDFs). Firstly, Fluent only allows for relations for specific heat as a function of temperature, $c_p = f(T)$. Secondly, the interface enthalpy, H_{qp}, must be defined as a single constant, here referred to as h_F. The latent heat of evaporation is lower for higher pressures than for lower pressures, and as the pressure changes significantly through the ejector, this difference must be taken into account.

The temperature field used by Fluent is normally calculated using specific heat as a function only of temperature, $c_p(T)$, which may lead to large errors for flashing flow. To correct this, a separate temperature field, T', is calculated using UDFs. The temperature field is calculated using a REFPROP look-up table in the liquid and gas regions up to the saturation point, such that $T' = f(P, h)$. Beyond the saturation point, the non-equilibrium temperature is estimated by:

$$T'_{\text{superheated}} = T_{\text{saturated}} + \frac{h - h_{\text{sat}}}{c_p} \tag{3.35}$$

To address the second issue, an additional source term, S_{pq}, is added to the enthalpy equation:

$$S_{pq} = [\Gamma_{pq} - \Gamma_{qp}](H_{pq}(P) - h_F) \tag{3.36}$$

such that the energy balance is compensated for the difference between the actual and Fluents constant latent heat, h_F. Due to the change in the temperature field, the interfacial heat exchange models would not give physical results. Therefore, the interfacial heat exchange is assumed to be zero, $Q_{pq} = 0$. Thus, all heat transfer is done by phase change. Furthermore, heat conduction is assumed negligible, $Q_{qk} = \lambda \frac{\partial^2 T}{\partial x_j x_j} = 0$. These limitations should be addressed in further work.

3.2.3.1 Phase change modeling

A simplifying reformulation of the Hertz-Knudsen equations is the Lee model, Eqns. (3.28) and (3.29). Here, several parameters are reformulated into two mass-transfer coefficients, Λ_e, and Λ_c. This mass transfer model has been previously used for CO_2 ejector modeling by Giacomelli et al. [97] [112]. Numerical investigations of the CO_2 ejector using the UDRGMM [97] found the evaporation and condensation

constants that best fit experimental results were $\Lambda_e = 100000$ and $\Lambda_c = 0.1$.

3.2.3.2 Momentum interaction

The interaction between liquid and gas is treated according to Eqn. (3.37).

$$R_{qp} = -R_{pq} = F_{qp}^{\text{mom}}(u_{qi} - u_{pi}) \tag{3.37}$$

This is closed by a relation for F_{qp}^{mom}, which takes the form:

$$F_{qp}^{\text{mom}} = \frac{\rho_b f^{\text{mom}}}{6\tau_b} d_b A_i \tag{3.38}$$

where the subscript b indicates the particulate matter. The particle relaxation time is defined as $\tau_b = \frac{\rho_b d_b^2}{18\mu_q}$. The friction factor, f^{mom}, has a large set of available sub-models. Several of these models are complex and require a more in-depth knowledge of the flow regime. This information is not known in the case of the CO_2 ejector. Therefore the symmetric variation of the Schiller-Neumann relations was used. This model assumes a dispersed flow of bubbles or droplets. This is valid for the regions of the ejector where the flow is predominantly a low gas void fraction bubbly flow or a high gas fraction droplet flow. Due to the high turbulence typical in ejectors, this is often valid, however, is dependent on the ejector operation. The most important region is here the pre-mixing and early mixing sections of the ejector where significant velocity slip may occur.

The Schiller-Neumann model is formulated as follows:

$$f^{\text{mom}} = \frac{C_D \text{Re}_b}{24} \tag{3.39}$$

where $\text{Re}_b = \rho_b |(u_{bi} - u_{qi})| d_b / \mu_q$ is the Reynolds number, and C_D is the friction factor defined as:

$$C_D = \begin{cases} 1 + 0.15\text{Re}_b^{0.687}/\text{Re}_b, & \text{if } \text{Re}_b \leq 1000 \\ 0.044, & \text{if } \text{Re}_b > 1000 \end{cases} \tag{3.40}$$

3.2.3.3 Recent literature review

Available models for two-phase CO_2 ejectors are reviewed in the previous sections and assessed in Ringstad et al. [71]. Since the paper's submission, additional models have been developed and reported in the literature. A new set of models are reported in this section to complement the review paper by Ringstad et al. [71].

A homogeneous nucleation boiling model (HNB), was developed by Bodys et al. [131] to cover very low-pressure motive conditions (between 50 and 70 bar). This mixture model treats non-equilibrium conditions similar to the model by Haida et

al. [124]. The model accounts for non-equilibrium void fractions considering the phase change process. The phase change process is governed by the phase change model based on kinetic theory [131]:

$$\Gamma_{=}(\frac{\hat{\Lambda}}{2-\hat{\Lambda}})\left(\frac{m_M}{2\pi C_c T_{sat}}\right)^{\frac{1}{2}}(P-P_{sat}). \tag{3.41}$$

This model is calibrated extensively with experimental measurements through a mapping procedure to produce accurate motive nozzle predictions. The results were compared to 150 experimental data points with less than 8% motive mass flow rate prediction error for 70% of the simulations. The suction mass flow rate was poorly predicted by the model with a 20-80 % error in suction mass flow rate. Therefore, there is still a need for further development of accurate and stable modeling approaches for CO_2 two-phase ejectors.

The effect of turbulence on motive nozzle cavitation as well as suction flow mixing was further investigated by Bodys et al. [120]. Five turbulence models were compared for their impact on suction flow rate and distribution of turbulent kinetic energy. In addition, the impact of including a turbulence formulation in the phase change model was investigated. They concluded that the most accurate formulations for their impact on motive flow prediction were the two-equation models.

Sampredro et al. [132] presented a two-fluid model accounting for the interfacial area density for CO_2 two-phase ejectors. This allows the calculation of phase change terms with high accuracy as long as appropriate sub-models for the area density are applied. Here, a non-symmetric area density formulation was used to account for the variation of area ratio with phase fraction. The Peng-Robinson equations of state were used for liquid and gas properties. The results were compared with the experimental measurements by Haida et al. [124]. The motive mass flow rate prediction error was below 2%, however, the suction mass flow rate was less accurately reproduced with errors ranging from 1-30%. Still, the accuracy of this formulation is promising and indicates that the accuracy of non-equilibrium property prediction (not accounted for by the authors) may be less important than the model formulation.

3.2.4 Model comparison and discussion

The different models available have different benefits and limitations in terms of accuracy and calculation stability. The HEM is among the most popular models in literature for simulating CO_2 two-phase ejectors [71]. It is characterized by its simplicity in development and implementation. The HEM also has comparatively better stability and convergence properties. These models are very accurate in motive MFR prediction for super-critical motive conditions corresponding to a

near-critical expansion, discussed in Section 3.1.2.1. To mitigate the larger motive mass flow rate error for off-critical expansion paths, CFD model development were focusing on the prediction of thermodynamic non-equilibrium conditions. These increase the model complexity, however, can be tuned such that the mass-flow rates are accurately predicted. Of these models, the UDRGMM has reported the highest accuracy [71] in both suction and motive mass flow rate prediction. Still, the model is very sensitive to mesh quality, and initial- and boundary conditions. Furthermore, the model was found to have a too-slow iterative convergence rate (up to weeks per simulation) for many practical applications [80] and is therefore not used for ejector design analysis in this work. Alternative formulations of the UDRGMM, the HRM, and the TFM have been developed. A challenge with the development of new models is numerical stability. One of the more stable configurations was the TFM presented by Ringstad et al. [80]. This TFM was found to be more stable than the UDRGMM, however, would in some cases generate transient oscillations in pressure in the motive nozzle. These oscillations are believed to be caused by the implementation of the non-equilibrium thermodynamics and the numerical stiffness of the phase change model. Several limitations in the ANSYS Fluent framework were overcome by the implementation of user-defined codes. In conclusion, a large number of parameters and submodels in the TFM would require extensive tuning based on experimental data which is today not available. Therefore, the research and further development of the TFM were discontinued and left for further work. However, as demonstrated by Sampedro [132], a TFM approach can accurately reproduce the ejector physics even with EoS formulations not including non-equilibrium effects.

In total, the ejector design investigations done in this work are based on the HEM, due to its stability, accuracy, and no necessity for parameter tuning. Furthermore, the cases investigated in this work are covered in the region where the HEM accuracy is acceptable.

3.3 Numerical considerations

3.3.1 Meshing

In this work, mesh generation was performed using the ANSYS ICEM software. This software can produce high-quality structured meshes with a high level of control over the mesh details. For stable and accurate simulation of CO_2 ejectors, high mesh quality is required due to the large gradients in flow variables and sharp corners in the geometry. An appropriately structured mesh is more aligned with the major flow direction. This can reduce numerical diffusivity improving accuracy [133, 134], especially in high gradient zones typically occurring in ejectors. Similar meshing strategies are used for both 2D and 3D meshes. The 3D meshing strategy is described in this chapter, as it is not presented in detail in the published works. The 2D meshing strategy is similarly defined, however, uses an axis-symmetric mesh and therefore does not need the O-grid blocking structure. The meshing steps are automated by the use of a Python algorithm that generates the ICEM meshing instructions as *.RPL* files. These scripts are found open-access available online, see Section 1.6. Meshing automation is further discussed in Section 5.3.3.

3.3.1.1 Meshing strategy

The full 3D mesh of the ejector geometry is generated using the ICEM block meshing method. This method produces structured hexahedral meshes with low skewness, which minimizes numerical viscosity. The blocking structure for three-dimensional meshing of the ejector geometry is illustrated in Figure 3.3. The ejector is blocked using four layers of O-grid blocks, describing corresponding from the inside to outside: 1) the inner motive nozzle flow chamber, 2) the outer motive nozzle flow chamber, 3) the solid motive nozzle construction (neglected in the CFD analysis), and 4) the suction flow chamber. The blocking zones 2-4) are then radial hexahedral meshes while the blocking zone 1) is a core of square hexahedral mesh, illustrated in Figure 3.4.

The meshes are refined toward the ejector walls with a constant refinement ratio of r=1.3. The x-direction cross-sectional mesh for different cross-sections is illustrated in Figure 3.5. The wall mesh distance is defined such that the corresponding turbulence wall models are resolved, i.e. $y^+ \approx 1-30$ for the $k-\omega$ SST and $y^+ \approx 30-300$ for the $k-\epsilon$ standard wall models [114]. ANSYS Fluent allows for transitional turbulent wall models that mix the resolved and unresolved turbulence wall models according to the local y^+ resolution. This approach was applied for the fully automated approaches where a lack of prior knowledge of velocities does not allow for the LRN wall model approach to be employed.

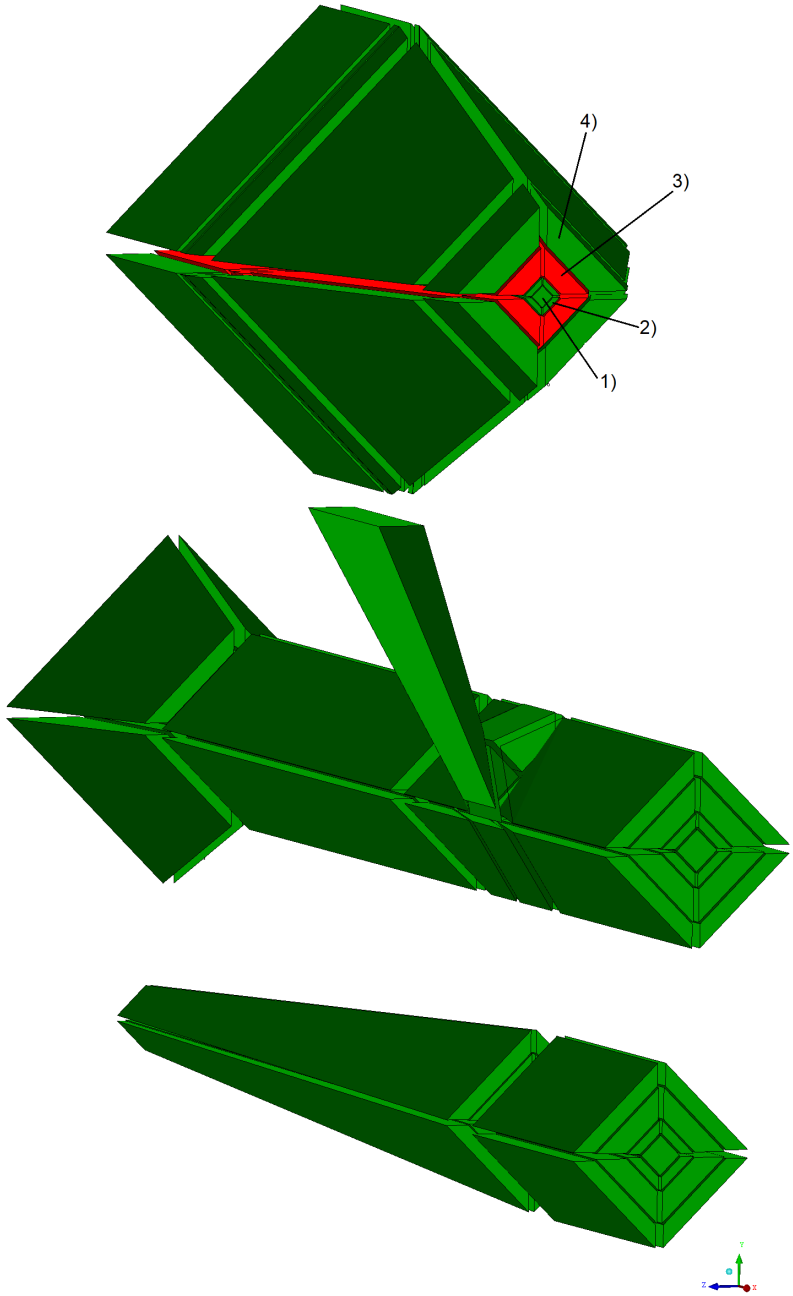

Figure 3.3: The blocking structure implemented in ANSYS ICEM, illustrated with motive nozzle construction (red) and flow chamber (green). Top: motive and suction nozzle inlets. Middle: premixing chamber, mixing chamber, and bypass inlet. Bottom: diffuser. The numbers correspond to the blocks: 1) inner motive nozzle, 2) outer motive nozzle, 3) solid motive nozzle construction, 4) suction chamber

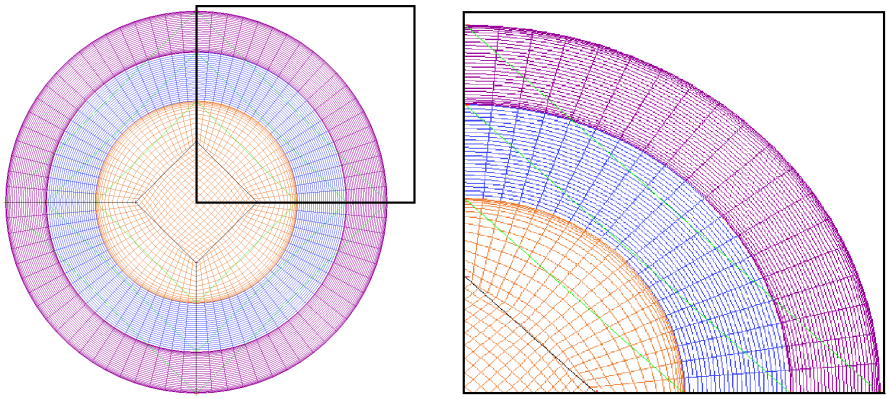

Figure 3.4: Cross section of mesh with O-grid blocking structure shown. Figure best viewed in electronic PDF version.

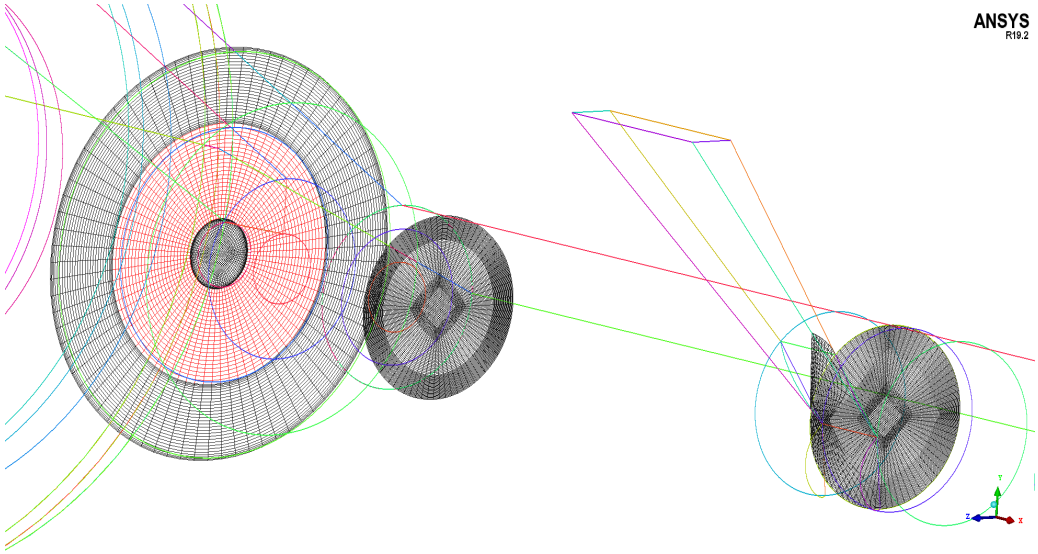

Figure 3.5: Different X-direction cross-sectional view of the 3D ejector mesh in the motive nozzle, suction nozzle, and mixing chamber. Figure best viewed in electronic PDF version.

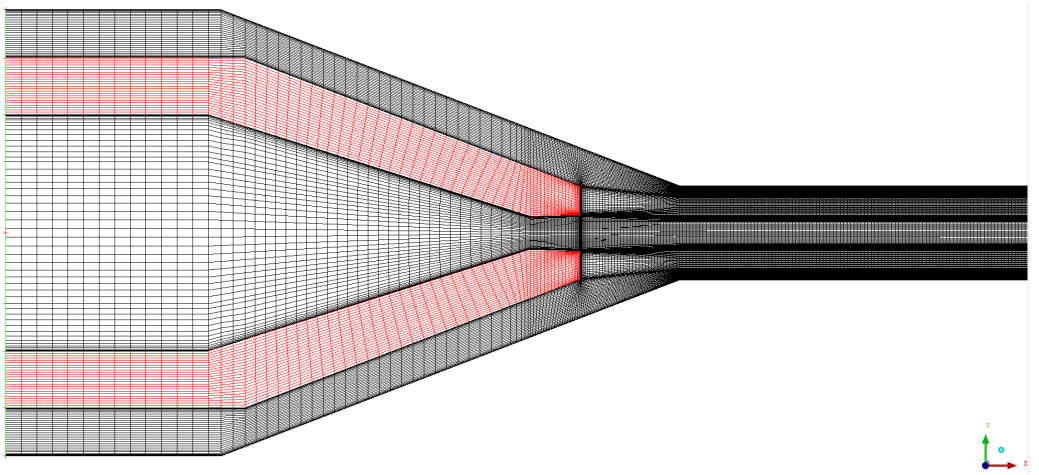

Figure 3.6: Z-direction cross-sectional view of the 3D ejector mesh layout. Figure best viewed in electronic PDF version.

The mesh for the swirl inlet bypass is discussed by Ringstad et al. [18]. The mesh of this domain is generated using an extruded block from the mixing section according to the geometry parameters θ_i, θ_t, and θ_w described in Ringstad et al. [18]. Depending on the angle of the bypass inlet, the zone near the intersection between the mixing and bypass chamber contains cells with high skewness. It is critical to produce a high-quality mesh for this zone, especially as the inclination angle, θ_i, is increased. This has a significant impact on the modeling of turbulence in this region, and poor mesh quality can produce instability. Therefore, a higher y^+-value (30) was used for stability considerations. For more details on the layout of the bypass inlet geometry, the reader is referred to the article by Ringstad et al. [18].

3.3.2 Boundary conditions

The boundary conditions used in this work are defined using the ANSYS Fluent "Pressure-boundary" boundary conditions. The static pressure is supplied at inlets and outlets. The enthalpy, void fraction (non-equilibrium models), and turbulent quantities are defined as constant inlet Dirichlet boundary conditions. The turbulence at the inlets is defined by the turbulent intensity and turbulent viscosity ratio. The prediction impact of turbulent inlet boundary conditions is commonly found to be negligible [120] due to the turbulence generated in the ejector typically being more significant than that occurring at the inlet. The outlet boundary conditions for void fraction and enthalpy are defined as zero-gradient Neumann conditions at the ejector outlet. The outlet is extended at the end with a straight section to avoid gradients in the outlet direction. The ejector walls are defined as adiabatic no-slip

walls with a constant wall roughness height of $H = 2\mu m$, commonly applied for ejector simulations [135, 78]. The assumption on adiabatic walls was investigated by Haida et al. [78] concluding that heat transfer through the converging-diverging nozzle wall has some influence on ejector flow. However, due to additional modeling complexity and limited influence this was neglected in this work.

3.3.3 Numerical solution schemes

The CFD model problem is solved using a steady-state pressure-based coupled algorithm in ANSYS Fluent 2020R2. The transient solution is often neglected in simulations for CO_2 ejectors. The assumption of steady-state CO_2 ejector flow has been considered in multiple studies [92, 112, 96, 135]. This assumption has still not been fully investigated for CO_2 ejectors and further work is needed. Still, due to the very high velocities of ejector flow, the time step required for a reasonable temporal resolution is often prohibitively low which limits calculation speed. Therefore, in this work, the steady-state approach was considered. The numerical schemes used were the second-order upwind scheme for the momentum, density, enthalpy (UDS), and turbulence transport equations. Second-order schemes were chosen to reduce the influence of numerical viscosity, while higher-order discretizations were disregarded due to numerical stability concerns near the swirl bypass inlet. Higher order accuracy will improve gradient estimation, which has an impact on shock resolution. The pressure was calculated using the PRESTO scheme, and gradients were evaluated with the Green Gauss node-based or the Least-squares gradient discretization scheme. These gradient schemes are considered to be higher-order accuracy than the cell-based approach for regions of high mesh non-orthogonality [114]. This is primarily a concern in the vicinity of the swirl-bypass inlet in the swirl-bypass ejector design (Ringstad et al. [18]), as the baseline mesh has otherwise high orthogonal quality. The discretization schemes are summarized in Table 3.3.

Table 3.3: Discretization schemes used in the CFD models.

Discretization	Scheme
Pressure	PRESTO!
Pressure-velocity coupling	Coupled
Gradient	Green Gauss node-based / Least squares
Momentum	Second order upwind
Density	–"–
Enthalpy	–"–
Turbulent kinetic energy	–"–
Turbulent energy dissipation	–"–

3.3.4 Thermodynamic look-up tables

The Span-Wagner EoS [101] is based on the Helmholtz equation for the determination of CO_2 properties. This EoS is widely considered for its high accuracy [102], however, it is highly CPU intensive. Thus, the published works have used look-up tables for more efficient simulations [103, 94, 92, 97].

In this work, a look-up table approach is used to reduce the computation time of the CFD calculations. The look-up tables were pre-generated using the CoolProp [130] software implemented in the Python programming language. The number of points in the thermodynamic look-up table has a significant impact on computation time and accuracy. To understand the impact of the look-up table density a comparative study is presented here. A thermodynamic look-up table for mixture density is generated with the number of tabulated points for enthalpy N_h and pressure N_P varied between 20 to 200. The error is calculated based on a comparison between the interpolated values and the real function values calculated with 5 times the density of the interpolation table. The results are shown in Table 3.4 and visualized for the different look-up table densities in a P-h diagram in Figures 3.7(a)-3.8(d).

Table 3.4: Comparison of the accuracy of different look-up table densities.

$N_h \times N_P$	Max error (%)	Mean error (%)
20×20	224.8	2.319
50×50	84.4	0.524
100×100	47.8	0.147
200×200	29.9	0.039

From Table 3.4, the accuracy of the lookup table procedure depends on the resolution of the look-up table. While the best accuracy is found for the 200×200 table, acceptable mean errors (below 1%) are observed for all tables with 50 or more entries in each variable. The errors are visualized in a P-h diagram in Figures 3.7(b), 3.7(d), 3.8(b), and 3.8(d). For the 100×100 table, errors above 1% only occur for pressures below 40 bar and at low specific enthalpy (150-200 [kJ/kg]) or very close to the phase envelope. The accuracy of the thermodynamic tables in this low-pressure region is neglected in this study as the operation of ejectors at these operating conditions is uncommon and the HEM model has been shown to have poor predictive power in this range. In total, the look-up table with density 100×100 is selected for the current work, for computational costs considerations.

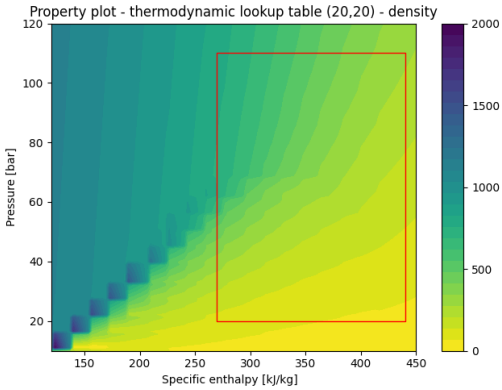

(a) Density interpolation in P-h diagram.

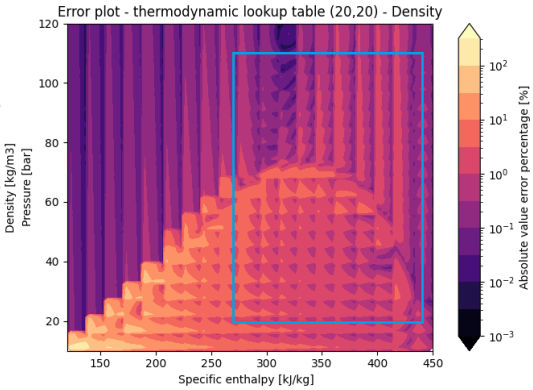

(b) Density interpolation error in P-h diagram. Colored by log scale.

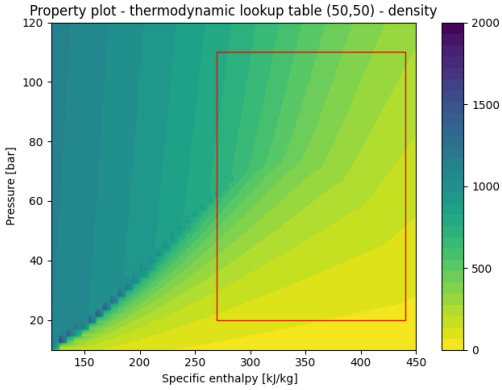

(c) Density interpolation in P-h diagram.

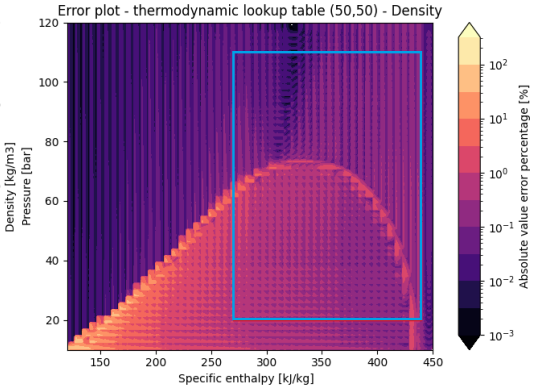

(d) Density interpolation error in P-h diagram. Colored by log scale.

Figure 3.7: Density interpolated heat map in a P-h diagram (left - **a)** and **c)**) and absolute percentage error in property interpolation heat map plotted in the same P-h diagram (right - **b)** and **d)**). Number of points in the tables: top - $N_h = 20, N_P = 20$, bottom - $N_h = 50, N_P = 50$. The red/light blue box indicates the intended zone of operating conditions where the assumptions of the HEM are valid.

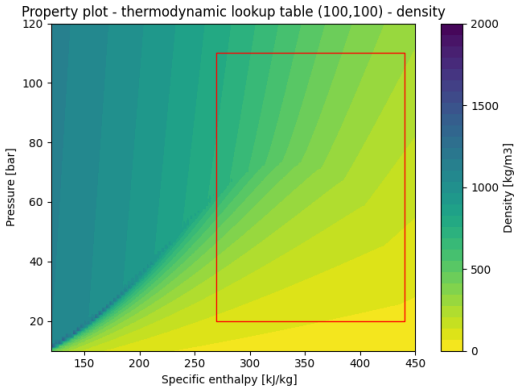

(a) Density interpolation in P-h diagram.

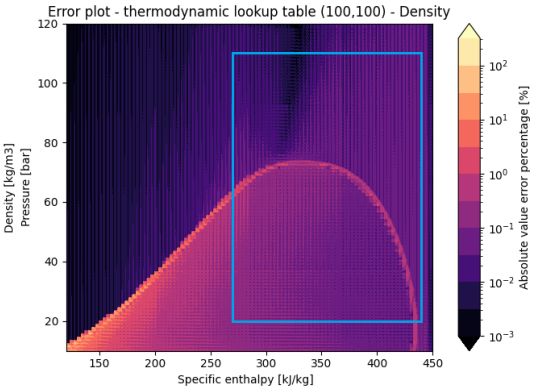

(b) Density interpolation error in P-h diagram. Colored by log scale.

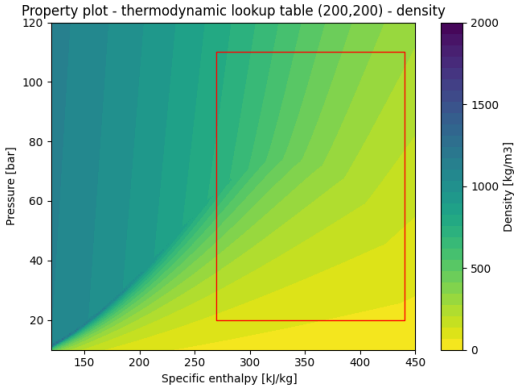

(c) Density interpolation in P-h diagram.

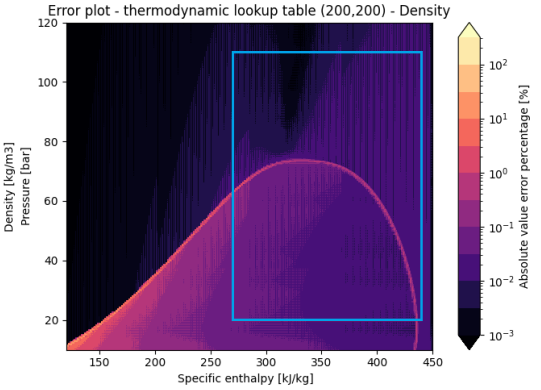

(d) Density interpolation error in P-h diagram. Colored by log scale.

Figure 3.8: Density interpolated heat map in a P-h diagram (left) and absolute percentage error in property interpolation heat map plotted in the same P-h diagram (right). Number of points in the tables: top - $N_h = 100, N_P = 100$, bottom - $N_h = 200, N_P = 200$. The red box indicates the intended zone of operating conditions where the assumptions of the HEM are valid.

3.4 Model validation

In this section, the validation of the HEM CFD model is presented. It is based on acquired background from previously published experimental and numerical studies [92, 93, 17, 135, 124, 94, 136, 137, 138]. Additionally, the model results are compared to the experimental results obtained by the author. In general, the motive flow rate prediction error for near-critical operating conditions is typically around 6%, however, it increases quickly to more than 30% as the motive pressure is reduced. The suction mass flow rate is much more difficult to predict due to the complex physics involved. Typically, the errors for suction range from 20-100%, depending on operating conditions. For a complete overview, the reader is referred to Ringstad et al. [71].

3.4.1 Experimental validation of the CFD model

In this work, an experimental test campaign was conducted to investigate the performance of a novel ejector design and validation of the different modeling approaches. The experimental work is presented in more detail in Chapter 4. Both the experimental work and model validation are described in more detail in Ringstad et al. [18].

Four data points will be used for validation of the CFD model corresponding to different motive conditions at 90 bar, 80 bar, 75 bar, and 83 bar and pressure lifts of 2.1 bar, 3.6 bar, 1.5 bar, and 2.5 bar, respectively. These cases will be referred to as cases I-IV, corresponding to the experimental data points 49, 59, 62, and 79 in Tables 4.2-4.4, respectively. The ejector geometry is presented in Table 3.5.

Table 3.5: Main dimensions of the ejector geometry with dimensions as defined in [80].

Parameter	D_{throat}	L_{mch}	L_{mix}	D_{mix}	D_{out}	θ_{diff}	$\theta_{\text{m-conv}}$	θ_{suction}
Value	0.85 mm	3 mm	34 mm	3.1 mm	10 mm	5°	30°	38°

Experimental data and the difference between numerical and experimental results are shown in Table 3.6. The experimental measurements were calculated from a time series close to a steady state. The standard deviation over the measurement period is also shown in Table 3.6.

It can be seen in Table 3.6 that good agreement between experimental measurements and CFD results is found for the motive MFR for the high motive pressure operating conditions. Errors less than 6% in predicted MFR for cases I, II, and IV were observed. The motive MFR is increasingly underpredicted as the pressure and temperature are reduced by the model and for case III is underpredicted by 12%.

Table 3.6: Comparison of experimental and CFD results at different operating conditions. δ = MFR_{CFD} - MFR_{Exp}. The MFR measurements are shown with the standard deviation over the experimental measurement period. Subscript *exp* refers to an experimentally obtained value.

	P_m [bar]	T_m [$^\circ C$]	P_s [bar]	T_s [$^\circ C$]	P_o [bar]	$MFR_{m,exp}$ [g/s]	δ_m [g/s]	$MFR_{s,exp}$ [g/s]	δ_s [g/s]
I	90.3	29.2	34.2	7.9	36.3	33.9 ± 0.2	-0.9	44.0 ± 0.5	+1.2
II	79.9	29.3	31.9	14.6	35.6	26.0 ± 0.5	-1.5	6.74 ± 0.05	+2.15
III	74.6	24.3	34.3	8.6	35.7	29.3 ± 1.2	-3.6	36.6 ± 1.9	+5.0
IV	82.8	34.5	34.3	9.1	37.0	21.6 ± 0.2	-1.1	26.3 ± 0.7	+13.4

This is in agreement with previous findings with the HEM and is in the literature attributed to non-equilibrium phase change [135].

The suction MFR is over-predicted by 3%, 31%, 14%, and 50.7% for cases I, II, III, and IV respectively. The prediction accuracy is thought to be more accurate for the high motive pressure (I, II) cases than the low motive pressure case (IV) due to the accuracy in the local flow pattern when operating closer to the validity range of the HEM model [139]. Accurate prediction of the suction flow is a common challenge in modeling CO_2 ejectors, and errors up to 100% are not uncommon which is often attributed to inaccurate turbulence modeling [71].

3.4.2 Mesh independence

Ensuring mesh independence is an important part to achieve accurate CFD results. Commonly, CFD simulations for CO2 ejectors were found in the literature to be conducted using a 2D mesh. Depending on the requirements of the model accuracy, mesh independence was reported for coarse mesh resolutions, e.g. 140k cells for 3D and 9k for 2D reported by Palacz et al. [17]. Bodys et al. [131] claim mesh independence is reached at 40k cells for 2D simulations. Though these ejectors did not have the same ejector dimensions, this discrepancy highlights the large variations in flow conditions found in ejectors.

Various authors have concluded that mesh independence is achieved using significantly different mesh resolutions. These differences can originate from different dominant ejector physics (e.g. differences in shock patterns) or differences in modeling approach (e.g. turbulence- and wall models). These deviations may also originate from the mesh independence study refining to a mesh size where further refinement would start resolving additional or different physics. An example of the latter is mesh refinement resolving unsteady turbulent structures at a small enough scale.

Two mesh independence studies have been conducted in this work for the HEM model. These are reported in this section and presented in detail in the works by Ringstad et al. [18, 80].

3.4.2.1 2D mesh independence

A mesh independence study with a 2D ejector geometry was conducted to ensure optimal mesh refinement and independent results. The main ejector geometry parameters are presented in Table 3.7. This ejector geometry is intended as an open-access geometry for simulations as sharing of this geometry is not limited by proprietary restrictions (which is often the case).

Table 3.7: All main ejector dimensions of the new proposed open design.

Parameter	Value
Motive Inlet diameter ($D_{\text{m-in}}$)	10.0 [mm]
Motive Throat diameter (D_{throat})	1.41 [mm]
Motive Outlet diameter ($D_{\text{m-out}}$)	1.52 [mm]
Nozzle tip thickness (L_{tip})	1.2 [mm]
Pre-mixer length (L_{mch})	4.2 [mm]
Mixer length (L_{mix})	26.0 [mm]
Mixer diameter (D_{mix})	4.0 [mm]
Diffuser diameter (D_{diff})	12.0 [mm]
Diffuser angle (θ_{d})	6 [o]
Motive converging angle ($\theta_{\text{m-c}}$)	35 [o]
Motive diverging angle ($\theta_{\text{m-d}}$)	3 [o]
Suction angle (θ_{s})	42 [o]

This mesh independence study was intended to find the mesh characteristics that capture the main ejector physics. The intention was to use this mesh for geometry optimization, which depends on a low mesh cell count for low computational costs. Mesh counts as low as 9k cells have been used for previous optimization studies [135] with a close-to-equivalent model setup. In this work, the ejector simulations were performed with five different mesh densities, A, B, C, D, and E that consisted of 2.2k, 8k, 26k, 60k, and 100k cells, respectively. The refinement was applied uniformly for all cells, halving/doubling the mesh size in each dimension. Better mesh refinement could be achieved by using adaptive mesh refinement methods, as long as appropriate refinement criteria are used. The boundary conditions of the ejector were: P_m=85 [bar], P_s=33 [bar], P_o=38 [bar], h_m=290 [kj/kg], h_s=432 [kJ/kg]. This corresponds to a reasonable operating condition for the CO_2 ejectors using the HEM. The required mesh refinement could be different for other operating conditions, especially as the type of shock structure changes with pressure.

More detailed mesh independence analysis would be beneficial when simulating ejectors under highly varied operating conditions. The calculated mass flow rates are presented in Table 3.8.

Table 3.8: Mesh independence study with different mesh sizes in 2D.

Mesh	Cells	OP1 [kg/s]	
		MFR_m	MFR_s
A	2.2k	0.0824	0.0538
B	8.0k	0.0812	0.0615
C	26k	0.0799	0.0613
D	62k	0.0795	0.0662
E	100k	0.0791	0.0609

The motive mass flow rate tends to reduce with mesh refinement, however, the differences in predicted flow rate were less than 5%. The suction mass flow rate error had more variance and, in general, the suction flow rate was decreased as the mesh was more refined. It was found that the prediction of the suction mass flow rate was less accurate when applying mesh A when compared to the most refined case (11% difference to mesh E). While for mesh B and C, the difference in predicted flow rate is less than 1% away from the results with the most refined mesh. Mesh C was chosen as a compromise between computational cost and similar results to the more refined simulations.

3.4.2.2 3D mesh independence

A mesh study was conducted by Ringstad et al. [18] to assure that the 3D physics effects are well represented in the model. More details are given in the publication. The mesh independence study was conducted at operating conditions corresponding to the four validation points, I, II, III, and IV discussed in Section 3.4.1, and the ejector geometry was previously presented in Table 3.5. The meshes A, B, and C were generated with 700k, 1000K, and 2000K cells, respectively. Two additional meshes D and E were generated with higher resolution in the premixing chamber and along the ejector walls, respectively.

The motive and suction MFR predicted at different resolutions of mesh quality for the different cases are shown in Table 3.9. The findings of this study were that the motive mass flow rate was close to independent of mesh resolution, varying with less than 1% between the coarsest and finest meshes, which is in agreement with previous results in the literature [71]. The suction mass flow rate prediction varied for the different meshes and the different cases. For cases I, III, and IV the suction flow rate prediction varies less than 5% between the coarsest and finest meshes. For mesh E (2500k) the accuracy of the suction MFR is for cases I, II, and IV

close to the experimentally obtained data points. This study would be improved by verifying mesh independence with an even more refined mesh.

Table 3.9: Mesh independence study with different mesh sizes in 3D.

Mesh	Case	Cells	MFR_m [kg/s]	MFR_s [kg/s]
A	I	700k	0.0333	0.0473
B	I	1000k	0.0331	0.0468
D	I	1400k	0.0330	0.0448
E	I	2500k	0.0330	0.0452
A	II	700k	0.0245	0.0105
B	II	1000k	0.0245	0.0101
E	II	2500k	0.0245	0.0089
A	III	700k	0.0257	0.0417
B	III	1000k	0.0257	0.0417
C	III	2000k	0.0257	0.0416
D	IV	1400k	0.0205	0.0396
E	IV	2500k	0.0206	0.0397

The numerical results obtained with meshes A, B, C, and E were compared for the resolution of the motive flow shock train. The pressure distribution along the center ejector axis for case I is shown in Figure 3.9. It was found that the shock strength is underpredicted by the coarser meshes (mesh A and B) in comparison to the finest mesh (mesh E). Figure 3.10 shows the Mach number distribution in the ejector for case IV for mesh D and E. The Mach number lines for Mach 1 are illustrated with a red contour line. It can be clearly seen from the figure that mesh refinement to 2500k cells improved the detailed resolution of the shock train. The results with mesh E shows that the high-velocity core is extended by refining the mesh. This is attributed to the reduction of numerical viscosity from mesh refinement. Based on this study it was decided for this thesis to use Mesh E including 2500k cells for 3D simulations.

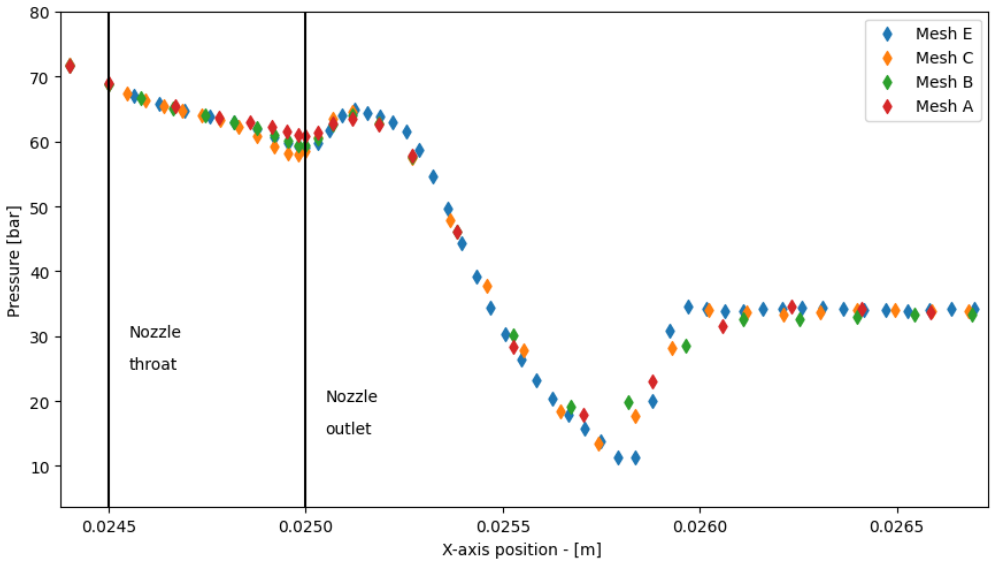

Figure 3.9: Pressure distribution for the case I along the x-axis for meshes A, B, C, and E.

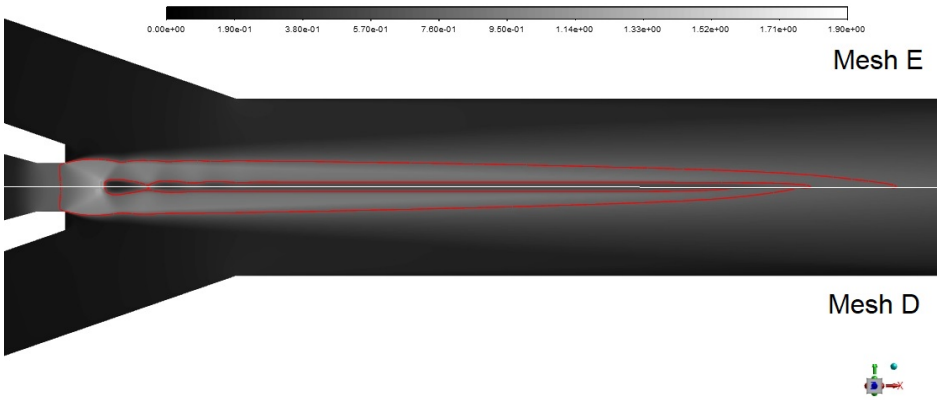

Figure 3.10: Mach number distribution for meshes E (top) and D (bottom) for case IV. The Red line illustrates Mach 1.

4 Experimental work

"Always be wary of any helpful item that weighs less than its operating manual."

— T. Pratchett

This chapter will summarize the experimental activities conducted to produce validation data for the ejector simulations.

4.1 Description of system

An experimental test campaign was set up at the NTNU/SINTEF energy research laboratory in Trondheim-Norway. The experimental rig is a CO_2 system with one base-load compressor and two parallel compressors, two CO_2 gas coolers for heat rejection to a glycol and a water loop, two evaporators, and an expansion device test section where a novel ejector was installed. The detailed system description can be found in the work by Banasiak et al. [140]. The system was equipped with pressure-, temperature, and mass flow sensors shown in Table 4.1.

Based on the measurement devices' accuracy and the deviation from steady state during the measurement periods the mean value of the measurement uncertainty was $\pm 0.42[^{\circ}C]$ for temperature measurements, ±6.5E-4 [kg s-1] for mass flow measurements, ±0.06 [bar] in the differential pressure measurements, and ±0.6 [bar] in the motive pressure measurements. The effect of motive pressure and temperature uncertainty on motive mass entrainment was calculated using the estimated steepest gradient in the data set. The uncertainties calculated were:

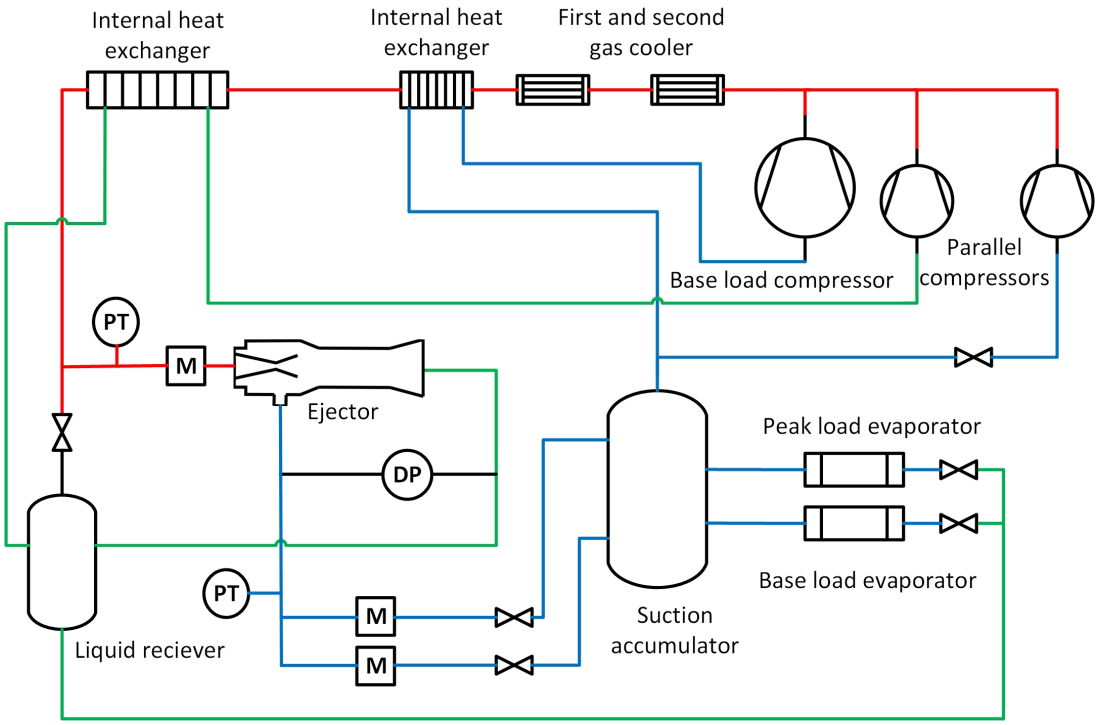

Figure 4.1: Simplified illustration of the system layout with new ejector and sensors installed.

$\Delta P_m \frac{\partial \dot{m}_m}{\partial P_m} \approx 4.3E-4[kg/s]$ and $\Delta T_m \frac{\partial \dot{m}_m}{\partial T_m} \approx 5.3E-4[kg/s]$. This indicates that uncertainty in pressure and temperature sensors have an effect on the uncertainty of mass flow rates, but that is less than 2% uncertainty for the collected data points. The uncertainty in suction mass flow measurement due to uncertainties in the differential pressure measurements is estimated to be $\Delta DP \frac{\partial \dot{m}_s}{\partial DP} \approx 2.8E-4[kg/s]$. For measurements with higher pressure lift and the lowest suction mass flow rate, this uncertainty can be close to 10%.

The deviation from steady state for each data point can be found in the repository: `https://github.com/knutringstad/Swirl_bypass_ejector`. As all model validation results are directly compared against the measured data (mass flow rates, pressure, and temperature), error propagation in calculation steps is not considered.

The system was installed with a CO_2 two-phase ejector not previously tested designed for low pressure-lift and high entrainment ratio intended for heat pump conditions. The main ejector dimensions are listed in Table 3.5. The ejector was produced in stainless steel with provided wall roughness class Ra0.8 (roughness average 0.8 micrometers). To evaluate ejector performance, additional pressure,

Table 4.1: Characteristics of the measuring devices

Parameter	Device	Accuracy
P	Cerabar PMP71	±0.25% of span
ΔP	Deltabar PMD75	±0.25% of span
T	PT 1000	±0.15°
MFR	Rheonik RHM 08 Coriolis meter	±0.1% of reading

temperature, and mass-flow rate sensors have been installed as shown in Figure 4.1.

4.2 Test campaign

The tested operating conditions in the rig were the motive conditions from T_m = 12°C (minimum in system) to T_m = = 35 °C, and motive pressures between P_m = 65 and 95 bar (maximum safety pressure). The outlet (liquid receiver) pressure was maintained at P_o = 34.6 bar. The conditions on the ejector suction side (suction accumulator) were approximately in the pressure range P= 33-34 bar. The pressure at the suction side was adjusted by manually closing the valve at the suction inlet. Three to four data points were collected at each motive pressure and temperature by varying suction pressure, thereby changing the pressure lift. A maximum pressure lift, with a fully closed valve, was also found for each condition. The data were collected over a span of 6 to 12 minutes. The data points were averaged over the period under steady state operation. The data was post-processed using a Python script, and the statistically averaged values and the corresponding standard deviation were calculated for each data point. All 130 data points are shown in a temperature-pressure diagram in Figures 4.2(a) and 4.2(b). All experimental results are shown in Tables 4.2-4.4.

4.3 Results

The ejector entrainment ratio at different pressure lifts and motive pressures is shown in Figure 4.3(a). Based on this figure, it can be seen that the maximum pressure lift was larger for higher motive pressures. This is more clearly visualized in Figure 4.3(c) where the data for a constant motive temperature are shown. Increasing motive pressure at a constant motive temperature increased the maximum

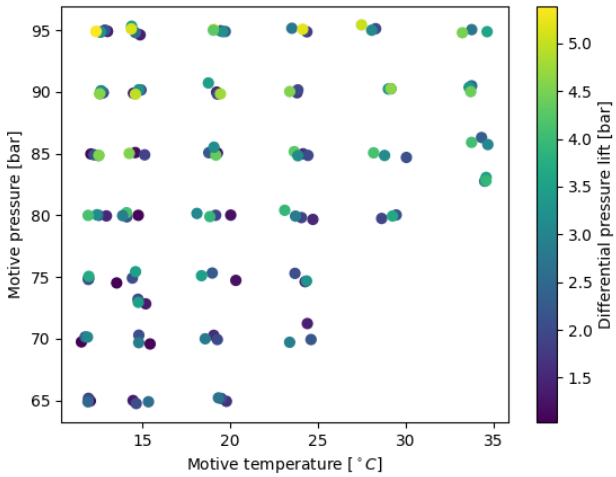

(a) All collected experimental data points illustrated on a motive temperature - motive pressure diagram, colored by pressure lift.

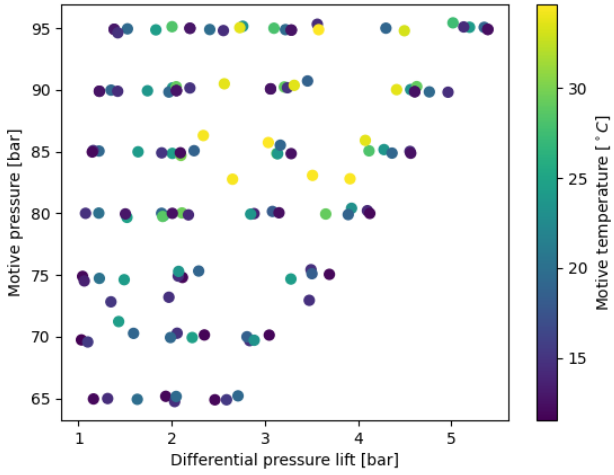

(b) All collected experimental data points are illustrated on a motive pressure - Pressure lift diagram, colored by motive temperature.

Figure 4.2: Visualization of the collected experimental data points plotted against pressure lift, motive pressure, and motive temperature.

achievable pressure lift. For a motive pressure of 65 bar, the maximum pressure lift was 3 bar, however by increasing the motive pressure to 95 bar the ejector could pump the secondary flow at pressure lifts above 5 bar, illustrated by red lines in the figure. The effect of increasing motive pressure at low pressure-lifts was less relevant, and a nearly equivalent entrainment ratio was reached at 1 bar pressure lift for motive pressures above 80 bar. An approximately linear drop in entrainment ratio with the pressure lift was observed. The linear decrease was more rapid for lower motive than for higher motive pressures.

It noted that the pressure lift is a function of both suction pressure and outlet pressure. Therefore, different results could be expected by varying the outlet pressure at constant suction pressure. This could be due to the influence of the motive flow expansion, depending on the outlet pressure. Thus, the ongoing discussion is primarily valid for a constant outlet pressure condition, which is common for some ejector-based systems, such as for modern super-market applications.

The ejector entrainment ratio at different pressure lifts and motive temperatures is shown in Figure 4.3(b). Based on this figure it can be noted that the maximum entrainment ratio was primarily governed by the motive temperature. This can be more clearly observed in Figure 4.3(d) where the data for a constant motive temperature is shown. By increasing the temperature at a constant pressure the maximum achievable entrainment ratio for a given pressure difference increased. At a 2 bar pressure lift, the entrainment ratio can be increased by approximately 40% by increasing the motive temperature from 12 to 32 °C. This is illustrated with a vertical line in Figure 4.3(d). The difference was more significant for low pressure-lifts than for high pressure-lifts and converges to the same point as the pressure lift is increased to the maximum achievable pressure lift.

Using Eqn. 2.4 the ejector efficiency was calculated at all data points. The efficiency at different pressure lifts at varied motive pressures is shown in Figure 4.4.

The ejector can achieve an efficiency $> 30\%$ for all motive pressures if operated at the pressure lift with the best performance. For low motive pressure operation, the optimum operation is for low pressure lifts around 1 bar. As motive pressure is increased the optimum efficiency is moved to higher pressure lift conditions. For motive pressures up to 80 bar, the highest efficiency is found with a pressure lift between 1 and 2 bar. For motive pressures between 80-90 bar, the best efficiency is reached near a 2 bar pressure lift. Above 90 bar motive pressure, the highest efficiency is recorded at a pressure lift of 2.5-3 bar.

The motive mass flow rate is solely dependent on the upstream motive conditions (pressure and temperature). The motive mass flow rate for different operating conditions is shown in Figure 4.5(a). From this figure, a close to linear trend of the motive mass flow rate with motive pressure can be observed. Similarly, the motive

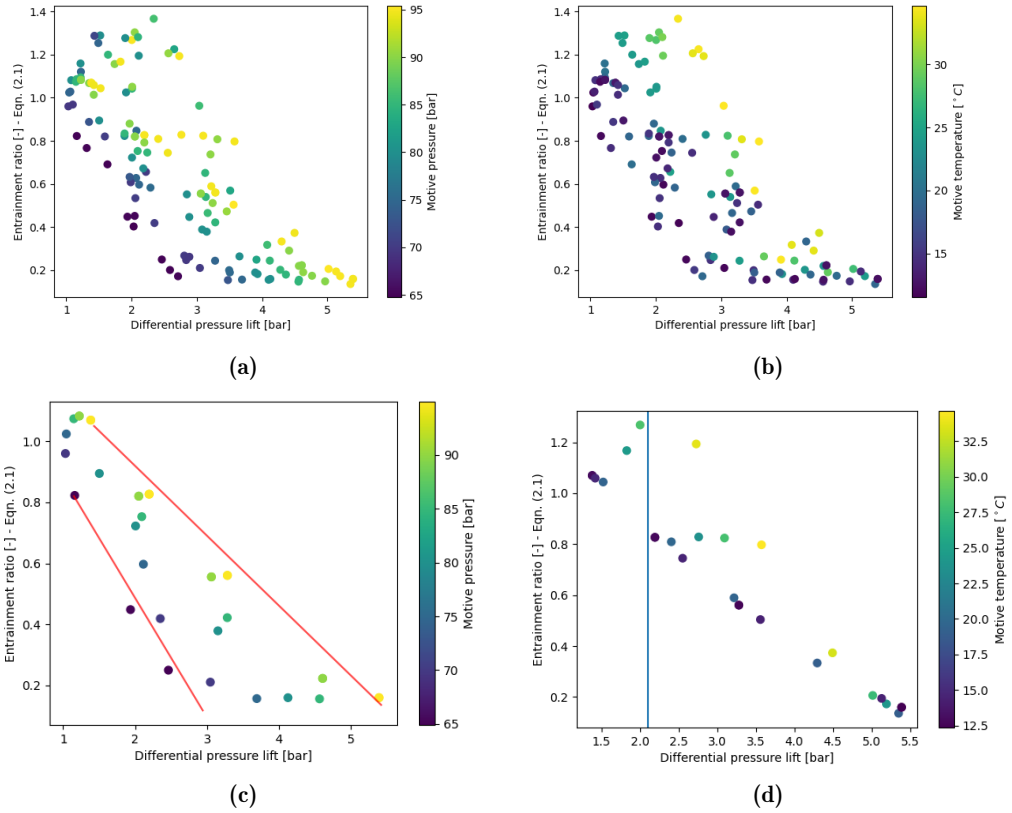

Figure 4.3: Experimental entrainment ratio data plotted against pressure lift colored by (a) motive pressure, (b) motive temperature, (c) motive temperature at $T_m = 12°C$, and (d) motive pressure at $P_m = 95$ bar.

mass flow rate is reduced as the motive temperature is decreased.

The suction mass flow rate was primarily dependent on both the motive flow and the pressure lift. The suction mass flow rate was plotted against differential pressure (pressure lift) and motive pressure. A close to linear decrease in suction mass flow was observed when increasing differential pressure at constant motive pressure, shown in Figure 4.5(b). When increasing the motive pressure, the suction mass flow and maximum pressure lift increased, shifting the suction mass flow data to higher differential pressures.

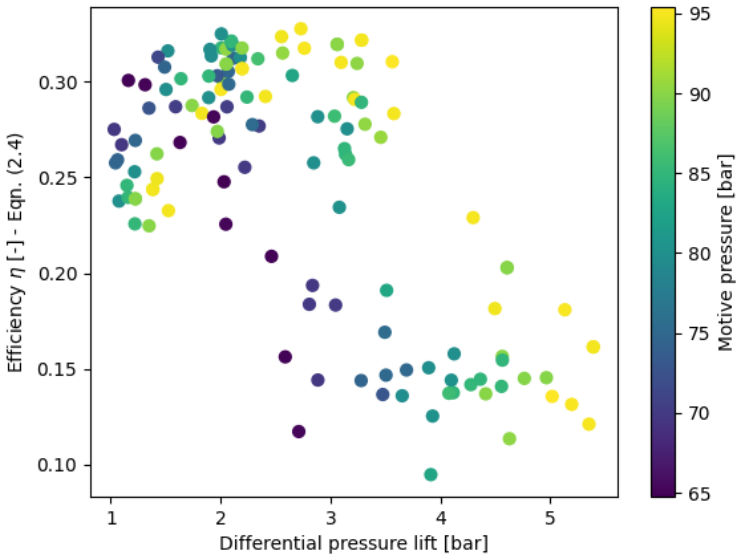

Figure 4.4: Experimentally obtained ejector efficiencies (Eqn. 2.4) as a function of pressure lift. Colored by motive pressure.

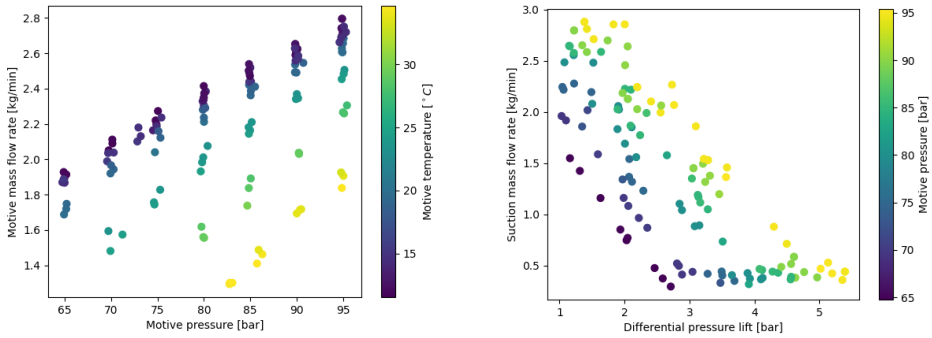

(a) Motive mass flow rates as a function of motive pressure and temperature.

(b) Suction mass flow rates as a function of differential pressure and motive pressure.

Figure 4.5: Suction and motive mass flow rate visualized for different operating conditions.

Table 4.2: Experimental test results, Part 1.

#	$P_m[bar]$	$T_m[^\circ C]$	$P_s[bar]$	$T_s[^\circ C]$	ΔP [bar]	$P_o[bar]$	$MFR_m[kg/s]$	$MFR_s[kg/s]$
1	79.7	24.7	34.5	14.6	1.5	36.0	0.0322	0.0414
2	79.8	24.1	34.5	9.6	1.9	36.4	0.0331	0.0337
3	80.4	23.1	31.5	9.8	3.9	35.5	0.0346	0.0062
4	85.0	24.2	34.5	13.2	1.6	36.2	0.0361	0.0431
5	84.9	24.4	33.7	11.6	2.0	35.7	0.0357	0.0371
6	85.2	23.7	30.8	9.6	4.3	35.1	0.0368	0.0073
7	89.9	23.8	34.3	10.1	1.7	36.0	0.0390	0.0450
8	90.2	23.9	33.6	9.2	2.0	35.6	0.0391	0.0410
9	90.0	23.4	30.6	8.1	4.6	35.2	0.0395	0.0086
10	94.9	24.4	34.4	9.6	1.8	36.2	0.0409	0.0476
11	95.2	23.5	32.7	8.3	2.8	35.4	0.0418	0.0345
12	95.1	24.1	30.2	7.5	5.2	35.4	0.0414	0.0070
13	65.0	12.0	34.4	12.1	1.2	35.5	0.0315	0.0258
14	69.7	11.5	34.4	11.0	1.0	35.4	0.0342	0.0327
15	74.9	11.9	34.4	9.4	1.0	35.4	0.0367	0.0374
16	65.2	11.9	33.6	13.2	1.9	35.5	0.0319	0.0142
17	70.1	11.7	32.8	9.6	2.4	35.2	0.0348	0.0145
18	74.8	11.9	33.0	8.3	2.1	35.1	0.0370	0.0220
19	64.9	11.9	33.0	16.0	2.5	35.4	0.0321	0.0079
20	70.1	11.9	32.2	9.4	3.0	35.2	0.0352	0.0073
21	75.1	11.9	31.4	8.3	3.7	35.0	0.0379	0.0058
22	65.0	14.5	34.2	13.7	1.3	35.5	0.0311	0.0237
23	69.6	15.4	34.5	11.1	1.1	35.6	0.0331	0.0320
24	74.5	13.5	34.5	10.9	1.1	35.5	0.0361	0.0370
25	64.7	14.6	33.5	13.7	2.0	35.5	0.0312	0.0124
26	70.3	14.8	33.5	11.9	2.1	35.5	0.0340	0.0180
27	74.9	14.4	33.0	9.7	2.1	35.1	0.0365	0.0228
28	64.9	15.3	32.9	14.2	2.6	35.5	0.0315	0.0062
29	69.7	14.8	32.9	14.1	2.8	35.7	0.0339	0.0083
30	75.4	14.6	31.6	9.7	3.5	35.1	0.0373	0.0073
31	70.3	19.1	33.9	10.3	1.6	35.5	0.0324	0.0264
32	74.7	20.3	34.0	12.5	1.2	35.2	0.0340	0.0380
33	80.0	20.0	34.5	10.1	1.2	35.8	0.0369	0.0426
34	85.0	19.3	34.4	9.4	1.2	35.6	0.0394	0.0430
35	90.0	19.2	34.1	7.5	1.3	35.5	0.0415	0.0442
36	94.9	19.5	33.9	7.4	1.5	35.4	0.0434	0.0452
37	69.9	19.3	33.5	11.3	2.0	35.5	0.0320	0.0193
38	75.3	19.0	32.9	11.2	2.3	35.2	0.0354	0.0205
39	80.0	19.2	33.8	9.9	1.9	35.7	0.0373	0.0305
40	85.1	18.8	33.1	8.0	2.2	35.3	0.0398	0.0296
41	89.8	19.3	33.5	6.7	2.0	35.4	0.0415	0.0364
42	94.9	19.7	32.9	7.6	2.4	35.3	0.0435	0.0351
43	70.0	18.6	32.7	16.0	2.8	35.5	0.0328	0.0086
44	75.1	18.4	31.8	11.1	3.5	35.3	0.0360	0.0067
45	79.9	18.8	31.6	11.4	3.9	35.5	0.0380	0.0071
46	84.9	19.2	30.5	6.9	4.4	34.8	0.0404	0.0071
47	89.8	19.4	30.6	8.5	4.8	35.4	0.0423	0.0072
48	95.1	19.1	29.5	6.7	5.4	34.9	0.0447	0.0060

Table 4.3: Experimental test results, Part 2.

#	$P_m[bar]$	$T_m[^\circ C]$	$P_m[bar]$	$T_s[^\circ C]$	ΔP [bar]	$P_o[bar]$	$MFR_m[kg/s]$	$MFR_s[kg/s]$
49	90.3	29.2	34.2	7.9	2.0	36.3	0.0339	0.0440
50	95.1	28.3	33.8	6.9	2.0	35.8	0.0377	0.0476
51	90.2	29.0	32.4	7.0	3.2	35.6	0.0340	0.0249
52	95.0	28.1	32.5	6.6	3.1	35.6	0.0378	0.0310
53	90.3	29.2	30.8	7.0	4.6	35.5	0.0338	0.0063
54	95.4	27.5	30.3	6.4	5.0	35.3	0.0384	0.0078
55	79.7	28.6	34.4	8.0	1.9	36.3	0.0270	0.0343
56	84.7	30.1	34.5	8.0	2.1	36.6	0.0290	0.0370
57	80.0	29.5	34.8	8.7	2.1	36.9	0.0259	0.0308
58	84.8	28.8	32.4	7.9	3.1	35.5	0.0306	0.0198
59	79.9	29.3	31.9	14.6	3.7	35.6	0.0260	0.0067
60	85.1	28.2	30.8	7.0	4.1	34.9	0.0315	0.0076
61	71.2	24.4	34.2	8.8	1.4	35.7	0.0262	0.0336
62	74.6	24.3	34.3	8.6	1.5	35.7	0.0293	0.0366
63	69.9	24.6	33.4	9.3	2.2	35.6	0.0247	0.0161
64	75.3	23.7	33.5	8.4	2.1	35.6	0.0305	0.0257
65	69.7	23.4	32.1	9.9	2.9	35.0	0.0266	0.0068
66	74.7	24.4	32.2	13.2	3.3	35.4	0.0291	0.0070
67	72.8	15.2	34.1	11.8	1.3	35.4	0.0350	0.0310
68	73.2	14.7	33.3	11.1	2.0	35.3	0.0355	0.0223
69	72.9	14.8	31.4	10.7	3.5	34.9	0.0363	0.0055
70	80.0	14.8	34.3	9.2	1.1	35.4	0.0384	0.0414
71	79.9	14.1	33.0	8.3	2.2	35.2	0.0388	0.0260
72	80.2	14.1	31.2	8.6	4.1	35.3	0.0397	0.0061
73	80.0	13.9	32.4	8.2	2.9	35.3	0.0391	0.0173
74	85.1	14.6	34.3	10.6	1.2	35.5	0.0407	0.0440
75	84.9	15.1	33.4	9.7	1.9	35.3	0.0406	0.0338
76	85.0	14.2	30.4	8.2	4.6	34.9	0.0420	0.0061
77	79.9	23.7	32.5	8.0	2.8	35.4	0.0335	0.0184
78	84.8	23.9	32.2	7.4	3.1	35.3	0.0364	0.0195
79	82.8	34.5	34.3	9.1	2.7	37.0	0.0216	0.0263
80	83.1	34.6	32.4	8.5	3.5	35.9	0.0217	0.0122
81	82.8	34.6	31.7	9.6	3.9	35.6	0.0217	0.0053
82	86.3	34.3	34.4	9.1	2.3	36.7	0.0244	0.0332
83	85.7	34.7	33.4	8.2	3.0	36.4	0.0235	0.0225
84	85.9	33.8	31.3	7.9	4.1	35.3	0.0248	0.0077
85	64.9	19.8	33.9	11.7	1.6	35.5	0.0281	0.0193
86	65.2	19.5	33.5	11.9	2.0	35.5	0.0286	0.0128
87	65.2	19.3	32.6	12.9	2.7	35.3	0.0291	0.0049
88	94.9	19.6	32.2	6.8	3.2	35.4	0.0438	0.0257
89	95.0	19.0	30.9	6.2	4.3	35.2	0.0443	0.0146
90	90.7	18.8	32.1	6.8	3.5	35.5	0.0424	0.0199
91	85.5	19.1	32.1	7.1	3.2	35.3	0.0402	0.0186
92	80.1	18.1	32.2	7.3	3.1	35.2	0.0382	0.0147
93	94.9	13.0	34.2	8.1	1.4	35.6	0.0450	0.0480
94	95.0	12.9	33.0	7.2	2.2	35.2	0.0454	0.0374
95	94.8	12.6	31.9	6.3	3.3	35.1	0.0457	0.0255
96	94.9	12.4	29.4	5.4	5.4	34.7	0.0466	0.0073
97	89.9	12.6	34.2	8.9	1.2	35.4	0.0432	0.0466

Table 4.4: Experimental test results, Part 3.

#	$P_m[bar]$	$T_m[°C]$	$P_m[bar]$	$T_s[°C]$	ΔP [bar]	$P_o[bar]$	MFR_m [kg/s]	MFR_s [kg/s]
98	89.9	12.7	33.1	8.3	2.1	35.2	0.0434	0.0355
99	90.1	12.6	32.1	7.1	3.1	35.2	0.0437	0.0242
100	89.9	12.6	30.5	6.6	4.6	35.1	0.0442	0.0097
101	85.0	12.0	34.3	10.2	1.1	35.5	0.0412	0.0441
102	84.9	12.2	33.0	9.0	2.1	35.1	0.0415	0.0311
103	84.8	12.5	31.9	8.2	3.3	35.1	0.0417	0.0175
104	84.9	12.5	30.5	8.1	4.6	35.0	0.0423	0.0065
105	80.0	12.9	34.1	11.7	1.5	35.6	0.0389	0.0347
106	80.0	12.5	33.4	11.0	2.0	35.4	0.0392	0.0282
107	80.0	12.4	32.2	10.1	3.2	35.3	0.0396	0.0149
108	80.0	11.9	31.0	9.7	4.1	35.1	0.0402	0.0063
109	89.9	12.6	34.2	8.9	1.2	35.4	0.0432	0.0466
110	89.9	12.7	33.1	8.3	2.1	35.2	0.0434	0.0355
111	90.1	12.6	32.1	7.1	3.1	35.2	0.0437	0.0242
112	89.9	12.6	30.5	6.6	4.6	35.1	0.0442	0.0097
113	94.9	13.0	34.2	8.1	1.4	35.6	0.0450	0.0480
114	95.0	12.9	33.0	7.2	2.2	35.2	0.0454	0.0374
115	94.8	12.6	31.9	6.3	3.3	35.1	0.0457	0.0255
116	94.9	12.4	29.4	5.4	5.4	34.7	0.0466	0.0073
117	89.9	14.5	34.0	13.1	1.4	35.4	0.0426	0.0431
118	90.2	14.9	33.1	11.9	2.2	35.3	0.0428	0.0338
119	90.2	14.8	32.1	10.6	3.2	35.3	0.0431	0.0219
120	89.8	14.6	30.1	9.3	5.0	35.0	0.0438	0.0064
121	94.6	14.9	34.1	11.2	1.4	35.6	0.0444	0.0469
122	94.8	14.6	32.7	9.5	2.6	35.2	0.0448	0.0333
123	95.3	14.4	31.7	8.2	3.6	35.2	0.0453	0.0227
124	95.1	14.4	29.8	7.1	5.1	35.0	0.0459	0.0088
125	90.5	33.8	34.4	9.7	2.6	37.0	0.0286	0.0344
126	90.4	33.6	32.5	7.7	3.3	35.8	0.0286	0.0229
127	90.0	33.7	30.9	6.9	4.4	35.3	0.0282	0.0081
128	95.0	33.8	34.1	9.4	2.7	36.8	0.0318	0.0378
129	94.9	34.7	33.1	8.9	3.6	36.7	0.0306	0.0243
130	94.8	33.2	30.8	7.6	4.5	35.3	0.0321	0.0118

5 Ejector design methodology

"Real stupidity beats artificial intelligence every time."

— T. Pratchett, *Hogfather*

5.1 Motivation for design tool

Ejector design is challenging due to the number of interdependent parameters involved. Ejector geometry parameters have a significant effect on the ejector operation. Furthermore, each design has a limited range of operating conditions where the ejector provides the highest efficiency. However, because of the wide range of operating conditions (e.g. motive mass flow rate, pressure lift, entrainment), available standardized ejectors cannot be used without compromising on ejector efficiency. This makes individual ejector designs for each system specification one of the few viable options. In this section, only static non-controlled ejectors are considered. One limitation to the use of individual optimization of ejectors is the cost. Mass-produced ejectors for commercial purposes are obviously less expensive. This limitation can potentially be overcome by investigating alternative manufacturing methods such as 3D printing. A second limitation is the lack of efficient, accurate, and easy-to-use design methodologies for CO_2 ejector design. In this work, a design tool is performed in order to bridge this gap.

Most ejectors are currently designed based on 0D or 1D models and iterative design. Such models cannot accurately account for multi-dimensionality and are sensitive to experimental tuning data. On the other hand, CFD models are more accurate

as they take into account the multidimensional geometry in the description of the fluid domain [71]. The major limitation of CFD is the computational time, which may be found costly depending on the problem's complexity.

Optimization algorithms for ejector design have been previously investigated. Palacz et al. [17] used an evolutionary optimization algorithm for CO_2 ejector design. This approach has some limitations when used without a response surface mapping method. It requires a large number of design evaluations at new data points which consequently requires significant CFD resources. Secondly, the data from previous simulations cannot be readily implemented into the algorithm.

In this chapter an alternative machine learning-based concept is presented for design exploration, mapping, and optimization, to overcome several of the previous limitations. The proof-of-concept and results from initial investigations are presented in Ringstad et al. [80]. This chapter includes an introduction to Machine learning (ML) with a focus on the Gaussian Process Regression approach in Section 5.2. Section 5.3 discusses the algorithms and systems used in the automated database generation tool.

5.2 Machine learning

The field of machine learning is rapidly growing and developing. Several easy-to-use computational tools are becoming readily available. This allows for rapid adoption and implementation of the technology. Over the last 20 years, the number of publications in the field of mechanical engineering using Machine Learning has been growing exponentially, as shown in Figure 5.1.

Several approaches are available to machine learning, depending on the application requirements. Due to the wide and complex field of learning, it is challenging to give a simple overview of the field. Shalev-Shwartz and Ben-David [142] classified machine learning algorithms according to four aspects:

- Supervised or non-supervised
- Active versus Passive Learners
- Active versus Passive teacher
- Online versus Batch Learning Protocol

Supervised or unsupervised learning is a primary classification method in ML and AI. Supervised learning is the approach where the observations are labeled, and

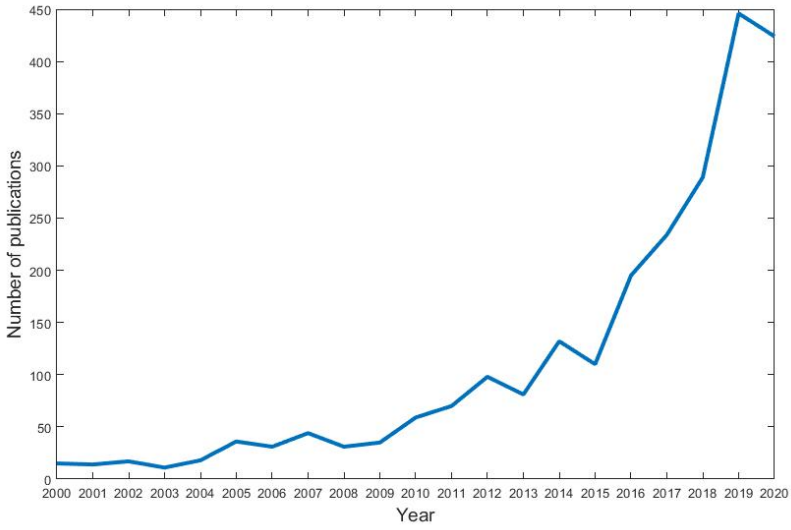

Figure 5.1: Number of publications on Machine learning based on key-word and abstract in the field of mechanical engineering. The data included are derived from Clarivate Web of Science. © Copyright Clarivate 2021. All rights reserved. [141].

the algorithm identifies the underlying reason for that label. Unsupervised learning then tries to find patterns and connections regardless of a specific output or label. Active or passive learning is associated with the algorithm's interaction with the learning process. Active learning is involved in the learning process by querying and experimenting with the learning data. Active teaching, on the other hand, involves feeding the learning model with examples and data that best improve the model. Their last distinction is in whether the learning is occurring in batch from a large data set, or whether the algorithm is learning while responding continuously.

There is a large set of available machine learning models available. A few common types are classification, clustering, regression, Bayesian (statistical) models, decision trees, artificial neural networks (ANN), and deep neural networks. In this work, a statistical non-linear non-parametric (infinitely parametric) machine learning approach was applied to the problem, referred to as Gaussian Process Regression.

5.2.1 Gaussian Process Regression

The Gaussian Process Regression (GPR) approach is a popular supervised machine learning method. GPR is a Bayesian non-parametric regression approach, that works well on smaller data sets and can account for uncertainty in the results. This is an ideal approach when analyzing problems with significant uncertainties and where the computation of a single data point is costly. Alternatively, ANN ML models have previously been used for ejector design and performance analysis [143, 144, 145]. Still, GPR models offer certain advantages over ANN methods, including more efficient data usage, lower overfitting risk, ease of use, and better explainability [146].

Gaussian Process Regression is a probabilistic supervised machine learning tool based on Bayesian regression to generate surrogate models. Essentially, the Gaussian Process ($\mathcal{GP}$) infers a probability distribution of functions $p(f(\cdot))$ based on assumptions given about the underlying functions, referred to as the *prior*. The training data is a set of labeled data $(y_i, \mathbf{X}_i)$, where y_i is the observations, and $\mathbf{X}_i$ is the vector of inputs for datapoint i. Assuming that our observations are of an unobservable underlying function f with a zero mean Gaussian noise, $n_i = \mathcal{N}(0, \sigma_n)$, where σ_n is the constant standard deviation, the input-output relationship can be written as:

$$\mathbf{y} = f(X) + \mathbf{n}. \tag{5.1}$$

Where $\boldsymbol{y}$ is the vector of outputs and X is the matrix of inputs. The inference of possible functions happens by considering Bayes theorem (conditional probability distribution) using the data $\mathbf{y}$ and X:

$$p(f(\cdot)|X, y) = \frac{p(y|f(X))p(f(\cdot))}{p(y|\mathbf{X})} \tag{5.2}$$

The *prior*, $p(f(\cdot)) = \mathcal{GP}(M, K)$ is a Gaussian process. The noise term, $p(y|f(X))$, specifies how likely a function value $f(X)$ is with the data y. The *marginal likelihood*, $p(y|\mathbf{X})$ is a normalizing term. The *posterior*, $p(f(\cdot)|X, y)$, is another Gaussian process defined by a new mean function and kernel, that is conditioned on the data set. An illustration of the GPR method before and after training is shown in Figure **??**.

The Gaussian Process (GP) can then be written as (Eqn. 5.3):

$$\mathbf{y} = \mathcal{GP}\left(M(X), K(X, X'; \zeta)\right) \tag{5.3}$$

The GP has a mean function, $M = \bar{E}[f(X)]$, where $\bar{E}$ is the expected value, a covariance function $K(X, X') = \bar{E}[f(X)f(X')]$, and a set of model hyper parameters, ζ.

The assumption on the possible functions is specified through the choice of the kernel and mean function. The choice of the kernel can change the possible solutions. For an overview of common kernels the reader is directed to the work by Duvenaud [147]. The most common kernel which is applicable for most applications is the squared exponential kernel. The squared exponential kernel, or Radial Basis Function, is considered the de-facto default kernel for GPR [147]. The kernel has two hyperparameters; σ_f and l, which are the signal standard deviation and the kernel length-scale, respectively. The parameter σ_f is a scaling parameter for the standard deviation in the data. The length-scale l governs the length over which two points X and X' are correlated. The correlation dies off as the squared exponential of the distance between the points in comparison to this length scale. Larger values of l enforce that f varies more smoothly. The length scale is in this work implemented as a dimensional parameter, which allows the model to optimize different length scales for each dimension of the input data (also referred to as feature). Noise in the observations can be accounted for by adding a White Noise kernel with a constant noise level σ_n, optimized in the algorithm. The combined kernel function is then defined as (Eqn. 5.4):

$$K(X, X'; \zeta, \sigma) = \sigma_f^2 \exp\left(-\frac{1}{2l^2}(X - X')^2\right) + \sigma_n^2 \mathbb{I} \tag{5.4}$$

where, $\mathbb{I}$ is the identity matrix.

The probability of a dataset given a set of hyperparameters $p(y|\zeta)$ can be calculated in closed form. By maximizing the log marginal likelihood of different hyperparameters the best set of hyperparameters can be obtained, Eqn. (5.5). In the Sklearn algorithm, the optimizer is a quasi-Newton L-BFGS optimizer [148] as:

$$\arg\max \log \mathrm{p}(\mathbf{y}|\zeta) \tag{5.5}$$

The model can be used for the prediction of unknown function values f^* evaluated at location X^* by drawing from a joint distribution of the training data y and test data $f*$.

$$\begin{bmatrix} y \\ f* \end{bmatrix} = \mathcal{N}\left(\begin{bmatrix} M \\ M^* \end{bmatrix}, \begin{bmatrix} K & K^* \\ K^* & K^{**} \end{bmatrix}\right) \tag{5.6}$$

For a more detailed description of Gaussian Process Regression the reader is referred to the thesis of Duvenaud [147].

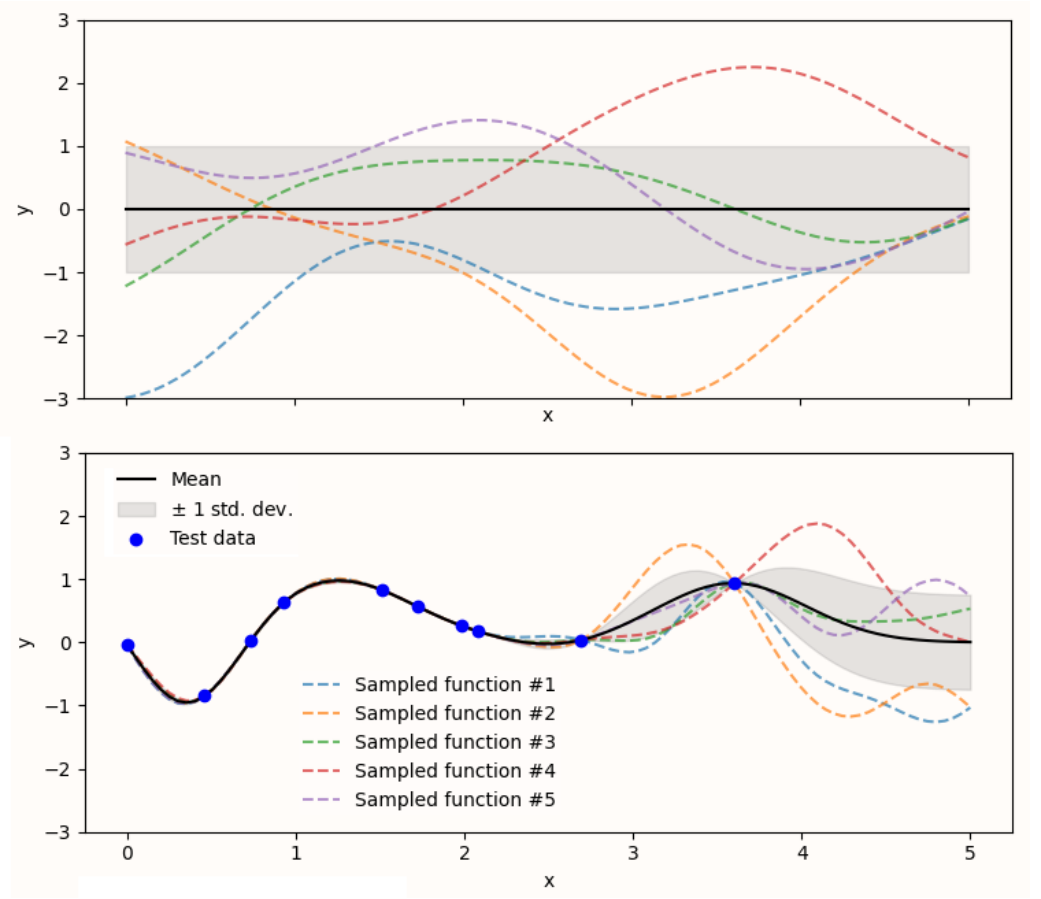

Figure 5.2: Illustration of samples of possible GPR function (top) before -prior distribution- and after -posterior distribution- conditioning based on data. The black line is the mean of the GPR solutions, the gray area represents the width of 1 standard deviation from the mean, the blue points are the test data, and the dashed lines are sampled functions from the Gaussian Process. Figure recreated based on Pedregosa et al. [148].

5.3 Database generation

The proposed machine learning method is based on a semi-large set of labeled data (supervised learning). The ejector shape dimensions, operating conditions, or a combination of these are used as the ML model inputs. For designing high-performing ejectors, different performance metrics are used as the predicted values. To collect a significant database, an automated approach to generating data points is necessary. In this work, a fully automated approach to generating such large databases is presented.

5.3.1 Automated CFD algorithm

The program is organized into cases, and each of them includes a folder structure to store CFD data, output files, and the database itself. The database is stored as a *.csv* file with columns for each potential model and shape parameter. In addition, the database stores the main post-processing results such as mass flow rates and outlet flow uniformity, described below. Each case is organized with its own case settings. Settings for sampling, meshing, CFD, and folder structure are stored. The input data dimensions (number of model parameters) used in the ML model are referred to as features. The data features and the number of data points are selected in the sampling settings. The design space defined by the features is then sampled by a sampling algorithm, see Section 5.3.2. The data points to be calculated are stored in the database, and the algorithm starts iterating over the data points. The algorithm is described below in Algorithm 1 and visualized in Figure 5.3:

Algorithm 5.1: Algorithm sequence for automated CFD workflow

```
Start;
Sampling feature space see Section 5.3.2;
for Datapoint in Number of samples do
    Generate mesh in ICEM, see Section 5.3.3;
    Generate journal file, see Section 5.3.4;
    Run ANSYS Fluent N iterations;
    if Converged CFD results then
        Post processing KPIs, see Section 5.3.5;
    else
        Run ANSYS Fluent N iterations;
    end
    Post-processing KPIs, see Section 5.3.5;
end
```

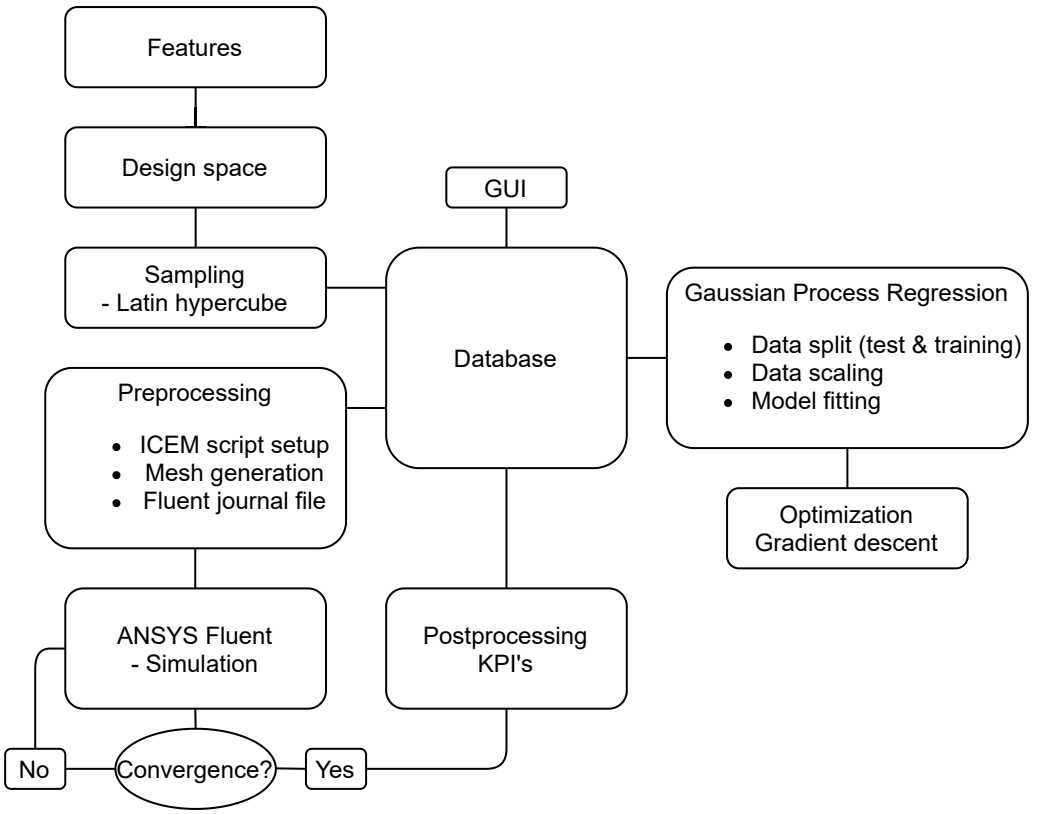

Figure 5.3: Layout of the Machine learning - Automation program, from Ringstad el al. [80]

5.3.2 Sampling

The feature space is sampled using a sampling algorithm. The main sampling algorithm used in this work is the Latin Hyper Cube (LHC) approach [149], which is a specific form of Monte Carlo sampling. LHC sampling is a statistical approach that samples N points from a statistical distribution in equiprobable zones. This approach ensures good sampling of a higher dimensional subspace with fewer data points than random or equidistant sampling. The LHC design gives an N-dimensional mapping to fill a space with low overlap. The design points χ_i are chosen from the range (0,1) and are transformed to a chosen sub-space, $\tilde{X}_i$. All variables are sampled evenly (uniform distribution) from the hypercube space according to Eqn. (5.7), using given maximum and minimum values.

$$\tilde{X}_i = \chi_i * (a_{\max} - a_{\min}) \tag{5.7}$$

In the example used in Ringstad et al. [80], the minimum and maximum ranges ($a_{\min}$ and $a_{\max}$) for the feature lengths were defined according to Table 5.1. A special sampling sequence was implemented when a sample range was defined by another feature. As an example, L_{mix} was defined as a multiple of D_{mix}. In addition, these transformations had to account for impossible shape configurations such as when the motive nozzle collides with the suction chamber. The operating condition sampling ranges were selected based on common operating ranges for ejectors in heat-pumping and super-market applications. The design sampling ranges were chosen based on previous knowledge of ejector design for the given operating conditions. However, these ranges were further refined during the study to better resolve the physics of ejectors close to a high-performance design.

Table 5.1: Available features and their parameter sampling range for LHC-sampling algorithm.

Parameter	$a_{\min}$	$a_{\max}$
$D_{\text{m-out}}$, [mm]	D_{throat}	1.5 D_{throat}
L_{mix}, [mm]	0	50 D_{mix}
D_{mix}, [mm]	D_{throat}	10 D_{throat}
D_{out}, [mm]	D_{mix}	10 D_{mix}
ζ_{d}, [°]	1	90
P_m, [bar]	75	140
P_s, [bar]	28	55
P_o, [bar]	P_s	P_s+15
h_m, [kJ/kg]	250	340
h_s, [kJ/kg]	380	460

5.3.3 Automated Meshing

The automated meshing algorithm is based on a Python program to generate an instruction file (.RPL) for the ANSYS ICEM meshing software. ANSYS ICEM generates structured meshes with high mesh quality. The algorithm uses a specified baseline cell size, Δ_b, that is used for the generation of the entire mesh. Together with the number of cells in boundary layers ($N_{\text{BL-cells}}$) the number of cells in the different ejector sections is calculated. An illustration of different ejector meshes the algorithm generates is presented in Figure 5.4.

The mesh generated by the method is generally of high quality in terms of mesh quality metrics such as mesh skewness and orthogonal quality. A limitation of this approach is distributing the number of cells between the suction and motive channels in the y-direction, as illustrated in Figure 5.4, where only 4 cells are used in the motive nozzle y-direction. A compromise between the mesh resolution in the two

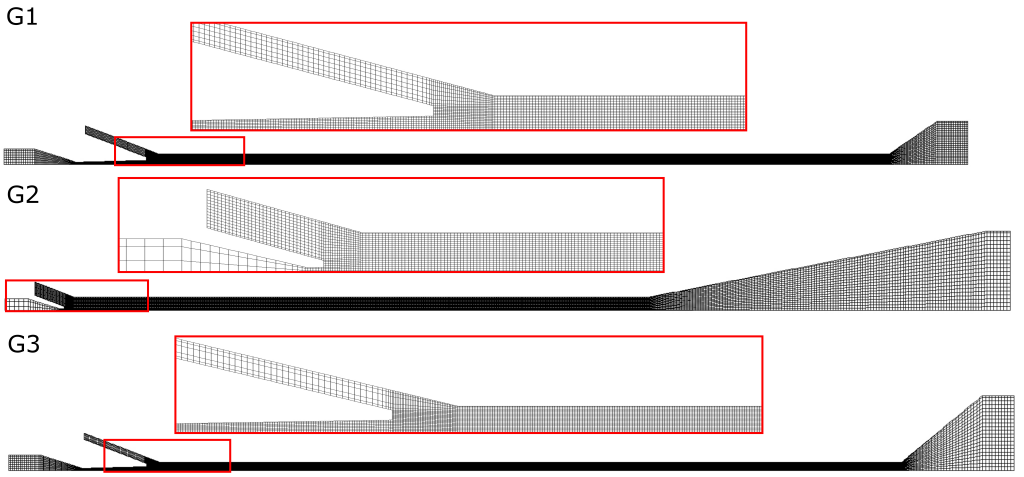

Figure 5.4: Illustration of produced meshes by the meshing algorithm. G1-G3 are three random samples of meshes generated by the meshing algorithm.

nozzles was found by having a slightly higher weighted mesh resolution in the motive nozzle than in the suction chamber. With the large range of ejector geometry dimensions used in the study, the number of cells in each calculation dramatically varied. As an example, an ejector with twice the length would have double the number of cells. These effects made some data points extremely computationally costly, as the number of cells could reach several hundred thousand cells. Further work should consider these effects, and consider computational load balancing or accounting for these effects in the meshing algorithms without reducing accuracy. In this work, the problem was considered by keeping a constant number of cells in the mixing chamber y-direction.

Different turbulence models are available in the ANSYS Fluent software, and as discussed in Ringstad et al. [71], there is no consensus on the most suitable turbulence model for CO_2 two-phase ejectors. One prominently used turbulence model is the k-ω SST model. This model is preferred when the turbulence boundary layer can be resolved down to a small y^+ value near 1 by the mesh. However, to simplify the wall resolution treatment in the meshing algorithm the k-ϵ Realizable turbulence model was chosen, and the wall turbulence model is treated by the scalable wall function, discussed previously in Section 3.1.3.2. This significantly reduces the complexity of the meshing algorithm and reduces some of the stability issues experienced with the k-ω models when using this method.

5.3.4 CFD setup

The CFD model is set up using the journal file scripting tool for ANSYS Fluent. A journal file is written automatically for each data point, with the defined boundary conditions and geometry parameters written into the journal file. To run multiple instances of ANSYS Fluent at the same time, the tasks are run in parallel using a multi-threading call in Python. The numerical schemes are used according to Table 3.3 defined in Section 3.3.3. The journal file pseudo code is presented in Algorithm 2. After the simulations, the Fluent output files are read and post-processed, and the results are stored in the database.

Algorithm 5.2: Journal file pseudo code used in the CFD automation.

```
Read and compile UDFs;
Read mesh, MeshID from Data;
Read boundary conditions from Data;
Set initial conditions based on boundary conditions;
Define under-relaxation factors;
Set numerical scheme to first order;
Run N/2 iterations;
Increase under-relaxation factors;
Run N/2 iterations;
Set numerical scheme to second order;
Run N iterations;
Write mass flow, entropy, and uniformity to file;
Write pathline variables to file;
```

5.3.5 KPIs

The post-processing was based on a few Key Performance Indicators (KPIs): motive and suction mass flow rate (entrainment ratio), ejector efficiency, mixing entropy generation rate, and ejector outlet flow uniformity for velocity and vapor fraction. Mass flow rates were calculated by Fluent at the inlets and outlets of the ejector. These were reported and post-processed by the algorithm. Using the mass flow rates and boundary conditions, the ejector efficiency was calculated from Eqn. (2.4) using calls to the CoolPack software [130]. Entropy generation was found by calculating the mass-weighted average of the incoming and outgoing entropy in each section. The ejector outlet flow uniformity was calculated using the Uniformity Index defined in ANSYS Fluent, Eqn. (5.8):

$$\gamma_a = 1 - \frac{\sum_{i=1}^{n} (|\phi_i - \bar{\phi}_a|) A_i}{2|\bar{\phi}_a| \sum_{i=1}^{n} A_i} \tag{5.8}$$

where $\bar{\phi}_a$ is the averaged value of the field variable ϕ. Here, the uniformity index is calculated for the vapor fraction α and the axial velocity u. These two KPIs indicate to well the flows are mixed at the outlet of the ejector, which would indicate if a lowered efficiency is caused by poor mixing in the ejector. It is not a direct indicator of ejector performance.

6 Articles

6.1 Background for articles

The research started with identifying key gaps in the field of CO_2 ejector modeling. First, while review papers on CO_2 ejectors were previously published [7, 11, 60, 63, 64, 62, 61, 53, 59, 53, 65], only limited attention was dedicated to two-phase ejectors models. To bridge this knowledge gap an extensive literature study was performed, covering all main aspects of CO_2 two-phase ejector modeling in detail. This literature study is published in Article I - *A detailed review on CO_2 two-phase ejector flow modeling* and Conference article II - *CO_2 ejector modeling using CFD: current status.*

Within the framework of this thesis, two main focus areas regarding ejector design research were identified: (A) development of accurate and fast multiphase models for CO_2 ejector modeling, and (B) development of efficient and useful tools and concepts for the design of future ejectors.

Multiphase model development work (A) was conducted in several stages. First, to ensure appropriate knowledge of ejector CFD modeling, an investigation of an ammonia ejector (R717) was conducted. This work is presented in Conference article I - *Investigation of CFD models for ammonia ejector design.* The conclusions were that additional experimental measurements are necessary for appropriate validation of the CFD models. One year into the thesis, after a visit to the Silesian University of Technology and the Università Degli Studi di Firenze, began an extended period of work on improvements and developments with the current state-of-the-art CFD models from these labs. One outcome from this work is presented in Conference article III - *Two-fluid CFD model for R744 two-phase ejectors*, where a novel two-fluid model for CO_2 ejectors was presented. Due to model complexity and computational limitations, further developments with this model are left for

future work. A key finding of the review work was the lack of experimental validation data for CO_2 ejectors in the literature. Therefore, an experimental study with an ejector design not yet presented in literature was conducted and used for further validation of the HEM CFD model in Article III - *Swirl-bypass nozzle for CO_2 two-phase ejectors: Numerical design exploration.*

Articles I, and Conference article I, II, III, and IV are intended to contribute to the completion of the stated thesis objectives: *implementing and comparing available CO_2 ejector models*, and *investigating novel ejector models for improved speed and accuracy.* The experimental campaign and model validation conducted in Articles III is intended to contribute to the objective of *conducting experimental measurements on CO_2 ejectors and validate the results against numerical models.*

This thesis has also explored the development of improved design tools in terms of speed, ease of use, and accuracy, and investigated novel concepts for CO_2 two-phase ejectors (B). A limiting factor in using CFD models for ejector design is the requirement for high-level manual setup for each computation, such as setting up models, designing the mesh, and post-processing. Therefore, a fully automated script for the CFD workflow for CO_2 ejectors was developed in Python. This tool allows for easy collection of CFD data with any ejector design and operating condition. This database tool was first presented in Conference article V- *CFD-based design algorithm for CO2 ejectors*, where an ejector was designed for a heat pump application for an industry partner using the automated algorithm. The work was extended to investigate the application for large database generation and machine learning. By generating large databases with hundreds of CFD data points, a Gaussian Process Regression (GPR) machine learning model was trained to predict ejector performance while varying ejector shape design and operating conditions. The work gave excellent results, being able to optimize ejector geometry and operating conditions accurately, and was presented in Article II - *Machine learning and CFD for mapping and optimization of CO_2 ejectors.* Lastly, this thesis explores a novel concept for CO_2 ejectors, namely a swirl-inducing bypass inlet. This concept has applications for motive flow rate control or off-design performance improvements. A detailed CFD analysis and design space exploration are conducted in Article III - *Swirl-bypass nozzle for CO_2 two-phase ejectors: Numerical design exploration.*

Articles II and III, and Conference article V are intended to contribute to the completion of the stated thesis objectives: *investigating novel ejector concepts for efficiency improvements*, and *the development of improved ejector design methodologies using automated model approaches and data analysis.*

The journal articles are summarized in Sections 6.2-6.4, and the conference article abstracts are stated in Section 6.5:

- Article I - Section 6.2
  - *A detailed review on CO_2 two-phase ejector flow modeling*
- Article II - Section 6.3
  - *Machine learning and CFD for mapping and optimization of CO_2 ejectors*
- Article III - Section 6.4
  - *Swirl-bypass nozzle for CO_2 two-phase ejectors: Numerical design exploration*
- Conference article I - Section 6.5.1
  - *Investigation of CFD models for ammonia ejector design*
- Conference article II - Section 6.5.2
  - *CO_2 ejector modelling using CFD: current status*
- Conference article III - Section 6.5.3
  - *Two-fluid CFD model for R744 two-phase ejectors*
- Conference article IV - Section 6.5.4
  - *Comparative study of R744 ejector CFD models*
- Conference article V - Section 6.5.5
  - *CFD-based design algorithm for CO2 ejectors*

6.2 Article I - A detailed review on CO_2 two-phase ejector flow modeling

6.2.1 Statement on co-authorship and contribution

The article was compiled and written over the course of 10 months. The primary work of compilation of references, summarizing, and writing was conducted on my part. Significant contributions in supervision, conceptualization, reference suggestions, proofreading, and article composition were done by the co-authors.

6.2.2 Summary of article

The contents of this article are to a degree repeated in Section 3. Therefore, a short description of the main topics, discussions, and findings are recounted here.

Abstract: *Ejector-equipped vapor-compression systems for refrigeration and cooling, relying solely on CO_2 (R744) as a natural working fluid, are perceived to be an eco-friendly and highly efficient solution for many applications. However, the complexity of two-phase ejector flows makes it very challenging to find reliable and efficient ejector designs. Improved design methods are necessary to achieve higher performance in R744 units compared to the traditional compressor-based systems with refrigerants that put a high strain on the environment. Consequently, the development of advanced models and tools for an accurate design of the R744 ejectors has been a highly prioritized research topic. To the best of the authors' knowledge, the current status of R744 ejector models and their limitations has not been thoroughly evaluated yet. To summarise the current state of the art and knowledge gaps, this work presents an exhaustive overview of the available numerical models applied to R744 two-phase ejectors, i.e. multiphase flow modeling, turbulence aspects, numerical solution methods, applications of models, to further encourage the adoption of R744 vapor-compression solutions. Finally, a thorough discussion of different focus points for future research as well as the main challenges in the field is presented.*

An overview of relevant two-phase ejector physics is presented discussing relevant topics such as two-phase flow topology and non-equilibrium conditions. Additionally, important non-dimensional numbers are defined and discussed.

Available multiphase models for CO_2 ejectors are presented and critically discussed. Each model's treatment of non-equilibrium conditions is emphasized, as this is identified as a key point for successful multiphase modeling of ejectors. The available

models discussed in this article are compared based on their advantages and disadvantages. A summary of the comparison is presented in Table 6.1. Based on published results the model accuracies are compared for the motive mass flow rate. This is illustrated in Figure 6.1. Some key findings were that motive mass flow rate predictions were well represented at supercritical pressures, however, to account for low-pressure conditions additional ejector physics must be considered. Additionally, the severe lack of accuracy in terms of suction mass flow rate accuracy and possible reasons were highlighted.

Table 6.1: Overview of currently available R744 two-phase ejector models, their limitations, and advantages.

Model	Advantages	Challenges and limitations
HEM		
[92], [93], [123] [94]	-Simplicity and stability -Accurate at supercritical conditions -Extensively tested in literature	-Does not consider meta-stability (underestimates flashing flows at low motive pressures)
HRM		
[95], [135], [124]	-Considers meta-stability, -Extended with variable relaxation time for subcritical conditions	-Empirically based parameters for relaxation time, -Requires tuning of parameters
Mixture		
[98], [112]	-Considers meta-stability, -Can more accurately evaluate the phase fractions by mass transfer modeling -Highly accurate results for motive flows	-Increased complexity, -Requires tuning of model parameters, -Less profound literature database on R744 ejectors -Not yet tested for low motive pressure

The use of turbulence models for CO_2 ejectors is reviewed, some turbulence models are further discussed and some potential future developments are highlighted.

Different numerical solution methods are presented for CFD models. Additionally, the differences between lower and higher-dimensional models (thermodynamic, 1D, CFD) are considered.

Available experimental validation data from the literature are discussed and reviewed. The main findings were that a lack of local experimental data (temperature, pressure, velocity) is limiting the validation and development of CO_2 ejector models. Some challenges regarding experimental data collection are highlighted and a compiled dataset of experimental data from several sources is presented.

Different applications of CO_2 two-phase ejector models are discussed and previous

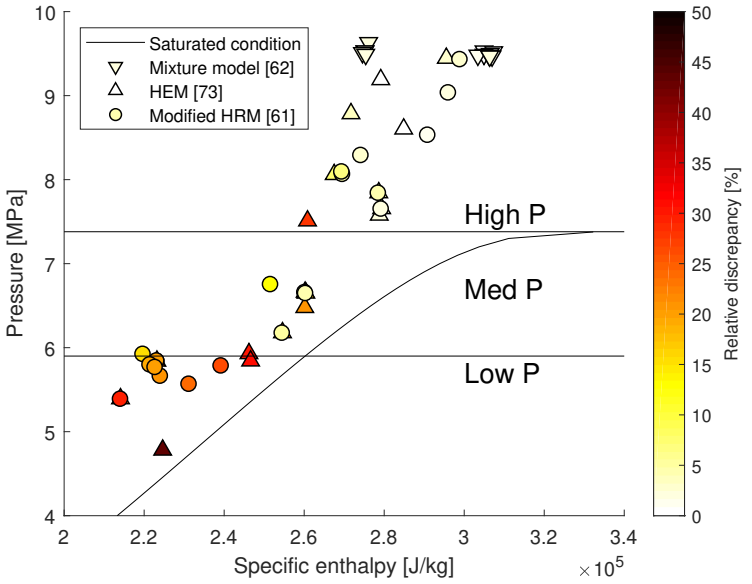

Figure 6.1: Relative discrepancy of motive mass flow rate plotted at the corresponding motive condition. Downward triangle - Mixture model [112], Upward triangle - HEM [135], Circle - modified HRM [96].

model applications are reviewed, such as reduced-order modeling, design optimization, and entropy production modeling.

Lastly, the future outlook of CO_2 ejector models is summarized, highlighting the need for more experimental data, improved ejector CFD models, and more design tools for ejectors.

6.3 Article II - Machine learning and CFD for mapping and optimization of CO_2 ejectors

6.3.1 Statement on co-authorship and contribution

The work of producing the database generation tool was done over the course of 6 months. Integration with the GPR tool took approximately one month. The generation of data and data analysis were conducted over a period of 4 months. Writing the article was done over the course of 3 months. The author's contribution to this article was the primary manuscript writing, data analysis, and programming/development of the design tool. Significant contributions on supervision, proofreading, and suggestions for applications were done by the co-authors.

6.3.2 Summary of article

Abstract: *In this study a novel simulation-based algorithm for CO_2 ejector design and performance evaluation is presented. The algorithm is based on an automated Computational Fluid Dynamics (CFD) workflow that can account for different ejector geometries and operating conditions. The CFD data points are used to train a Gaussian Process Regression (GPR) machine learning model to predict the ejector performance indicators; efficiency, mass flow rates, outflow uniformity, and entropy growth. Two use cases are investigated using this methodology: 1) performance mapping for off-design operating conditions of a given ejector and 2) design mapping of ejector performance with 5 geometry variables investigated. The results show that this algorithm can be used to efficiently explore ejector design and look for optimized geometries, as well as produce ejector performance maps.*

6.3.2.1 Underlying models

The machine learning model is based on a GPR surrogate approach, a description can be found in Section 5.2.1. Gaussian Process Regression (GPR) is a supervised machine learning tool based on Bayesian regression to generate surrogate models.

The CFD model is based on the homogeneous equilibrium model (HEM), described in detail in Chapter 3.2.1. This model is accurate for supercritical operating conditions, which this article is limited to. However, the approach is easily extendable to use other CFD models. The CFD model validation is discussed in the article, and a mesh study was conducted using the new meshing algorithm.

6.3.2.2 Database generation

The GPR modeling approach requires a significant database to improve surrogate model accuracy. The database is generated using a novel automated CFD workflow. The algorithm includes automatic meshing, pre- and postprocessing of results, and running simulations. The design space is sampled using a Latin Hyper Cube approach. More details on the database generation tool are given in Section 5.3.4.

6.3.2.3 Results

Three use cases were investigated using this methodology: 1) performance mapping for off-design operating conditions of a given ejector, 2) design mapping of ejector performance with 5 geometry variables investigated, and 3) flow structure prediction along pathlines in the ejector.

For the first use case, the database size was discussed and a comparison of three different-sized databases (100, 300, and 600 data points) was conducted. The accuracy was estimated using 15% of the data as hidden test data that is left out of the model training and 85% as training data. The comparison showed that increasing the database size directly improved model accuracy for most of the KPIs.

The feature length-scales were analyzed for cases 1) and 2). In case 1), some important relationships in the dataset were identified and discussed, such as a negligible dependence on suction enthalpy on the performance KPIs, and relationships between pressure and flow uniformity. Similarly, for the second use case, the model found relationships between motive mass flow rate and nozzle geometry, as well as the importance of diffuser geometry for flow outlet uniformity.

Surrogate model heat maps were generated for cases 1) and 2) using two features. An example from case 1 is shown in Figure 6.2(a) using motive pressure and enthalpy as the independent variables. Similarly, in Figure 6.2(b) a heat map of ejector efficiency is shown using mixing chamber length and diameter as plotting variables. These plots illustrate the performance mapping that can be generated using the algorithm.

Using the surrogate model mapping, an optimization algorithm was used to identify high-efficiency designs. The optimization algorithm is based on a gradient descent method. An illustration of the optimization paths is shown in Figure 6.2(c). The results show that the model can find an optimal operating condition for the ejector. A similar optimization was done for the shape design parameters. The optimized design lies very close to the initial ejector design, showing that the algorithm can find good designs with limited manual work. The suggested designs were compared to new CFD calculations which confirmed the high accuracy of the GPR surrogate model.

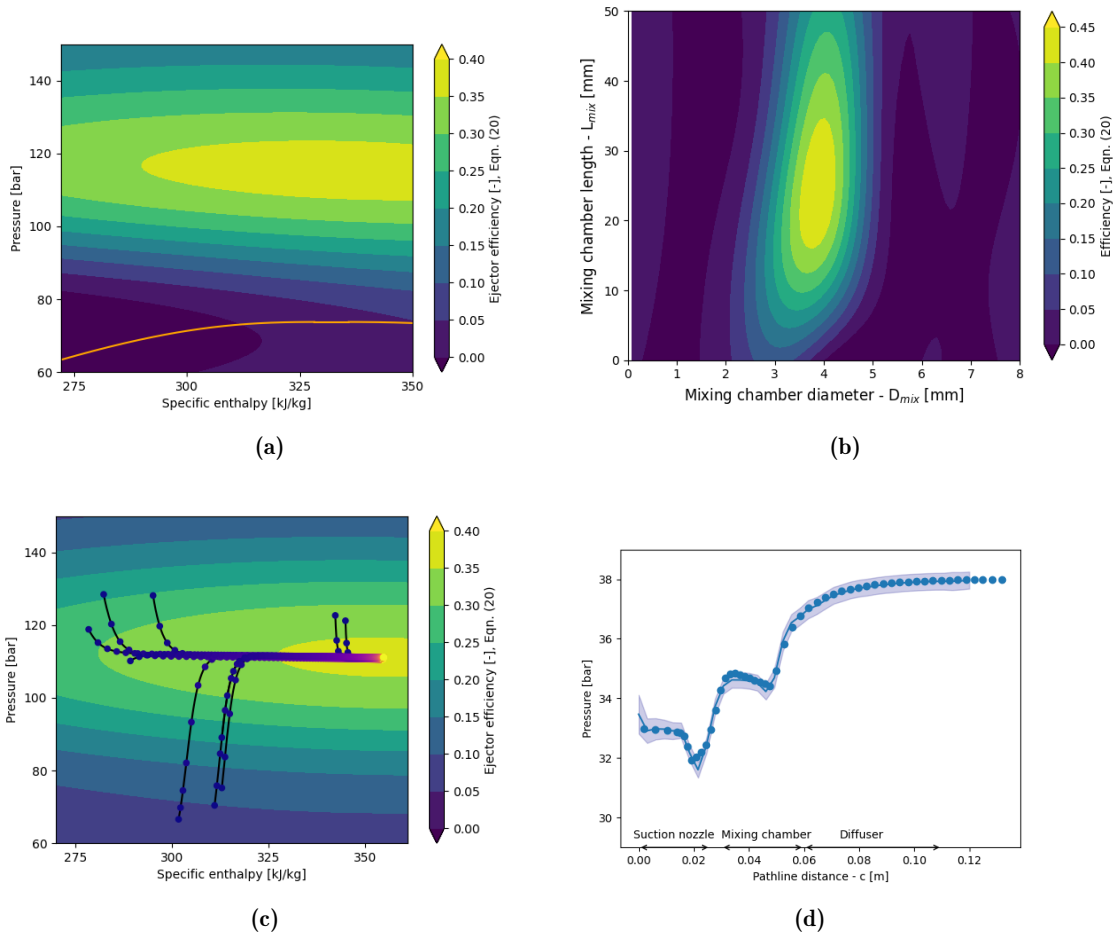

Figure 6.2: (a) GPR predicted efficiency (Eqn. 2.4) heat map in a P-h diagram for motive conditions at different pressure lifts. The saturation line for CO_2 is plotted in orange. Conditions: h_s= 430 [kJ/kg], P_s = 38 [bar], P_{lift}=7 [bar]. (b) GPR predicted efficiency heat contour plot in a D_{mix}-L_{mix} design space. (c) Optimization paths in a P-h diagram of ejector efficiency from randomized starting positions. The optimization path is colored black, and every tenth iteration is plotted with a circle colored according to the iteration number to illustrate convergence. (d) Predicted velocity distribution (line plot) along the central suction pathline with a mixing chamber diameter of $D_{mix} = 0.004$ [m]. CFD data are marked with circles. The colored area corresponds to the predicted velocity +− 1 standard deviation.

The significance of mixing chamber geometry on flow structure was investigated with the GPR approach. The findings were that the flow structure was represented with decent accuracy, with a mean error of 2.2 [m/s] and 0.13 [bar], however, flow gradients were challenging to resolve accurately. An example is shown in Figure 6.2(d), where the velocity along a suction flow path line is predicted using the methodology.

6.4 Article III - Swirl-Bypass Nozzle for CO_2 Two-Phase Ejectors: Numerical Design Exploration

6.4.1 Statement on co-authorship and contribution

The model setup, experimental test campaign, model simulation, article production, and result analysis was conducted over 18 months. The author's contribution to this article was the primary writing, conducting the experimental tests, model setup, and simulation. Significant contributions on supervision, proofreading, guidance, setup of the experimental test rig, and help in analyzing the results were done by the co-authors.

6.4.2 Summary of article

Abstract: *In this work, a novel ejector design concept of a swirl-bypass nozzle is proposed to improve the off-design performance of CO_2 two-phase ejectors. The swirl-bypass nozzle allows part of the flow to bypass into the ejector mixing chamber to generate swirl. The design of such a device is investigated using a 3D multiphase CFD model. An extensive experimental test campaign is conducted to validate the baseline homogeneous equilibrium CFD model. The model's prediction motive mass flow rate was within a 2–12% error and the suction mass flow rate was predicted with a 3–50% error. Based on the tested ejector geometry, simulations of different ejector swirl-bypass inlets are conducted. The results show that, for the current design, total entrainment of the ejector is reduced by 2–20% with the swirl-bypass inlet. The axial position of the bypass inlet plays a primary role in the bypass inlet flow rate, and, consequently, in suction flow reduction. This is found to be due to the bypass flow blocking off the suction mass flow rate, which has a net negative impact on performance. Finally, several design improvements to improve future designs are proposed.*

6.4.2.1 Swirl bypass concept

The article proposes a novel ejector design concept where a secondary inlet is introduced in the mixing section of the ejector. This secondary inlet is designed to generate a swirl component to the mixing process in the ejector. Theoretically, the swirl component allows for better mixing of the primary and secondary flow. The specific design of such a swirl port is not yet discussed in the literature. Several possible applications of such a port exist. One example is to use it to allow for the flow of additional suction flow, this allows the port to function as a bypass inlet for off-design operation. Alternatively, the port can be used for control of the primary

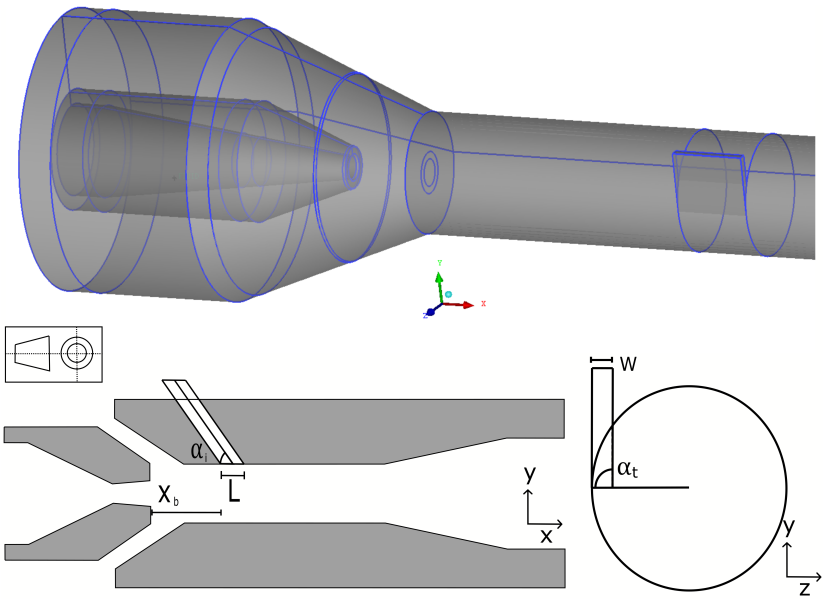

Figure 6.3: Generic ejector geometry with geometry parameters. Gray color signifies solid parts.

flow by allowing a part of the motive flow to enter through the swirl inlet.

As opposed to the standard bypass, the novel swirl bypass nozzle is angled with a tangential component to the ejector. The effect of such a design is investigated in detail in this study. Several studies have shown that positive efficiency effects can be gained by increasing mixing by the use of swirl flow. To the best of the authors' knowledge, the bypass injection for swirl generation in ejectors has not yet been explored in the literature. For this design, a compromise has to be made between moving the swirl bypass inlet downstream for better off-design performance or upstream in the mixing chamber for optimal mixing performance. The swirl-bypass port is illustrated with the main parameters shown in Figure 6.3.

6.4.2.2 Model setup and experimental validation

The model was set up using the 3D two-phase HEM for CO_2 ejectors described in Section 3.2.1. The mesh was generated using a 3D ejector meshing script in ANSYS ICEM, and the mesh independence study was presented in Section 3.4.2.2.

An experimental test campaign was conducted to gather validation data for the ejector model. The results with the HEM are compared against experimental data, discussed in detail in Section 4. The comparison between the experimental and computational results indicates that the motive flow rate can be well predicted at

super-critical pressures, however, accuracy drops at lower-pressure motive conditions. This agrees well with previous literature on CO_2 CFD ejector modeling [71]. This part of the study was restated in Section 3.4.1.

6.4.2.3 Results and discussion

A study of the swirl bypass position, the swirl inclination and tangential angle, and the pressure lift parameters was conducted. The results were compared to a baseline simulation without a bypass inlet. The results are shown in Table 6.2. The findings of the study were that for the presented baseline ejector geometry, the swirl bypass inlet caused a decrease in ejector performance for all geometry configurations of the swirl bypass inlet. The decrease in performance was found to be more significant for higher flow rates of the bypass flow. This was attributed to the bypass flow blocking the suction flow illustrated Figure 6.4. The bypass flow rate was relatively insensitive to the tangential- (α_t) and inclination angle (α_i), however, was primarily governed by the inlet position. For an inlet position close to the start of the mixing chamber ($x_b \approx$2-4 D_{mix}), a larger bypass flow was generated, while for an inlet position further back, the bypass flow was reduced to nearly no flow.

The flow structure of the swirl mixing process in the ejector was studied in detail in the article. Different possibilities for improvements to this concept are suggested that could bring up the efficiency of this ejector design concept. These design improvements include:

- Increase in mixing-chamber diameter.
- Reduction in bypass inlet size.
- Optimization of bypass inlet opening shape.
- Adding additional bypass inlets with a constant offset.

Additionally, several directions for future research have been presented that can potentially improve future generations of the swirl-bypass ejector design:

- Combined design optimization of ejector and swirl bypass inlet.
- Identification of optimal operating ranges.
- Designing for simple and low-cost manufacturing.
- Exploration of the combination of different ejector concepts.
- Definition of appropriate control strategies.

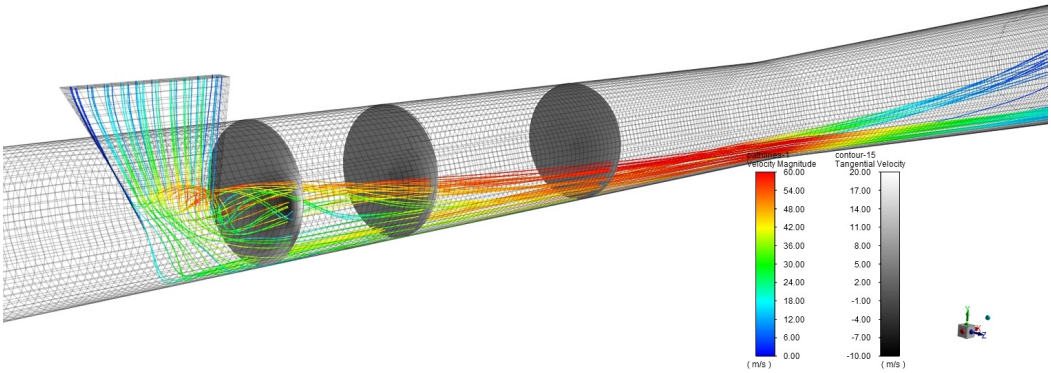

Figure 6.4: Flowpath illustration of the flow coming from the bypass inlet. Different cross-sectional contour plots of the tangential velocity are shown for locations along the axial direction after the bypass inlet.

Table 6.2: Parameter study of the different geometric features of the bypass inlet on bypass performance. Simulations are identified by the simulation ID Sim, where the prefix N indicates no bypass. The column named Diff is defined as the difference in percentage between the total entrainment (bypass and suction) compared to the same operating condition without bypass.

Case	**Sim**	x_b [-]	α_i [°]	α_t [°]	P_{lift} [bar]	MFR_s [kg/s]	MFR_b [kg/s]	**Diff [%]**
Case IV	1	2	0	90	2.5	0.0295	0.0016	−21.3
	2	4	0	90	2.5	0.0321	0.0015	−15.0
	3	7	0	90	2.5	0.0375	0.0006	−3.6
	4	10	0	90	2.5	0.0385	0.0003	−1.8
	5	4	20	90	2.5	0.0324	0.0015	−14.2
	6	4	45	90	2.5	0.0328	0.0012	−13.9
	7	4	0	40	2.5	0.0303	0.0027	−16.5
	8	4	0	60	2.5	0.0308	0.0025	−15.7
	9	4	45	90	2	0.0395	0.0019	−20.0
	10	10	0	90	1	0.0454	0.0025	−14.0
Case I	11	2	0	90	2	0.0328	0.0021	−22.8
	12	4	0	60	2	0.0320	0.0039	−20.6
	13	4	0	90	2	0.0335	0.0021	−21.3
	14	4	20	90	2	0.0340	0.0020	−20.5
	15	7	0	90	2	0.0357	0.0015	−17.7
	16	4	20	90	1	0.0378	0.0024	−18.8
	17	4	20	90	0.5	0.0426	oscillating	
No bypass								
Case IV	N1	-	-	-	2.5	0.0395	-	
	N2	-	-	-	2	0.0518	-	
	N3	-	-	-	1	0.0557	-	
Case I	N4	-	-	-	2	0.0452	-	
	N5	-	-	-	1	0.0495	-	
	N6	-	-	-	0.5	oscillating	-	

6.5 Collection of conference articles

6.5.1 Investigation of CFD models for ammonia ejector design - 2019

Ringstad, Knut Emil; Hafner, Armin; Allouche, Yosr. (2019) Investigation of CFD models for ammonia ejector design. 8th Conference on Ammonia and CO2 Refrigeration Technologies, Proceedings.

Abstract: *In this work, the flow structures inside a transonic- single-phase ammonia ejector are investigated using CFD. The efficiency of ammonia (R717) vapor compression cycles can be improved by including an ejector component in the system. A good understanding of the flow phenomena inside the ejector is required for the proper design of these components. In the present work, a 2D axisymmetric CFD model using ANSYS Fluent software is used to investigate the flow characteristics of the ejector. The model uses a steady-state coupled pressure-based solver together with the k-omega SST turbulence model. A mesh refinement study has been done to investigate grid independence. Results indicate that the model can predict the correct trends of ejector operation, however, fails to accurately reproduce the experimental results. The results suggest that more advanced multiphase models may be required to accurately model super-sonic ammonia ejectors.*

6.5.2 CO_2 ejector modelling using CFD: current status - 2019

Ringstad, Knut Emil; Allouche, Yosr; Gullo, Paride; Banasiak, Krzysztof; Hafner, Armin. (2019) CO2 ejector modelling using CFD: current status. Proceedings of the 25th IIR International Congress of Refrigeration. Montréal, Canada, August 24-30, 2019.

Abstract: *This article reviews the current status of CFD models for two-phase CO_2 ejectors. The models that are most prominent in the literature are the HEM, HRM, DEM, and mixture models. These are similar modeling approaches, but treat the prediction and properties of phase change inside the motive nozzle differently. The accuracy of the different approaches and their challenges and benefits are highlighted in this work.*

6.5.3 Two-fluid CFD model for R744 two-phase ejectors - 2020

Ringstad, Knut Emil; Hafner, Armin. (2020) Two-fluid CFD model for R744 two-phase ejectors. Proceedings of the 14th IIR-Gustav Lorentzen Conference on Natural Refrigerants - GL2020.

Abstract: *This paper presents early results from a novel two-fluid Eulerian-Eulerian multiphase model for R744 two-phase ejectors, which to the authors' knowledge has not previously been presented in the literature. As opposed to previous R744*

ejector models, this formulation includes non-equilibrium states for temperature, momentum, and chemical potential. The model is implemented into ANSYS Fluent using user-defined functions and can achieve converged results faster than previous non-equilibrium formulations. Results are compared with experimental results. The mesh and model parameters are studied for their impact on accuracy.

6.5.4 Comparative study of R744 ejector CFD models - 2021

Ringstad, Knut Emil; Hafner, Armin. (2021) Comparative study of R744 ejector CFD models. Proceedings of the IIR - 10th International Conference on Compressors and Coolants.

Abstract: *This work presents a comparative study of four different R744 ejector CFD models at a wide range of operating conditions. The models compared are the homogeneous equilibrium model, the UDRGM mixture model, a homogeneous relaxation model, and an Eulerian two-fluid model. The results are also compared to experimental data available in the literature. The models are tested for high and low operating pressures, and the effects of non-equilibrium are discussed. The results are discussed and recommendations for model development are suggested.*

6.5.5 CFD-based design algorithm for CO2 ejectors- 2021

Ringstad, Knut Emil; Banasiak, Krzysztof; Hafner, Armin; (2021) CFD-based design algorithm for CO2 ejectors. 9th Conference on Ammonia and CO2 Refrigeration Technologies, Proceedings.

Abstract: *In this work, a novel CFD-database generation algorithm for CO2 ejectors is presented. The algorithm is explained and its details are discussed. A case for CFD database generation is then performed based on an ejector design for an industry client. The ejector design is investigated with different design parameters around the suggested design. Design improvements are suggested based on the numerical results, and a final design is suggested. The final design had a high ejector efficiency of simulated to be 46% at the design point, and the ejector performance is evaluated and discussed for off-design conditions.*

7 Conclusions and suggestions for further work

"The presence of those seeking the truth is infinitely to be preferred to the presence of those who think they've found it."

— T. Pratchett, *Monstrous Regiment*

7.1 Conclusions

The innovative aim of this thesis was to identify and implement novel methods for an improved design of two-phase ejectors to be integrated into natural refrigeration systems. In this work, an exhaustive study on appropriate design methodologies, accurate flow modeling, and novel design concepts was carried out. The main findings clearly show that the application of ejectors can significantly improve the performance of refrigeration systems by the recovery of expansion losses, consequently increase of COP, when properly designed. Ejector CFD modeling was found to be the key tool for an accurate ejector design due to the large complexity and interdependence of the ejector design parameters.

7.1.1 Literature review and CFD modeling

In this thesis, a fundamental background about ejector modeling was built based on a thorough literature review and numerical studies. Different models were evaluated

and compared in terms of computation time and accuracy. The main conclusions reported from the literature review and the conducted CFD model comparisons are summarised as follows.

It was established that the non-equilibrium thermodynamics of CO_2 is a key feature to accurately model the CO_2 ejector at motive temperatures and pressures below the critical point. However, clear evidence that this is the main effect causing the discrepancies in motive mass flow rate prediction at low pressures needs to be demonstrated. The ejector motive mass flow rate can be accurately predicted using CFD models (within 10% error) with equilibrium models at high operating pressures (above or near critical pressure), however, the suction mass flow rate is less accurately modeled (20-100% error). This is generally associated with the complexity of multiphase turbulence and the lack of an accurate prediction of the mixing process. In addition, the accuracy of suction flow rate prediction is dependent on accurate multiphase formulations and phase change. In the literature, it is found that though several advanced and accurate CFD models have been presented, their computational costs are prohibitively high. A need for engineering accurate models with low computational costs is often reported as important for future design algorithms. Furthermore, a lack of experimental validation data with measurements inside the ejector is often reported. Such data is difficult to obtain due to the high velocities taking place inside the ejector and the small size scales of the ejector geometry. More experimental data is needed to compare different modeling approaches on other data than just mass flow rates.

The results of the CFD investigations conducted in this work agree well with these findings. An experimental test campaign was conducted to obtain data for validation of the CFD models used in this work. These experiments were carried out for a large range of operating conditions and with an ejector geometry designed for low pressure lift, which had not yet been reported in the literature, which makes the results valuable for future model validation. It was found that the HEM model predicted the experimental results with errors within the range of 2-12% for the motive mass flow rate and between 3-50% for the suction mass flow rate. Reduced accuracy of the motive mass flow rate predictions (12% error) was found for the lower motive pressure conditions, while more accurate results (2% error) were observed for the high motive pressure conditions. These observations agree in accuracy in comparison to previous literature on CO_2 ejector modeling. In this thesis, a comparison of several of the most commonly used CFD model approaches was conducted. The findings were that the HEM model was the most accurate approach at high-pressure operating conditions, and less accurate at low-pressure operating conditions. It was also found that the computation time requirements and simulation stability characteristics for the most advanced model (UDRGM mixture model) made simulations prohibitively slow.

This work has also included extensive investigations of different CFD models and formulations for two-phase CO_2 and ammonia ejectors. A two-fluid model formulation in ANSYS Fluent 2019 was implemented. The model includes a pressure-dependent formulation for latent heat modeling. Furthermore, this model is able to account for non-equilibrium thermodynamic properties of liquid and gaseous CO_2. It was found that the model could predict the motive flow rate within 15% error in motive mass flow rate when selecting appropriate model parameters, however further developments are needed to identify more accurate sub-models. A numerical instability caused by oscillations in the pressure in the motive nozzle was identified. This caused the model to be difficult to converge for some boundary conditions. In addition, the validation of these models requires a large amount of experimental data with varied ejector designs and operating conditions.

The main novelties presented in this thesis on the topic of CFD modeling for CO_2 ejectors are:

- An extensive literature review of modeling of CO_2 two-phase ejectors is conducted.
- A novel two-fluid model for CO_2 two-phase ejectors with non-equilibrium properties is presented.
- Different CFD models for CO_2 two-phase ejectors are compared.

7.1.2 Ejector design tool

A way to efficiently design and optimize ejectors through CFD simulations and performance mapping has been explored in Ringstad et al. [80]. A surrogate response surface model based on a GPR-machine learning approach was implemented using a large database compiled from CFD simulations using a novel automated approach. The CFD database included hundreds of data points at various operating conditions (temperatures and pressures) and with different ejector designs (5 design parameters). This database may further be used for future design optimization and is therefore made available open access. The high accuracy of the presented GPR machine learning method (average absolute error in entrainment ratio prediction less than 0.1) was established for ejector performance maps for different ejector design parameters. It was found that the prediction error was reduced with an increased number of data points, and a large number of CFD simulations was required for high-accuracy model prediction. The databases can be efficiently generated by automated CFD calculations, which accelerate computations and improve data reliability. Using the surrogate response surface model, optimization of the ejector shape dimensions and operating conditions was conducted. Lastly, the GPR model was used to map the flow structures inside the ejector using the

detailed CFD data. However, further developments will be necessary to implement these models on a larger scale due to the sharp gradients in ejector flow variables.

Main novelties presented in this thesis on the topic of machine-learning-based design optimization:

- A machine learning approach was used for performance mapping of CO_2 ejectors in terms of design and operating conditions.
- An automated CFD model script was developed and presented (openly available)
- Prediction and optimization using a gradient descent method on the response surface mapping was demonstrated.
- This new design tool was used to design a high novel performance ejector for industry partner [129].

7.1.3 Swirl bypass ejector

A novel concept for ejector design with two potential applications was proposed in this thesis. The ejector was designed with an additional inlet that was placed in the mixing chamber of the ejector. This bypass inlet was oriented such that it was entering tangentially through the ejector wall. The flow that enters through this port generates a swirl motion, intended to improve ejector mixing. The port can be open to the suction flow to increase entrainment at off-design conditions or to motive flow for capacity control. The swirl-generating suction bypass ejector was numerically investigated using CFD with various bypass inlet geometries.

The flow structure was analyzed and discussed in detail in terms of swirl motion. Furthermore, key observations about ejector performance and suggestions to improve future swirl bypass designs were given. The swirl bypass inlet concept has the potential for improving ejector efficiency, however, it is found that the bypass geometry and overall ejector design need to be integrated to achieve higher performance. Performance drops between 2–20% in terms of total entrainment ratio (suction + bypass flow) were predicted for the different ejector bypass inlet designs. This reduction in performance was attributed to the bypass flow blocking the flow path of the suction flow. Consequently, the total entrainment ratio was reduced in the initial suction swirl bypass ejector design. Some possible solutions to address this issue are: increase the mixing-chamber diameter, reduce the bypass inlet diameter, optimize the bypass inlet opening shape and axial position, and add additional bypass inlets with a constant angular offset from each other. The mixing-layer thickness was defined by the ratio of velocity difference over the maximum velocity gradient. The thickness of this layer was analyzed with and without

the swirl bypass. The bypass flow was found to force the motive flow to divert its path off-center. This off-center motive flow was found to influence the mixing layer thickness to be thicker near the bypass outlet and thinner on the opposite side of the ejector mixing chamber.

The main novelties presented in this thesis on the swirl bypass ejector concept:

- A novel ejector design concept was proposed that can be used for off-design performance improvements and motive capacity control
- A numerical design exploration of the suction swirl bypass design was conducted.
- A detailed flow structure analysis was undertaken.
- Several design improvements for future swirl bypass devices were suggested.

7.2 Suggestions for further work

Several suggestions for ways to improve and further investigate knowledge gaps identified in this work are given in the following sections.

7.2.1 Integrated ejector design optimization

The response surface approach to ejector design presented in this work is demonstrated to be able to perform accurate geometry optimization. Experimental testing of the optimized ejector shapes should be conducted to test the optimization tool's accuracy for real applications. Further improvements to the design tool are suggested to be studied in detail. Investigating the use of robust design optimization approaches (optimization with statistical variation in design parameters, e.g. [150]), the use of alternative machine learning approaches such as physics-informed neural networks or symbolic regression [151], and the use of larger databases by for instance including previous numerical and experimental work, is topics that may bring significant improvements to the tool. Producing system-specific ejectors to achieve COP improvements may be possible at an affordable price. This could be achieved by combining low-cost and easy-to-use optimization algorithms, such as the one presented in this work together with low-cost production methods for low-quantity production such as additive manufacturing (3D printing), especially for the suction chamber geometry. The flexibility of additive manufacturing techniques furthermore allows for more detailed ejector design, enabling novel designs with improved ejector efficiencies for instance by applying topology optimization methods. Multi-disciplinary optimization of the ejector to not only improve efficiencies but

also to look at production cost, material costs, environmental impact, and total system efficiency is suggested for further studies. Applying the optimization methods discussed to other ejector devices (e.g. needle position in needle-controlled ejectors), or investigations of other components or ejectors with different working fluids is left for future work. Lastly, it is suggested to integrate the operating condition performance maps developed here with system simulation tools, allowing for easier system design with optimized ejectors given the system operating conditions.

7.2.2 Swirl bypass design

The novel concept of the swirl bypass ejector design was proposed in this thesis work. The two concepts of suction swirl bypass flow for off-design improvements and motive swirl bypass for capacity control both need extensive investigation to bring to their full potential. Several design improvements were found and are highlighted in Ringstad et al. [18], however further work is needed to find general design recommendations. Future studies should investigate using a holistic approach to device design, and optimization of all ejector design parameters is expected to bring significant performance improvements. The swirl bypass design is expected to perform best when operated at pressure lifts lower than the design point. The work conducted by Ringstad et al. [18] implemented an ejector designed for low pressure-lift, therefore further study of the design concept with ejectors designed for high pressure-lifts is suggested. Finally, the exploration of potential applications, control strategies, experimental testing, and integration with system and manufacturing methods is left for further work.

7.2.3 Accurate modeling

Further research should be focused on the development and validation of accurate and computationally fast models for CO_2 two-phase ejectors. The key areas for further development of accurate modeling are highlighted in the conclusions. Models such as two-fluid models can account for more non-equilibrium effects than pseudo-fluid models, which will increase model accuracy if properly integrated and should be further studied. Further investigation into the phase change process is still needed, and models accounting for bubble nucleation and bubble growth may improve model accuracy. Further work on the prediction of the liquid-vapor interface could provide key insights for the future development of ejectors. Indeed, further work on the use of multiscale models for the prediction of bubble and droplet scales and their interactions could be of high value for model accuracy. Detailed investigations into the suction flow and mixing process are suggested, and introducing more advanced turbulence models for multiphase flows may be necessary. Looking toward DNS or LES turbulence modeling for CO_2 ejectors can be valuable to gain a detailed understanding of the mixing process, though the computational costs for this for a full ejector geometry are estimated to be prohibitively high.

Turbulence models such as the GEKO model in ANSYS Fluent [114] that have parameters that can be tuned for different physics could improve mixing predictions and should be further explored. Alternative ways of post-processing data, such as entropy analysis or using machine learning on CFD data, is a promising and not well-explored field for CO_2 ejectors. Further study towards understanding the role of transient flow phenomena in ejectors, both turbulent and inherent, and the required temporal resolution to resolve these is needed. Improved accuracy can be obtained by using density-based solvers to better capture the shocks dynamics in the ejector [94]. The differences between density and pressure-based CFD solvers for CO_2 ejectors are still not fully understood and need further investigation. High-quality experimental measurement data collected inside the ejector are required for validating the different model predictions locally. Though global measurements, such as mass flow rates, can effectively be used for comparing model accuracy, it is of limited use for comparing models where the mass flow rate can be tuned by different model parameters. Advances in flow visualization techniques such as PIV or high-speed imaging in combination with local pressure and temperature measurements can give insight into the phenomena occurring in the ejector. Validation of CO2 ejector models under diverse operating conditions and geometries is crucial for model calibration and a better comprehension of ejector flow physics. Consequently, conducting experimental studies involving various ejector geometries and operating conditions is still necessary.

References

[1] Masson-Delmotte, V., Zhai, P., Pirani, A., Connors, S. L., Péan, C., Berger, S., Caud, N., Chen, Y., Goldfarb, L., Gomis, M. I., Huang, M., Leitzell, K., Lonnoy, E., Matthews, J. B. R., Maycock, T. K., Waterfield, T., Yelekçi, O., Yu, R., and Zhou, B. (2021). *Climate Change 2021: The Physical Science Basis. Contribution of Working Group I to the Sixth Assessment Report of the Intergovernmental Panel on Climate Change*. Tech. rep. IPCC.

[2] Calm, J. M. (Nov. 2008). "The next generation of refrigerants – Historical review, considerations, and outlook". In: *International Journal of Refrigeration* 31.7, pp. 1123–1133. DOI: 10.1016/J.IJREFRIG.2008.01.013.

[3] Gullo, P., Hafner, A., and Banasiak, K. (Sept. 2018). "Transcritical R744 refrigeration systems for supermarket applications: Current status and future perspectives". In: *International Journal of Refrigeration* 93, pp. 269–310. DOI: 10.1016/j.ijrefrig.2018.07.001. URL: https://www.sciencedirect.com/science/article/pii/S0140700718302287?via%7B%5C%%7D3Dihub.

[4] European Commision (2014). *Regulation (EU) No 517/2014 of the European Parliament and of the Council of 16th April 2014 on fluorinated greenhouse gases and repealing Regulation (EC) No 842/2006.*

[5] Kauffeld, M. and Dudita, M. (2021). *Environmental impact of HFO refrigerants & alternatives for the future*. URL: https://www.openaccessgovernment.org/hfo-refrigerants/112698/?fbclid=IwAR25EQxzVeW3diCC8jazvNR0SBUv6%7B%5C_%7Dr76o8bGJL6YyBtorix7fLcWbYNOiA.

[6] Holland, R., Khan, M. A. H., Driscoll, I., Chhantyal-Pun, R., Derwent, R. G., Taatjes, C. A., Orr-Ewing, A. J., Percival, C. J., and Shallcross, D. E. (2021). "Investigation of the Production of Trifluoroacetic Acid from Two Halocarbons, HFC-134a and HFO-1234yf and Its Fates Using a Global

Three-Dimensional Chemical Transport Model". In: *ACS Earth and Space Chemistry* 5.4, pp. 849–857. DOI: 10.1021/acsearthspacechem.0c00355.

[7] Gullo, P., Hafner, A., Banasiak, K., Minetto, S., Kriezi, E., Gullo, P., Hafner, A., Banasiak, K., Minetto, S., and Kriezi, E. E. (Jan. 2019). "Multi-Ejector Concept: A Comprehensive Review on its Latest Technological Developments". In: *Energies* 12.3, p. 406. DOI: 10.3390/en12030406. URL: http://www.mdpi.com/1996-1073/12/3/406.

[8] Coulomb, D., Dupont, L. J., and Pichard, A. (2015). *The Role of Refrigeration in the Global Economy*. URL: https://iifiir.org/en/fridoc/the-role-of-refrigeration-in-the-global-economy-2015-138763 (visited on 12/08/2022).

[9] European Commision (2019). *2030 climate & energy framework*. URL: https://ec.europa.eu/clima/policies/strategies/2030%7B%5C_%7Den.

[10] Gullo, P., Tsamos, K. M., Hafner, A., Banasiak, K., Ge, Y. T., and Tassou, S. A. (Dec. 2018). "Crossing CO2 equator with the aid of multi-ejector concept: A comprehensive energy and environmental comparative study". In: *Energy* 164, pp. 236–263. DOI: 10.1016/J.ENERGY.2018.08.205. URL: https://www.sciencedirect.com/science/article/pii/S0360544218317419.

[11] Elbel, S. and Lawrence, N. (Feb. 2016). "Review of recent developments in advanced ejector technology". In: *International Journal of Refrigeration* 62, pp. 1–18. DOI: 10.1016/j.ijrefrig.2015.10.031. URL: https://www.sciencedirect.com/science/article/pii/S0140700715003266.

[12] Nakagawa, M., Marasigan, A., Matsukawa, T., and Kurashina, A. (Nov. 2011). "Experimental investigation on the effect of mixing length on the performance of two-phase ejector for CO2 refrigeration cycle with and without heat exchanger". In: *International Journal of Refrigeration* 34.7, pp. 1604–1613. DOI: 10.1016/J.IJREFRIG.2010.07.021. URL: https://www.sciencedirect.com/science/article/pii/S0140700710001672.

[13] Hafner, A., Försterling, S., and Banasiak, K. (July 2014). "Multi-ejector concept for R-744 supermarket refrigeration". In: *International Journal of Refrigeration* 43, pp. 1–13. DOI: 10.1016/j.ijrefrig.2013.10.015. URL: https://www.sciencedirect.com/science/article/pii/S0140700714000668.

[14] Liu, F., Li, Y., and Groll, E. A. (Sept. 2012). "Performance enhancement of CO2 air conditioner with a controllable ejector". In: *International Journal of Refrigeration* 35.6, pp. 1604–1616. DOI: 10.1016/j.ijrefrig.2012.05.005. URL: https://www.sciencedirect.com/science/article/pii/S0140700712001193.

[15] Elbel, S. and Hrnjak, P. (May 2008). "Experimental validation of a prototype ejector designed to reduce throttling losses encountered in transcritical R744 system operation". In: *International Journal of Refrigeration* 31.3, pp. 411–422. DOI: 10.1016/J.IJREFRIG.2007.07.013. URL: https://www.sciencedirect.com/science/article/pii/S0140700707001508.

[16] Bodys, J., Smolka, J., Palacz, M., Haida, M., Banasiak, K., and Nowak, A. J. (July 2021). "Experimental and numerical study on the R744 ejector with a suction nozzle bypass". In: *Applied Thermal Engineering* 194, p. 117015. DOI: 10.1016/j.applthermaleng.2021.117015.

[17] Palacz, M., Smolka, J., Kus, W., Fic, A., Bulinski, Z., Nowak, A. J., Banasiak, K., and Hafner, A. (Feb. 2016). "CFD-based shape optimisation of a CO2 two-phase ejector mixing section". In: *Applied Thermal Engineering* 95, pp. 62–69. DOI: 10.1016/j.applthermaleng.2015.11.012. URL: https://www.sciencedirect.com/science/article/pii/S1359431115012478.

[18] Ringstad, K. E., Banasiak, K., Ervik, Å., and Hafner, A. (Sept. 2022). "Swirl-Bypass Nozzle for CO2 Two-Phase Ejectors: Numerical Design Exploration". In: *Energies 2022, Vol. 15, Page 6765* 15.18, p. 6765. DOI: 10.3390/EN15186765. URL: https://www.mdpi.com/1996-1073/15/18/6765/htm%20https://www.mdpi.com/1996-1073/15/18/6765.

[19] Zhu, J. and Elbel, S. (Jan. 2018). "Experimental investigation of a novel expansion device control mechanism: Vortex control of initially subcooled flashing R134a flow expanded through convergent-divergent nozzles". In: *International Journal of Refrigeration* 85, pp. 167–183. DOI: 10.1016/j.ijrefrig.2017.09.023.

[20] Zheng, L., Deng, J., and Zhang, Z. (Apr. 2016). "Dynamic simulation of an improved transcritical CO2 ejector expansion refrigeration cycle". In: *Energy Conversion and Management* 114, pp. 278–289. DOI: 10.1016/J.ENCONMAN.2016.01.069. URL: https://www.sciencedirect.com/science/article/pii/S0196890416300139.

[21] Liu, F. and Groll, E. A. (Apr. 2013). "Study of ejector efficiencies in refrigeration cycles". In: *Applied Thermal Engineering* 52.2, pp. 360–370. DOI: 10.1016/J.APPLTHERMALENG.2012.12.001. URL: https://www.sciencedirect.com/science/article/pii/S135943111200806X.

[22] Taslimi Taleghani, S., Sorin, M., Poncet, S., and Nesreddine, H. (Apr. 2019). "Performance investigation of a two-phase transcritical CO2 ejector heat pump system". In: *Energy Conversion and Management* 185, pp. 442–454. DOI: 10.1016/J.ENCONMAN.2019.02.004. URL: https://www.sciencedirect.com/science/article/pii/S0196890419301578.

[23] Taslimi Taleghani, S., Sorin, M., and Poncet, S. (Mar. 2018). "Modeling of two-phase transcritical CO2 ejectors for on-design and off-design conditions". In: *International Journal of Refrigeration* 87, pp. 91–105. DOI: 10.1016/j.ijrefrig.2017.10.025. URL: https://www.sciencedirect.com/science/article/pii/S0140700717304279.

[24] Nekså, P., Walnum, H. T., and Hafner, A. (2010). "CO2- A refrigerant from the past with prospects of being one of the main refrigerants in the future". In: *9th IIR Gustav Lorentzen Conference 2010 - natural refrigerants – real alternatives*.

[25] Lorentzen, G. (1989). *Method of operating a vapour compression cycle under trans- or supercritical conditions*.

[26] Lorentzen, G. and Pettersen, J. (Jan. 1993). "A new, efficient and environmentally benign system for car air-conditioning". In: *International Journal of Refrigeration* 16.1, pp. 4–12. DOI: 10.1016/0140-7007(93)90014-Y.

[27] Lorentzen, G. (Jan. 1994). "Revival of carbon dioxide as a refrigerant". In: *International Journal of Refrigeration* 17.5, pp. 292–301. DOI: 10.1016/0140-7007(94)90059-0. URL: https://www.sciencedirect.com/science/article/pii/0140700794900590?via%7B%5C%%7D3Dihub.

[28] Lorentzen, G. (Mar. 1995). "The use of natural refrigerants: a complete solution to the CFC/HCFC predicament". In: *International Journal of Refrigeration* 18.3, pp. 190–197. DOI: 10.1016/0140-7007(94)00001-E.

[29] Nekså, P., Rekstad, H., Zakeri, G. R., and Schiefloe, P. A. (May 1998). "CO2-heat pump water heater: Characteristics, system design and experimental results". In: *International Journal of Refrigeration* 21.3, pp. 172–179. DOI: 10.1016/S0140-7007(98)00017-6.

[30] Kim, M.-H., Pettersen, J., and Bullard, C. W. (Jan. 2004). "Fundamental process and system design issues in CO2 vapor compression systems". In: *Progress in Energy and Combustion Science* 30.2, pp. 119–174. DOI: 10.1016/J.PECS.2003.09.002. URL: https://www.sciencedirect.com/science/article/pii/S0360128503000765.

[31] Karampour, M. and Sawalha, S. (Oct. 2017). "Energy efficiency evaluation of integrated CO2 trans-critical system in supermarkets: A field measurements and modelling analysis". In: *International Journal of Refrigeration* 82, pp. 470–486. DOI: 10.1016/J.IJREFRIG.2017.06.002. URL: https://www.sciencedirect.com/science/article/pii/S0140700717302360.

[32] Rony, R., Yang, H., Krishnan, S., Song, J., Rony, R. U., Yang, H., Krishnan, S., and Song, J. (Jan. 2019). "Recent Advances in Transcritical CO2 (R744)

Heat Pump System: A Review". In: *Energies* 12.3, p. 457. DOI: 10.3390/en12030457. URL: http://www.mdpi.com/1996-1073/12/3/457.

[33] Austin, B. T. and Sumathy, K. (Oct. 2011). "Transcritical carbon dioxide heat pump systems: A review". In: *Renewable and Sustainable Energy Reviews* 15.8, pp. 4013–4029. DOI: 10.1016/J.RSER.2011.07.021. URL: https://www.sciencedirect.com/science/article/pii/S1364032111002607?via%7B%5C%%7D3Dihub.

[34] Jin, Z., Eikevik, T. M., Nekså, P., and Hafner, A. (Feb. 2016). "Investigation on CO2 hybrid ground-coupled heat pumping system under warm climate". In: *International Journal of Refrigeration* 62, pp. 145–152. DOI: 10.1016/J.IJREFRIG.2015.10.005. URL: https://www.sciencedirect.com/science/article/pii/S0140700715002996.

[35] Yang, J., Yu, B., and Chen, J. (May 2019). "Improved genetic algorithm-based prediction of a CO2 micro-channel gas-cooler against experimental data in automobile air conditioning system". In: *International Journal of Refrigeration*. DOI: 10.1016/J.IJREFRIG.2019.05.017. URL: https://www.sciencedirect.com/science/article/pii/S0140700719302130.

[36] Luger, C. and Rieberer, R. (Aug. 2018). "Multi-objective design optimization of a rail HVAC CO2 cycle". In: *International Journal of Refrigeration* 92, pp. 133–142. DOI: 10.1016/J.IJREFRIG.2018.05.033. URL: https://www.sciencedirect.com/science/article/pii/S0140700718301968.

[37] G. Ozcana, H., Gunerhanb, H., Hepbaslia, A., and Yaldirakc, H. (2014). "Environmental Impact and Performance Comparison of Refrigerants (R744 and R134a) in a Mobile Air Conditioning System Used for Cooling Buses". In: *International Journal of Engineering and Technology* 7.3, pp. 233–241. DOI: 10.7763/ijet.2015.v7.798.

[38] Kimura de Carvalho, B. Y., Melo, C., and Pereira, R. H. (Apr. 2019). "An experimental study on the use of variable capacity two-stage compressors in transcritical carbon dioxide light commercial refrigerating systems". In: *International Journal of Refrigeration*. DOI: 10.1016/J.IJREFRIG.2019.03.026. URL: https://www.sciencedirect.com/science/article/pii/S0140700719301252.

[39] Mastrullo, R., Mauro, A. W., and Perrone, A. (June 2015). "A model and simulations to investigate the effects of compressor and fans speeds on the performance of CO2 light commercial refrigerators". In: *Applied Thermal Engineering* 84, pp. 158–169. DOI: 10.1016/J.APPLTHERMALENG.2015.03.035. URL: https://www.sciencedirect.com/science/article/pii/S1359431115002586.

[40] Sian, R. A. and Wang, C.-C. (May 2019). "Comparative study for CO2 and R-134a heat pump tumble dryer – A rational approach". In: *International Journal of Refrigeration*. DOI: 10.1016/J.IJREFRIG.2019.05.027. URL: https://www.sciencedirect.com/science/article/pii/S0140700719302269.

[41] Mancini, F., Minetto, S., and Fornasieri, E. (June 2011). "Thermodynamic analysis and experimental investigation of a CO2 household heat pump dryer". In: *International Journal of Refrigeration* 34.4, pp. 851–858. DOI: 10.1016/J.IJREFRIG.2010.12.012. URL: https://www.sciencedirect.com/science/article/pii/S0140700710002872.

[42] Purohit, N., Sharma, V., Fricke, B., Gupta, D. K., and Dasgupta, M. S. (Mar. 2019). "Parametric analysis and optimization of CO2 trans-critical cycle for chiller application in a warm climate". In: *Applied Thermal Engineering* 150, pp. 706–719. DOI: 10.1016/J.APPLTHERMALENG.2019.01.023. URL: https://www.sciencedirect.com/science/article/pii/S1359431118349081.

[43] Dai, B., Zhao, X., Liu, S., Yang, Q., Zhong, D., Hao, Y., and Hao, Y. (Apr. 2020). "Energetic, exergetic and exergoeconomic assessment of transcritical CO2 reversible system combined with dedicated mechanical subcooling (DMS) for residential heating and cooling". In: *Energy Conversion and Management* 209, p. 112594. DOI: 10.1016/j.enconman.2020.112594.

[44] Smitt, S., Tolstorebrov, I., Gullo, P., Pardiñas, A., and Hafner, A. (May 2021). "Energy use and retrofitting potential of heat pumps in cold climate hotels". In: *Journal of Cleaner Production* 298, p. 126799. DOI: 10.1016/j.jclepro.2021.126799.

[45] Matthiesen, O., Madsen, K., and Mikhailov, A. (2010). "Evolution of CO2 systems design based on practical experiences from supermarket installations in Northern Europe". In: *9th IIR Gustav Lorentzen conference on natural working fluids*. Sydney, Australia.

[46] Gullo, P., Elmegaard, B., and Cortella, G. (July 2016a). "Advanced exergy analysis of a R744 booster refrigeration system with parallel compression". In: *Energy* 107, pp. 562–571. DOI: 10.1016/j.energy.2016.04.043.

[47] Gullo, P., Birkelund, M., Kriezi, E. E., and Ryhl Kærn, M. (June 2021). "Novel flow modulation method for R744 two-phase ejectors – Proof of concept, optimization and first experimental results". In: *Energy Conversion and Management* 237, p. 114082. DOI: 10.1016/j.enconman.2021.114082.

[48] Gullo, P., Elmegaard, B., and Cortella, G. (Apr. 2016b). "Energy and environmental performance assessment of R744 booster supermarket refrig-

eration systems operating in warm climates". In: *International Journal of Refrigeration* 64, pp. 61–79. DOI: 10.1016/j.ijrefrig.2015.12.016.

[49] Haida, M., Smolka, J., Hafner, A., Palacz, M., Ostrowski, Z., Bodys, J., Kriezi, E. K., Försterling, S., Nowak, A. J., and Banasiak, K. (Feb. 2020). "Performance operation of liquid ejectors for a R744 integrated multi-ejector supermarket system using a hybrid ROM". In: *International Journal of Refrigeration* 110, pp. 58–74. DOI: 10.1016/j.ijrefrig.2019.10.020.

[50] Murthy, A. A., Subiantoro, A., Norris, S., and Fukuta, M. (Oct. 2019). "A review on expanders and their performance in vapour compression refrigeration systems". In: *International Journal of Refrigeration* 106, pp. 427–446. DOI: 10.1016/J.IJREFRIG.2019.06.019.

[51] Dai, B., Liu, S., Zhu, K., Sun, Z., and Ma, Y. (Mar. 2017). "Thermodynamic performance evaluation of transcritical carbon dioxide refrigeration cycle integrated with thermoelectric subcooler and expander". In: *Energy* 122, pp. 787–800. DOI: 10.1016/J.ENERGY.2017.01.029.

[52] Yang, J. L., Ma, Y. T., and Zhang, J. H. (Jan. 2014). "Optimal heat rejection pressure for transcritical CO2 refrigeration cycle with an expander". In: *http://dx.doi.org/10.1080/15435075.2014.938339* 13.2, pp. 208–212. DOI: 10.1080/15435075.2014.938339. URL: https://www.tandfonline.com/doi/abs/10.1080/15435075.2014.938339.

[53] Elbel, S. (Nov. 2011). "Historical and present developments of ejector refrigeration systems with emphasis on transcritical carbon dioxide air-conditioning". In: *International Journal of Refrigeration* 34.7, pp. 1545–1561. DOI: 10.1016/j.ijrefrig.2010.11.011. URL: https://www.sciencedirect.com/science/article/pii/S0140700710002720.

[54] Kranakis, E. F. (1982). "The French Connection: Giffard's Injector and the Nature of Heat". In: *Technology and Culture* 23.1, pp. 3–38. URL: http://www.jstor.org/stable/3104441.

[55] Nikiforow, K., Koski, P., Karimäki, H., Ihonen, J., and Alopaeus, V. (Sept. 2016). "Designing a hydrogen gas ejector for 5 kW stationary PEMFC system – CFD-modeling and experimental validation". In: *International Journal of Hydrogen Energy* 41.33, pp. 14952–14970. DOI: 10.1016/j.ijhydene.2016.06.122.

[56] Zheng, P., Li, B., and Qin, J. (July 2018). "CFD simulation of two-phase ejector performance influenced by different operation conditions". In: *Energy* 155, pp. 1129–1145. DOI: 10.1016/j.energy.2018.04.066.

[57] Gay, N. H. (1931). *Refrigerating system.* URL: https://www.freepatentsonline.com/1836318.html.

[58] Kornhauser, A. A. (1990). "The use of an ejector as a refrigerant expander". In: *International Refrigeration and Air Conditioning Conference.*

[59] Besagni, G., Mereu, R., and Inzoli, F. (Jan. 2016). "Ejector refrigeration: A comprehensive review". In: *Renewable and Sustainable Energy Reviews* 53, pp. 373–407. DOI: 10.1016/J.RSER.2015.08.059. URL: https://www.sciencedirect.com/science/article/pii/S1364032115009223.

[60] Chen, J., Jarall, S., Havtun, H., and Palm, B. (Sept. 2015). "A review on versatile ejector applications in refrigeration systems". In: *Renewable and Sustainable Energy Reviews* 49, pp. 67–90. DOI: 10.1016/J.RSER.2015.04.073. URL: https://www.sciencedirect.com/science/article/pii/S1364032115003433.

[61] Sumeru, K., Nasution, H., and Ani, F. N. (Sept. 2012). "A review on two-phase ejector as an expansion device in vapor compression refrigeration cycle". In: *Renewable and Sustainable Energy Reviews* 16.7, pp. 4927–4937. DOI: 10.1016/j.rser.2012.04.058. URL: https://www.sciencedirect.com/science/article/pii/S1364032112003565.

[62] Sarkar, J. (2012). "Ejector enhanced vapor compression refrigeration and heat pump systems - A review". In: *Renewable and Sustainable Energy Reviews* 16.9, pp. 6647–6659. DOI: 10.1016/j.rser.2012.08.007.

[63] Tashtoush, B. M., Al-Nimr, M. A., and Khasawneh, M. A. (Apr. 2019). "A comprehensive review of ejector design, performance, and applications". In: *Applied Energy* 240, pp. 138–172. DOI: 10.1016/J.APENERGY.2019.01.185. URL: https://www.sciencedirect.com/science/article/pii/S0306261919301588.

[64] Aidoun, Z., Ameur, K., Falsafioon, M., Badache, M., Aidoun, Z., Ameur, K., Falsafioon, M., and Badache, M. (Mar. 2019). "Current Advances in Ejector Modeling, Experimentation and Applications for Refrigeration and Heat Pumps. Part 2: Two-Phase Ejectors". In: *Inventions* 4.1, p. 16. DOI: 10.3390/inventions4010016. URL: https://www.mdpi.com/2411-5134/4/1/16.

[65] Besagni, G. (Jan. 2019). "Ejectors on the cutting edge: The past, the present and the perspective". In: *Energy*, pp. 998–1003. DOI: 10.1016/j.energy.2018.12.214. URL: https://www.sciencedirect.com/science/article/pii/S0360544218325945.

[66] Gullo, P., Kærn, M. R., Haida, M., Smolka, J., and Elbel, S. (Nov. 2020). *A review on current status of capacity control techniques for two-phase ejectors*. DOI: 10.1016/j.ijrefrig.2020.07.014.

[67] Lucas, C. and Koehler, J. (Sept. 2012). "Experimental investigation of the COP improvement of a refrigeration cycle by use of an ejector". In: *International Journal of Refrigeration*. Vol. 35. 6. Elsevier, pp. 1595–1603. DOI: 10.1016/j.ijrefrig.2012.05.010.

[68] Minetto, S., Brignoli, R., Banasiak, K., Hafner, A., and Zilio, C. (Sept. 2013). "Performance assessment of an off-the-shelf R744 heat pump equipped with an ejector". In: *Applied Thermal Engineering* 59.1-2, pp. 568–575. DOI: 10.1016/j.applthermaleng.2013.06.032.

[69] Banasiak, K., Hafner, A., and Andresen, T. (Sept. 2012). "Experimental and numerical investigation of the influence of the two-phase ejector geometry on the performance of the R744 heat pump". In: *International Journal of Refrigeration* 35.6, pp. 1617–1625. DOI: 10.1016/J.IJREFRIG.2012.04.012. URL: https://www.sciencedirect.com/science/article/pii/S014070071200093X.

[70] Lee, J. S., Kim, M. S., and Kim, M. S. (Nov. 2011). "Experimental study on the improvement of CO2 air conditioning system performance using an ejector". In: *International Journal of Refrigeration* 34.7, pp. 1614–1625. DOI: 10.1016/J.IJREFRIG.2010.07.025. URL: https://www.sciencedirect.com/science/article/pii/S0140700710001714.

[71] Ringstad, K. E., Allouche, Y., Gullo, P., Ervik, Å., Banasiak, K., and Hafner, A. (Dec. 2020). "A detailed review on CO2 two-phase ejector flow modeling". In: *Thermal Science and Engineering Progress* 20, p. 100647. DOI: 10.1016/j.tsep.2020.100647.

[72] Liao, Y. and Lucas, D. (Aug. 2017). "Computational modelling of flash boiling flows: A literature survey". In: *International Journal of Heat and Mass Transfer* 111, pp. 246–265. DOI: 10.1016/j.ijheatmasstransfer.2017.03.121. URL: https://www.sciencedirect.com/science/article/pii/S001793101730460X.

[73] Lawrence, N. and Elbel, S. (2015). "Analysis of two-phase ejector performance metrics and comparison of R134a and CO2 ejector performance". In: *Science and Technology for the Built Environment* 21.5, pp. 515–525. DOI: 10.1080/23744731.2015.1030327. URL: https://www.tandfonline.com/action/journalInformation?journalCode=uhvc21.

[74] Takeuchi, H., Nakagawa, M., and Nakajima, M. (1998). "Performance of two phase ejector in refrigeration cycle; Reito cycle ni tekiyosareru nisoryu

ejector no ryudo tokusei (Journal Article) | ETDEWEB". In: *Proceedings of the 3rd International Conference on Multiphase Flow*. Lyon. URL: https://www.osti.gov/etdeweb/biblio/334826.

[75] Butrymowicz, D., Karwacki, J., and Trela, M. (2005). "Investigation of two-phase ejector in application in compression refrigeration systems." In: *Proceedings of the IIR International Conference on Thermophysical Properties and Transfer Processes of Refrigerants*. Vicenza.

[76] Ozaki, Y., Takeuchi, H., and Hirata, T. (2004). "Regeneration of expansion energy by ejector in CO2 cycle." In: *Proceedings of the 6th IIR Gustav Lorentzen Conference on Natural Working Fluids*. Glasgow.

[77] Haider, M. and Elbel, S. (Apr. 2021). "Development of Ejector Performance Map for Predicting Fixed-geometry Two-phase Ejector Performance for Wide Range of Operating Conditions". In: *International Journal of Refrigeration*. DOI: 10.1016/j.ijrefrig.2021.03.022.

[78] Haida, M., Smolka, J., Hafner, A., Mastrowski, M., Palacz, M., Madsen, K. B., Nowak, A. J., and Banasiak, K. (Nov. 2018a). "Numerical investigation of heat transfer in a CO2 two-phase ejector". In: *Energy* 163, pp. 682–698. DOI: 10.1016/j.energy.2018.08.175. URL: https://www.sciencedirect.com/science/article/pii/S0360544218317110?via%7B%5C%%7D3Dihub.

[79] Bodys, J., Smolka, J., Banasiak, K., Palacz, M., Haida, M., and Nowak, A. J. (June 2018). "Performance improvement of the R744 two-phase ejector with an implemented suction nozzle bypass". In: *International Journal of Refrigeration* 90, pp. 216–228. DOI: 10.1016/J.IJREFRIG.2018.03.020. URL: https://www.sciencedirect.com/science/article/pii/S0140700718300999.

[80] Ringstad, K. E., Banasiak, K., Ervik, Å., and Hafner, A. (Nov. 2021). "Machine learning and CFD for mapping and optimization of CO2 ejectors". In: *Applied Thermal Engineering* 199, p. 117604. DOI: 10.1016/J.APPLTHERMALENG.2021.117604.

[81] Grazzini, G., Milazzo, A., and Mazzelli, F. (2018). *Ejectors for efficient refrigeration: Design, applications and computational fluid dynamics*. Springer International, pp. 1–176. DOI: 10.1007/978-3-319-75244-0.

[82] Zhu, J. and Elbel, S. (2016). "A New Control Mechanism for Two-Phase Ejector in Vapor Compressions Cycles Using Adjustable Motive Nozzle". In: *Proceedings of the 16th International Refrigeration and Air Conditioning Conference*.

[83] Liu, F., Groll, E. A., and Li, D. (Sept. 2012). "Investigation on performance of variable geometry ejectors for CO2 refrigeration cycles". In: *Energy* 45.1,

pp. 829–839. DOI: 10.1016/j.energy.2012.07.008. URL: https://www.sciencedirect.com/science/article/pii/S0360544212005385.

[84] Boccardi, G., Botticella, F., Lillo, G., Mastrullo, R., Mauro, A. W., and Trinchieri, R. (Oct. 2017). "Experimental investigation on the performance of a transcritical CO2 heat pump with multi-ejector expansion system". In: *International Journal of Refrigeration* 82, pp. 389–400. DOI: 10.1016/j.ijrefrig.2017.06.013.

[85] Danfoss (2023). *Multi Ejector Solution™*. URL: https://www.danfoss.com/en/products/dcs/valves/electric-expansion-valves/multi-ejector-solution/.

[86] Haida, M., Banasiak, K., Smolka, J., Hafner, A., and Eikevik, T. M. (Apr. 2016). "Experimental analysis of the R744 vapour compression rack equipped with the multi-ejector expansion work recovery module". In: *International Journal of Refrigeration* 64, pp. 93–107. DOI: 10.1016/J.IJREFRIG.2016.01.017. URL: https://www.sciencedirect.com/science/article/pii/S0140700716000232?via%7B%5C%%7D3Dihub.

[87] Zhu, J. and Elbel, S. (Jan. 2020). "Experimental investigation into the influence of vortex control on transcritical R744 ejector and cycle performance". In: *Applied Thermal Engineering* 164, p. 114418. DOI: 10.1016/J.APPLTHERMALENG.2019.114418.

[88] Rahimi, H., Buttsworth, D., and Malpress, R. (Aug. 2017). "CFD Study of a Variable Flow Geometry Radial Ejector". In: *Proceedings of the 4 th International Conference of Fluid Flow, Heat and Mass Transfer (FFHMT'17)*. 123. Toronto, Canada. DOI: 10.11159/ffhmt17.123.

[89] Bodys, J., Smolka, J., Palacz, M., Haida, M., Banasiak, K., Nowak, A. J., and Hafner, A. (Dec. 2016). "Performance of fixed geometry ejectors with a swirl motion installed in a multi-ejector module of a CO2 refrigeration system". In: *Energy* 117, pp. 620–631. DOI: 10.1016/j.energy.2016.07.037. URL: https://www.sciencedirect.com/science/article/pii/S0360544216309616.

[90] Ishii, M. and Hibiki, T. (2006). *Thermo-Fluid Dynamics of Two-Phase Flow*. Boston, MA: Springer US, pp. 155–216. DOI: 10.1007/978-0-387-29187-1_9. URL: http://link.springer.com/10.1007/978-0-387-29187-1%7B%5C_%7D9.

[91] Linga, G. and Flåtten, T. (2019). "A hierarchy of non-equilibrium two-phase flow models". In: *ESAIM: Proceedings and Surveys*. Vol. 66. EDP Sciences, pp. 109–143. DOI: 10.1051/PROC/201966006.

[92] Smolka, J., Bulinski, Z., Fic, A., Nowak, A. J., Banasiak, K., and Hafner, A. (Feb. 2013). "A computational model of a transcritical R744 ejector based

on a homogeneous real fluid approach". In: *Applied Mathematical Modelling* 37.3, pp. 1208–1224. DOI: 10.1016/j.apm.2012.03.044. URL: https://www.sciencedirect.com/science/article/pii/S0307904X12002077.

[93] Lucas, C., Rusche, H., Schroeder, A., and Koehler, J. (July 2014). "Numerical investigation of a two-phase CO2 ejector". In: *International Journal of Refrigeration* 43, pp. 154–166. DOI: 10.1016/J.IJREFRIG.2014.03.003. URL: https://www.sciencedirect.com/science/article/pii/S0140700714000504.

[94] Fang, Y., Poncet, S., Nesreddine, H., and Bartosiewicz, Y. (May 2019). "An open-source density-based solver for two-phase CO2 compressible flows: verification and validation". In: *International Journal of Refrigeration*. DOI: 10.1016/j.ijrefrig.2019.05.016. URL: https://www.sciencedirect.com/science/article/pii/S0140700719302129%7B%5C#%7Dbib0034.

[95] Colarossi, M., Trask, N., Schmidt, D. P., and Bergander, M. J. (Mar. 2012). "Multidimensional modeling of condensing two-phase ejector flow". In: *International Journal of Refrigeration* 35.2, pp. 290–299. DOI: 10.1016/j.ijrefrig.2011.08.013. URL: https://www.sciencedirect.com/science/article/pii/S0140700711002635?via%7B%5C%7D3Dihub.

[96] Haida, M., Smolka, J., Hafner, A., Palacz, M., Banasiak, K., and Nowak, A. J. (Jan. 2018b). "Modified homogeneous relaxation model for the R744 trans-critical flow in a two-phase ejector". In: *International Journal of Refrigeration* 85, pp. 314–333. DOI: 10.1016/j.ijrefrig.2017.10.010. URL: https://www.sciencedirect.com/science/article/pii/S0140700717303948.

[97] Giacomelli, F., Mazzelli, F., and Milazzo, A. (Nov. 2018). "A novel CFD approach for the computation of R744 flashing nozzles in compressible and metastable conditions". In: *Energy* 162, pp. 1092–1105. DOI: 10.1016/j.energy.2018.08.050. URL: https://www.sciencedirect.com/science/article/pii/S0360544218315706.

[98] Yazdani, M., Alahyari, A. A., and Radcliff, T. D. (Oct. 2012). "Numerical modeling of two-phase supersonic ejectors for work-recovery applications". In: *International Journal of Heat and Mass Transfer* 55.21-22, pp. 5744–5753. DOI: 10.1016/j.ijheatmasstransfer.2012.05.071. URL: https://www.sciencedirect.com/science/article/pii/S0017931012003924.

[99] Ringstad, K. E. and Hafner, A. (2020). "Two-fluid CFD model for R744 two-phase ejectors". In: *14th IIR-Gustav Lorentzen Conference on Natural Refrigerants - GL2020*.

[100] Plesset, M. S. (Apr. 1949). "The Dynamics of Cavitation Bubbles". In: *Journal of Applied Mechanics* 16.3, pp. 277–282. DOI: 10.1115/1.4009975. URL: https://doi.org/10.1115/1.4009975.

[101] Span, R. and Wagner, W. (Nov. 1996). "A new equation of state for carbon dioxide covering the fluid region from the triple-point temperature to 1100 K at pressures up to 800 MPa". In: *Journal of Physical and Chemical Reference Data* 25.6, pp. 1509–1596. DOI: 10.1063/1.555991. URL: http://aip.scitation.org/doi/10.1063/1.555991.

[102] Munkejord, S. T., Hammer, M., and Løvseth, S. W. (May 2016). "CO2 transport: Data and models - A review". In: *Applied Energy* 169, pp. 499–523. DOI: 10.1016/j.apenergy.2016.01.100. URL: https://www.sciencedirect.com/science/article/pii/S0306261916300885%7B%5C#%7Df0005.

[103] Fang, Y., De Lorenzo, M., Lafon, P., Poncet, S., and Bartosiewicz, Y. (2018). "An Accurate and Efficient Look-up Table Equation of State for Two-Phase Compressible Flow Simulations of Carbon Dioxide". In: *Industrial and Engineering Chemistry Research* 57.22, pp. 7676–7691. DOI: 10.1021/acs.iecr.8b00507. URL: https://pubs.acs.org/sharingguidelines.

[104] Fenghour, A., Wakeham, W. A., and Vesovic, V. (Jan. 1998). "The Viscosity of Carbon Dioxide". In: *Journal of Physical and Chemical Reference Data* 27.1, pp. 31–44. DOI: 10.1063/1.556013. URL: http://aip.scitation.org/doi/10.1063/1.556013.

[105] Laesecke, A. and Muzny, C. D. (Mar. 2017). "Reference correlation for the viscosity of carbon dioxide". In: *Journal of Physical and Chemical Reference Data* 46.1. DOI: 10.1063/1.4977429.

[106] Amar, M. N., Ghriga, M. A., Ouaer, H., El Amine Ben Seghier, M., Pham, B. T., and Andersen, P. Ø. (May 2020). "Modeling viscosity of CO2 at high temperature and pressure conditions". In: *Journal of Natural Gas Science and Engineering* 77, p. 103271. DOI: 10.1016/j.jngse.2020.103271.

[107] Awad, M. M. and Muzychka, Y. S. (Oct. 2008). "Effective property models for homogeneous two-phase flows". In: *Experimental Thermal and Fluid Science* 33.1, pp. 106–113. DOI: 10.1016/j.expthermflusci.2008.07.006. URL: https://www.sciencedirect.com/science/article/pii/S0894177708001027.

[108] Wilhelmsen, Ø., Aasen, A., Skaugen, G., Aursand, P., Austegard, A., Aursand, E., Gjennestad, M. A., Lund, H., Linga, G., and Hammer, M. (Apr. 2017). "Thermodynamic Modeling with Equations of State: Present Challenges with Established Methods". In: *Industrial & Engineering Chemistry*

Research 56.13, pp. 3503–3515. DOI: 10.1021/acs.iecr.7b00317. URL: https://pubs.acs.org/doi/10.1021/acs.iecr.7b00317.

[109] Aursand, P., Gjennestad, M. A., Aursand, E., Hammer, M., and Wilhelmsen, Ø. (Mar. 2017). "The spinodal of single- and multi-component fluids and its role in the development of modern equations of state". In: *Fluid Phase Equilibria* 436, pp. 98–112. DOI: 10.1016/J.FLUID.2016.12.018. URL: https://www.sciencedirect.com/science/article/pii/S0378381216306227.

[110] Lund, H. and Flåtten, T. (2010). "Equilibrium conditions and sound velocities in two-phase flows". In: *SIAM Annual Meeting (AN10)*.

[111] Brennen, C. E. (2005). *Fundamentals of multiphase flow*. Cambridge: Cambridge University Press, p. 345. DOI: 10.1017/CBO9780511807169.

[112] Giacomelli, F., Mazzelli, F., Banasiak, K., Hafner, A., and Milazzo, A. (Nov. 2019). "Experimental and computational analysis of a R744 flashing ejector". In: *International Journal of Refrigeration* 107, pp. 326–343. DOI: 10.1016/j.ijrefrig.2019.08.007.

[113] Lorenzo, M. de (2018). "Modelling and numerical simulation of metastable two-phase flows". PhD thesis. l'Université Paris-Saclay.

[114] ANSYS (2018). *ANSYS fluent theory guide. Release 19.0.* Canonsburg.

[115] Coutier-Delgosha, O., Fortes-Patella, R., and Reboud, J. L. (2003). "Evaluation of the turbulence model influence on the numerical simulations of unsteady cavitation". In: *Journal of Fluids Engineering, Transactions of the ASME* 125.1, pp. 38–45. DOI: 10.1115/1.1524584.

[116] Morel, C. (2015). *Mathematical Modeling of Disperse Two-Phase Flows*. Vol. 114, pp. 57–76. DOI: 10.1007/978-3-319-20104-7. URL: http://link.springer.com/10.1007/978-3-319-20104-7.

[117] Mazzelli, F., Little, A. B., Garimella, S., and Bartosiewicz, Y. (Dec. 2015). "Computational and experimental analysis of supersonic air ejector: Turbulence modeling and assessment of 3D effects". In: *International Journal of Heat and Fluid Flow* 56, pp. 305–316. DOI: 10.1016/j.ijheatfluidflow.2015.08.003. URL: https://www.sciencedirect.com/science/article/pii/S0142727X15001101.

[118] Hemidi, A., Henry, F., Leclaire, S., Seynhaeve, J. M., and Bartosiewicz, Y. (June 2009). "CFD analysis of a supersonic air ejector. Part I: Experimental validation of single-phase and two-phase operation". In: *Applied Thermal Engineering* 29.8-9, pp. 1523–1531. DOI: 10.1016/j.applthermaleng.2008.07.003.

[119] Besagni, G. and Inzoli, F. (May 2017). "Computational fluid-dynamics modeling of supersonic ejectors: Screening of turbulence modeling approaches". In: *Applied Thermal Engineering* 117, pp. 122–144. DOI: 10.1016/j.applthermaleng.2017.02.011. URL: https://www.sciencedirect.com/science/article/pii/S1359431116328290.

[120] Bodys, J., Smolka, J., Palacz, M., Haida, M., Banasiak, K., and Nowak, A. J. (Jan. 2022). "Effect of turbulence models and cavitation intensity on the motive and suction nozzle mass flow rate prediction during a non-equilibrium expansion process in the CO2 ejector". In: *Applied Thermal Engineering* 201, p. 117743. DOI: 10.1016/J.APPLTHERMALENG.2021.117743.

[121] Banasiak, K., Palacz, M., Hafner, A., Buliński, Z., Smołka, J., Nowak, A. J., and Fic, A. (Apr. 2014). "A CFD-based investigation of the energy performance of two-phase R744 ejectors to recover the expansion work in refrigeration systems: An irreversibility analysis". In: *International Journal of Refrigeration* 40, pp. 328–337. DOI: 10.1016/j.ijrefrig.2013.12.002. URL: https://www.sciencedirect.com/science/article/pii/S0140700713003812.

[122] Palacz, M., Smolka, J., Fic, A., Bulinski, Z., Nowak, A. J., Banasiak, K., and Hafner, A. (Nov. 2015). "Application range of the HEM approach for CO2 expansion inside two-phase ejectors for supermarket refrigeration systems". In: *International Journal of Refrigeration* 59, pp. 251–258. DOI: 10.1016/j.ijrefrig.2015.07.006. URL: https://www.sciencedirect.com/science/article/pii/S0140700715002030.

[123] Giacomelli, F., Mazzelli, F., and Milazzo, A. (2016). "Evaporation in supersonic CO2 ejectors: analysis of theoretical and numerical models". In: *9th International Conference on Multiphase Flow*. URL: https://www.researchgate.net/publication/303689693.

[124] Haida, M., Smolka, J., Hafner, A., Palacz, M., Banasiak, K., and Nowak, A. J. (Jan. 2018c). "Modified homogeneous relaxation model for the R744 trans-critical flow in a two-phase ejector". In: *International Journal of Refrigeration* 85, pp. 314–333. DOI: 10.1016/J.IJREFRIG.2017.10.010. URL: https://www.sciencedirect.com/science/article/pii/S0140700717303948.

[125] Giacomelli, F., Banasiak, K., and Hafner, A. (2018). "Experimental and Numerical Investigation on an Ejector for CO2 Vapor Compression Systems". In: *13th IIR Gustav Lorentzen Conference*, pp. 1179–1187.

[126] Croquer, S., Poncet, S., and Aidoun, Z. (Jan. 2016). "Turbulence modeling of a single-phase R134a supersonic ejector. Part 1: Numerical benchmark". In: *International Journal of Refrigeration* 61, pp. 140–152. DOI: 10.1016/

J.IJREFRIG.2015.07.030. URL: https://www.sciencedirect.com/science/article/pii/S0140700715002376.

[127] Troshko, A. A. and Hassan, Y. A. (Feb. 2001). "Law of the wall for two-phase turbulent boundary layers". In: *International Journal of Heat and Mass Transfer* 44.4, pp. 871–875. DOI: 10.1016/S0017-9310(00)00128-9.

[128] Končar, B. and Borut, M. (Nov. 2010). "Wall function approach for boiling two-phase flows". In: *Nuclear Engineering and Design* 240.11, pp. 3910–3918. DOI: 10.1016/J.NUCENGDES.2010.08.004.

[129] Ringstad, K. E. and Hafner, A. (2021). "Comparative study of R744 ejector CFD models". In: *IIR - 10th International Conference on Compressors and Coolants*.

[130] Bell, I. H., Wronski, J., Quoilin, S., and Lemort, V. (2014). "Pure and Pseudo-pure Fluid Thermophysical Property Evaluation and the Open-Source Thermophysical Property Library CoolProp". In: *Industrial & Engineering Chemistry Research* 53, pp. 2498–2508.

[131] Bodys, J., Smolka, J., Palacz, M., Haida, M., and Banasiak, K. (June 2020). "Non-equilibrium approach for the simulation of CO2 expansion in two-phase ejector driven by subcritical motive pressure". In: *International Journal of Refrigeration* 114, pp. 32–46. DOI: 10.1016/j.ijrefrig.2020.02.015.

[132] Sampedro, E. O. (2021). "A Non Symmetric Interfacial Area Density Formulation for Transcritical CO2 Ejectors CFD Modeling". In: *18th International Refrigeration and Air Conditioning Conference at Purdue*. URL: https://hal-mines-paristech.archives-ouvertes.fr/hal-03238075.

[133] Holleman, R., Fringer, O., and Stacey, M. (Aug. 2013). "Numerical diffusion for flow-aligned unstructured grids with application to estuarine modeling". In: *International Journal for Numerical Methods in Fluids* 72.11, pp. 1117–1145. DOI: 10.1002/FLD.3774. URL: https://onlinelibrary.wiley.com/doi/full/10.1002/fld.3774%20https://onlinelibrary.wiley.com/doi/abs/10.1002/fld.3774%20https://onlinelibrary.wiley.com/doi/10.1002/fld.3774.

[134] Michalcová, V. and Kotrasová, K. (Dec. 2020). "The Numerical Diffusion Effect on the CFD Simulation Accuracy of Velocity and Temperature Field for the Application of Sustainable Architecture Methodology". In: *Sustainability 2020, Vol. 12, Page 10173* 12.23, p. 10173. DOI: 10.3390/SU122310173. URL: https://www.mdpi.com/2071-1050/12/23/10173/htm%20https://www.mdpi.com/2071-1050/12/23/10173.

[135] Palacz, M., Haida, M., Smolka, J., Nowak, A. J., Banasiak, K., and Hafner, A. (Mar. 2017). "HEM and HRM accuracy comparison for the simulation of CO2 expansion in two-phase ejectors for supermarket refrigeration systems". In: *Applied Thermal Engineering* 115, pp. 160–169. DOI: 10.1016/j.applthermaleng.2016.12.122. URL: https://www.sciencedirect.com/science/article/pii/S135943111634399X.

[136] Haida, M., Fingas, R., Szwajnoch, W., Smolka, J., Palacz, M., Bodys, J., Nowak, A., Haida, M., Fingas, R., Szwajnoch, W., Smolka, J., Palacz, M., Bodys, J., and Nowak, A. J. (Apr. 2019). "An Object-Oriented R744 Two-Phase Ejector Reduced-Order Model for Dynamic Simulations". In: *Energies* 12.7, p. 1282. DOI: 10.3390/en12071282. URL: https://www.mdpi.com/1996-1073/12/7/1282.

[137] He, Y., Deng, J., Li, Y., and Ma, L. (Sept. 2019). "A numerical contrast on the adjustable and fixed transcritical CO2 ejector using exergy flux distribution analysis". In: *Energy Conversion and Management* 196, pp. 729–738. DOI: 10.1016/j.enconman.2019.06.031.

[138] He, Y., Deng, J., Li, Y., and Zhang, X. (Feb. 2021). "Synergistic effect of geometric parameters on CO2 ejector based on local exergy destruction analysis". In: *Applied Thermal Engineering* 184, p. 116256. DOI: 10.1016/j.applthermaleng.2020.116256.

[139] Ringstad, K. E., Allouche, Y., Gullo, P., Banasiak, K., and Hafner, A. (2019). "CO2 ejector modelling using CFD: current status." In: *25th IIR International Congress of Refrigeration Proceedings.*

[140] Banasiak, K., Hafner, A., Kriezi, E. E., Madsen, K. B., Birkelund, M., Fredslund, K., and Olsson, R. (Sept. 2015). "Development and performance mapping of a multi-ejector expansion work recovery pack for R744 vapour compression units". In: *International Journal of Refrigeration* 57, pp. 265–276. DOI: 10.1016/J.IJREFRIG.2015.05.016. URL: https://www.sciencedirect.com/science/article/pii/S0140700715001553.

[141] Clarivate (2021). *Web of Science.*

[142] Shai Shalev-Shwartz and Shai Ben-David (2014). *Understanding Machine Learning: From Theory to Algorithms.* Cambridge University Press.

[143] Maghsoodi, A., Afshari, E., and Ahmadikia, H. (Oct. 2014). "Optimization of geometric parameters for design a high-performance ejector in the proton exchange membrane fuel cell system using artificial neural network and genetic algorithm". In: *Applied Thermal Engineering* 71.1, pp. 410–418. DOI: 10.1016/J.APPLTHERMALENG.2014.06.067.

[144] Rashidi, M. M., Aghagoli, A., and Raoofi, R. (June 2017). "Thermodynamic analysis of the ejector refrigeration cycle using the artificial neural network". In: *Energy* 129, pp. 201–215. DOI: 10.1016/J.ENERGY.2017.04.089.

[145] Haoran, C. and Wenjian, C. (Oct. 2014). "Artificial neural network modeling for variable area ratio ejector". In: *Proceedings of the 2014 9th IEEE Conference on Industrial Electronics and Applications, ICIEA 2014*. Institute of Electrical and Electronics Engineers Inc., pp. 220–225. DOI: 10.1109/ICIEA.2014.6931162.

[146] Chaurasia, P., Younis, K., Qadri, O. S., Srivastava, G., and Osama, K. (Apr. 2019). "Comparison of Gaussian process regression, artificial neural network, and response surface methodology modeling approaches for predicting drying time of mosambi (Citrus limetta) peel". In: *Journal of Food Process Engineering* 42.2, e12966. DOI: 10.1111/JFPE.12966. URL: https://onlinelibrary.wiley.com/doi/full/10.1111/jfpe.12966.

[147] Kristjanson Duvenaud, D. (2014). "Automatic Model Construction with Gaussian Processes Declaration". PhD thesis. Pembroke College.

[148] Pedregosa, F., Varoquaux, G., Gramfort, A., Michel, V., Thirion, B., Grisel, O., Blondel, M., Prettenhofer, P., Weiss, R., Dubourg, V., Vanderplas, J., Passos, A., Cournapeau, D., Brucher, M., Perrot, M., and Duchesnay, E. (2011). "Scikit-learn: Machine Learning in Python". In: *Journal of Machine Learning Research* 12, pp. 2825–2830.

[149] Tang, B. (Dec. 1993). "Orthogonal Array-Based Latin Hypercubes". In: *Journal of the American Statistical Association* 88.424, pp. 1392–1397. DOI: 10.1080/01621459.1993.10476423. URL: http://www.tandfonline.com/doi/abs/10.1080/01621459.1993.10476423.

[150] Chatterjee, T., Chakraborty, S., and Chowdhury, R. (Jan. 2019). "A Critical Review of Surrogate Assisted Robust Design Optimization". In: *Archives of Computational Methods in Engineering* 26.1, pp. 245–274. DOI: 10.1007/S11831-017-9240-5/FIGURES/11. URL: https://link.springer.com/article/10.1007/s11831-017-9240-5.

[151] Cai, S., Mao, Z., Wang, Z., Yin, M., and Karniadakis, G. E. (May 2021). "Physics-informed neural networks (PINNs) for fluid mechanics: A review". In: *Acta Mechanica Sinica/Lixue Xuebao* 37.12, pp. 1727–1738. DOI: 10.48550/arxiv.2105.09506. arXiv: 2105.09506. URL: https://arxiv.org/abs/2105.09506v1.

Appendix

Paper I

Ringstad, Knut Emil; Allouche, Yosr; Gullo, Paride; Ervik, Åsmund; Banasiak, Krzysztof; Hafner, Armin. (2020) A detailed review on CO2 two-phase ejector flow modeling. *Thermal Science and Engineering Progress.* vol 20.
DOI: https://doi.org/10.1016/j.tsep.2020.100647

Thermal Science and Engineering Progress 20 (2020) 100647

Contents lists available at ScienceDirect

Thermal Science and Engineering Progress

journal homepage: www.elsevier.com/locate/tsep

A detailed review on CO_2 two-phase ejector flow modeling

Knut Emil Ringstad[a,*], Yosr Allouche[a], Paride Gullo[b], Åsmund Ervik[c], Krzysztof Banasiak[c], Armin Hafner[a]

[a] Norwegian University of Science and Technology, Department of Energy and Process Engineering, Kolbjørn Hejes vei 1B, 7491 Trondheim, Norway
[b] Technical University of Denmark, Department of Mechanical Engineering, Nils Koppels Allé 403, 2800 Kgs. Lyngby, Denmark
[c] SINTEF Energy, Kolbjørn Hejes vei 1d, 7465 Trondheim, Norway

ARTICLE INFO

Keywords:
CFD
Expansion work recovery
Multiphase flow
CO_2
Trans-critical
Vapor-compression system
Ejector

ABSTRACT

Ejector-equipped vapor-compression systems for refrigeration and cooling, relying solely on CO_2 (R744) as a natural working fluid, are perceived to be an eco-friendly and highly efficient solution for many applications. However, the complexity of two-phase ejector flows makes it very challenging to find realiable and efficient ejector designs. Improved design methods are necessary in order to achieve higher performance in R744 units compared to the traditional compressor-based systems with refrigerants that put a high strain on the environment. Consequently, the development of advanced models and tools for an accurate design of the R744 ejectors has been a highly prioritized research topic. To the best of the authors' knowledge, the current status of R744 ejector models and their limitations has not been thoroughly evaluated yet. To summarise the current state of the art and knowledge gaps, this work presents an exhaustive overview of the available numerical models applied to R744 two-phase ejectors, i.e. multiphase flow modeling, turbulence aspects, numerical solution methods, applications of models, to further encourage the adoption of R744 vapor-compression solutions. Finally, a thorough discussion of different focus points for future research as well as the main challenges in the field is presented.

1. Introduction

Growing concern for human impact on the environment has brought about a major shift in the field of Heating, Ventilation, Air Conditioning, and Refrigeration (HVAC&R). The transition from high global warming potential (GWP) working fluids, e.g. hydro-fluorocarbons (HFCs), to environmentally friendly refrigerants is a critical milestone to achieve carbon neutrality. Legislative agreements aiming at HFC phase-down, such as the Kigali Amendment to the Montreal Protocol and the EU F-gas Regulation 517/2014 [1] (European Commission, 2014), have been in force since 2015 and apply for both developed and developing countries. Particular emphasis has been placed on developing solutions using natural refrigerants as these are cheap, available, and have no unknown bi-effects on the atmosphere.

Vapor compression refrigeration systems consist of a circulating refrigerant (working fluid) that absorb latent and sensible heat at a low temperature and releases it at a higher temperature. This is possible by compressing and decompressing the refrigerant to reach appropriate temperature levels. A compressor supplies mechanical work, increasing the refrigerant temperature and pressure. At the higher temperature, the heat is released to the ambient air through a condenser or gas-cooler. The refrigerant is then reduced in pressure and temperature in an expansion device and collects heat through an evaporator. In the simplest cycles, the expansion device is a simple expansion valve. However, these devices do not recover any of the supplied mechanical energy and therefore impose a throttling loss. Alternatively, work-recovery devices, such as expanders or two-phase ejectors are used. This is especially important for refrigerants that operate at high pressures (such as CO_2).

Of the natural and environmentally friendly refrigerants, CO_2 (R744) stands out as an efficient, long term solution. R744 is characterized by negligible GWP, non-flammability, non-toxicity, low cost, favorable thermophysical properties [2]. Additionally, the R744 cycle can use smaller and more compact components due to its thermodynamic properties. These characteristics make R744 refrigeration systems a hot research topic. Significant work is currently being carried out, highlighting the benefits of R744 for many applications, such as supermarkets [3,4], heat pump units [5–7], vehicles [8–10], light commercial refrigeration [11,12], tumble dryers [13,14], chillers [15]. R744 HVAC&R systems are rapidly becoming widely accepted for many purposes worldwide. The wide recognition of this ascending technology is furthermore a consequence of its high performance in any operating

* Corresponding author.
E-mail address: knut.e.ringstad@ntnu.no (K.E. Ringstad).

https://doi.org/10.1016/j.tsep.2020.100647

Available online 17 September 2020

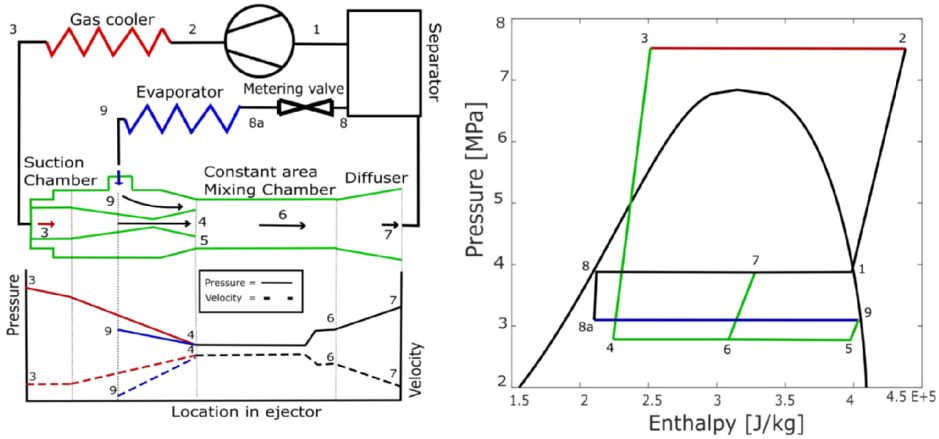

Fig. 1. (a) Schematic of a standard transcritical ejector cycle (b) Pressure-enthalpy diagram of the transcritical ejector cycle. Illustration from Elbel and Hrnjak [18].

mode, such as at high ambient temperatures (in warm climates). The high efficiency of R744 HVAC&R systems is highly dependent on support by a two-phase ejector. It has been shown that the recovery of part of the available expansion work allows energy savings up to 25% compared to HFC-based systems in supermarkets [16].

Compared to the expanders, two-phase ejectors are characterized by low cost, absence of moving parts (i.e. great reliability), and the ability to handle two-phase flows without risks of damage. Consequently, Lawrence and Elbel claimed that the adoption of an ejector should be favored for HVAC&R units [17].

The conventional trans-critical R744 cycle with ejector and its pressure-enthalpy (P-h) diagram are shown in Fig. 1a and b, respectively. Furthermore, the refrigerant flow and a qualitative pressure and velocity profile are presented in Fig. 1 (a). In this solution, CO_2 exiting the gas cooler as vapor (thermodynamic state 3, identifying the high pressure) is referred to as the primary or motive flow.

The high pressure at the motive inlet accelerates the flow in the motive nozzle converging section to sonic conditions ($Ma = 1$) at the throat and further accelerates it to super-sonic flow ($Ma > 1$) in the motive nozzle diverging section. The acceleration is coupled to a pressure reduction, which initiates a phase change process of the liquid CO_2 in the nozzle, called flashing [19]. The motive flow fans out from the divergent part of the nozzle creating a low-pressure region (thermodynamic state 4) which drives the CO_2 from the secondary inlet (thermodynamic state 9) into the suction chamber (thermodynamic state 5). The entrained CO_2 stream is generally referred to as the secondary or suction flow. The primary and secondary streams are then mixed in the mixing chamber (thermodynamic state 6) due to the exchange of mass, momentum, and energy (heat). As the flow subsequently decelerates in the diffuser, a part of the residual kinetic energy is converted into a pressure increase (thermodynamic state 7, identifying the intermediate pressure). Thus, the energy lost due to the expansion of the motive flow is recovered and used to increase the pressure of the suction flow to produce the wanted pressure lift of the suction flow.

An ejector-equipped vapor compression system presents two main advantages when compared to the conventional R744 cycle: (I) Reduction in energy consumption thanks to pre-compression of R744 through the ejector from the low evaporator pressure to the intermediate one; (II) Increase in the refrigerating capacity, as the R744 enters into the evaporator with a lower vapor quality and enthalpy. The performance of a two-phase ejector is generally evaluated using the following indicators: the mass entrainment ratio (ω), the suction pressure ratio (Π), the pressure lift (P_{lift}) and the ejector isentropic efficiency ($\eta_{ejector}$). The mass entrainment ratio (ω) is defined as the ratio of the entrained mass flow rate ($\dot{m}$) to the motive mass flow rate and describes the ability of the ejector to entrain the low-pressure secondary flow:

$$\omega = \frac{\dot{m}_9}{\dot{m}_3} \tag{1}$$

where the subscript indicates the thermodynamic state referred to in Fig. 1.

The suction pressure ratio (Π) is used to evaluate the compression ratio between the ejector outlet pressure and the ejector suction pressure. The pressure lift (P_{lift}) is used to evaluate the difference between the ejector outlet pressure and the ejector suction pressure.

$$\Pi = \frac{P_7}{P_5} \tag{2}$$

$$P_{lift} = P_7 - P_5 \tag{3}$$

Lastly, the ejector efficiency ($\eta_{ejector}$) is the ratio between the actual amount of work recovered by the ejector ($\dot{W}_r$) and the total work recovery potential for an isentropic process ($\dot{W}_{r,max}$) [18]:

$$\eta_{ejector} = \frac{\dot{W}_r}{\dot{W}_{r,max}} = \omega \cdot \frac{h(P_7, s_9) - h_9}{h_3 - h(P_7, s_3)} \tag{4}$$

Here, h is the specific enthalpy. The importance of the two-phase ejector for R744 systems was highlighted by Elbel and Lawrence [17], who showed that the adoption of a two-phase ejector is much more beneficial to R744 systems compared to HFC-based units. The R744 ejector efficiency generally ranges between 0.2 and 0.4 [20], whereas the efficiency that of both R410A and R134a ejectors is normally less than 0.2 [17]. Therefore, the characteristics of R744 favorable for expansion recovery, combined with the high energy efficiency offered by the adoption of a two-phase ejector, are further promoting the application of R744 refrigeration system at an industrial scale [21–26]. However, due to the significant complexity of ejector flow, connected to the interactions between the motive and entrained flow, the performance of a two-phase ejector is highly dependent on its mechanical design. Furthermore, R744 ejector designs are significantly different from ejectors with other working fluids, due to different thermodynamic properties and component size.

Experimental work is the most reliable approach to identify the optimal design of the ejector and has so far been the most used design methodology. However, it is characterized by some limitations. Primarily, the large time- and resource costs of experimental design are

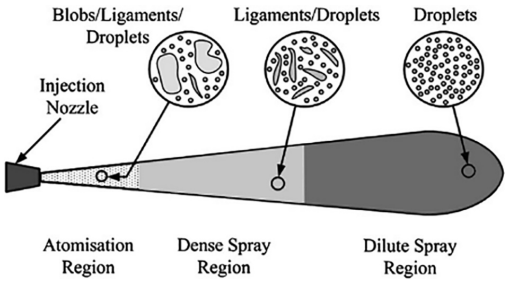

Fig. 2. Schematic of a liquid spray – Jiang et al. [44].

prohibitive for large scale test campaigns since the performance of each ejector is defined for at least 5 degrees of freedom: motive nozzle pressure and density, suction nozzle inlet pressure, and density, and outlet pressure.

Extensive experimental work has been carried out to investigate efficient ejector designs, looking into the geometry of the mixing section [27,28], motive nozzle [29,18], diffuser [28,18], adjustable needles [30,31]. However, as stated by Elbel and Lawrence [17] the specific geometry obtained in each study is only optimal for that specific case and operation. Furthermore, Elbel and Lawrence [17] point out the need for studies that cover generalized ejector geometries. However, it is costly to produce results with large variations in operating conditions, ejector design, and system layout.

Fortunately, many of these limitations can be bridged using experimentally validated numerical modeling. Additionally, such models can provide a better understanding of the flow patterns. Such a solution can allow identification of optimal operation and ejector design based on optimization algorithms.

The first interest in two-phase ejector modeling started in the 1990s using a one-dimensional approach [32] and has since then been extended with additional experimental data and newly developed models to achieve better prediction of two-phase ejector flow. The current state of the art within fluid flow modeling involves solving the full equations of fluid motion in three dimensions, i.e. the Navier–Stokes equations, using computational fluid dynamics (CFD). Computational fluid dynamics is a powerful numerical tool that can capture the local flow behavior realistically and can yield more accurate predictions and more physically realistic solutions than simpler models. Furthermore, CFD is not dependent on extensively tuned parameters based on experiments, which improves the applicability of the models.

For literature on the modeling of other flows with relevance for R744 ejectors, the authors refer to research investigating atomizers [33], diesel injector [34], and accidental leaks in devices such as nuclear reactors, engines or hazardous gas containers [19].

Even though two-phase ejector technologies has been thoroughly reviewed in the past, covering such topics as cycles and applications [16,17,35–38], thermodynamic modeling [17,39,40,37,36,41] geometric design [37,38] and historic developments [38,41,42], to the best of the authors' knowledge limited attention was given to the determination of appropriate modeling approaches for two-phase ejectors [43]. R744 two-phase ejectors models have been previously reviewed by Nowak et al. [43], however, several modeling aspects were not covered by this overview. This work attempts to further detail modeling aspects previously left untouched, such as in-depth multiphase modeling, turbulence approaches, model applications, new experimental validation data, numerical methods, and model accuracy comparisons. This work intends to fill this knowledge gap by providing a complete state of knowledge, summarizing the recent progress within R744 ejector modeling.

In this review, first, the state of the art of multiphase flow models are presented and compared. A thorough discussion about the available turbulence models such as different two-equation models and more advanced multiphase models for R744 ejector models is given. Different numerical methods and their significance for accuracy and convergence are examined, and currently available experimental data for model validation is exhaustively reviewed. Lastly, the available modeling strategies and suggestions for further work are summarised.

2. Two-phase ejector flow physics

2.1. Flow characteristics

The fluid flow in an R744 two-phase ejector is characterized by multiple two-phase flow regimes in the different sections of the ejector. These flow regimes are dependent on operating pressures and ejector design. Due to this complexity, there is a lack of knowledge of these flow regimes, which poses a modeling challenge.

The flow characteristics in the motive nozzle depend on the nozzle inlet conditions. Two types of expansion paths can be identified: expansion from a supercritical state that intersects the phase envelope close to the critical point, and an expansion that intersects the phase envelope far away from the critical point. The former will be referred to as "near-critical" expansion and the latter as "off-critical" expansion. At near-critical conditions bubble nucleation in the motive nozzle is almost instantaneous, while the phase change is delayed at off-critical conditions due to non-equilibrium effects, discussed in Section 2.2. The bubbles quickly reach the velocity of the surrounding liquid flow. As the bubbly flow leaves the motive nozzle, the flow is supersonic and can go through a series of two-phase shocks. At some point, the flow becomes predominantly vapor and the flow regime inverts from a bubbly flow to a droplet flow. An illustration of such a jet flow is presented in Fig. 2 (Jiang et al. [44]).

Dimensionless numbers are commonly used to evaluate flow characteristics in fluid mechanics. These numbers help in quantifying the scales of different flow phenomena in the flow. A limited number of the most relevant dimensionless numbers will be presented below.

The Reynolds number, Eq. (5), is defined as the ratio between inertial and viscous forces, and is commonly used to quantify turbulent flows. The Weber number, Eq. (6), is defined as the ratio between inertia and surface tension, and is used for discussing the breakup and coalescence of bubbles and droplets. The Ohnesorge number, Eq. (7), is a combined dimensionless number that describes the effects of surface tension, inertia, and viscous forces. The Prandtl number, Eq. (8), is defined by the ratio between momentum and heat diffusion. The gas and liquid Prandtl numbers of R744 vary from $Pr \approx 1.5 - 6$ in the temperature range 0–30 °C. The Biot number, Eq. (9), is a number compare the heat transfer within and at the surface of a bubble or droplet. For low Biot numbers, $Bi \ll 1$ the temperature inside a bubble or droplet can be assumed homogeneous. The Nusselt number, Eq. (10), is similarly defined, however, compare convective and conductive heat transfer at the surface.

$$Re = \frac{\rho U l}{\mu}, \tag{5}$$

$$We = \frac{\rho U^2 l}{\sigma}, \tag{6}$$

$$Oh = \frac{\mu}{\rho \sigma l} = \frac{\sqrt{We}}{Re}, \tag{7}$$

$$Pr = \frac{c_p \mu}{k}, \tag{8}$$

$$Bi = \frac{h_c L}{k_i}, \tag{9}$$

$$Nu = \frac{h_c L}{k_e}. \tag{10}$$

Table 1
Estimates values in Motive nozzle and Mixing chamber based on values from Smolka et al. [45].

	U [m/s]	β [–]	P [MPa]	l [m]	ρ[kg/s]	σ [N/m]	μ [Pa s]
Motive nozzle	128	0.3	4.7	0.001	342.7	$2.5{\cdot}10^{-3}$	$5.2{\cdot}10^{-5}$
Mixing chamber	35	0.4	5	0.003	305.0	$2.1{\cdot}10^{-3}$	$6.1{\cdot}10^{-5}$

Here, U is the characteristic velocity, l is a characteristic length, σ is the surface tension, c_p is the specific heat, μ is the fluid viscosity, h_c is the convective heat transfer coefficient, and ρ is the density. k is the thermal conductivity. Subscripts are used for numbers where two bodies are in contact, i.e. bubbles or droplets, i and e denote internal and external heat transfer for that body, respectively.

Based on numerical values for an R744 ejector by Smolka et al. [45], the dimensionless numbers were calculated at two locations; the centerline after the motive nozzle exit and the end of the mixing chamber/start of the diffuser. The presented quality, pressure, and velocity plots in Smolka et al. [45] were used to estimate the dimensionless numbers. The REFPROP library [46] is used to calculate the viscosity and surface tension. The operating conditions presented by Smolka et al. [45], correspond to $P_m = 9.5$ MPa, $T_m = 36.3$ °C, $P_s = 4.8$ MPa, $T_s = 15.1$ °C, $P_o = 5.2$ MPa. The estimated variables are presented in Table 1: where β is the vapor mass fraction defined as $\alpha_m = m_{gas}/(m_{liquid} + m_{gas})$. The characteristic lengths were chosen to be the mixing chamber diameter and the nozzle throat diameter. Based on these estimations the dimensionless numbers are calculated in Table 2.

From these calculations the estimated Reynolds numbers are very high due to the high velocities in the flow, indicating that the flow is highly turbulent, both in the mixing chamber and in the motive nozzle. Furthermore, the very high Weber numbers indicate that bubble breakup will happen very rapidly.

2.2. A discussion on non-equilibrium

Knowledge of non-equilibrium effects is critical to properly understand two-phase ejectors. In a two-phase flow, there exists non-equilibrium states can be divided into thermodynamic and transport non-equilibriums. Thermodynamic non-equilibrium relates to the superheated or subcooled state of a liquid or gas, respectively. Transport non-equilibrium relates to differing temperatures, pressures, or velocities of the phases.

During rapid depressurization, as in the motive of an R744 ejector, the saturation temperature will drop below the liquid temperature, superheating the liquid. The liquid starts to evaporate until the equilibrium state is reached. The degree of superheat is therefore limited by the phase change mechanism. Beyond the homogeneous nucleation line any perturbation will instantly force the phase change, imposing the upper limit on superheating. This is illustrated in Fig. 3, where the saturation and homogeneous nucleation lines of R744 are illustrated. Three cases of ejector motive conditions are plotted with an illustrated isenthalpic expansion process, corresponding to the expansion process in the motive nozzle (points 3–4 in Fig. 1). Case 1 is a near-critical expansion, and cases 2 and 3 are off-critical expansions, in terms of the previously established notions. This figure demonstrates that as the degree of sub-cooling at the motive nozzle inlet increases (lower enthalpy) and moves towards off-critical expansion, the theoretically achievable superheat increases, and therefore the relevance of chemical potential non-equilibrium. As mentioned in Section 2.1, it is clear that for near-critical expansion the possible thermodynamic non-equilibrium is very small, and therefore the phase change will occur very rapidly. The figure was generated based on the framework established by Wilhelmsen et al. [47] and Aursand et al. [48].

Table 2
Dimensionless numbers in a R744 ejector based on numerical estimates [45]

	Motive nozzle	Mixing chamber
Re	$7.2{\cdot}10^5$	$6.1{\cdot}10^5$
We	$2.3{\cdot}10^9$	$1.8{\cdot}10^8$
Oh	0.072	0.028

Transport (or mechanical) non-equilibrium relates to flow characteristics, as well as fluid properties. The commonly considered disequilibria are velocity, temperature, and pressure. Thermal non-equilibrium refers to a state where the phases exist at differing temperatures. In this case, heat transfer between the bubbles and the surrounding liquid must be considered. These states can also affect the thermodynamic non-equilibrium as two phases can co-exist at thermodynamic equilibrium, however at different temperatures. Furthermore, within a bubble or droplet the temperature is not homogeneously distributed. A droplet or a bubble may, for example, contain regions where the fluid is at equilibrium and other regions where it is at non-equilibrium. For low Biot numbers, the heat transfer inside a bubble or droplet is much faster than heat transfer to the surrounding fluid. In this case, the temperature within the particulate can be assumed homogeneous. Still, limited knowledge is available on the Biot number for R744 ejector flows, and further research is needed. This was investigated by Bartosiewicz and Seynhaeve [49], where it is shown that a non-equilibrium temperature front may in some cases only penetrate a short distance into a droplet. This is illustrated in Fig. 4, where different control volume resolutions and the corresponding resolved temperature distributions are presented. The effects of pressure non-equilibrium are often neglected due to the very short time scale of these disequilibria.

A summary of the currently available experimental literature discussing the importance of non-equilibrium modeling in R744 ejectors is given in this paper. Firstly, measurements of wall pressure in a converging–diverging nozzle with R744 were conducted by Nakagawa et al. [50]. It was found that the observed pressures were close to equilibrium conditions. However, for low operating temperatures, the experiments suggested the occurrence of non-equilibrium phase change as pressures lower than saturation pressures were observed in the nozzle. Secondly, shock waves in the nozzle were further discussed by Berana et al. [51]. They put forward that equilibrium flow is an ideal limiting case, and that for some conditions dispersed and pseudo shocks were observed. These shocks are weaker and thicker than equilibrium shocks. Berana et al. [51] suggested that velocity non-equilibrium could significantly impact shock solutions due to its effect on the speed of sound. Thirdly, Li et al. [52] used the wall pressure and a visualization technique to investigate the phase change point for different operating conditions in an R744 ejector. Also here, the measurements showed conditions approximately at equilibrium conditions. The aforementioned studies were conducted at supercritical motive pressures. These investigations agree that the expansion in a nozzle is in general at homogeneous equilibrium. However, non-equilibrium effects have been suggested by the aforementioned authors to be important to capture transcritical flow at certain operating conditions.

3. Multiphase flow models for R744 ejectors

Accurate multiphase flow modeling is generally considered as the most challenging aspect of R744 ejector modeling and the key factor for successful modeling of R744 ejectors. Compared to single-phase flows,

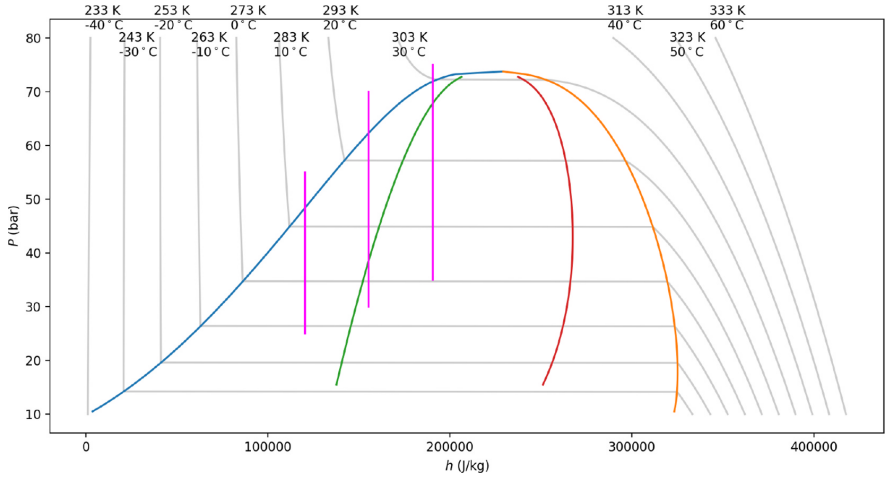

Fig. 3. P-h plot of the saturation- and homogeneous nucleation lines based on framework by [47] and Aursand et al. [48]. The phase envelope is shown as blue and orange lines indicating the liquid and vapor sides, respectively. These lines meet in the critical point. The red and green lines are the limits where homogeneous nucleation will occur, of bubbles in the liquid phase (crossing the green line from the left) or droplets in the vapor phase (crossing the red line from the right). The magenta lines indicate isenthalpic expansion for three different initial state points with near-critical and off-critical expansion. The grey lines are isotherms, as labelled at the top. (For interpretation of the references to color in this figure legend, the reader is referred to the web version of this article.)

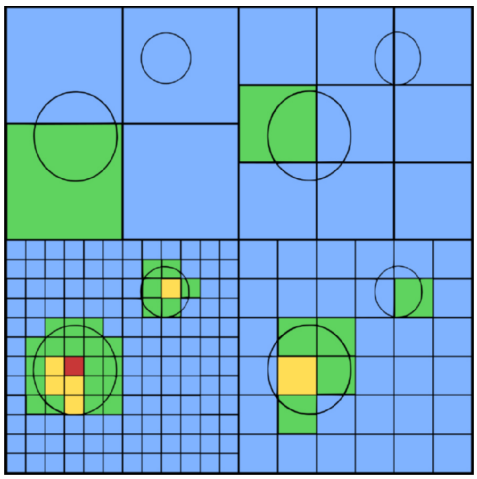

Fig. 4. Illustration of the effect of mesh refinement on resolved temperature field in two-phase flows. The colors signify increasing temperatures as follows: blue, green, yellow and red. (For interpretation of the references to color in this figure legend, the reader is referred to the web version of this article.)

multiphase flows introduce complex interactions at the interface between the liquid and vapor phases. In addition, R744 ejector flow involves sudden and complex phase change through flashing. The reader is referred to Polanco et al. [53] and Liao and Lucas [19] for additional information on flashing flow modeling. As previously mentioned, R744 ejector modeling is not yet fully explored, thus many simplifying assumptions are used in the available models. Assumptions such as equilibrium of velocity i.e. homogeneous flow (assumed in most currently available models), thermal equilibrium (assumed in mixture and equilibrium models), thermodynamic/chemical equilibrium (assumed in Equilibrium models) and pressure equilibrium (assumed in all currently available models) are considered to achieve well-posed and consistent models.

Ejector models are predominantly based on inputs of operating conditions, i.e. temperature and pressure, at the motive, suction, and outlet of the ejector. The two primary objectives of an ejector are to provide pressure lift and entrainment of the secondary fluid. Therefore, most models attempt to predict the entrainment ratio (ω) from the pressures and temperatures at the boundaries. These variables can easily be obtained experimentally, and are the variables used for control of most refrigeration systems.

The accuracy of current R744 ejector models varies significantly based on operating conditions, ejector geometry, and model complexity. As an example, thermodynamic relation models (0-D) can achieve accuracy within a 10–15% error in the motive mass flow rate [54]. However, such models have typically a narrow range of validity in terms of varying ejector geometry and operating conditions, and are based on tuning from previous experimental data. On the other hand, more complex models (CFD) can achieve higher accuracies with a much wider range of validity, at the expense of much higher computational costs.

The understanding of two-phase ejector models is further complicated by their high sensitivity to the model inputs. Smolka et al. [45] discussed the effects of small changes in the numerical boundary conditions. Changing the boundary conditions within the experimental uncertainty had a large impact on the model's predicted mass flow rate. This result is summarised in Table 3, and highlights the importance of improved models and high accuracy experimental data. The reason for the motive mass flow rate being easier to predict is due to the flow becoming choked when reaching supersonic speeds. A chocked flow is

Table 3
Percentage point (pp) of error change in the secondary and primary flow rate, $\dot{m}_s$, $\dot{m}_p$, respectively, when model inputs is changed by the measurement uncertainty.

Varied parameter	Uncertainty	Difference [%]	
		$\dot{m}_s$	$\dot{m}_p$
Inlet suction temperature	1.1 °C	1.0	–
Inlet suction pressure	0.01 MPa	10.0	–
Inlet motive pressure	0.048 MPa	0.6	1.0

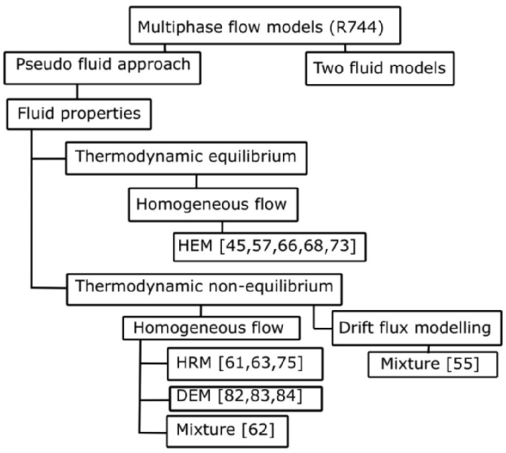

Fig. 5. Classification of current two-phase R744 ejector models.

insensitive to the downstream conditions and is, therefore, easier to predict. On the other hand, the prediction of the suction mass flow rate is highly sensitive to downstream conditions. This is because the downstream conditions, such as mixing chamber pressure, is one of the main driving mechanism of the suction flow. It is therefore hard to say whether the low model accuracy for suction flow is due to wrong modeling of the mixing process, i.e. turbulence, or the wrong modeling of the motive flow downstream of being chocked. This will be further discussed in the following sections.

An illustrative overview of models found in R744 ejector literature is presented in Fig. 5. The models are classified according to the multiphase aspects considered. Firstly, the models are classified according to the number of fluid flow equation sets solved; in the two-fluid approach, one set of equations is solved for each phase, while in the pseudo-fluid approach the equations of both phases are averaged into one set. Thus far, all currently available ejector models fall under this latter category. Secondly, the models are classified according to whether or not the pseudo fluid transport properties are evaluated assuming equilibrium or not. Thirdly, the models are classified according to their treatment of velocity non-equilibrium. Only one study has thus far evaluated velocity slip [55], and most models consider the flow as homogeneous.

3.1. Homogeneous flow models

In multiphase flow modeling, a commonly used assumption is that of homogeneous flow. This approach assumes the phases to be at mechanical equilibrium, i.e. both phases are described with a single velocity-($\vec{u}$) and pressure-field (P) in order to reduce the complexity of the model, as it neglects the modeling of the slip velocity. Essentially, the two phases can then be treated as a single pseudo-fluid with transport properties derived according to an averaging procedure. This pseudo-fluid will be governed by the equations of fluid motion, Eqs. (11)–(12) as well as an energy equation, Eq. (13).

$$\frac{\partial \rho_m}{\partial t} + \frac{\partial}{\partial x_j}[\rho_m u_{mj}] = 0, \tag{11}$$

$$\frac{\partial}{\partial t}(\rho_m u_{mi}) + \frac{\partial}{\partial x_j}[\rho_m u_{mi} u_{mj} + p\delta_{ij} - \tau_{ij\_\mathrm{eff}}] = 0, \tag{12}$$

$$\frac{\partial}{\partial t}(\rho_m E_m) + \frac{\partial}{\partial x_j}[\rho_m u_{mj} h_m - q_{j,\mathrm{eff}} - u_{mi}\tau_{ij,\mathrm{eff}}] = 0, \tag{13}$$

Here the Einstein notation is used with subscript-indexes i and j, and the subscript m indicates the pseudo-fluid mixture properties. ρ, u, p, E, h, q refer to the density, velocity, pressure, total energy, enthalpy and heat flux, respectively. The effective stress tensor $\tau_{ij,\mathrm{eff}}$ is the laminar (Newtonian) and turbulent stress tensors combined, $\tau_{ij,\mathrm{eff}} = \tau_{ij} + \tau_{\bar{r}ij}$.

The homogeneous flow approach is prevalent in R744 two-phase ejector models and will, therefore, be a focal point of this review. However, the transport properties of a mixture of two phases have to be defined as they are derived from the averaging of the equations. Therefore, estimates of these properties must be carefully considered. For example, the mixture viscosity is typically defined as a volume-weighted average of the two phases μ_l, and μ_v. In this case, the mixture viscosity, μ_m, is a function of the liquid and vapor viscosities and the vapor fraction:

$$\mu_m = f(\alpha, \mu_v, \mu_l) \tag{14}$$

To evaluate this property (Eq. 14), three factors must be considered: (I- Phase-fraction) The evaluation of phase fraction of the mixture, α (II- Properties) The fluid properties of the phases, μ_l and μ_v in Eq. (14). (III- Averaging) Mixture averaging procedure i.e. the function f in Eq. (14). As an example is a volume-weighted average presented below (Eq. (14)

$$\mu_m = \alpha\mu_v + (1-\alpha)\mu_l \tag{15}$$

These three factors will be discussed in terms of each model. Factors (II- Properties) and (III- Averaging) are discussed further in Section 3.3.

3.1.1. Homogeneous equilibrium

One simple, yet reasonable solution to evaluate the phase fraction (I- Phase-fraction) and the fluid properties (II- Properties) is to assume thermodynamic equilibrium of the phases at all points in the flow. This is the main concept adopted in the Homogeneous Equilibrium Model (HEM). This model has been extensively used in the literature to model R744 ejector flow structure and characteristics [31,45,56,57].

Bulinski et al. [58] conducted an early exploratory investigation in 2010 to investigate two different multiphase CFD models for an R744 ejector. A heterogeneous model, similar to the mixture model, and a temperature-based homogeneous model was implemented into the ANSYS Fluent software and tested. Unfortunately, the models performed poorly and the model results could not reproduce the experimental data. This led to investigating a homogeneous equilibrium model formulation based on total enthalpy.

One preferable property of equilibrium flow is that the pressure and enthalpy uniquely define the thermodynamic state, and thus the properties in the two-phase dome. Properties are typically divided into thermophysical- (Eq. 16) and transport (Eq. 17) properties.

$$\rho,\ c_p,\ \alpha,\ T = f(p,\ h), \tag{16}$$

$$\mu,\ k = f(p,\ h), \tag{17}$$

where ρ, α, μ, k, c_p are the pseudo-fluid density, vapor volume fraction, kinematic viscosity, thermal conductivity and heat capacity, respectively. In general, to achieve the most accurate thermodynamic relations, it is preferred to use density-energy formulations as they always conserve mass and energy, however these are less practical for comparisons with experimental results and require more computations.

This property was exploited in the work by Smolka et al. [45]. Furthering their previous work [58], a full 3D steady-state CFD model for R744 ejectors was implemented such that all properties were defined using the pressure and total enthalpy. To obtain the total enthalpy, an alternative formulation of the energy equation, Eq. (18), was implemented using user-defined functions in the ANSYS Fluent software [59].

$$\frac{\partial}{\partial t}\rho h + \nabla\cdot\left(\rho\vec{u}h\right) = \nabla\cdot\left(\Gamma_{\mathrm{eff}}\nabla h\right) + \dot{S}_{h1} + \dot{S}_{h2} + \dot{S}_{h3} \tag{18}$$

In this equation, h is the specific enthalpy, $\vec{u}$ is the velocity vector,

Γ_{eff} the effective diffusion coefficient. The source terms $\dot{S}_{h1,2,3}$ describe the mechanical energy, the irreversible dissipation of the kinetic energy variations, and the dissipation of the turbulent kinetic energy, respectively [45].

The two-phase mixture properties were evaluated in Smolka et al. [45] using the REFPROP library [46]. The results were validated with experimental data obtained from a lab-test campaign carried out by the SINTEF Energy Research laboratory in Trondheim (Norway) [60–62]. The experimental results were obtained using an ejector implemented in an R744 transcritical heat pump system under varied conditions. It was found that the non-symmetries were significant and that 3D flow modeling should be performed, in contrast to previous investigations with 2D flow [63]. The disagreeing results indicate that the significance of 3D effects depend on the ejector design and should be verified on a case to case basis. This is further discussed in Section 5.2. The authors found that global parameters (e.g. mass flow rate) were well approximated by the HEM approach for operation near the critical point, i.e. for near-critical expansion. The average deviation from experimental data was 5.6% and 10.1% for the motive and suction mass flow rates (MFR), respectively.

Later, Lucas et al. [57] presented a similar CFD model using the total enthalpy HEM approach. This model was implemented in the OpenFOAM framework [64] with the TEMO-media library. The investigations compared the results of the pressure recovery with those carried out by Lucas et al. [65] in earlier experimental work. When operating without suction flow up to 10% deviation in pressure distribution between model and experimental results were observed. However, this error increased to 20% when the suction flow was included. It was concluded that the larger deviation when simulating with the suction flow was due to inaccurate modeling of the pressure losses associated with flow mixing.

Furthermore, a HEM was implemented in Giacomelli et al. [66,67] using look-up tables implemented into ANSYS Fluent from the REFPROP library. They conclude that the HEM is an efficient tool for achieving reasonable results. Still, they state that further model development, in terms of meta-stable properties, is required to properly describe the flow physics.

Recently, Fang et al. [68] implemented a HEM based on a thermodynamic look-up table [69] with an inviscid density-based solver in the OpenFOAM framework, (discussed in Section 5), to model converging–diverging (CD) nozzle with R744. The results were compared to the wall pressure profile [27] with reasonable accuracy for the larger expansion angle. Interestingly, the model performed similarly for the sub-cooled as for the super-critical motive conditions. They state that work is ongoing for an R744 ejector simulation.

Following their previous work [45], Palacz et al. [56] investigated the application range of the HEM approach within typical supermarket refrigeration conditions. The model was validated with experimental results for 24 running modes. The results showed that for operating conditions close to or above the critical point of R744, the HEM approach can accurately reproduce the experimental results (within 5% error of mass flow rate). However, as the temperature and pressure are reduced below the critical point, to off-critical expansion, the HEM approach accuracy is reduced to approximately 50% deviation in motive mass flow rate. The significant errors were attributed to the non-equilibrium effects that are not considered by the HEM approach, which had been argued for in previous ejector models [70].

3.1.2. Homogeneous relaxation

Palacz et al. [56] concluded that non-equilibrium modeling is necessary to model the whole range of common supermarket R744 applications. At equilibrium the pressure and enthalpy define the vapor quality of the flow. However, at non-equilibrium an additional transport equation for the vapour fraction, Eq. (19), with a phase change model is needed to evaluate (I- Phase-fraction).

$$\frac{\partial \rho_v \alpha}{\partial t} + u_j \frac{\partial \rho_v \alpha}{\partial x_j} = \Gamma, \tag{19}$$

where Γ is a phase source term modeling phase change. One potential extension to the HEM for non-equilibrium conditions is the homogeneous relaxation model (HRM) introduced by Bilicki and Kestin [71]. Similarly to the HEM, the HRM assumes homogeneous multiphase flow. The HRM treats the phase change as a relaxation process toward the equilibrium vapor-quality:

$$\Gamma = -\rho \frac{\beta - \bar{\beta}_{eq}}{\theta_\mu} \tag{20}$$

where θ_μ is a relaxation factor, ρ is the mixture density, β is the instantaneous vapor mass fraction and $\bar{\beta}_{eq}$ the time-averaged equilibrium vapor mass fraction. The discussed relaxation introduces a delay to the onset of phase-change with a time-scale referred to as the relaxation time, θ_μ. In relation to the previously established notation, this yields a more accurate description of the phase fraction (I- Phase-fraction). This improvement is, however, based on an appropriate estimate of the relaxation time scale.

Downar-Zapolski et al. [72] defined the relaxation time as described in presented in Eq. (21), validated for the case of flashing water.

$$\theta_\mu = \theta_0 \alpha^a \phi^b, \tag{21}$$

where θ_0 is the initial relaxation, a and b are empirical coefficients, and α is the mixture void fraction parameter defined as:

$$\alpha = \frac{\rho_{sl} - \rho}{\rho_{sl} - \rho_{sv}}, \tag{22}$$

where ρ_{sl} , ρ_{sv} are the saturated liquid and vapor density.

This formulation was extended for R744 by Angielczyk et al. [70], who investigated a formulation of ϕ, the pressure parameter in Eq. (21), more appropriate for supercritical conditions, Eq. (23):

$$\phi = \left| \frac{p_{sat\,(s_{\text{Motive}})} - p}{p_c - p_{sat\,(s_{\text{Motive}})}} \right|, \tag{23}$$

where p_c is the critical pressure at the given conditions and the subscript *sat* indicates saturated conditions. The mentioned authors found that the appropriate empirical coefficients were, $a = -0.54$, $b = -1.76$, $\theta_0 = 2.14e-07$.

Such an HRM was implemented by Colarossi et al. [63] into a 2D CFD model using the OpenFOAM framework [64] for R744 ejectors. The study aimed to investigate the presence of non-equilibrium effects. As an initial approach, the authors used the relaxation time for flashing water [72]. A comparison with the experimental results obtained for the pressure recovery performed by Nakagawa et al. [27] revealed an average error of 18.6% and a maximum error of 50%. It was also stated that the expansion follows a path of equilibrium states, and concluded that non-equilibrium effects were negligible. The study was evaluated at supercritical conditions so these results are not contradicting the results of Palacz et al. [56].

In a later study, Palacz et al. [73] compared an HRM and a HEM approach. The constant relaxation time parameters suggested by Angielczyk et al. [70] was employed. The investigation showed that the HRM outperformed the HEM for operating regimes distant from the critical point. However, the HEM was more accurate than the HRM approach at supercritical conditions. Overall up to 5% improved accuracy was observed for the HRM only in the sub-critical range. This improvement was found unsatisfactory, and it was concluded that further investigation into the relaxation time parameter should be conducted to achieve higher accuracies.

Recently, Colombo et al. [74] presented an HRM approach based on the relaxation parameter of Angielczyk et al. [70] and compared with the experimental results by Palacz et al. [75]. Relatively low errors were observed for the three operating points (2–14% error in motive

MFR, 2–16% error in suction MFR), however, investigations with at wider operating ranges are needed for further validation.

The investigations carried out by Palacz et al. [73] revealed that the assumption of a constant relaxation time parameters decreased the model accuracy for some operating conditions. To generalize the HRM for a wider range of operating conditions investigation into a variable relaxation time parameters was conducted by Haida et al. [61]. The parameters in Eq. (21), ie. θ_0, a and b, were thoroughly investigated to understand their impact on the flow. Furthermore, an optimization algorithm was used to construct an optimal set of relaxation time parameters for different operating ranges, to better replicate experimental results and achieve higher accuracy. The motive nozzle conditions were divided into a high, a medium, and a low-pressure range. In each pressure range, the parameters were optimized to minimize the discrepancy in the results. The empirical coefficients that best reproduced the experimental results were identified as follows:

$$a = 0, \quad b = 0, \quad \theta_0 = 1.0{\cdot}10^{-7} \quad if \ p_m \geqslant 73.77 \ bar$$
$$a = -0.67, \quad b = -1.73, \quad \theta_0 = 9.0{\cdot}10^{-6} \quad if \ 59 < p_m < 73.77 \ bar$$
$$a = -0.67, \quad b = -2.0, \quad \theta_0 = 1.5{\cdot}10^{-6} \quad if \ p_m < 59 \ bar$$

The optimization was based on a set of operating conditions and validated with experimental results outside this set. The modified HRM was able to produce similar accuracy to the HEM approach for transcritical operating conditions while retaining the benefits of the HRM for sub-critical conditions. However, further work is needed to validate the transferability of this model to other geometries.

3.1.3. Mixture models

A modeling approach that has recently garnered attention from the research community is the mixture model. These 4-equation models aim to model the phase change mechanisms in the flow. Here, the transport equation for the volume fraction (Eq. 19) is solved with the mass transfer terms for evaporation and condensation explicitly included:

$$\Gamma = \Gamma_e - \Gamma_c, \tag{24}$$

where Γ_e and Γ_c are the mass transfer sources due to evaporation and condensation, respectively. Such an improved estimation of the phase composition, i.e. (I- Phase-fraction), allows for a more accurate estimate of the mixture properties. The properties are calculated based on a mass weighted average (Eq. 25) for the thermodynamic variables, e.g. enthalpy or total energy, or volume weighted average (Eq. 26) for the variables mixture density, molecular viscosity or thermal conductivity:

$$\xi_m = \beta_l \xi_l + (1 - \beta_l)\xi_v, \tag{25}$$

$$\chi_m = \alpha_l \chi_l + (1 - \alpha_l)\chi_v, \tag{26}$$

where ξ, and χ are generic properties, α and β are the volume and mass fractions respectively. The subscripts l, v, and m correspond to the liquid, vapor and mixture properties, respectively.

Different approaches have been proposed to model the phase change mechanisms. Yazdani et al. [55] implemented a mixture model into the ANSYS Fluent framework to model the R744 ejector. Here, two-phase transfer mechanisms were considered (I- Phase-fraction), ie. in the terms Γ_e and Γ_c of Eq. (24); a cavitation model adopted from the work by Singhal et al. [76], and a boiling model based on kinetic theory [77,78]. However, as noted by Giacomelli et al. [62] the superposition of these two phase-change mechanisms is not justified during flashing, as cavitation and boiling cannot be considered as two independent mechanisms.

Yazdani et al. [55] implemented different methods to estimate the thermodynamic fluid properties that enter the interpolation schemes, Eq. (25)–(26). The thermal conductivity and viscosity were set as a constant mean value for each phase, the liquid and vapor specific heats were set at saturated conditions, and the density of the liquid and vapor phase were estimated based on the REFPROP-database [46] and a Peng-Robinson equation of state. Additionally, this paper introduced a drift flux model to account for velocity-slip between the phases. This will be further discussed in Section 3.4.

Recently, a more extensive mixture model was presented by Giacomelli et al. [67] to model the nozzle flow in the R744 ejector ([50]). In this work, the full set of thermodynamic fluid properties for both phases were found through look-up tables based on the NIST REFPROP library. This was implemented by introducing two non-interacting "species", where one represents the R744 vapor phase and one represents the R744 liquid phase. This allows for each phase to be defined with a User Defined Real Gas Model (UDRGM). Giacomelli et al. [67] considered a mass transfer model based on the Clausius–Clapeyron and Hertz–Knudsen equations, referred to as the Lee model [59]:

$$\Gamma_e = \sigma_e \alpha_l \rho_l \frac{T - T_{sat}}{T_{sat}}, \tag{27}$$

$$\Gamma_c = \sigma_c \alpha_v \rho_v \frac{T - T_{sat}}{T_{sat}}. \tag{28}$$

The two parameters σ_e and σ_c require tuning, and can be analogously compared to the relaxation time. This model is similar to the boiling model employed by Yazdani et al. [55], through the Clausius–Clapeyron equation.

The phase change models used Yazdani et al. [55] and Giacomelli et al. [67] indirectly assume an interface area, A_i, given the form:

$$A_i = \frac{6\alpha(1 - \alpha)}{d_B},$$

ie. assuming spherical bubbles or droplets of uniform diameter d_B modified by the phase fraction. This assumption is likely to become invalid, especially in the motive nozzle. Giacomelli et al. [62] state that further work will be devoted to including interface density tracking to overcome the limitation of this assumption. Similar mixture models have also been implemented for flashing steam in converging–diverging nozzles [79], two-phase R600a [80] and LNG-BOG [81] ejectors.

The discussed mixture model was recently applied to simulate an R744 ejector by Giacomelli et al. [62]. Only a 2% error was observed for the motive mass flow rate showing the high accuracy of the model, however, significant deviations are still observed for the suction mass flow rate (10–17%). The parameter σ_e was found to have a significant impact on the model accuracy in terms of mass flow rate. The parameter σ_c was found to have a negligible impact on the mass flow rate, however, up to 11% higher values of outlet volume fraction were observed as this value was varied from $\sigma_c = 0.1$ to $\sigma_c = 10000$. Giacomelli et al. [62] compared their results with those obtained using a HEM and found that the mixture model performed significantly better (19% error for the mixture compared to 48% error for the HEM in terms of entrainment ratio). The difference is flow pattern prediction is depicted in Fig. 6, where the difference between the density field predicted by the HEM and mixture is highlighted. This illustrates the effect of relaxing the phase transition, where the HEM shows sharp discontinuities in density, the mixture model produces a smoother transition. However, the model by Giacomelli et al. [62] displayed problems with numerical stability and slow convergence. Giacomelli et al. [62] reported convergence times up to 8–10 days on a 12-core workstation, which was close to ten times higher than a similar HEM. This slow convergence rate is prohibitively high for applications such as optimization.

3.1.4. Delayed equilibrium

The mixture model allows for the existence of meta-stable and saturated states of liquid and vapor phases, whereas the HEM allows only for saturated conditions of both phases. An alternative approach is the Delayed Equilibrium Model (DEM), where the liquid phase is treated as a combination of saturated and meta-stable liquid. This coexistence is supported by the assumption is that only a fraction of the liquid is held

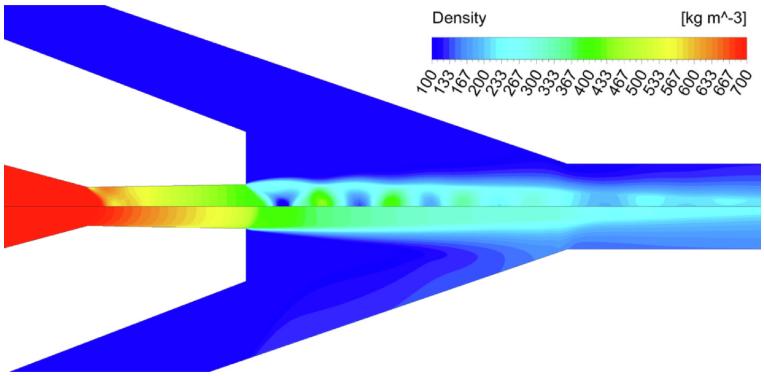

Fig. 6. Density contours comparison of the HEM (top) and mixture (bottom) in a sub-critical R744 ejector – Giacomelli et al. [62].

at a superheated temperature, and the other fraction is at saturation temperature, which is discussed by Bartosiewicz and Seynhaeve [49]. The fractions are typically defined by a vaporization index y, defined as:

$$y = \frac{m_{sl} + m_{sg}}{m_{sl} + m_{ml} + m_{sg}}, \tag{29}$$

where the subscripts s, m, l, and g indicate saturated condition, metastable condition, liquid, and gas, respectively. This approach has been used in 1D modeling in an R744 converging–diverging nozzle to predict the critical mass flow rate by Angielczyk et al. [82] and to model an R744 ejector by Banasiak and Hafner [83]. Angielczyk et al. [82] compared the pressure distribution of the HEM and DEM in a converging–diverging nozzle. Their results showed that the non-equilibrium introduced in the DEM reduced the model accuracy, however, the limiting case of equilibrium (the HEM approach) still revealed significant discrepancies.

Later, Banasiak and Hafner [84] combined the DEM with both homogeneous and heterogeneous nucleation theory to model an R744 ejector. The authors divided the flow path of the expanding refrigerant into three sections, based on the fluid's thermodynamic state and degree of thermal equilibrium reached: (i) the thermodynamically stable single-phase section (containing either pure liquid or pure vapor), (ii) the metastable two-phase section (containing a mixture of the metastable fluid, saturated liquid, and saturated gas), and (iii) the equilibrium two-phase section (containing only the equilibrium liquid–gas mixture). The fluid bulk temperature in the different regions was defined and calculated according to the fluid properties except in the two-phase metastable zone, where two temperatures should be distinguished: the metastable liquid temperature and the equilibrium temperature. The authors replaced the isentropic expansion of the liquid as formulated in the work by Banasiak and Hafner [85], with a more general approach, independent of any transition trails, allowing for a more realistic assumption for the non-isentropic expansion profiles.

3.2. Modeling non-equilibrium

A full compressible two-phase model introduces seven degrees of freedom, independent of the turbulence modeling [86]. Such a model allows for disequilibrium of pressure (subscript p), velocity (subscript u), temperature (subscript T) and chemical potential (subscript μ) [87]. The time scale to reach equilibrium for each of these variables is often denoted θ. The relaxation time discussed for the HRM and mixture model is the chemical potential relaxation time, θ_μ. An analysis of the magnitudes of these time scales [88,89] for flashing water found that the thermal and chemical relaxation times were dominant in comparison with velocity and pressure relaxation times.

The complexity of the model and the required sub-models increase as additional non-equilibrium are introduced. The models are typically arranged into a hierarchy [90], describing the different combinations of relaxation models available. Model choice also changes the predicted speed sound [90,87]. The introduction of a velocity disequilibrium is discussed in Section 3.4. Pressure non-equilibrium is often neglected in most multiphase flow models, due to the rapid response of pressure waves. However, it is considered a challenge to show that problems with pressure non-equilibrium can be well-posed [91]. Thermal non-equilibrium is treated in the two-fluid models, where one energy equation is solved for each of the phases, and coupled by sub-models for heat transfer. The effects of thermal non-equilibrium are dependent on the mesh resolution (i.e. the control volume size). If the mesh is refined up to a resolution where each cell contains primarily one phase, see Fig. 4, thermal disequilibrium can be neglected. Potentially, it may be that both liquid and vapor phase exist in *chemical potential equilibrium*, however at differing temperatures (i.e. thermal non-equilibrium). Such a flow exists at equilibrium however will be poorly described by any current R744 model. Table 4 presents an overview of current R744 models and which non-equilibrium states are considered in each model.

3.3. Two-phase mixture properties

Different models and data sets for R744 properties are available, for a thorough overview see Banasiak and Hafner [92]. When approximating the fluid properties of R744 (II- Properties), the property library REFPROP [46] has been extensively used. REFPROP uses the equation of state (EOS) by [93] based on the Helmholtz equation for the determination of R744 properties. This EOS is widely regarded for its high accuracy [92], however, it is highly CPU intensive. Thus, the published literature has used look-up tables for more efficient simulations [69,68,45,67]. The accuracy of these tables must be considered, which is a trade-off between storage size and accuracy. As an example, Giacomelli et al. [67] found errors in property estimate up to 1.6% in their coarse look-up table. This look-up table was, however, preferred to reduce computation time. Alternatively, look-up tables based on

Table 4
Overview of the considered disequilibrium of different models, a) not yet studied.

Non-equilibrium	Chem	Mom	Temp	Press
HEM [45,57,68]	×	×	×	×
HRM [63,61]	✓	×	×	×
Mixture [67]	✓	×	×	×
Mixture [55]	✓	✓	×	×
Two-Fluid[a]	✓	✓	✓	×

variable step size is preferred, such as implemented by Banasiak and Hafner [69]. This is especially important near the critical point of R744, where large variations in properties occur. Since the work by Banasiak and Hafner [93], further work has improved upon the modeling of fluid properties of R744. Especially on the modeling of liquid and near-critical viscosity has been improved [94–96], however uncertainties up to 3–4% in liquid viscosity are still observed in newer correlations. The effect of bulk viscosity (volume viscosity) can be significant for compressible flow with poly-atomic gases. Fang et al. [68] studied the effect of bulk viscosity on a converging–diverging nozzle with R744 using CFD, concluding that the bulk viscosity had no noticeable effect on the flow. When mixture properties are considered, it is important to consider appropriate averaging laws for the mixture properties [97], which corresponds to (III- Averaging) in the previously established notion.

Due to the high velocity and often supersonic flow in the ejector, the evaluation of the speed of sound can significantly impact model results and/or convergence. A recent discussion on critical two-phase speed of sound for different models in pipe-flow was presented by De Lorenzo et al. [89], Fang et al. [69], and Lund [90]. In density-based models [68], the speed of sound directly modifies the propagation speed of acoustic waves and is critical for proper model results. On the other hand, for pressure-based solvers, such as the mixture model [67] and HRM [61], the speed of sound does not explicitly enter the solution algorithm. However, improper speed of sound models can still cause slow convergence or instabilities [62]. In the mixture model presented by Giacomelli et al. [67], the speed of sound could not be set as an independent variable due to limitations in the ANSYS Fluent software [59]. In this software, the Wallis speed of sound model is built into the UDRGM approach [98]. Giacomelli et al. [67] compared the Wallis model with a model by Brennen [99] by calculating the solution speed of sound in post-processing. Their investigation suggests that the Brennen model may be more accurate than the Wallis model.

Zhu and Elbel [24] state that the presence of fluids other than R744 in an ejector can dramatically affect the flow physics. As an example, oil flow through the ejector could impact ejector performance. Numerical simulations can be useful to model these effects and can help develop novel solutions to the treatment of oil in R744 ejector systems.

3.4. Velocity slip models

In Section 3 the homogeneous flow assumption, where all phases move with the same velocity, was considered. However, velocity slip (velocity non-equilibrium) can have a significant impact on the speed of sound [100,90], two-phase turbulence [101], and shock-wave pressure distribution [55].

To incorporate velocity slip, the models can be extended by including additional terms in the void-fraction (Eq. 19) and momentum equations (Eq. 12) to model the phase velocity slip. Velocity slip is considered in terms of the drift velocity, ie. the relative velocity between a phase (p) and the mixture (m). This is formulated as:

$$\vec{v}_{dr,p} = \vec{v}_p - \vec{v}_m, \tag{30}$$

or formulated in terms of relative velocities, $\vec{v}_{pq} = \vec{v}_p - \vec{v}_q$:

$$\vec{v}_{dr,p} = \vec{v}_{pq} - \sum_{k=1}^{n} \frac{\alpha_k \rho_k}{\rho_m} \vec{v}_{kq}. \tag{31}$$

where subscript k is the phase index 1 to n, subscript m referres to the mixture velocity. Several relations have been presented to estimate the velocity slip in the literature on flashing flows, see the review by Liao and Lucas [19]. Typically the velocity slip models account for drag related forces, neglecting other two-phase interactions.

Still, research considering the phase velocity slip condition is very limited. Yazdani et al. [55] introduced a simple velocity slip model based on the formulation for mixture models proposed by Manninen et al. [102]. The drag formulation used was based on the relations of Schiller and Naumann [103], where drag is considered as a modified Stokes drag coefficient for low particle Reynolds number $Re_p < 1000$, and a constant drag coefficient at $Re_p > 1000$. The particle Reynolds number is the Reynolds number, Eq. (5), based on the slip-velocity and particle diameter. Yazdani et al. [55] demonstrated that the slip model produced pressure waves at the nozzle exit, which were smoothed by the homogeneous flow model. However, the slip model was found to only have a minor effect on global ejector performance.

The relative importance of velocity slip depends on the velocity relaxation time, θ_v. An estimate of this time scale can be found by considering Stokes drag on a spherical particle. The relevant time scale for velocity slip is the drag relaxation time, ie. the time to accelerate a particulate to the surrounding fluid velocity. Considering the Newtonian (laminar) flow regime at a constant drag coefficient, C_D, yields [102]:

$$\theta_v = \frac{2\rho_p d_p}{3\rho_c C_D u_t} \tag{32}$$

Hence, the ratio of the particulate to continuum density is critical for velocity slip. For bubbly flows, where the particulate is at a lower density than the surrounding fluid, this ratio is low and bubbles will quickly be accelerated to the velocity of the surrounding liquid. As the flow inverts from a bubbly flow regime with increasing vapor fraction, the flow regime turns into a droplet flow. Compared to bubbles, droplets, on the other hand, will be largely independent of the surrounding gas velocity.

3.5. Advanced two-phase modeling

The models presented so far (HEM, HRM, mixture, DEM) have considered the two-phase problem by treating the phase change and phase slip indirectly using supplementary models, coupled to the pseudo-fluid solver. Alternatively, these issues can be treated more directly through the use of a two-fluid model (TFM) [91]. The two-fluid model treats each of the two phases as a separate fluid. This involves the use of separate equations for mass, momentum, and energy transfer for both fluids. In 3D CFD models, this yields a set of 10 equations; 2 for mass, 6 for momentum (one for each direction and phase), and 2 for energy. Such an approach has the benefit of being able to capture non-equilibria (such as temperature and velocity) between the phases directly. However, additional modeling is required to capture the interactions between the phases. The TFM was tried by Menegay [104] in 1998 for R134a ejectors, however, the CFD model was eventually significantly simplified due to its complexity.

Many additional effects of two-phase flow have not yet been thoroughly investigated for R744 ejectors, such as the effects of bubble and droplet collisions, interphase drag, and jet break up (atomization). As an example, the breakup process after a nozzle displays a complex flow pattern, illustrated in Fig. 2. Furthermore, these effects are interdependent with multiphase turbulent effects, which increases problem complexity. Additionally, the close relationships for multiphase flows are strongly dependent on the flow regime, as discussed in Section 2.1. Unfortunately, more advanced investigations will typically require more accurate experimental data for validation. Such experimental data is not yet available, see Section 6.

3.6. Comparison of multiphase models

This paper has mainly discussed three approaches for advanced modeling of R744 ejectors: HEM, HRM, and the mixture approach. A comparison of the errors is presented in Fig. 7 and summarized in Appendix A. These data are compiled from the studies carried out by Giacomelli et al. [62], Palacz et al. [73], and Haida et al. [61]. To the best of the authors' knowledge, no such comparison has been done in the literature. Ejector geometry has not been considered in this

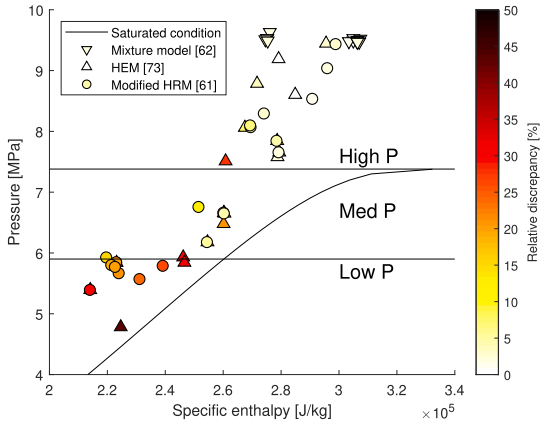

Fig. 7. Relative discrepancy of motive mass flow rate plotted at the corresponding motive condition. Downward triangle – Mixture model [62], Upward triangle – HEM [73], Circle – modified HRM [61].

comparison and could potentially have a significant impact on model accuracy.

In Fig. 7 the modeling error, i.e. the discrepancy between model and experimental data, is presented for the different studies. The points are color-coded according to the percentage model error in the motive MFR. Fig. 7 illustrates that current R744 ejector models are able to reasonably capture near-critical motive flow conditions. The recently developed mixture model [62] shows a very low motive MFR discrepancy (error 0.1–2%). However, as can be observed in Fig. 7 this model has not yet been tested for pressures below critical. Moreover, the method shows promise for future development. The motive MFR errors increase for lower motive pressures, as the expansion moves from near-critical to off-critical. As previously discussed in this review, this is likely due to the increased effect of non-equilibrium conditions during off-critical operation.

The average errors of the mentioned models are shown in Table 5 and organized into three categories. Similarly to the choice in Haida, three categories are used to compare the models; supercritical pressures ($P_{motive} > P_{crit}$), intermediate pressures ($59bar < P_{motive} < P_{crit}$) and low pressures ($P_{motive} < 59bar$). The lowest average MFR error was observed for the mixture model both for suction and motive flow rate at supercritical conditions. Nevertheless, this approach should be further tested for sub-critical pressure conditions for a full comparison. Currently, the modified HRM formulation has demonstrated the best accuracy in the sub-critical pressures. However, this approach still significantly deviates from experimental measurements, especially for suction MFR at low pressures.

From Appendix A and Table 5 it is clear that the *suction* MFR is still not well described by any current model. The relative error in suction MFR varies from 20–100%. The challenge of correctly capturing the suction mass-flow rate stems from its complicated governing mechanisms. Firstly, the suction mass flow rate is induced by the motive flow, which means that errors in the motive flow compound for the suction flow. The motive flow rate can be predicted by a wide range of models, as it is primarily affected by the upstream and downstream pressures. In comparison, the suction flow is more sensitive to local flow phenomena, such as the local velocity, vapor quality, turbulence, and pressure. This means that even if the global mass flow rate of the motive flow is well predicted, if the local solution of the motive flow is not correctly reproduced, it will give cause errors for the suction flow. Secondly, the physics that produces the motive and suction flow is very different. The motive flow is decided primarily by thermodynamics, phase-change, and the motive pressure. While the suction flow is entrained by the motive flow, which is governed primarily by turbulence, the local velocity field, and multiphase momentum interaction.

Table 5
Averaged discrepancy in motive and suction MFR observed with available R744 ejector CFD models. $P_b = 59$ bar.

Study	$P > P_{crit}$	$P_b < P < P_{crit}$	$P < P_b$
		Average error motive MFR	
HEM – [73]	5.5%	11.0%	30.5%
HRM – [73]	5.4%	9.4 %	27.7%
Modified HRM – [61]	3.3%	5.4%	23.2%
Mixture – [62]	1.1%	–	–
		Average error suction MFR	
Modified HRM – [61]	20.1%	21.2%	64.1%
Mixture – [62]	14.4%	–	–

A summary of the main advantages and challenges of each of these approaches is presented in Table 6. The more recently implemented methods (Modified HRM and mixture model) have been less extensively tested in the literature than the classic HEM. The HEM is generally regarded to produce reasonably accurate results at super-critical conditions. Furthermore, the simplicity of the HEM helps the stability of the model, which is important for use in optimization algorithms. However, this model fails to describe the ejector operation at low-pressure motive conditions. This effect is thought to be connected to relaxation effects. Two ways to deal with this non-equilibrium relaxation is presented in the literature; the relaxation approach (HRM) and the mixture approach. The HRM applies the equilibrium properties of R744, similarly to the HEM, but introduces a time-delay depending on the flow conditions. The studies show that a single relaxation parameter is not suitable for a wide range of operating conditions. By using three different zones for the relaxation time formulation fairly reasonable results can be achieved for most motive conditions. The mixture approach treats the phase change mechanisms explicitly and uses properties in meta-stable conditions for gas and liquid. While the mixture model can produce highly accurate motive MFR results for super-critical pressures, validation at low pressures has yet to be conducted. Taking into account the phase change mechanisms in the model, such as done in the mixture model and TFM, allows for a more realistic and physical description of the flow. This approach makes the model less dependent on experimental data, but it requires more extensive sub modeling. Still, this model suffers from numerical stability issues that can cause slow computations.

4. Turbulence

An accurate description of the mixing phenomenon and the flow structure inside the ejector is highly dependent on accurate modeling of the turbulent flow. Due to the complexity and lack of insight into multiphase turbulence, modeling turbulence in R744 ejectors is significantly more challenging than for single-phase ejectors. Multiphase turbulence has therefore often been left disregarded in current R744 ejector models.

To model compressible multiphase turbulence, fluctuations in velocity, density, and mass fraction, as well as interface effects must be accounted for. Thus, different averaging procedures of the flow fields are considered to reduce the need for excessive sub-modeling. A common approach is to use ensemble- and phase averaging. Model complexity can then be reduced to modeling to a few additional terms in the momentum and energy equations. Most prominant is the non-linear momentum fluctuation $u_i' u_j'$, typically modelled by a Boussinesq approximation, Eq. (33), where turbulent fluctuations are treated as a diffusive turbulent viscosity.

Table 6
Overview of currently available R744 two-phase ejector models, their limitations and advantages. Presented in previous work [105].

Model	Advantages	Challenges and limitations
HEM		
Smolka et al. [45], Lucas et al. [57], Giacomelli et al. [66] Fang et al. [68]	-Simplicity and stability -Accurate at supercritical conditions -Extensively tested in literature	-Does not consider meta-stability (underestimates flashing flows at low motive pressures)
HRM		
Colarossi et al. [63], Palacz et al. [73], Haida et al. [106]	-Considers meta-stability, -Extended with variable relaxation time for subcritical conditions	-Empirically based parameters for relaxation time, -Requires tuning of parameters
Mixture		
Yazdani et al. [55], Giacomelli et al. [62]	-Considers meta-stability, -Can more accurately evaluate the phase fractions by mass transfer modeling -Highly accurate results for motive flows	-Increased complexity, -Requires tuning of model parameters, -Less profound literature database on R744 ejectors -Not yet tested for low motive pressure

$$\overline{u_i' u_j'} = \nu_t \left(\frac{\partial u_i}{\partial x_j} + \frac{\partial u_j}{\partial x_i} \right) - \frac{2}{3} k \delta_{ij} \tag{33}$$

Here, u' is a turbulent fluctuation in the velocity field, and ν_t is the turbulent viscosity. Commonly, a set of transport equation for turbulent kinetic energy, k Eq. (34), and the turbulent energy dissipation ϵ Eq. (34), is solved to close the relation for turbulent viscosity relation, according to: $\nu_t = c_\nu \frac{k^2}{\epsilon}$.

$$\frac{\partial(\rho_m k)}{\partial t} + \frac{\partial(\rho k u_i)}{\partial x_i} = \frac{\partial}{\partial x_j}\left[\frac{\mu_t}{\sigma_k} \frac{\partial k}{\partial x_j} \right] + G_{k,m} - \rho_m \epsilon + \Pi_{\epsilon,m} \tag{34}$$

$$\frac{\partial(\rho \epsilon)}{\partial t} + \frac{\partial(\rho \epsilon u_i)}{\partial x_i} = \frac{\partial}{\partial x_j}\left[\frac{\mu_t}{\sigma_\epsilon} \frac{\partial \epsilon}{\partial x_j} \right] + \frac{\epsilon}{k}\left[C_{1\epsilon} G_{k,m} - C_{2,\varepsilon} \rho_m \right] + \Pi_{k,m} \tag{35}$$

where the subscript, m, indicates mixture properties based on mass or volume weighted averaging. $G_{k,m}$ is the strain rate production of k, $G_{k,m} = \mu_t (\partial u_j/\partial x_i + \partial u_i/\partial x_j)^2$. Interfacial turbulence interactions are included in the terms $\Pi_{k,m}$ and $\Pi_{\epsilon,m}$, which are further sub-modelled [59]. Additional multiphase effects, such as bubble induced turbulence, dispersion forces, and the influence of other neglected terms have so far not been discussed in any of the current models. For further details on multiphase turbulence see Ishii and Hibiki [91], Coutier-Delgosha et al. [107], and Morel [108].

The current state of the art R744 ejector models consider pseudo-fluid turbulence, i.e. assuming that the turbulent structures behave similarly to single-phase turbulence. Already, a large set of turbulence models have been studied for R744 ejector modeling, as shown in Table 7. The latest approaches recommend the use of k-ω SST models due to its better predictions of local and global flow parameters for single-phase flows [109–111].

Table 7
Presentation of the different turbulence models used for R744 ejector modeling and the corresponding multiphase model.

Study	Turbulence model	Model
Colarossi et al. [63]	$k-\epsilon$	HRM
Yazdani et al. [55]	$k-\omega$ SST	Mixture
Smolka et al. [45]	$k-\epsilon$ RNG	HEM
Banasiak et al. [113]	$k-\epsilon$ RNG	HEM
Lucas et al. [57]	$k-\omega$ SST	HEM
Palacz et al. [56]	$k-\epsilon$ Realizable	HEM
Palacz et al. [60]	$k-\epsilon$ Realizable	HEM & HRM
Giacomelli et al. [66]	$k-\epsilon$ RNG	HEM
Haida et al. [106]	$k-\omega$ SST	HRM
Giacomelli et al. [114]	$k-\epsilon$ Realizable	HEM
Giacomelli et al. [67]	$k-\omega$ SST	Mixture & HEM
Haida et al. [112]	Comparative (4 models)	HRM
Fang et al. [68]	Comparative (2 models)	HEM

Recently, a comparison of turbulence model performance for R744 ejectors was conducted by Haida et al. [112]. In this work, the authors compared four commonly used turbulence models, namely the k-ϵ Realizable model, the k-ω SST model, the Transition SST model, and the Reynolds stress model. It was found that the Transition SST model and the Reynold stress model were best at predicting the local wall temperatures. Furthermore, the global entrainment ratio was found to be best predicted by the k-ϵ Realizable and the Transition SST. The authors noted a significant dependence on the near-wall turbulence formulations for the Reynolds stress model and the k-ϵ Realizable model.

The disagreements in the literature indicate that further research is needed into appropriate turbulence models for two-phase ejector flow. Two-phase turbulence effects have largely been neglected in current literature and will require detailed investigations.

A more accurate, however computationally costly, turbulence model is the Large Eddy Simulation (LES). LES resolves more of the turbulent spectrum by using a very fine mesh and only modeling the effects of the smallest turbulent length scales (Kolmogorov length scale). For further literature on LES turbulence modelling for multiphase flows and atomization see the reviews by Sher et al. [33], Jiang et al. [44], Gorokhovski and Herrmann [115], Balachandar and Eaton [116], and Fox [117]. Current work is planned on LES simulation for R744 ejectors [68]. However, this model is considered immature for multiphase flows and not well established for ejectors. Furthermore, a good understanding of the bubble size distribution, as well as the Kolmogorov length scales, is critical for the appropriate use of the LES models [44]. Further work is needed for such models to be accurately applied for two-phase ejectors.

Looking forward, with the current developments in computational speed and massive parallelization, it will likely be possible to achieve full Direct Numerical Simulation (DNS) of the two-phase ejector within the next decade. DNS simulation a turbulence approach that fully resolves all turbulent length scales in a flow. This approach has already seen use for multiphase atomization [118].

5. Solution methods

5.1. Numerical solution methods

While model equations can provide highly accurate descriptions of the two-phase flow, the correct solution of these equations needs consideration. Among other things, achieving accurate numerical solutions involves choosing appropriate meshing, solver settings, and convergence strategies. Therefore, this section treats the applied numerical

approaches in modeling of R744 ejectors using CFD.

Numerical solutions to fluid dynamic problems are actively researched. For an introduction to numerical fluid mechanics and heat transfer see e.g. the books by Patankar [119] and Pletcher et al. [120]. In the available literature on R744 ejectors, the most extensively used CFD frameworks are ANSYS Fluent and OpenFOAM. This section will therefore just discuss the numerical procedures used available in these software-frameworks. Solution algorithms in CFD have traditionally been divided into density-based and pressure-based solvers. The density-based solvers were initially developed for highly compressible flows and shock solutions, where the pressure-based were intended for low-speed incompressible flows. These solvers have since been extended to be able to handle most ranges of flow conditions. However, it is generally agreed that density-based solvers have an advantage for highly compressible flows, though good results for compressible multiphase flows with pressure-based solvers have been presented in the literature [121]. The pressure-based solvers typically use the coupled approach in ANSYS Fluent, combined with the PRESTO! pressure interpolation scheme and a second-order upwind [61] or a third-order QUICK [67] scheme.

So far, the R744 ejector models available in the literature have primarily been based on segregated or coupled pressure-based solvers [45,73,62,55]. This has been necessary as density-based solvers are incompatible with multiphase solvers in the ANSYS Fluent CFD software. Recently, an alternative numerical approach was considered by Fang et al. [68] for R744 converging–diverging nozzles. Their approach uses the rhoCentralFoam density solver which is based on the KT (Kurganov and Tadmor [122]) and KNP (Kurganov et al. [123]) second-order spatial scheme. Boundary conditions based on in- and outgoing characteristics was applied for improved stability of the solution. Higher-order schemes for investigations of flashing R744 was conducted in the study by Gjennestad et al. [124]. Here, a higher-order CFD method based on the third-order Weighted Essentially Non-Oscillatory method and Span–Wagner EOS at equilibrium was presented.

The transient solution is often neglected in simulations for R744 ejectors. The assumption of steady-state R744 ejector flow has been considered in multiple studies [45,73,61,62]. This assumption has still not been fully investigated for R744 ejectors and further work is needed. Transient effects may be significant for other ejector geometries and CFD models and should be verified for each model case.

5.2. Model dimensionality

The simplicity of the ejector geometry makes a low dimensional model an attractive option. Ejector flow is commonly considered a 1D problem, as it primarily involves one flow direction. The one-dimensional models are typically divided into true 1D models and pseudo-1D models (also referred to as 0D models or thermodynamic models). The pseudo-1D models use empirical coefficients for the different sections of the ejector (nozzle, suction chamber, mixture chamber, diffuser) and connect these to predict performance. Such models have been extensively proposed in the available literature [24,125,126,18]. Among the first two-phase ejector models is that of Kornhauser [32], which has been extensively utilized and developed in later works [127,31]. Recently, Taslimi Taleghani et al. [54] presented a thermodynamic R744 ejector model able to reproduce both single choking and double choking conditions. Taslimitaleghani et al. [22] also used such a model to study the benefits of R744 ejectors in different cycle configurations. The authors concluded that the greatest benefits of ejectors were gained when used for expansion work recovery, noting an improvement of up to 23% in COP compared to throttling. The benefit of these simplified models is that design optimization comes at a much lower computational cost.

On the other hand, true 1D models treat the flow as two interacting 1D streams, one representing the motive flow and one representing the suction flow. Banasiak and Hafner [83] combined such an approach with multiphase models to account for meta-stable effects.

However, 1D models offer limited insight into the local flow field inside the ejector and are derived from assumptions that limit their range of validity. 3D models may have a significant effect on model fidelity as noted by Smolka et al. [128]. This is especially true for non-axisymmetric suction chambers and high swirl flows. Mazzelli et al. [109] supported this by investigating 2D and 3D CFD models for ejectors, showing that for off-design conditions 2D models would fail to yield acceptable results. While full three-dimensional simulations of ejectors are fully feasible with CFD, the computational cost can be drastically reduced by assuming 2D flow. Ejector CFD models have extensively used a two-dimensional flow approach. The 2D flow assumption can give results with reasonable accuracy [67,62,57,68], which makes it suitable for model development as well as optimization algorithms where computational costs are limiting.

6. Experimental validation data

Experimental investigations on R744 ejector systems have been extensively reviewed in previous work [37,17]. In this section, some recent developments and future opportunities for model validation will be explored. Furthermore, a compiled data set used in some previous works for validation purposes will be presented. Extensive literature is available for ejectors with other working fluid. However, these are not applicable for validation purposes as R744 ejectors are significantly different from ejectors with other fluids. Specifically, in terms of ejector size, operating conditions (supercritical motive conditions), refrigerant properties, multiphase effects, and non-equilibrium flow, R744 ejectors deviate from other working fluids.

Ideally, to properly validate a model a large set of accurate experimental data for different flow variables, such as velocity profile, turbulence intensity, vapor quality, and pressure distribution, is required. Nonetheless, the typical R744 ejector dimensions are of magnitude millimeters, which heavily restrict the available experimental measurement techniques that can unobtrusively be applied. As an example, a common way to measure local velocity, even for supersonic flows, is using hotwire anemometers [129]. However, these devices typically still have a wire length of 1.2 mm [129], where the size of an R744 ejector mixing section can be 3 mm [113].

To date, the most common validation parameter is the mass flow rates (MFR) and the entrainment ratio. These have been extensively measured for different R744 ejectors at different operating conditions [73,65,18]. A compiled data set of some of the investigations conducted at SINTEF Energy Research (Trondheim, Norway) [60–62] that has been used for R744 ejector models in previous studies is presented in Table Appendix A for ease of use in future model validation and comparison to other models. The operating conditions of the different investigations are illustrated in a P-h diagram in Fig. 8 and include both near-critical and off-critical flows.

Even though the prediction of global parameters is an important validation parameter, proper validation of model results should be assessed based on local parameters. Local parameters give insight into the physical realism of the applied model, which is critical for reliable ejector models at large ranges of operating conditions and ejector designs. Some literature has been presented that considers local parameters are discussed below and summarized in Table 8.

An experimental study that has been extensively used for model validation is that of Nakagawa et al. [50]. A converging–diverging nozzle, similar to those used in ejectors, was equipped with pressure sensors. While this can be used to validate the expansion process in the nozzle, the full ejector was not considered. A visualization technique was used in the study by Berana et al. [51]. Here, the converging–diverging nozzle with transcritical R744 was investigated using direct photography and pressure measurements. This work followed up on the study by Nakagawa et al. [50] and further discussed the observed shock waves.

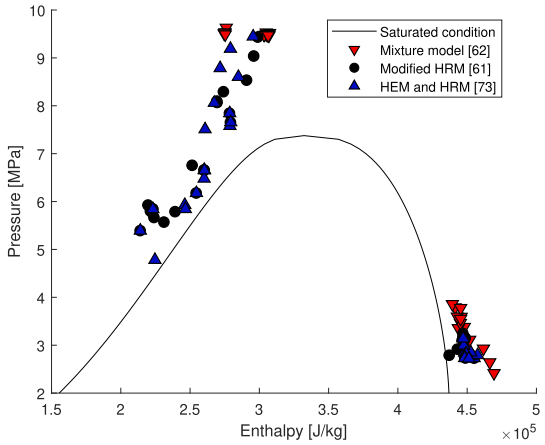

Fig. 8. Collected data points from Palacz et al. [73], Haida et al. [61] and Giacomelli et al. [62]. Points on the right are suction inlet conditions, top left are motive inlet conditions, corresponding to thermodynamic state 9 and 3, respectively.

Table 8
Experimental studies where local parameters in an R744 ejector or converging diverging nozzle have been measured. * indicates an ongoing study.

Study	Messurement
Ejector	
Elbel [41]	P_{wall}
Banasiak and Hafner [83]	P_{wall}
Zhu et al. [130]	Visual, P_{wall}
Haida et al. [112]	T_{wall}
Li et al. [52]131	Visual, P_{wall}
Haida et al. [132]*	PIV
Converging – Diverging Nozzle	
Nakagawa et al. [27]51	P_{wall}, T_{wall}

Haida et al. [61] presented experimentally obtained wall temperature data for an R744 ejector. Temperature probes were introduced into the ejector outer walls. However, validating a model using wall temperature data requires that the model includes wall heat transfer effects, adding additional model complexity.

Recently, visualization techniques have been used for imaging of the flow inside an R744 ejector. Such investigations were conducted by Zhu et al. [130] and Li et al. [52]. Using a direct photography visualization technique, the images identify the expansion angle of the primary flow. Zhu et al. [130] analyzed the different operating conditions and identified the expansion angle at different primary and secondary pressures. An example-image is included in Fig. 9. Furthermore, assuming an isentropic expansion with an irreversibility efficiency a liquid fraction in the suction chamber was estimated and compared with the observed grayscale in the images. The experiments showed that low primary flow pressure increased the expansion angle. The larger flow area caused by the increased expansion angle blocks the suction flow, limiting the entrainment.

Li et al. [52]131 used a high-speed camera as well as pressure sensors to investigate the phase change position for different operating conditions in an R744 ejector. Their findings indicate that the location of the phase change is largely dependent on the motive pressure. Furthermore, the obtained grayscale values were analyzed, and, under the assumption of a set bubble diameter, a qualitative bubble number density distribution was presented, shown in Fig. 10.

Looking forward, certain techniques not yet applied to two-phase

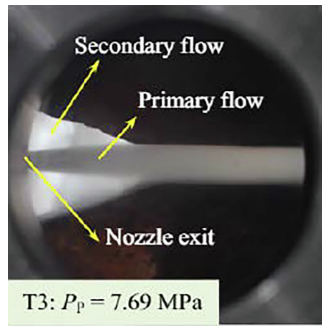

Fig. 9. Image of the flows in the suction and mixing chambers at motive pressure P_p = 7.69 MPa – Zhu et al. [130].

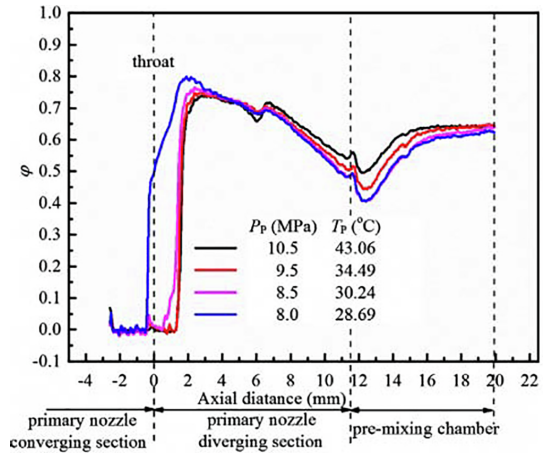

Fig. 10. Qualitative bubble number density distribution curves for various operating conditions. -Li et al. [52].

ejectors may give more detailed insights into the ejector flow. As an example, Particle Image Velocimetry (PIV) is a velocity measurement technique that involves seeding particles into the flow and tracking these. The PIV method has already been used in single-phase-[133,134] and multiphase ejectors [135] with good results. Such an approach is, however, more challenging in the case of R744 ejectors due to their small size and high pressure. Currently, Haida et al. [132] are performing the first particle image velocimetry (PIV) measurements for a circular R744 ejector. Such an investigation could provide detailed insights into the local velocity field within a circular R744 ejector.

7. Applications of models

7.1. Generation of entropy

One primary interest in ejector modeling is the understanding of the origins of irreversibilities. The ejector is a theoretically isentropic expansion device, however, due to irreversible viscous forces, supersonic shocks, and turbulence, isentropic expansion is physically unobtainable. It is therefore of interest to examine how entropy is generated in ejector flows. Such an investigation was conducted by Banasiak et al. [113], where the CFD model of Smolka et al. [45] was used to identify zones of entropy generation in the R744 ejector. The results indicate that the largest production was located in the mixing section, primarily due to turbulent and shock losses. The authors argue that geometry

optimization should be conducted with respect to the interdependency of the geometric parameters, i.e. that optimization of one parameter in isolation does not in general yield optimal results. Further investigation of entropy can be found in the study by Sierra-Pallares et al. [136]. In this work entropy generation was evaluated for an R134a ejector by direct entropy method, solving a differential equation for entropy transport. This investigation supported that the primary contributor to irreversibilities in an ejector is turbulent viscous dissipation produced near the nozzle exit, as claimed by Banasiak et al. [113].

7.2. Shape design and optimization

Model-based design approaches have been extensively been used for design improvement for R744 ejectors. The studies based on modern CFD approaches are presented here. The HEM presented by Smolka et al. [45] has been extensively applied for R744 ejector shape design. One such study was conducted by Palacz et al. [60], where an R744 ejector was optimized using the EjectorPL software. This software was designed to automate parts of the CFD workflow, such as geometry generation and meshing, allowing for the rapid development of a large set of CFD results. This set can then be fed into an optimization algorithm to search for optimized geometry designs. In the work by Palacz et al. [60], six geometric dimensions were investigated to optimize for the maximal ejector efficiency. This was done using both an evolutionary and a genetic optimization algorithm. Later, Palacz et al. [75] furthered this study by investigating additional ejector geometries and geometric parameters, achieving up to 6% (percentage points) increase in ejector efficiency. The findings of these studies show that CFD models can be used to improve ejector efficiency robustly and reliably.

An interesting prospect for model design optimization is the implementation of adjoint methods [137,138]. Adjoint methods attempt to optimize an objective by looking at small changes in the design parameters. Adjoint methods then solve simultaneously the flow solution and the solution with different design parameters. However, adjoint methods are not sufficiently developed for complex multiphase flow, such as two-phase ejector flows.

7.3. Ejector flow control

An ejector can be used to control the high-side pressure in a refrigeration system and to regulate to achieve the optimal cooling capacity. The capacity control strategy of two-phase ejectors, i.e. the control of ejector pressure lift and entrainment, plays a pivotal role in guaranteeing high overall energy efficiency [20]. Therefore, different concepts have been proposed for flow control in ejectors. The methods which have gained to the most attention are the multi-ejector block [139], the adjustable needle design [31,18], and motive swirl control [140], see Fig. 11. CFD models have been a useful tool for investigating these solutions.

A comparative study between the fixed geometry ejector, used in a multi-ejector block solution, and the controllable needle ejector was conducted by Smolka et al. [128]. In this work, the two designs were modeled with the HEM CFD model and compared. The fixed geometry ejector showed good performance for all investigated operating conditions. The adjustable geometry design was able to outperform the fixed geometry design. The drawback of such an approach was that identifying the needle positions that yielded the best efficiency at a given flow rate were found difficult to asses, making the efficiency using such an ejector less predictable.

A numerical study of a full-scale multi-ejector module using the HEM approach was presented in Bodys et al. [141]. Their results indicated the high importance of properly designing outlet collectors. From this study, the authors considered the regulation capabilities of the multi-ejector block suitable for industrial refrigeration. Furthermore, Bodys et al. [142] looked into the swirl motion generation for multi-ejector applications. The study suggests that at high motive rotational speeds increased mass entrainment ratios could be achieved, independent of ejector size.

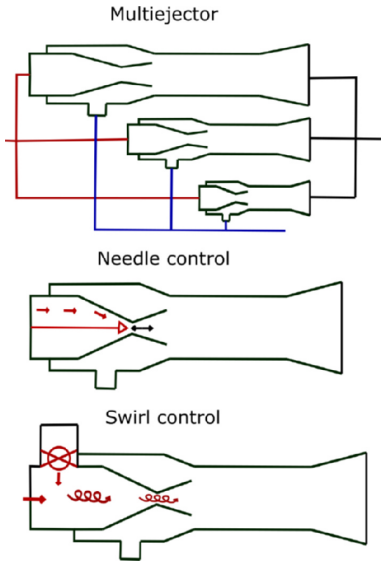

Fig. 11. Illustration of ejector layout for three ejector control solutions.

Bodys et al. [143] performed a numerical investigation on an R744 ejector with a bypass inlet [144], see Fig. 12. Different configurations of bypass placement and inlet angles were analyzed using the HEM approach. According to this study, up to 39% increase in mass entrainment ratio could be gained by using the suction flow bypass.

7.4. Model reduction

Besagni [42] emphasized the need for large reductions in model size to achieve coupling between the local scale modeling (such as CFD) to the large scale system simulations. The use of CFD models to approximate reasonable component scale Lumped Parameter Models (LPM) was indicated as an attractive prospect. However, large scale production of high accuracy CFD results is in many cases unfeasible due to the large computational and time costs. Nonetheless, advanced methods to achieve CFD-level fidelity at much lower computational costs have recently been presented in the literature. One such approach is the reduced-order models (ROM). ROM is a modeling approach where a set of results are processed to establish a reduced basis which optimally represents the previous results. Typically, high accuracy CFD and experimental results at a wide operating range are used as the input.

Such a ROM approach was applied for R744 ejector modeling by Haida et al. [106,145]. In these studies, the HEM model was used to create a set of results (referred to as *snapshots*) for the optimization of the reduced model. These snapshots were used to generate ejector performance maps [106] (such as those experimentally obtained by Banasiak et al. [20]) and develop accurate system models [145] based on the CFD model results. The model was implemented into a dynamic system scale simulation for different climate zones in Haida et al. [132]. This ROM was compared with simpler 0- and 1D models, commonly used in the literature. It was shown that the ROM predicted the ejector performance with superior accuracy to the thermodynamic models and could efficiently be implemented into system scale simulations. The accuracy of a ROM is however, limited by the accuracy of the analyzed input, and can therefore not be used to explore designs beyond the given input data. Therefore, more accurate CFD models will improve the ROM accuracy, which motivates further research into CFD

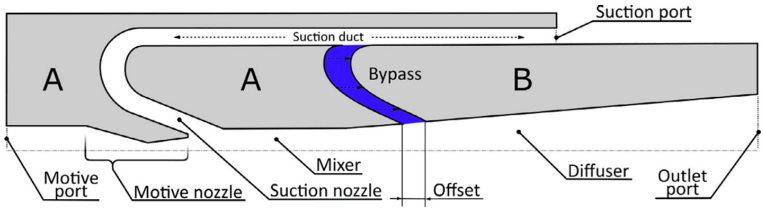

Fig. 12. Illustration of the ejector bypass concept – Bodys et al. [143].

modeling.

8. Conclusions and future developments

This paper has presented a complete overview of the current state of the art within two-phase R744 ejector modeling. The adoption of two-phase ejector technology presents a substantial improvement in the energy efficiency of R744 vapor-compression systems, potentially leading the HVAC&R sector to have a future-proof solution for many applications. However, a rigorous design of the R744 two-phase ejector is necessary to achieve this target. As a consequence, the implementation of advanced models and tools for an accurate ejector design has become one of today's most important research topics. The implementation of computer-assisted tools, such as CFD, can improve R744 two-phase ejector design and operation. However, to the best of the authors' knowledge, no detailed review works have been carried out yet despite the importance of the research.

Therefore, the purpose of this investigation has been to bridge this knowledge gap by comprehensively evaluating all the aspects as well as challenges related to R744 two-phase ejector models, i.e. multiphase flow modeling, turbulence aspects, numerical solution methods, applications of models. This work has found that significant discrepancies can be observed when comparing ejector-model results with experimental measurements. The models are trending toward more advanced two-phase models that can treat motive flows at a wide range of operating conditions. The focus of recent research has been on the treatment of non-equilibrium expansion that occurs at low-pressure motive conditions. This review has shown that while the currently most advanced models can achieve reasonable accuracy at supercritical motive pressures, the accuracy quickly drops at lower pressures. Furthermore, current models still struggle to predict suction mass flow rates, likely due to its dependency on other flow features as well as models for turbulent momentum diffusion. Increasing model complexity does, however, require detailed knowledge about the ejector flow conditions, such as local pressures, velocity profile, turbulence intensity, and vapor quality. Currently, this knowledge is very limited due to the challenge of achieving accurate experimental measurements in the R744 ejector.

Future work should explore many aspects of ejector models. Special interest should be devoted to better the understanding of basic two-phase effects, ie. meta-stability, velocity slip, atomization of jets, two-phase turbulence, and multiphase thermodynamic properties. Additionally, exploration of the effects of various mixtures like oil-CO_2 in ejectors could uncover significant design improvements. More advanced modeling, such as two-fluid models, could enable better model accuracy while being less dependent on experimental tuning. Further development of thermodynamic and 1D models can be highly useful for optimization procedures and system modeling. Accounting for different non-equilibrium effects has been shown to improve accuracy in CFD models, and should be investigated further for thermodynamic and 1D models. 1D and thermodynamic models can also be supported by reduced-order models based on experiments and CFD modeling. Improving post-processing tools, such as exergy tubes [146], may allow for quantification of losses in ejectors and improve optimization tools. Artificial neural networks could be introduced to improve flow models by optimization of flow parameters [147], improving thermodynamic libraries [96], or predicting flow characteristics [148]. Improved design tools based on these models could provide an efficient way to explore and optimize ejector geometries at a limited computational cost. Modelling the near-wall flow is important for capturing important turbulent structures as well as flow separation. Such effects have been extensively discussed for single-phase ejectors [109,149–153,152,151], however further work should be conducted for multiphase R744 ejectors. Achieving high accuracy local experimental measurements should also be highly prioritized as it can enable validation and tuning of future advanced models. Further experimental work using PIV could give insights into the local velocity- and turbulence fields. Additionally, further research using tools such as Phase Doppler Interferometry or high-resolution Schlieren imaging could help in understanding bubble size distributions and temperatures. Adapting such techniques may aid in achieving local experimental validation data, which will greatly improve future R744 ejector models.

Declaration of Competing Interest

The authors declare that they have no known competing financial interests or personal relationships that could have appeared to influence the work reported in this paper.

Acknowledgement

The work is part of HighEFF - Centre for an Energy Efficient and Competitive Industry for the Future, an 8-year Research Centre under the FME-scheme (Centre for Environment-friendly Energy Research, 257632/E20). The authors gratefully acknowledge the financial support from the Research Council of Norway and user partners of HighEFF.

Appendix A. Tables

Compiled set of operating conditions and observed mass flow rate errors for motive and suction flows. Data from Giacomelli et al. [62], Palacz et al. [73] and Haida et al. [61]. P_M, T_M, P_S, T_S, and P_O refer to the motive pressure, motive temperature, suction pressure, suction temperature, and outlet pressure, respectively. *ER* is the entrainment ratio, $err_{m,s}$ MFR is the percentage of discrepancy between experiment and numerical results in mass flow rate, where the subscripts *s* and *m* correspond to suction and motive flow mass flow rate. The subscript *m*, *s*, and *o*, refer to motive, suction and outlet conditions, respectively. *err MFR* is the relative error in mass flow rate in the suction or motive flow.

P_M [MPa]	T_M [K]	P_S [MPa]	T_S [K]	P_D [MPa]	ER	err_m MFR [%]	err_s MFR [%]
Giacomelli et al. [62]							
9.53	310.5	3.79	283.2	4.14	0.46	−0.7	−12
9.52	310.9	2.929	286.8	4.02	0.2	0.6	−62
9.5	310.7	3.382	282.2	4.08	0.36	−0.1	−16.9
9.49	310.4	3.594	283.4	4.15	0.42	−0.4	−12.1
9.48	310.1	3.859	282.9	4.13	0.48	−1	−9.8
9.48	310.6	2.417	287	3.87	0.12	0.3	
9.47	310.7	2.643	287.1	39.95	0.14	1.3	
9.47	310.6	3.114	281.5	40.34	0.27	1.8	−35
9.63	304	3.357	279	3.96	0.21	−1.7	−15.2
9.53	303.6	3.465	281.4	3.96	0.23	−2	−17.3
9.53	303.6	3.598	281.7	3.97	0.25	−2	−13
9.51	303.4	3.777	285.5	3.98	0.28	−2.1	−13.4
9.49	303.6	3.55	282.6	3.95	0.25	−1.8	−15.8
Palacz et al. [73]							
5.393	279.53	3.357	279	3.423	0.3	23.4	
5.841	283.2	3.465	281.4	3.483	0.07	24.4	
4.782	282.99	3.598	281.7	3.189	0.08	43.3	
5.93	290.87	3.777	285.5	3.387	0.15	30.3	
5.843	290.89	3.55	282.6	3.101	0.33	31	
6.179	293.47	2.993	276.78	3.387	0.26	22.4	
6.479	295.29	2.801	275.68	3.377	0.22	20.8	
6.662	295.58	2.787	274.98	3.288	0.31	15.6	
6.651	295.61	2.821	275.41	3.485	0.19	15.9	
7.51	296.9	3.201	279.18	3.734	0.28	27.5	
8.062	299.45	3.158	278.54	3.848	0.28	7.2	
8.786	301.6	3.155	278.71	3.829	0.33	3.4	
7.845	301.76	3.172	278.91	3.828	0.36	4.1	
7.579	301.27	2.817	275.78	3.68	0.28	2.2	
9.191	304.18	3.141	278.48	3.824	0.35	0.3	
7.656	301.54	2.733	274.06	3.287	0.42	1.5	
8.604	304.53	2.732	273.66	3.29	0.42	−0.3	
9.446	308.48	2.721	275.8	3.285	0.42	−2.9	
Palacz et al. [73]							
5.393	279.53	2.73	278.9	3.423	0.3	20.4	
5.841	283.2	2.782	277.76	3.483	0.07	21.7	
4.782	282.99	2.793	281.69	3.189	0.08	42	
5.93	290.87	2.849	278.62	3.387	0.15	25.7	
5.843	290.89	2.845	275.18	3.101	0.33	26.6	
6.179	293.47	2.993	276.78	3.387	0.26	18.9	
6.479	295.29	2.801	275.68	3.377	0.22	15.3	
6.662	295.58	2.787	274.98	3.288	0.31	11.6	
6.651	295.61	2.821	275.41	3.485	0.19	11.9	
7.51	296.9	3.201	279.18	3.734	0.28	21.7	
8.062	299.45	3.158	278.54	3.848	0.28	−0.7	
8.786	301.6	3.155	278.71	3.829	0.33	−1.3	
7.845	301.76	3.172	278.91	3.828	0.36	−3.2	
7.579	301.27	2.817	275.78	3.68	0.28	−0.8	
9.191	304.18	3.141	278.48	3.824	0.35	−3.9	
7.656	301.54	2.733	274.06	3.287	0.42	−3.9	
8.604	304.53	2.732	273.66	3.29	0.42	−4.8	
9.446	308.48	2.721	275.8	3.285	0.42	−8	
Haida et al. [61]							
9.435	309.12	3.069	277.61	3.586		−3	14
8.535	305.57	3.142	278.45	3.824		−1	20
8.069	299.97	3.097	278.15	3.439		4	16
7.656	301.49	2.733	274.01	3.287		2	22
9.039	307.67	3.122	278.45	3.727		−2	17
8.294	301.48	3.152	279.68	3.732		3	26
8.098	299.97	3.115	278.15	3.439		7	20
7.845	301.71	3.172	278.86	3.828		4	26
6.757	293.33	2.836	277.44	3.677		13	16
6.662	295.53	2.787	274.93	3.288		4	42
6.651	295.56	2.821	275.36	3.485		4	17
6.179	293.42	2.993	276.73	3.387		5	20
5.927	281.91	2.914	275.72	3.483		15	11
5.841	283.15	2.782	277.71	3.483		21	12
5.667	283.35	2.779	276.13	3.487		21	10
5.571	285.79	3.246	279.72	3.601		24	74
5.393	279.48	2.73	278.85	3.423		29	4
5.848	283.14	2.791	266.59	3.68		20	100
5.802	282.49	3.173	279.11	3.675		19	87
5.789	288.59	2.918	272.45	3.679		26	100
5.771	282.94	3.17	279.21	3.717		20	90
5.308	284.49	2.786	270.83	3.485		29	100

References

[1] European Commision, Regulation (EU) No 517/2014 of the European Parliament and of the Council of 16th April 2014 on fluorinated greenhouse gases and repealing Regulation (EC) No 842/2006, 2014.

[2] M.-H. Kim, J. Pettersen, C.W. Bullard, Fundamental process and system design issues in CO2 vapor compression systems, Progress in Energy and Combustion Science 30 (2004) 119–174, https://doi.org/10.1016/J.PECS.2003.09.002 URL: https://www.sciencedirect.com/science/article/pii/S0360128503000765.

[3] P. Gullo, A. Hafner, K. Banasiak, Transcritical R744 refrigeration systems for supermarket applications: Current status and future perspectives, International Journal of Refrigeration 93 (2018) 269–310, https://doi.org/10.1016/j.ijrefrig.2018.07.001 URL: https://www.sciencedirect.com/science/article/pii/S0140700718302287?via%3Dihub.

[4] M. Karampour, S. Sawalha, Energy efficiency evaluation of integrated CO2 transcritical system in supermarkets: A field measurements and modelling analysis, International Journal of Refrigeration 82 (2017) 470–486, https://doi.org/10.1016/J.IJREFRIG.2017.06.002 URL: https://www.sciencedirect.com/science/article/pii/S0140700717302360.

[5] R. Rony, H. Yang, S. Krishnan, J. Song, R.U. Rony, H. Yang, S. Krishnan, J. Song, Recent advances in transcritical CO2 (R744) heat pump system: a review, Energies 12 (2019) 457, https://doi.org/10.3390/en12030457 URL: http://www.mdpi.com/1996-1073/12/3/457.

[6] B.T. Austin, K. Sumathy, Transcritical carbon dioxide heat pump systems: A review, Renewable and Sustainable Energy Reviews 15 (2011) 4013–4029, https://doi.org/10.1016/J.RSER.2011.07.021 URL: https://www.sciencedirect.com/science/article/pii/S1364032111002607?via%3Dihub.

[7] Z. Jin, T.M. Eikevik, P. Nekså, A. Hafner, Investigation on CO2 hybrid ground-coupled heat pumping system under warm climate, International Journal of Refrigeration 62 (2016) 145–152, https://doi.org/10.1016/J.IJREFRIG.2015.10.005 Z. Jin, T.M. Eikevik, P. Nekså, A. Hafner, Investigation on CO2 hybrid ground-coupled heat pumping system under warm climate, International Journal of Refrigeration 62 (2016) 145–152. URL: https://www.sciencedirect.com/science/article/pii/S0140700715002996. 10.1016/J.IJREFRIG.2015.10.005..

[8] J. Yang, B. Yu, J. Chen, Improved genetic algorithm-based prediction of a CO2 micro-channel gas-cooler against experimental data in automobile air conditioning system, International Journal of Refrigeration (2019), https://doi.org/10.1016/J.IJREFRIG.2019.05.017 URL: https://www.sciencedirect.com/science/article/pii/S0140700719302130.

[9] C. Luger, R. Rieberer, Multi-objective design optimization of a rail HVAC CO2 cycle, International Journal of Refrigeration 92 (2018) 133–142, https://doi.org/10.1016/J.IJREFRIG.2018.05.033 URL: https://www.sciencedirect.com/science/article/pii/S0140700718301968.

[10] H.G. Ozcana, H. Gunerhanb, A. Hepbaslia, H. Yaldirakc, Environmental impact and performance comparison of refrigerants (R744 and R134a) in a mobile air conditioning system used for cooling buses, International Journal of Engineering and Technology 7 (2014) 233–241, https://doi.org/10.7763/ijet.2015.v7.798.

[11] B.Y. Kimura de Carvalho, C. Melo, R.H. Pereira, An experimental study on the use of variable capacity two-stage compressors in transcritical carbon dioxide light commercial refrigerating systems, International Journal of Refrigeration (2019), https://doi.org/10.1016/J.IJREFRIG.2019.03.026 URL: https://www.sciencedirect.com/science/article/pii/S0140700719301252.

[12] R. Mastrullo, A.W. Mauro, A. Perrone, A model and simulations to investigate the effects of compressor and fans speeds on the performance of CO2 light commercial refrigerators, Applied Thermal Engineering 84 (2015) 158–169, https://doi.org/10.1016/J.APPLTHERMALENG.2015.03.035 URL: https://www.sciencedirect.com/science/article/pii/S1359431115002586.

[13] R.A. Sian, C.-C. Wang, Comparative study for CO2 and R-134a heat pump tumble dryer – A rational approach, International Journal of Refrigeration (2019), https://doi.org/10.1016/J.IJREFRIG.2019.05.027 URL: https://www.sciencedirect.com/science/article/pii/S0140700719302269.

[14] F. Mancini, S. Minetto, E. Fornasieri, Thermodynamic analysis and experimental investigation of a CO2 household heat pump dryer, International Journal of Refrigeration 34 (2011) 851–858, https://doi.org/10.1016/J.IJREFRIG.2010.12.012 URL: https://www.sciencedirect.com/science/article/pii/S0140700710002872.

[15] N. Purohit, V. Sharma, B. Fricke, D.K. Gupta, M.S. Dasgupta, Parametric analysis and optimization of CO2 trans-critical cycle for chiller application in a warm climate, Applied Thermal Engineering 150 (2019) 706–719, https://doi.org/10.1016/J.APPLTHERMALENG.2019.01.023 URL: https://www.sciencedirect.com/science/article/pii/S1359431118349081.

[16] P. Gullo, A. Hafner, K. Banasiak, S. Minetto, E. Kriezi, P. Gullo, A. Hafner, K. Banasiak, S. Minetto, E.E. Kriezi, Multi-ejector concept: a comprehensive review on its latest technological developments, Energies 12 (2019) 406, https://doi.org/10.3390/en12030406 URL: http://www.mdpi.com/1996-1073/12/3/406.

[17] S. Elbel, N. Lawrence, Review of recent developments in advanced ejector technology, International Journal of Refrigeration 62 (2016) 1–18, https://doi.org/10.1016/j.ijrefrig.2015.10.031 URL: https://www.sciencedirect.com/science/article/pii/S0140700715003266.

[18] S. Elbel, P. Hrnjak, Experimental validation of a prototype ejector designed to reduce throttling losses encountered in transcritical R744 system operation, International Journal of Refrigeration 31 (2008) 411–422, https://doi.org/10.1016/j.ijrefrig.2007.07.013 URL: https://www.sciencedirect.com/science/article/pii/S0140700707001508.

[19] Y. Liao, D. Lucas, Computational modelling of flash boiling flows: A literature survey, International Journal of Heat and Mass Transfer 111 (2017) 246–265, https://doi.org/10.1016/j.ijheatmasstransfer.2017.03.121 URL: https://www.sciencedirect.com/science/article/pii/S001793101730460X.

[20] K. Banasiak, A. Hafner, E.E. Kriezi, K.B. Madsen, M. Birkelund, K. Fredslund, R. Olsson, Development and performance mapping of a multi-ejector expansion work recovery pack for R744 vapour compression units, International Journal of Refrigeration 57 (2015) 265–276, https://doi.org/10.1016/J.IJREFRIG.2015.05.016 URL: https://www.sciencedirect.com/science/article/pii/S0140700715001553.

[21] P. Gullo, K.M. Tsamos, A. Hafner, K. Banasiak, Y.T. Ge, S.A. Tassou, Crossing CO2 equator with the aid of multi-ejector concept: A comprehensive energy and environmental comparative study, Energy 164 (2018) 236–263, https://doi.org/10.1016/J.ENERGY.2018.08.205 URL: https://www.sciencedirect.com/science/article/pii/S0360544218317419.

[22] S. Taslimitaleghani, M. Sorin, S. Poncet, Energy and exergy efficiencies of different configurations of the ejector-based CO2 refrigeration systems, International Journal of Energy Production and Management 3 (2018) 22–33, https://doi.org/10.2495/EQ-V3-N1-22-33.

[23] S. Taslimi Taleghani, M. Sorin, S. Poncet, H. Nesreddine, Performance investigation of a two-phase transcritical CO2 ejector heat pump system, Energy Conversion and Management 185 (2019) 442–454, https://doi.org/10.1016/J.ENCONMAN.2019.02.004 URL: https://www.sciencedirect.com/science/article/pii/S0196890419301578.

[24] J. Zhu, S. Elbel, Application of vortex control to an automotive transcritical R744 ejector cycle, SAE Technical Paper Series 1 (2018) 1–6, https://doi.org/10.4271/2018-01-0060.

[25] J. Bodys, A. Hafner, K. Banasiak, J. Smolka, Y. Ladam, Design and simulations of refrigerated sea water chillers with CO2 ejector pumps for marine applications in hot climates, Energy 161 (2018) 90–103, https://doi.org/10.1016/J.ENERGY.2018.07.126 URL: https://www.sciencedirect.com/science/article/pii/S0360544218314245.

[26] Z. Jin, A. Hafner, T.M. Eikevik, P. Nekså, Preliminary study on CO2 transcritical ejector enhanced compressor refrigeration system for independent space cooling and dehumidification, International Journal of Refrigeration 100 (2019) 13–20, https://doi.org/10.1016/J.IJREFRIG.2019.01.027 URL: https://www.sciencedirect.com/science/article/pii/S014070071930043X.

[27] M. Nakagawa, A. Marasigan, T. Matsukawa, A. Kurashina, Experimental investigation on the effect of mixing length on the performance of two-phase ejector for CO2 refrigeration cycle with and without heat exchanger, International Journal of Refrigeration 34 (2011) 1604–1613, https://doi.org/10.1016/J.IJREFRIG.2010.07.021 URL: https://www.sciencedirect.com/science/article/pii/S0140700710001672.

[28] K. Banasiak, A. Hafner, T. Andresen, Experimental and numerical investigation of the influence of the two-phase ejector geometry on the performance of the R744 heat pump, International Journal of Refrigeration 35 (2012) 1617–1625, https://doi.org/10.1016/J.IJREFRIG.2012.04.012 URL: https://www.sciencedirect.com/science/article/pii/S014070071200093X.

[29] J.S. Lee, M.S. Kim, M.S. Kim, Experimental study on the improvement of CO2 air conditioning system performance using an ejector, International Journal of Refrigeration 34 (2011) 1614–1625, https://doi.org/10.1016/J.IJREFRIG.2010.07.025 URL: https://www.sciencedirect.com/science/article/pii/S0140700710001714.

[30] G.-M. Chen, L.-X. Liang, L.-M. Tang, X.-X. Xu, Z.-J. Zhu, Q. Chen, Experimental investigation of an adjustable ejector for CO2 heat pump water heaters, Journal of Zhejiang University - Science A 10 (2009) 1678–1682, https://doi.org/10.1631/jzus.A0920116 URL: http://link.springer.com/10.1631/jzus.A0920116.

[31] F. Liu, E.A. Groll, D. Li, Investigation on performance of variable geometry ejectors for CO2 refrigeration cycles, Energy 45 (2012) 829–839, https://doi.org/10.1016/j.energy.2012.07.008 URL: https://www.sciencedirect.com/science/article/pii/S0360544212005385.

[32] A. Kornhauser, The use of an ejector in a geothermal flash system, in: Proceedings of the 25th Intersociety Energy Conversion Engineering Conference, vol. 5, 2005, pp. 79–84. URL: http://ieeexplore.ieee.org/document/747930/ doiI: 10.1109/iecec.1990.747930.

[33] E. Sher, T. Bar-Kohany, A. Rashkovan, Flash-boiling atomization, Progress in Energy and Combustion Science 34 (2008) 417–439, https://doi.org/10.1016/J.PECS.2007.05.001 URL: https://www.sciencedirect.com/science/article/pii/S0360128507000500.

[34] G.J. Smallwood, O.L. Gulder, Views on the structure of transient diesel sprays, Atomization and Sprays 10 (2000) 355–386, https://doi.org/10.1615/AtomizSpr.v10.i3-5.70 URL: http://www.dl.begellhouse.com/journals/6a7c7e10642258cc,1a3008e01332192c,782209561899eba7.html.

[35] J. Chen, S. Jarall, H. Havtun, B. Palm, A review on versatile ejector applications in refrigeration systems, Renewable and Sustainable Energy Reviews 49 (2015) 67–90, https://doi.org/10.1016/J.RSER.2015.04.073 URL: https://www.sciencedirect.com/science/article/pii/S1364032115003433.

[36] K. Sumeru, H. Nasution, F.N. Ani, A review on two-phase ejector as an expansion device in vapor compression refrigeration cycle, Renewable and Sustainable Energy Reviews 16 (2012) 4927–4937. URL: https://www.sciencedirect.com/science/article/pii/S1364032112003565. DOI: 10.1016/j.rser.2012.04.058.

[37] J. Sarkar, Ejector enhanced vapor compression refrigeration and heat pump systems – A review, Renewable and Sustainable Energy Reviews 16 (2012) 6647–6659, https://doi.org/10.1016/j.rser.2012.08.007.

[38] G. Besagni, R. Mereu, F. Inzoli, Ejector refrigeration: A comprehensive review,

Renewable and Sustainable Energy Reviews 53 (2016) 373–407. URL: https://www.sciencedirect.com/science/article/pii/S1364032115009223. DOI: 10.1016/J.RSER.2015.08.059.
[39] B.M. Tashtoush, M.A. Al-Nimr, M.A. Khasawneh, A comprehensive review of ejector design, performance, and applications, Applied Energy 240 (2019) 138–172. URL: https://www.sciencedirect.com/science/article/pii/S0306261919301588. DOI: 10.1016/J.APENERGY.2019.01.185.
[40] Z. Aidoun, K. Ameur, M. Falsafioon, M. Badache, Z. Aidoun, K. Ameur, M. Falsafioon, M. Badache, Current advances in ejector modeling, experimentation and applications for refrigeration and heat pumps. part 2: two-phase ejectors, Inventions 4 (2019) 16. URL: https://www.mdpi.com/2411-5134/4/1/16. DOI: 10.3390/inventions4010016.
[41] S. Elbel, Historical and present developments of ejector refrigeration systems with emphasis on transcritical carbon dioxide air-conditioning, International Journal of Refrigeration 34 (2011) 1545–1561. URL: https://www.sciencedirect.com/science/article/pii/S0140700710002720. DOI: 10.1016/j.ijrefrig.2010.11.011.
[42] G. Besagni, Ejectors on the cutting edge: The past, the present and the perspective, Energy (2019) 998–1003. URL: https://www.sciencedirect.com/science/article/pii/S0360544218325945. DOI: 10.1016/j.energy.2018.12.214.
[43] A.J. Nowak, M. Palacz, J. Smolka, K. Banasiak, Z. Bulinski, A. Fic, A. Hafner, CFD simulations of transport phenomena during transcritical flow of real fluid (CO2) within ejector, International Journal of Numerical Methods for Heat and Fluid Flow 26 (2016) 805–817, https://doi.org/10.1108/HFF-09-2015-0395 URL: http://www.emeraldinsight.com/doi/10.1108/HFF-09-2015-0395.
[44] X. Jiang, G.A. Siamas, K. Jagus, T.G. Karayiannis, Physical modelling and advanced simulations of gas-liquid two-phase jet flows in atomization and sprays, Progress in Energy and Combustion Science 36 (2010) 131–167. URL: https://www.sciencedirect.com/science/article/pii/S0360128509000458. DOI: 10.1016/j.pecs.2009.09.002.
[45] J. Smolka, Z. Bulinski, A. Fic, A.J. Nowak, K. Banasiak, A. Hafner, A computational model of a transcritical R744 ejector based on a homogeneous real fluid approach, Applied Mathematical Modelling 37 (2013) 1208–1224. URL: https://www.sciencedirect.com/science/article/pii/S0307904X12002077. DOI: 10.1016/j.apm.2012.03.044.
[46] E.W. Lemmon, I.H. Bell, M.L. Huber, M.O. McLinden, NIST: standard reference database 23: reference fluid thermodynamic and transport properties-REFPROP, Version 9.0, National Institute of Standards and Technology (2018) URL: https://www.nist.gov/srd/refprop. https://doi.org/10.18434/T4JS3C.
[47] Ø. Wilhelmsen, A. Aasen, G. Skaugen, P. Aursand, A. Austegard, E. Aursand, M.A. Gjennestad, H. Lund, G. Linga, M. Hammer, Thermodynamic modeling with equations of state: present challenges with established methods, Industrial & Engineering Chemistry Research 56 (2017) 3503–3515, https://doi.org/10.1021/acs.iecr.7b00317 URL: https://pubs.acs.org/doi/10.1021/acs.iecr.7b00317.
[48] P. Aursand, M.A. Gjennestad, E. Aursand, M. Hammer, Ø. Wilhelmsen, The spinodal of single- and multi-component fluids and its role in the development of modern equations of state, Fluid Phase Equilibria 436 (2017) 98–112. URL: https://www.sciencedirect.com/science/article/pii/S0378381216306227. DOI: 10.1016/J.FLUID.2016.12.018.
[49] Y. Bartosiewicz, J.-M. Seynhaeve, Delayed equilibrium model (dem) of flashing choked flows relevant to loca, Multiphase Science and Technology 25 (2014) 117–131. URL: http://www.dl.begellhouse.com/journals/5af8c23d50e0a883,576264641be74a20,2fa83d084a42b177.html. DOI: 10.1615/multscientechn.v25.i2-4.50.
[50] M. Nakagawa, M.S. Berana, A. Kishine, Supersonic two-phase flow of CO2 through converging-diverging nozzles for the ejector refrigeration cycle, International Journal of Refrigeration 32 (2009) 1195–1202. URL: https://www.sciencedirect.com/science/article/pii/S0140700709000164. DOI: 10.1016/j.ijrefrig.2009.01.015.
[51] M.S. Berana, M. Nakagawa, A. Harada, Shock waves in supersonic two-phase flow of CO2 in converging-diverging nozzles, HVAC and R Research 15 (2009) 1081–1098. URL: https://www.tandfonline.com/action/journalInformation?journalCode=uhvc21. DOI: 10.1080/10789669.2009.10390880.
[52] Y. Li, J. Deng, L. Ma, Y. Zhang, Visualization of two-phase flow in primary nozzle of a transcritical CO2 ejector, Energy Conversion and Management 171 (2018) 729–741. URL: https://www.sciencedirect.com/science/article/pii/S0196890418306319. DOI: 10.1016/j.enconman.2018.06.022.
[53] G. Polanco, A.E. Holdø G. Munday, General review of flashing jet studies, Journal of Hazardous Materials 173 (2010) 2–18. URL: https://www.sciencedirect.com/science/article/pii/S0304389409013090. DOI: 10.1016/j.jhazmat.2009.08.138.
[54] S. Taslimi Taleghani, M. Sorin, S. Poncet, Modeling of two-phase transcritical CO2 ejectors for on-design and off-design conditions, International Journal of Refrigeration 87 (2018) 91–105. URL: https://www.sciencedirect.com/science/article/pii/S0140700717304279. DOI: 10.1016/j.ijrefrig.2017.10.025.
[55] M. Yazdani, A.A. Alahyari, T.D. Radcliff, Numerical modeling of two-phase supersonic ejectors for work-recovery applications, International Journal of Heat and Mass Transfer 55 (2012) 5744–5753. URL: https://www.sciencedirect.com/science/article/pii/S0017931012003924. DOI: 10.1016/j.ijheatmasstransfer.2012.05.071.
[56] M. Palacz, J. Smolka, A. Fic, Z. Bulinski, A.J. Nowak, K. Banasiak, A. Hafner, Application range of the HEM approach for CO2 expansion inside two-phase ejectors for supermarket refrigeration systems, International Journal of Refrigeration 59 (2015) 251–258. URL: https://www.sciencedirect.com/science/article/pii/S0140700715002030. DOI: 10.1016/j.ijrefrig.2015.07.006.
[57] C. Lucas, H. Rusche, A. Schroeder, J. Koehler, Numerical investigation of a two-phase CO2 ejector, International Journal of Refrigeration 43 (2014) 154–166. URL: https://www.sciencedirect.com/science/article/pii/S0140700714000504. DOI: 10.1016/j.ijrefrig.2014.03.003.
[58] Z. Bulinski, J. Smolka, A. Fic, K. Banasiak, A.J. Nowak, A comparison of heterogenous and homogenous models of two-phase transonic compressible CO2 flow through a heat pump ejector, IOP Conference Series: Materials Science and Engineering 10 (2014) 012019, , https://doi.org/10.1088/1757-899X/10/1/012019 URL: http://stacks.iop.org/1757-899X/10/i=1/a=012019?key=crossref.38d6e7a942f3ab537098b89531e492a4.
[59] ANSYS, ANSYS fluent theory guide. Release 19.0., Canonsburg, 2018.
[60] M. Palacz, J. Smolka, W. Kus, A. Fic, Z. Bulinski, A.J. Nowak, K. Banasiak, A. Hafner, CFD-based shape optimisation of a CO2 two-phase ejector mixing section, Applied Thermal Engineering 95 (2016) 62–69. URL: https://www.sciencedirect.com/science/article/pii/S1359431115012478. DOI: 10.1016/j.applthermaleng.2015.11.012.
[61] M. Haida, J. Smolka, A. Hafner, M. Palacz, K. Banasiak, A.J. Nowak, Modified homogeneous relaxation model for the R744 trans-critical flow in a two-phase ejector, International Journal of Refrigeration 85 (2018) 314–333. URL: https://www.sciencedirect.com/science/article/pii/S0140700717303948. DOI: 10.1016/j.ijrefrig.2017.10.010.
[62] F. Giacomelli, F. Mazzelli, K. Banasiak, A. Hafner, A. Milazzo, Experimental and computational analysis of a R744 flashing ejector, International Journal of Refrigeration 107 (2019) 326–343, https://doi.org/10.1016/j.ijrefrig.2019.08.007.
[63] M. Colarossi, N. Trask, D.P. Schmidt, M.J. Bergander, Multidimensional modeling of condensing two-phase ejector flow, International Journal of Refrigeration 35 (2012) 290–299. URL: https://www.sciencedirect.com/science/article/pii/S0140700711002635?via%3Dihub. DOI: 10.1016/j.ijrefrig.2011.08.013.
[64] H.G. Weller, G. Tabor, H. Jasak, C. Fureby, A tensorial approach to computational continuum mechanics using object-oriented techniques, Computers in Physics 12 (1998) 620, https://doi.org/10.1063/1.168744 URL: http://scitation.aip.org/content/aip/journal/cip/12/6/10.1063/1.168744.
[65] C. Lucas, J. Koehler, A. Schroeder, C. Tischendorf, Experimentally validated CO2 ejector operation characteristic used in a numerical investigation of ejector cycle, International Journal of Refrigeration 36 (2013) 881–891. URL: https://www.sciencedirect.com/science/article/pii/S0140700712002952?via%3Dihub. DOI: 10.1016/j.ijrefrig.2012.10.035.
[66] F. Giacomelli, F. Mazzelli, A. Milazzo, Evaporation in supersonic CO2 ejectors: analysis of theoretical and numerical models, 9th International Conference on Multiphase Flow, 2016 URL: https://www.researchgate.net/publication/303689693.
[67] F. Giacomelli, F. Mazzelli, A. Milazzo, A novel CFD approach for the computation of R744 flashing nozzles in compressible and metastable conditions, Energy 162 (2018) 1092–1105. URL: https://www.sciencedirect.com/science/article/pii/S0360544218315706. DOI: 10.1016/j.energy.2018.08.050.
[68] Y. Fang, S. Poncet, H. Nesreddine, Y. Bartosiewicz, An open-source density-based solver for two-phase CO2 compressible flows: verification and validation, International Journal of Refrigeration (2019). URL: https://www.sciencedirect.com/science/article/pii/S0140700719302129#bib0034. DOI: 10.1016/j.ijrefrig.2019.05.016.
[69] Y. Fang, M. De Lorenzo, P. Lafon, S. Poncet, Y. Bartosiewicz, An accurate and efficient look-up table equation of state for two-phase compressible flow simulations of carbon dioxide, Industrial and Engineering Chemistry Research 57 (2018) 7676–7691, https://doi.org/10.1021/acs.iecr.8b00507 URL: https://pubs.acs.org/sharingguidelines.
[70] W. Angielczyk, Y. Bartosiewicz, D. Butrymowicz, J.-M. Seynhaeve, 1-D modeling of supersonic carbon dioxide two-phase flow through ejector motive nozzle, International Refrigeration and Air Conditioning Conference (2010) 1–8 URL: http://docs.lib.purdue.edu/iracc/1102.
[71] Z. Bilicki, J. Kestin, Physical aspects of the relaxation model in two-phase flow, Proceedings of the Royal Society A: Mathematical, Physical and Engineering Sciences 428 (2006) 379–397. URL: http://rspa.royalsocietypublishing.org/cgi/doi/10.1098/rspa.1990.0040. DOI: 10.1098/rspa.1990.0040.
[72] P. Downar-Zapolski, Z. Bilicki, L. Bolle, J. Franco, The non-equilibrium relaxation model for one-dimensional flashing liquid flow, International Journal of Multiphase Flow 22 (1996) 473–483. URL: https://www.sciencedirect.com/science/article/pii/030193229500078X. DOI: 10.1016/0301-9322(95)00078-X.
[73] M. Palacz, M. Haida, J. Smolka, A.J. Nowak, K. Banasiak, A. Hafner, HEM and HRM accuracy comparison for the simulation of CO2 expansion in two-phase ejectors for supermarket refrigeration systems, Applied Thermal Engineering 115 (2017) 160–169. URL: https://www.sciencedirect.com/science/article/pii/S135943111634399X. DOI: 10.1016/j.applthermaleng.2016.12.122.
[74] A. Colombo, P. Conti, M. Orlandi, F. Visconti, P. Mitra, D.P. Schmidt, S. Applicate, Cfd simulations of a two-phase ejector for transcritical CO2 cycles applied to supermarket refrigeration systems, 13th IIR Gustav Lorentzen Conference on Natural Refrigerants (2018), https://doi.org/10.18462/iir.gl.2018.1173.
[75] M. Palacz, J. Smolka, A.J. Nowak, K. Banasiak, A. Hafner, Shape optimisation of a two-phase ejector for CO2 refrigeration systems, International Journal of Refrigeration 74 (2017) 210–221. URL: https://www.sciencedirect.com/science/article/pii/S0140700716303425. DOI: 10.1016/j.ijrefrig.2016.10.013.
[76] A.K. Singhal, M.M. Athavale, H. Li, Y. Jiang, Mathematical basis and validation of the full cavitation model, Journal of Fluids Engineering 124 (2002) 617, https://doi.org/10.1115/1.1486223 URL: http://asmedl.org/.
[77] R.W. Schrage, A Theoretical Study of Interphase Mass Transfer, Columbia University Press, New York, 1953.
[78] V.P. Carey, Liquid-Vapor Phase-Change Phenomena: An Introduction to the Thermophysics of Vaporization and Condensation Processes in Heat Transfer

Equipment, Taylor & Francis group, LLC, 2008 URL: https://books.google.no/books?id=XF1ZDwAAQBAJ&pg=PT3&lpg=PT3&dq=V.P.+Carey,+Liquid-Vapor+Phase-change+Phenomena,+second+ed.,+Taylor+and+Francis,+New+York,+2007.&source=bl&ots=Vkef55nKbf&sig=ACfU3U0ctbuEPmmBKFcUV8C8oCROOlYzZw&hl=no&sa=X&ved=2ahUKEwjAkPKE0b.

[79] Q. Dang Le, R. Mereu, G. Besagni, V. Dossena, F. Inzoli, Computational Fluid Dynamics Modeling of Flashing Flow in Convergent-Divergent Nozzle, Journal of Fluids Engineering 140 (2018) 101102, , https://doi.org/10.1115/1.4039908 URL: http://fluidsengineering.asmedigitalcollection.asme.org/article.aspx?doi=10.1115/1.4039908.

[80] M.S. Lee, H. Lee, Y. Hwang, R. Radermacher, H.M. Jeong, Optimization of two-phase R600a ejector geometries using a non-equilibrium CFD model, Applied Thermal Engineering 109 (2016) 272–282. URL: https://www.sciencedirect.com/science/article/pii/S1359431116314375?via%3Dihub. DOI: 10.1016/j.applthermaleng.2016.08.078.

[81] P. Zheng, B. Li, J. Qin, CFD simulation of two-phase ejector performance influenced by different operation conditions, Energy 155 (2018) 1129–1145. URL: https://www.sciencedirect.com/science/article/pii/S036054421830673X. DOI: 10.1016/J.ENERGY.2018.04.066.

[82] W. Angielczyk, J.M. Seynhaeve, J. Gagan, Y. Bartosiewicz, D. Butrymowicz, Prediction of critical mass rate of flashing carbon dioxide flow in convergent-divergent nozzle, Chemical Engineering and Processing – Process Intensification 143 (2019) 107599. URL: https://www.sciencedirect.com/science/article/pii/S0255270119302004. DOI: 10.1016/J.CEP.2019.107599.

[83] K. Banasiak, A. Hafner, 1D Computational model of a two-phase R744 ejector for expansion work recovery, International Journal of Thermal Sciences 50 (2011) 2235–2247. URL: https://www.sciencedirect.com/science/article/pii/S1290072911001876. DOI: 10.1016/j.ijthermalsci.2011.06.007.

[84] K. Banasiak, A. Hafner, Mathematical modelling of supersonic two-phase R744 flows through converging–diverging nozzles: The effects of phase transition models, Applied Thermal Engineering 51 (2013) 635–643. URL: https://www.sciencedirect.com/science/article/pii/S1359431112006618. DOI: 10.1016/J.APPLTHERMALENG.2012.10.005.

[85] C. Lackme, Incompleteness of the flashing of a supersaturated liquid and sonic ejection of the produced phases, International Journal of Multiphase Flow 5 (1979) 131–141. URL: https://www.sciencedirect.com/science/article/pii/0301932279900417. DOI: 10.1016/0301-9322(79)90041-7.

[86] M. Baer, J. Nunziato, A two-phase mixture theory for the deflagration-to-detonation transition (ddt) in reactive granular materials, International Journal of Multiphase Flow 12 (1986) 861–889. URL: https://www.sciencedirect.com/science/article/pii/0301932286900339. DOI: 10.1016/0301-9322(86)90033-9.

[87] M. de Lorenzo, Modelling and numerical simulation of metastable two-phase flows, Ph.D. thesis, Université Paris-Saclay (2018) URL: https://pastel.archives-ouvertes.fr/tel-01889103/.

[88] M. Labois, Modélisation des déséquilibres mécaniques pour les écoulements diphasiques: approches par relaxation et par modèle réduit, Ph.D. thesis, Université de Provence – Aix-Marseille I (2008) URL: https://tel.archives-ouvertes.fr/tel-00338818/.

[89] M. De Lorenzo, P. Lafon, J.M. Seynhaeve, Y. Bartosiewicz, Benchmark of Delayed Equilibrium Model (DEM) and classic two-phase critical flow models against experimental data, International Journal of Multiphase Flow 92 (2017) 112–130. URL: https://www.sciencedirect.com/science/article/pii/S0301932216304475. DOI: 10.1016/j.ijmultiphaseflow.2017.03.004.

[90] H. Lund, A hierarchy of relaxation models for two-phase flow, SIAM Journal on Applied Mathematics 72 (2012) 1713–1741, https://doi.org/10.1137/12086368X URL: http://epubs.siam.org/doi/10.1137/12086368X.

[91] M. Ishii, T. Hibiki, Thermo-Fluid Dynamics of Two-Phase Flow, Springer, US, Boston, MA, 2006, https://doi.org/10.1007/978-0-387-29187-1_9 URL: http://link.springer.com/10.1007/978-0-387-29187-1_9.

[92] S.T. Munkejord, M. Hammer, S.W. Løvseth, CO2 transport: Data and models – A review, Applied Energy 169 (2016) 499–523. URL: https://www.sciencedirect.com/science/article/pii/S0306261916300885#f0005. DOI: 10.1016/j.apenergy.2016.01.100.

[93] R. Span, W. Wagner, A new equation of state for carbon dioxide covering the fluid region from the triple-point temperature to 1100 K at pressures up to 800 MPa, Journal of Physical and Chemical Reference Data 25 (1996) 1509–1596, https://doi.org/10.1063/1.555991 URL: http://aip.scitation.org/doi/10.1063/1.555991.

[94] A. Fenghour, W.A. Wakeham, V. Vesovic, The viscosity of carbon dioxide, Journal of Physical and Chemical Reference Data 27 (1998) 31–44, https://doi.org/10.1063/1.556013 URL: http://aip.scitation.org/doi/10.1063/1.556013.

[95] A. Laesecke, C.D. Muzny, Reference correlation for the viscosity of carbon dioxide, Journal of Physical and Chemical Reference Data 46 (2017), https://doi.org/10.1063/1.4977429.

[96] M.N. Amar, M.A. Ghriga, H. Ouaer, M. El Amine Ben, B.T. Seghier, P.Ø. Pham, Andersen: Modeling viscosity of CO2 at high temperature and pressure conditions, Journal of Natural Gas Science and Engineering 77 (2020) 103271, , https://doi.org/10.1016/j.jngse.2020.103271.

[97] M.M. Awad, Y.S. Muzychka, Effective property models for homogeneous two-phase flows, Experimental Thermal and Fluid Science 33 (2008) 106–113. URL: https://www.sciencedirect.com/science/article/pii/S0894177708001027. DOI: 10.1016/j.expthermflusci.2008.07.006.

[98] F. Mazzelli, F. Giacomelli, A. Milazzo, CFD modeling of condensing steam ejectors: Comparison with an experimental test-case, International Journal of Thermal Sciences 127 (2018) 7–18. URL: https://www.sciencedirect.com/science/article/pii/S1290072917309638. DOI: 10.1016/J.IJTHERMALSCI.2018.01.012.

[99] C.E. Brennen, Fundamentals of multiphase flow, Cambridge University Press, Cambridge, 2005. URL: https://books.google.no/books/about/Fundamentals_of_Multiphase_Flow.html?id=F7hEfx2GUPYC&redir_esc=y. DOI: 10.1017/CBO9780511807169.

[100] M. Nakagawa, A. Harada, M.S. Berana, Analysis of expansion waves appearing in the outlets of two-phase flow nozzles, HVAC and R Research 15 (2009) 1065–1079. URL: https://www.tandfonline.com/action/journalInformation?journalCode=uhvc21. DOI: 10.1080/10789669.2009.10390879.

[101] B. Magolan, N. Lubchenko, E. Baglietto, A quantitative and generalized assessment of bubble-induced turbulence models for gas-liquid systems, Chemical Engineering Science: X 2 (2019) 100009. URL: https://www.sciencedirect.com/science/article/pii/S2590140019300164. DOI: 10.1016/J.CESX.2019.100009.

[102] M. Manninen, V. Taivassalo, S. Kallio, On the Mixture Model for Multiphase Flow, VTT Publications (1996).

[103] L. Schiller, A. Naumann, A drag coefficient correlation, Zeitschrift des Vereins Deutscher Ingenieure 77 (1935) 318–320, https://doi.org/10.1155/2010/976254 URL: http://journals.sagepub.com/doi/10.1155/2010/976254.

[104] P. Menegay, A computational model for two-phase ejector flow, Phd thesis, Virginia Polytechnic Institute and State University, 1998. URL: https://vtechworks.lib.vt.edu/handle/10919/30340.

[105] K.E. Ringstad, Y. Allouche, P. Gullo, K. Banasiak, A. Hafner, CO2 ejector modelling using CFD: current status, 25th IIR International Congress of Refrigeration Proceedings, 2019.

[106] M. Haida, J. Smolka, A. Hafner, Z. Ostrowski, M. Palacz, A.J. Nowak, K. Banasiak, System model derivation of the CO2 two-phase ejector based on the CFD-based reduced-order model, Energy 144 (2018) 941–956. URL: https://www.sciencedirect.com/science/article/pii/S0360544217320881?via%3Dihub. DOI: 10.1016/j.energy.2017.12.055.

[107] O. Coutier-Delgosha, R. Fortes-Patella, J.L. Reboud, Evaluation of the turbulence model influence on the numerical simulations of unsteady cavitation, Journal of Fluids Engineering, Transactions of the ASME 125 (2003) 38–45, https://doi.org/10.1115/1.1524584.

[108] C. Morel, Mathematical Modeling of Disperse Two-Phase Flows, vol. 114, 2015. URL: http://link.springer.com/10.1007/978-3-319-20104-7. DOI: 10.1007/978-3-319-20104-7.

[109] F. Mazzelli, A.B. Little, S. Garimella, Y. Bartosiewicz, Computational and experimental analysis of supersonic air ejector: Turbulence modeling and assessment of 3D effects, International Journal of Heat and Fluid Flow 56 (2015) 305–316. URL: https://www.sciencedirect.com/science/article/pii/S0142727X15001101. DOI: 10.1016/j.ijheatfluidflow.2015.08.003.

[110] A. Hemidi, F. Henry, S. Leclaire, J.M. Seynhaeve, Y. Bartosiewicz, CFD analysis of a supersonic air ejector. Part II: Relation between global operation and local flow features, Applied Thermal Engineering 29 (2009) 2990–2998. URL: https://www.sciencedirect.com/science/article/pii/S1359431109000969. DOI: 10.1016/j.applthermaleng.2009.03.019.

[111] G. Besagni, F. Inzoli, Computational fluid-dynamics modeling of supersonic ejectors: Screening of turbulence modeling approaches, Applied Thermal Engineering 117 (2017) 122–144. URL: https://www.sciencedirect.com/science/article/pii/S1359431116328290. DOI: 10.1016/j.applthermaleng.2017.02.011.

[112] M. Haida, J. Smolka, A. Hafner, M. Mastrowski, M. Palacz, K.B. Madsen, A.J. Nowak, K. Banasiak, Numerical investigation of heat transfer in a CO2 two-phase ejector, Energy 163 (2018) 682–698. URL: https://www.sciencedirect.com/science/article/pii/S0360544218317110?via%3Dihub. DOI: 10.1016/j.energy.2018.08.175.

[113] K. Banasiak, M. Palacz, A. Hafner, Z. Buliński, J. Smołka, A.J. Nowak, A. Fic, A CFD-based investigation of the energy performance of two-phase R744 ejectors to recover the expansion work in refrigeration systems: An irreversibility analysis, International Journal of Refrigeration 40 (2014) 328–337. URL: https://www.sciencedirect.com/science/article/pii/S0140700713003812. DOI: 10.1016/j.ijrefrig.2013.12.002.

[114] F. Giacomelli, K. Banasiak, A. Hafner, Experimental and Numerical Investigation on an Ejector for CO2 Vapor Compression Systems, 13th IIR Gustav Lorentzen Conference (2018) 1179–1187.

[115] M. Gorokhovski, M. Herrmann, Modeling primary atomization, Annual Review of Fluid Mechanics 40 (2008) 343–366, https://doi.org/10.1146/annurev.fluid.40.111406.102200 URL: http://www.annualreviews.org/doi/10.1146/annurev.fluid.40.111406.102200.

[116] S. Balachandar, J.K. Eaton, Turbulent dispersed multiphase flow, Annual Review of Fluid Mechanics 42 (2010) 111–133, https://doi.org/10.1146/ANNUREV.FLUID.010908.165243 URL: https://www.annualreviews.org/doi/full/10.1146/annurev.fluid.010908.165243.

[117] R.O. Fox, Large-eddy-simulation tools for multiphase flows, Annual Review of Fluid Mechanics 44 (2012) 47–76, https://doi.org/10.1146/annurev-fluid-120710-101118 URL: http://www.annualreviews.org/doi/10.1146/annurev-fluid-120710-101118.

[118] R. Lebas, T. Menard, P. Beau, A. Berlemont, F. Demoulin, Numerical simulation of primary break-up and atomization: DNS and modelling study, International Journal of Multiphase Flow 35 (2009) 247–260. URL: https://www.sciencedirect.com/science/article/pii/S0301932208001821. DOI: 10.1016/J.IJMULTIPHASEFLOW.2008.11.005.

[119] S.V. Patankar, Numerical Heat Transfer and Fluid Flow, Hemisphere Pub. Corp, New York, 1980 URL: https://books.google.no/books/about/Numerical_Heat_Transfer_and_Fluid_Flow.html?id=N2MVAQAAIAAJ&redir_esc=y.

[120] R.H. Pletcher, J.C. Tannehill, D.A.D.A. Anderson, Computational Fluid Mechanics

and Heat Transfer, Hemisphere Pub. Corp. (1997).
[121] C.-N. Xiao, F. Denner, B.G. van Wachem, Fully-coupled pressure-based finite-volume framework for the simulation of fluid flows at all speeds in complex geometries, Journal of Computational Physics 346 (2017) 91–130. URL: https://www.sciencedirect.com/science/article/pii/S0021999117304540. DOI: 10.1016/J.JCP.2017.06.009.
[122] A. Kurganov, E. Tadmor, New High-Resolution Central Schemes for Nonlinear Conservation Laws and Convection-Diffusion Equations, Journal of Computational Physics 160 (2000) 241–282. URL: https://www.sciencedirect.com/science/article/pii/S0021999100964593. DOI: 10.1006/jcph.2000.6459.
[123] A. Kurganov, S. Noelle, G. Petrova, Semidiscrete Central-Upwind Schemes for Hyperbolic Conservation Laws and Hamilton-Jacobi Equations, Technical Report 3, 2001. URL: http://www.siam.org/journals/sisc/23-3/37341.html.
[124] M.A. Gjennestad, A. Gruber, K.Y. Lervåg, Ø. Johansen, Å. Ervik, M. Hammer, S.T. Munkejord, Computation of three-dimensional three-phase flow of carbon dioxide using a high-order WENO scheme, Journal of Computational Physics 348 (2017) 1–22. URL: https://www.sciencedirect.com/science/article/pii/S0021999117305181?via%3Dihub. DOI: 10.1016/j.jcp.2017.07.016.
[125] L. Zheng, J. Deng, Z. Zhang, Dynamic simulation of an improved transcritical CO2 ejector expansion refrigeration cycle, Energy Conversion and Management 114 (2016) 278–289. URL: https://www.sciencedirect.com/science/article/pii/S0196890416300139. DOI: 10.1016/J.ENCONMAN.2016.01.069.
[126] F. Liu, E.A. Groll, Study of ejector efficiencies in refrigeration cycles, Applied Thermal Engineering 52 (2013) 360–370. URL: https://www.sciencedirect.com/science/article/pii/S135943111200806X. DOI: 10.1016/J.APPLTHERMALENG.2012.12.001.
[127] D. Li, E.A. Groll, Transcritical CO2 refrigeration cycle with ejector-expansion device, International Journal of Refrigeration 28 (2005) 766–773. URL: https://www.sciencedirect.com/science/article/pii/S0140700705000022. DOI: 10.1016/j.ijrefrig.2004.10.008.
[128] J. Smolka, M. Palacz, J. Bodys, K. Banasiak, A. Fic, Z. Bulinski, A.J. Nowak, A. Hafner, Performance comparison of fixed- and controllable-geometry ejectors in a CO2 refrigeration system, International Journal of Refrigeration 65 (2016) 172–182. URL: https://www.sciencedirect.com/science/article/pii/S0140700716000311. DOI: 10.1016/j.ijrefrig.2016.01.025.
[129] G.P. Russo, Aerodynamic Measurements, Woodhead Publishing, 2011. URL: https://www.sciencedirect.com/science/article/pii/B9781845699925500036. DOI: 10.1533/9780857093868.67.
[130] Y. Zhu, Z. Wang, Y. Yang, P.X. Jiang, Flow visualization of supersonic two-phase transcritical flow of CO2 in an ejector of a refrigeration system, International Journal of Refrigeration 74 (2017) 352–359. URL: https://www.sciencedirect.com/science/article/pii/S0140700716303784. DOI: 10.1016/j.ijrefrig.2016.11.012.
[131] Deng, Jianqiang, Y. Zhang, Y. He, L. Zheng, T.F. Email, Visual investigation on effect of structural parameters and operation condition of two-phase ejector, in: International Compressor Engineering, Refrigeration and Air Conditioning, and High Performance Buildings Conferences, 2005, 2016, pp. 1–9. URL: http://docs.lib.purdue.edu/iracc/1632.
[132] M. Haida, R. Fingas, W. Szwajnoch, J. Smolka, M. Palacz, J. Bodys, A. Nowak, M. Haida, R. Fingas, W. Szwajnoch, J. Smolka, M. Palacz, J. Bodys, A.J. Nowak, An object-oriented R744 two-phase ejector reduced-order model for dynamic simulations, Energies 12 (2019), https://doi.org/10.3390/en12071282 URL: https://www.mdpi.com/1996-1073/12/7/1282.
[133] J. Gagan, K. Smierciew, D. Butrymowicz, J. Karwacki, Comparative study of turbulence models in application to gas ejectors, International Journal of Thermal Sciences 78 (2014) 9–15. URL: https://www.sciencedirect.com/science/article/pii/S1290072913002779. DOI: 10.1016/J.IJTHERMALSCI.2013.11.009.
[134] A. Bouhanguel, P. Desevaux, Y. Bailly, L. Girardot, Particle image velocimetry in a supersonic air ejector, 15th International Symposium on Flow Visualization June 25–28, 2012, Minsk, Belarus (2012). URL: http://www.itmo.by/doc/en/isfv_15/ABSTRACTS/ISFV15-038.pdf.
[135] S.-Q. Zheng, Y. Yao, F.-F. Guo, R.-S. Bi, J.-Y. Li, Local bubble size distribution, gas-liquid interfacial areas and gas holdups in an up-flow ejector, Chemical Engineering Science 65 (2010) 5264–5271. URL: https://www.sciencedirect.com/science/article/pii/S0009250910003933. DOI: 10.1016/J.CES.2010.06.027.
[136] J. Sierra-Pallares, J. García Del Valle, P. García Carrascal, F. Castro Ruiz, A computational study about the types of entropy generation in three different R134a ejector mixing chambers, International Journal of Refrigeration 63 (2016) 199–213. URL: https://www.sciencedirect.com/science/article/pii/S0140700715003473. DOI: 10.1016/j.ijrefrig.2015.11.007.
[137] C. Othmer, Adjoint methods for car aerodynamics, Journal of Mathematics in Industry 4 (2014) 6, https://doi.org/10.1186/2190-5983-4-6 URL: http://mathematicsinindustry.springeropen.com/articles/10.1186/2190-5983-4-6.
[138] J. Springer, Multiphase adjoint optimization for efficient calculation of rigid body positions in Navier-Stokes flow, Ph.D. thesis, Universität Ulm (2014) URL: https://d-nb.info/1054045518/34.
[139] A. Hafner, S. Försterling, K. Banasiak, Multi-ejector concept for R-744 supermarket refrigeration, International Journal of Refrigeration 43 (2014) 1–13. URL: https://www.sciencedirect.com/science/article/pii/S0140700714000668. DOI: 10.1016/j.ijrefrig.2013.10.015.
[140] J. Zhu, S. Elbel, Experimental investigation of a novel expansion device control mechanism: Vortex control of initially subcooled flashing R134a flow expanded through convergent-divergent nozzles, International Journal of Refrigeration 85 (2018) 167–183. URL: https://www.sciencedirect.com/science/article/pii/S0140700717303791. DOI: 10.1016/j.ijrefrig.2017.09.023.
[141] J. Bodys, M. Palacz, M. Haida, J. Smolka, A.J. Nowak, K. Banasiak, A. Hafner, Full-scale multi-ejector module for a carbon dioxide supermarket refrigeration system: Numerical study of performance evaluation, Energy Conversion and Management 138 (2017) 312–326. URL: https://www.sciencedirect.com/science/article/pii/S019689041730105X. DOI: 10.1016/j.enconman.2017.02.007.
[142] J. Bodys, J. Smolka, M. Palacz, M. Haida, K. Banasiak, A.J. Nowak, A. Hafner, Performance of fixed geometry ejectors with a swirl motion installed in a multi-ejector module of a CO2 refrigeration system, Energy 117 (2016) 620–631. URL: https://www.sciencedirect.com/science/article/pii/S0360544216309616. DOI: 10.1016/j.energy.2016.07.037.
[143] J. Bodys, J. Smolka, K. Banasiak, M. Palacz, M. Haida, A.J. Nowak, Performance improvement of the R744 two-phase ejector with an implemented suction nozzle bypass, International Journal of Refrigeration 90 (2018) 216–228. URL: https://www.sciencedirect.com/science/article/pii/S0140700718300999. DOI: 10.1016/J.IJREFRIG.2018.03.020.
[144] W. Chen, H. Chen, C. Shi, K. Xue, D. Chong, J. Yan, A novel ejector with a bypass to enhance the performance, Applied Thermal Engineering 93 (2016) 939–946. URL: https://www.sciencedirect.com/science/article/pii/S135943111501114X. DOI: 10.1016/J.APPLTHERMALENG.2015.10.067.
[145] M. Haida, J. Smolka, A. Hafner, Z. Ostrowski, M. Palacz, K.B. Madsen, S. Försterling, A.J. Nowak, K. Banasiak, Performance mapping of the R744 ejectors for refrigeration and air conditioning supermarket application: A hybrid reduced-order model, Energy 153 (2018) 933–948. URL: https://www.sciencedirect.com/science/article/pii/S0360544218306959. DOI: 10.1016/j.energy.2018.04.088.
[146] O. Lamberts, P. Chatelain, Y. Bartosiewicz, New methods for analyzing transport phenomena in supersonic ejectors, International Journal of Heat and Fluid Flow 64 (2017) 23–40, https://doi.org/10.1016/j.ijheatfluidflow.2017.01.009.
[147] A. Alizadehdakhel, M. Rahimi, J. Sanjari, A.A. Alsairafi, CFD and artificial neural network modeling of two-phase flow pressure drop, International Communications in Heat and Mass Transfer 36 (2009) 850–856, https://doi.org/10.1016/j.icheatmasstransfer.2009.05.005.
[148] C. Haoran, C. Wenjian, Artificial neural network modeling for variable area ratio ejector, in: Proceedings of the 2014 9th IEEE Conference on Industrial Electronics and Applications, ICIEA 2014, Institute of Electrical and Electronics Engineers Inc., 2014, pp. 220–225. DOI: 10.1109/ICIEA.2014.6931162.
[149] D.V. Brezgin, K.E. Aronson, F. Mazzelli, A. Milazzo, The surface roughness effect on the performance of supersonic ejectors, Thermophysics and Aeromechanics 24 (2017) 553–561, https://doi.org/10.1134/s0869864317040060 URL: http://link.springer.com/10.1134/S0869864317040060.
[150] Y. Han, X. Wang, H. Sun, G. Zhang, L. Guo, J. Tu, CFD simulation on the boundary layer separation in the steam ejector and its influence on the pumping performance, Energy 167 (2019) 469–483. URL: https://www.sciencedirect.com/science/article/pii/S0360544218321923. DOI: 10.1016/j.energy.2018.10.195.
[151] Y. Bartosiewicz, Z. Aidoun, P. Desevaux, Y. Mercadier, Numerical and experimental investigations on supersonic ejectors, International Journal of Heat and Fluid Flow 26 (2005) 56–70. URL: https://www.sciencedirect.com/science/article/pii/S0142727X04001158. DOI: 10.1016/j.ijheatfluidflow.2004.07.003.
[152] Y. Bartosiewicz, Z. Aidoun, Y. Mercadier, Numerical assessment of ejector operation for refrigeration applications based on CFD, Applied Thermal Engineering 26 (2006) 604–612. URL: https://www.sciencedirect.com/science/article/pii/S1359431105002206. DOI: 10.1016/j.applthermaleng.2005.07.003.
[153] J. García del Valle, J. Sierra-Pallares, P. Garcia Carrascal, F. Castro Ruiz, An experimental and computational study of the flow pattern in a refrigerant ejector. Validation of turbulence models and real-gas effects, Applied Thermal Engineering 89 (2015) 795–811. URL: https://www.sciencedirect.com/science/article/pii/S1359431115006237. DOI: 10.1016/J.APPLTHERMALENG.2015.06.064.

Paper II

Ringstad, Knut Emil; Ervik, Åsmund; Banasiak, Krzysztof; Hafner, Armin. (2021) Machine learning and CFD for mapping and optimization of CO2 ejectors. *Applied Thermal Engineering.* vol 199.
DOI: https://doi.org/10.1016/j.applthermaleng.2021.117604

Applied Thermal Engineering 199 (2021) 117604

Contents lists available at ScienceDirect

Applied Thermal Engineering

journal homepage: www.elsevier.com/locate/apthermeng

Machine learning and CFD for mapping and optimization of CO_2 ejectors

Knut Emil Ringstad [a,*], Krzysztof Banasiak [b], Åsmund Ervik [b], Armin Hafner [a]

[a] Norwegian University of Science and Technology, Kolbjørn Hejes vei 1B, 7491 Trondheim, Norway
[b] SINTEF Energy, Kolbjørn Hejes vei 1d, 7465 Trondheim, Norway

ARTICLE INFO

Keywords:
Computational fluid dynamics
Two-phase ejector
CO_2
Gaussian process regression
Optimization

ABSTRACT

In this study, a novel simulation-based algorithm for CO_2 ejector design and performance evaluation is presented. The algorithm is based on an automated Computational Fluid Dynamics (CFD) workflow that can account for different ejector geometries and operating conditions. The CFD data points are used to train a Gaussian Process Regression (GPR) machine learning model to predict the ejector performance indicators; efficiency, mass flow rates, outflow uniformity, and entropy generation. Three use cases are investigated using this methodology: 1) performance mapping for off-design operating conditions of a given ejector, 2) design mapping of ejector performance with 5 geometry variables investigated, and 3) flow structure prediction between different ejector mixing chamber geometries. The results show that this algorithm can be used to efficiently explore ejector designs with mean average errors between 0.07 and 0.1 [–] in entrainment ratio. Furthermore, the method can to look for optimized geometries using gradient descent methods, as well as produce ejector performance maps. Additionally, the method is able to predict local flow structures of velocity and pressure inside the ejector with varied ejector geometries. The databases and GPR method implementation from this work is made available open-source for further development and research.

1. Introduction

The urgent need to rapidly reduce greenhouse gas emissions calls for unprecedented action from individuals, industry, and governments. The Heating, Ventilation, Air-conditioning, and Refrigeration (HVAC & R) industry is accountable for a significant part of global greenhouse gas emissions. If not limited, large-scale adoption of high GWP synthetic working fluids like hydrofluorocarbons (HFCs) is expected to be a major contributor to global emissions within 2050 [1]. In response, international agreements to phase out high GWP working fluids have been ratified, such as the Kigali amendment to the Montreal Protocol and the EU F-gas regulation [2]. A promising alternative to the use of synthetic refrigerants is natural working fluids such as CO_2 (R744). R744 has a GWP of 1 and is a non-toxic, non-flammable, and natural refrigerant that can be efficiently implemented for many applications [3]. Furthermore, R744 has several favorable thermodynamic properties that allow for efficient and compact units. However, the high operating pressures common in R744 systems introduce large expansion losses, that can significantly reduce system COP. Therefore, expansion-loss recovery devices are often implemented to achieve higher system efficiency.

Ejectors are low-cost work-recovery devices with no moving parts that can use the lost expansion energy to pump a secondary flow to a higher pressure [4,5]. An ejector can improve system performance by as much as 10–30% [4] at design conditions. However, they are highly dependent on the correct design and minor changes in ejector geometry can dramatically reduce ejector efficiency [6–9]. Therefore, the development of efficient and accurate methods for ejector design has in recent years gained attention.

The flow within a two-phase ejector is challenging to model as it involves several interdependent and highly complex features such as compressible, super-sonic, and multiphase flow with phase change, and multiphase turbulence and flow jet atomization. Therefore, over the last decade, much research has been devoted to developing high-resolution CFD models to accurately predict ejector performance and improve their design. CFD models have seen extensive applications within R744 ejector design and performance prediction [10–16]. Today, the most commonly used model is the homogeneous equilibrium model (HEM). HEM models have been studied extensively [17,18,12,13,10,19,11,16,5,14] and can reasonably predict motive mass flow rates (MFR) for supercritical motive conditions [5]. For better prediction of the motive mass flow rate at lower motive inlet pressure conditions Palacz et al. [12] concluded that non-equilibrium effects should be considered. In general, CFD models are able to accurately

* Corresponding author.
E-mail address: knut.e.ringstad@ntnu.no (K.E. Ringstad).

https://doi.org/10.1016/j.applthermaleng.2021.117604
Received 31 May 2021; Received in revised form 30 July 2021; Accepted 16 September 2021
Available online 27 September 2021

Nomenclature

Abbreviations

ANN	Artificial Neural Network
CFD	Computational fluid dynamics
EoS	Equation of state
GP	Gaussian Process
GPR	Gaussian process regression
GWP	Global warming potential
HEM	homogeneous equilibrium model
HFC	Hydrofluorocarbon
HRM	Homogeneous relaxation model
HVAC	Heating, ventilation, air-conditioning, and refrigeration
KPI	Key performance indicator
LHC	Latin hyper cube
MFR	Mass flow rate
MSE	Mean squared error
ROM	Reduced Order Model
UDF	User defined function

Symbols

α_d	Diffuser angle
$\overline{E}$	Expectation value
χ	Scaled sampling variable
$\dot{S}_{h1,2,3}$	Enthalpy source term
ϵ	Turbulent kinetic energy dissipation
η	Efficiency
Γ	Diffusion coefficient
λ	Thermal conductivity
μ	viscosity
ϕ	vapour volume fraction
ψ	Generic field variable
ρ_m	Density
σ	Data variance
τ	Stress tensor
θ	Hyperparameter
$\overline{u}$	Velocity vector
c_p	heat capacity
D_{diff}	Diffuser outlet diameter
$D_{\text{m-out}}$	Motive outlet diameter
D_{mix}	Mixing chamber diameter
L_{mix}	Mixing chamber length
T	Temperature
a	Sampling range
E	Total Energy
f	Underlying unobservable function
G	Learning rate
h	Enthalpy
K	Covariance function - kernel
k	Turbulent kinetic energy
l	Characteristic length scale
M	Data mean
n	Noise
P	Pressure
Pr	Prandtl number
q	Heat flux
s	Entropy
W	Work
x	Direction vector
X,y	Data in dataset

Subscripts

eff	Effective
i,j	Notation indices
m	Motive
m	Pseudo-fluid mixture property
o	Outlet
s	Suction
t	Turbulent

predict motive MFR typically within 10%. However, the suction MFR is less accurately predicted, with errors ranging up to 20–100%. For a detailed review on ejector modeling, its applications, and available experimental data, the reader is referred to Ringstad et al. [5].

While the high sensitivity of ejector performance to their design has been noted in several studies[6,7,14], major knowledge gaps remain in the field of high-performance ejector design. Nakagawa et al. [6] investigated the effect of different mixing chamber geometries experimentally, noting the significant impact of the mixing chamber length on ejector performance. This was followed up in the work by Banasiak et al. [7] and Banasiak et al. [15] where the mixing chamber and diffuser geometries were investigated experimentally and numerically. They concluded that these geometry parameters were important for achieving high ejector efficiency and that the most important parameters for ejector performance were the mixing chamber diameter, both with a significant impact on entropy production. Furthermore, they concluded that the different parameters must be optimized simultaneously and not in isolation. Entropy production in R744 ejectors was further investigated by He et al. [14] using CFD. The results showed that the motive outlet diameter plays a critical role in ejector performance and that the nozzle exit position plays a key role in momentum exchange and exergy destruction.

In this work, a method for producing a machine learning-based surrogate model from numerical results is presented. Using this surrogate model, it is possible to replace several different calculation tools with a single one. Here, three distinct cases are presented (1) performance mapping for different operating conditions given a specific ejector geometry, (2) design mapping and optimization of ejector performance with different geometric parameters, (3) flow structure mapping for different ejector geometries.

Performance mapping of off-design performance has been investigated using CFD in previous works by Haida et al. [20,11]. CFD data was used to generate a Reduced Order Model (ROM) to quickly predict ejector performance at any operating condition. Such ROM models has great applicability for dynamic simulations [11] or Digital Twins.

CFD based shape optimization for R744 ejectors has been previously carried out by Palacz et al. [12,13], resulting in the EjectorPL system for automated CFD model generation. The study compared two evolutionary optimization approaches for ejector design. The results showed that up to 6% improvement in ejector efficiency is possible from an existing design based on 1D model calculations. Barta et al. [21] recently presented a design optimization methodology for R744 ejectors based on 0D sub-component polynomial modeling. The methodology can accurately predict ejector performance and offers insights into design trade-offs in ejector design.

Alternatively, optimization may be performed on performance maps using optimization methods such as gradient descent. This, however, depends on quick evaluation of results and their gradient at any given point in the design space. For complex flow devices, such as ejectors, evaluating the flow at a single design point with CFD tools requires significant computational effort (from hours to days). Therefore, it is better to perform the optimization on a surrogate meta-model such that performance can be quickly evaluated.

In this work, the Gaussian Process Regression (GPR) machine

learning approach is used to generate such a surrogate model from a large set of CFD data. The CFD database is built using an automated workflow for different shape designs, model parameters, and operating conditions. Using CFD results to generate a large database has several advantages. Firstly, it enables one to investigate local flow structures in detail. Secondly, CFD models implicitly take into account 2D or even 3D geometric effects which are impossible to account for using simpler zero or one-dimensional approaches.

The datasets are used for the training of a Gaussian Process Regression model to predict different ejector performance indicators and flow structures inside the ejector. GPR has been extensively used for a wide range of model problems [22]. Alternative machine learning methods, such as artificial neural networks (ANN), have previously been used in ejector design [23] and performance analysis [24,25]. Still, GPR models have advantages over ANN methods, such as more efficient use of data, lower risk of overfitting, ease of use, and explainability [26].

Using this GPR surrogate modeling approach, both performance- and shape mapping are handled with one tool. This simplification also allows for combined studies of shape and operating conditions in a novel way. In addition, the mapping can be used for the optimization of both operating conditions and geometry. This approach has several advantages over other methods:

1. It can give a full mapping of performance at any combination of parameters, allowing for a full investigation of possible designs and what-if scenarios.
2. The method can take advantage of experimental and numerical results from previous works to improve model accuracy.
3. The GPR method provides estimated prediction uncertainty at any point. This information can be used to improve modeling tools or refine database coverage.
4. The method can produce maps of local flow structures with varied geometries and operating conditions.

2. Ejector CFD model

2.1. Multiphase model

In this work, the multiphase flow within a two-phase R744 ejector is modeled using a homogeneous equilibrium model (HEM) based on the formulation of Smolka et al. [17]. The HEM is based on the assumption of strongly coupled phases at mechanical, thermal, and thermodynamic equilibrium, i.e. both phases can be described with a single velocity-($\overline{u}$), temperature- (T), and pressure-field (P). By these assumptions, a single set of partial differential equations for the mixture of liquid and gas needs to be solved. Essentially, the two phases are then treated as a single pseudo-fluid with transport properties derived according to an averaging procedure. This pseudo-fluid will be governed by the equations of fluid motion and energy:

$$\frac{\partial \rho_m}{\partial t}+\frac{\partial}{\partial x_j}\left[\rho_m u_{mj}\right]=0, \tag{1}$$

$$\frac{\partial}{\partial t}\left(\rho_m u_{mi}\right)+\frac{\partial}{\partial x_j}\left[\rho_m u_{mi}u_{mj}+P\delta_{ij}-\tau_{ij\_\mathrm{eff}}\right]=0, \tag{2}$$

$$\frac{\partial}{\partial t}\left(\rho_m E_m\right)+\frac{\partial}{\partial x_j}\left[\rho_m u_{mj}h_m-q_{j,\mathrm{eff}}-u_{mi}\tau_{ij,\mathrm{eff}}\right]=0, \tag{3}$$

Here the Einstein notation is used with subscript-indexes i and j, and the subscript m indicates the pseudo-fluid mixture properties. Here, ρ_m, u_m, P, E, h_m, q refer to the density, velocity, pressure, total energy, mixture enthalpy and heat flux, respectively. The effective stress tensor $\tau_{ij,\mathrm{eff}}$ is the laminar (Newtonian) and turbulent stress tensors combined:

$$\tau_{ij,\mathrm{eff}}=\tau_{ij}+\tau_{ij,t}. \tag{4}$$

To obtain the total mixture enthalpy, an alternative formulation of the energy equation, Eq. (5), was implemented using user-defined functions (UDF) in the ANSYS Fluent software [27], replacing Eq. 3.

$$\frac{\partial}{\partial t}\rho h+\nabla\cdot\left(\rho\overrightarrow{u}h\right)=\nabla\cdot\left(\Gamma_{\mathrm{eff}}\nabla h\right)+\dot{S}_{h1}+\dot{S}_{h2}+\dot{S}_{h3} \tag{5}$$

In this equation, h is the specific enthalpy, $\overrightarrow{u}$ is the velocity vector, Γ_{eff} the effective diffusion coefficient. The source terms $\dot{S}_{h1,2,3}$ describe the mechanical energy, the irreversible dissipation of the kinetic energy variations, and the dissipation of the turbulent kinetic energy, respectively [17].

Γ_{eff} is defined as:

$$\Gamma_{\mathrm{eff}}=\frac{\mu_t}{Pr}+\frac{\lambda}{c_p}, \tag{6}$$

where μ_t is the turbulent viscosity, Pr is the Prandtl number, c_p is the mixture specific heat capacity, and λ is the thermal conductivity.

2.2. Equation of state

One preferable property of the equilibrium assumption is that the pressure and enthalpy uniquely define the thermodynamic state, and thus the properties in the two-phase dome. Properties are typically divided into thermophysical (Eq. 7) and transport (Eq. 8) properties.

$$\begin{bmatrix}\rho\\ c_p\\ \phi\\ T\\ s\end{bmatrix}=f\left(P,h\right), \tag{7}$$

$$\begin{bmatrix}\mu\\ \lambda\end{bmatrix}=g\left(P,h\right), \tag{8}$$

where $\rho, \phi, \mu, \lambda, c_p, s$ are the pseudo-fluid density, vapour volume fraction, kinematic viscosity, thermal conductivity, specific heat capacity, and specific entropy, respectively.

The properties of liquid and gas are evaluated by the pressure and enthalpy, interpolated from a look-up table. The CoolProp library [28] for R744 is based on the Span-Wagner equation of state, which is considered the most accurate equation of state (EoS) for CO_2 and is widely used for R744 ejector simulations [5]. Here, CoolProp is used to generate the look-up tables that are imported in Fluent using UDFs. This study is limited to the operating range suited for the HEM model, however, the methods presented here are easily extended to cover non-equilibrium conditions.

2.3. Turbulence model

Accurately describing the mixing process inside two-phase ejectors is largely dependent on modelling the two-phase turbulent flow inside the mixing chamber. The turbulent viscosity, μ_t, is then sub-modeled by the $k-\epsilon$ realizable turbulence model. This model involves solving the set of transport equations for the turbulent properties, Eqs. (9) and (10):

$$\frac{\partial}{\partial t}\left(\rho_m k\right)+\frac{\partial}{\partial x_j}\left(\rho_m k u_{mj}\right)=\frac{\partial}{\partial x_j}\left[\left(\mu+\frac{\mu_t}{\sigma_k}\right)\frac{\partial k}{\partial x_j}\right]+p_k+p_b-\rho\epsilon-\mathrm{Y_M}+\mathrm{S_k}, \tag{9}$$

$$\frac{\partial}{\partial t}\left(\rho_m \epsilon\right)+\frac{\partial}{\partial x_j}\left(\rho_m \epsilon u_{mj}\right)=\frac{\partial}{\partial x_j}\left[\left(\mu+\frac{\mu_t}{\sigma_\epsilon}\right)\frac{\partial \epsilon}{\partial x_j}\right]+\rho C_1 S\epsilon-\rho_{\mathrm{m}}C_2\frac{\epsilon^2}{\mathrm{k}+\sqrt{\mu\epsilon}/\rho_{\mathrm{m}}}+C_{1\epsilon}\frac{\epsilon}{\mathrm{k}}C_{3\epsilon}\mathrm{p_b}+\mathrm{S_\epsilon}, \tag{10}$$

$$\mu_t = \rho_m \frac{k^2}{\epsilon}, \tag{11}$$

where the subscript, m, indicates mixture properties based on mass or volume weighted averaging, C is a model specific constant, S and Y are model specific source terms, p is the strain rate production of $k; p = \mu_t E_{ij} E_{ij}$. This model has favourable stability properties in comparison to k-ω based models and scalable wall functions simplifies the automated meshing algorithm [5].

3. Machine learning approach

3.1. Gaussian process regression

Gaussian Process Regression (GPR) is a supervised machine learning tool based on Bayesian regression to generate surrogate models. The model is trained using a labeled data set ($y_i, \mathbf{X}_i$), where y is the observations, and X is the input for datapoint i. The data used in the machine learning model are referred to as features. The feature data is rescaled to be zero mean with unit variance, according to Eq. (12), using the Sklearn toolset StandardScaling [29]:

$$z = \frac{X - M}{\sigma} \tag{12}$$

Here, X and z are the unscaled and scaled feature data, respectively, μ is the feature data mean, and σ is the feature data standard deviation.

Assuming that the observations are obtained from an unobservable underlying function f with zero mean Gaussian noise, $n_i = \mathcal{N}(0, \sigma)$, the input-output relationship can be written as (Eq. 13):

$$\mathbf{y} = f(\mathbf{X}) + n_i \tag{13}$$

The Gaussian Process (GP) can then be written as (Eq. 14):

$$\mathbf{y} = \mathcal{GP}(M(X), K(X, X'; \theta)) \tag{14}$$

The GP has a mean function, $M = \overline{E}[f(X)]$, where $\overline{E}$ is the expectation value, a covariance function $K(X, X') = \overline{E}[f(X)f(X')]$, and a set of model hyperparameters θ. The co-variance function is also referred to as the kernel, which measures the correlation between the outputs variable at two points X_i, X_j, and is specified as a prior.

In this paper, the Squared Exponential kernel is used as a covariance function and a white noise kernel is added to account for numerical errors. The combined kernel function is then defined as (Eq. 15):

$$K\left(X, X'; \theta, \sigma\right) = \sigma_f^2 \exp\left(-\frac{1}{2l^2}(X - X')^2\right) + \sigma_n^2 \mathbb{I} \tag{15}$$

where, $\mathbb{I}$ is the identity matrix. The kernel has three hyper parameters; σ_f, l, and σ_n, which are the signal standard deviation, the characteristic length-scale, and the noise level (variance) respectively. The parameter σ_f is a scaling parameter and the length-scale l governs the length over which two points X and X' are correlated. Larger values of l enforces that f varies more smoothly. The characteristic length scale is dimensional and can vary between features.

Hyperparameters (l, σ_n, σ_f) are optimized during the fitting of the data using a gradient descent optimizer on the log-marginal-likelihood of the hyper-parameters. The optimizer is a quasi-Newton L-BFGS optimizer [30,29,31] with $n = 10$ optimizer restarts, commonly used in the literature [32]. Characteristic length scales are bounded to upper and lower limits of 1.0×10^{-3} and 3.0×10^{1}, respectively, for all dimensionless features. The kernel optimizer is initialized with $\sigma_{f,0} = 0.2, l_0 = 0.5$, $\sigma_{n,0} = 0.02$. Using the training data with dimensions A $\times$ (B_{total} - $B_{training}$), where A is the number of features and B the number of data points, a posterior distribution can be found by drawing from a joint distribution of the training data y and test data $y*$.

$$\begin{bmatrix} y \\ y* \end{bmatrix} = \mathcal{N}\left(\begin{bmatrix} M \\ M* \end{bmatrix}, \begin{bmatrix} K & K^* \\ K^* & K^{**} \end{bmatrix}\right) \tag{16}$$

This GPR algorithm was implemented using the Scikit-learn Python package [29].

3.2. Gradient descent based optimization

The GPR model predicts the ejector operation at any point in the defined feature domain. By using a gradient-based optimization algorithm on the function it is possible to optimize the ejector parameters for a given output. Here, a gradient descent optimization algorithm was implemented according to, Eq. (17):

$$\mathbf{X}_{i+1} = \mathbf{X}_i + G\nabla f(\mathbf{X}_i) \tag{17}$$

Here, G is a specified learning rate and f is the chosen function to optimize. A first-order finite difference method for evaluating the gradient. The initial points were chosen randomly from a uniform distribution of the feature space.

4. CFD automation algorithm

To generate the data sets needed to train the GPR model, an algorithm was developed in the Python 3.9 programming language [33] for automatically generating CFD data. This algorithm incorporates automatic meshing, automatic generation of Fluent journal files, and post-processing the results. An illustration of the system layout is presented in Fig. 1. The program takes in data points from the boundary condition - geometry design space and automatically simulates the flow case.

Initially, the automated algorithm settings need to be defined. This involves choosing the features to be explored and choosing the remaining constant parameters. In this step, different sampling algorithms, meshing strategies, and post-processing settings are available. Based on the chosen features and sampling algorithms, a user-specified number of data points are sampled from the design space. The sampling algorithm used is further discussed in Section 4.1. The algorithm then iteratively simulates each flow case in three steps.

The first step is to generate the specified 2D structured mesh using an in-house automated meshing script for the ICEM meshing program according to the specified geometry parameters. The script generates high-quality meshes with average orthogonal quality of 99.9% for a 10k cell mesh. The mesh parameters included are the baseline cell size, refinement ratio, and aspect ratio of the mixing section cells. A mesh sensitivity study is conducted and discussed in Section 4.3.1. Acceptable results were obtained using meshes around 8k cells. To limit computational cost while keeping the high accuracy a mesh of 24k cells was chosen as the average design case.

The second step is to generate an ANSYS Fluent journal file to automatically run the flow case with the prescribed boundary conditions from the algorithm for pressure and enthalpy. The inlets and outlets were prescribed with the ANSYS pressure-inlet and pressure-outlet boundary conditions, respectively. The boundary conditions for the specific enthalpy defined for the HEM model were zero gradient enthalpy at the outlet and constant inlet enthalpy. The wall conditions were defined as adiabatic with a wall roughness of $H_{rough} = 2[\mu m]$, commonly used in CFD literature for R744 ejectors [13,34]. All calculations were done using a steady solver. The discretization schemes used are described in Table 1.

Each case is simulated in ANSYS Fluent 2019R3 with the standard initialization procedure, starting the simulations with first-order schemes for the first 20k iterations, before changing to second-order schemes. Convergence was judged based on low mass flow rate imbalance below 1.0×10^{-5} [kg/s] and residuals below 1.0×10^{-5}. The majority of the simulations would converge within 40–50k iterations. Simulations that did not converge were continued until either conver-

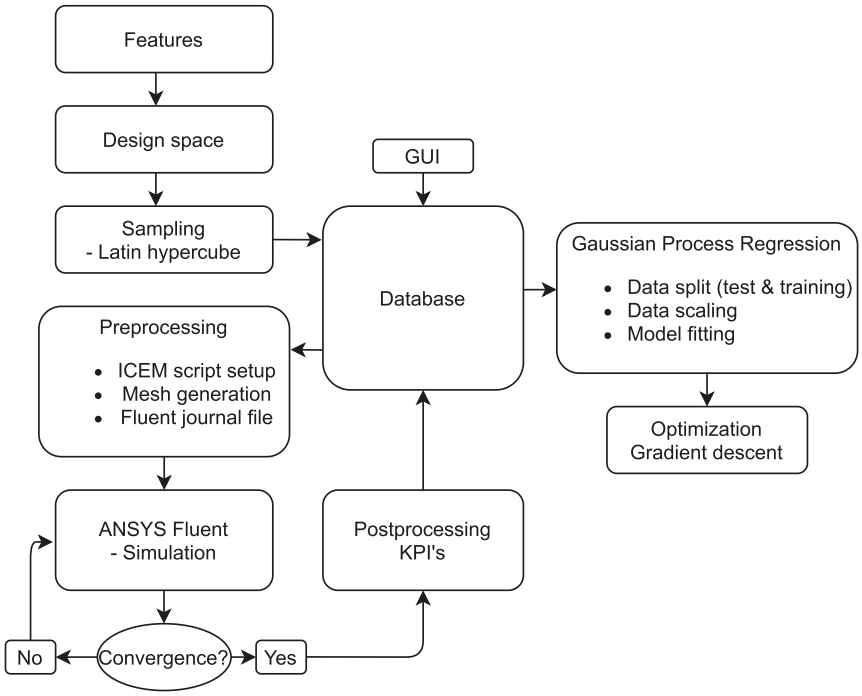

Fig. 1. Illustration of the algorithm layout.

Table 1
Discretization schemes used in the CFD models.

Discretization	Scheme
Pressure	PRESTO!
Pressure-velocity coupling	Coupled
Gradient	Green Gauss cell-based
Momentum	Second order upwind
Density	–"–
Enthalpy	–"–
Turbulent kinetic energy	–"–
Turbulent energy dissipation	–"–

gence or reaching 80k iterations. Simulations that were oscillating after 80k iterations were removed from the results. These oscillations typically occurred at low motive inlet specific enthalpy (below 270 [kJ/kg]) and high motive pressures (above 110 [bar]), which is close to the limit of the HEM range of validity.

The third step is to post-process the CFD results, collecting the different output KPI parameters and storing these in a database. The different output parameters and their calculation are discussed in Section 4.2. After all the steps are completed the database is stored and duplicated. After which the data can be analyzed by the machine learning model.

4.1. Sampling

The design space is initially sampled using a Latin HyperCube (LHC) approach [35] with the Python package LHC-Python. Latin hypercube sampling is a statistical sampling approach that samples N points from a statistical distribution in equiprobable zones. This approach ensures good sampling of a higher dimensional subspace with fewer data points than random or equidistant sampling. The LHC design gives an N-dimensional mapping to fill a space with low overlap. The design points χ_i are chosen from the range (0,1) and is transformed to a chosen subspace for each feature, x_i. All variables are sampled evenly according to Eq. (18),

$$X_i = \chi_i * (a_{\max} - a_{\min}), \tag{18}$$

using the maximum and minimum values, $a_{\min/\max}$, presented in Table 2. This is to get a well-represented operational mapping for different given ejectors.

To avoid sampling unphysical ejector geometry combinations a sampling constraint had to be added. The motive outlet diameter was constrained such that the motive nozzle is smaller than the suction chamber at the nozzle exit position according to:

$$D_{\mathrm{m-out}} < 2(tan(\alpha_s/2)L_{\mathrm{mch}} + D_{\mathrm{mix}}/2 - t) \tag{19}$$

Table 2
Available features and their parameter sampling range for LHC-sampling algorithm.

Parameter	$a_{\min}$	$a_{\max}$
$D_{\mathrm{m-out}}$, [mm]	D_{throat}	1.5 D_{throat}, Eq. (19)
L_{mix}, [mm]	0	50 D_{mix}
D_{mix}, [mm]	D_{throat}	10 D_{throat}
D_{diff}, [mm]	D_{mix}	10 D_{mix}
α_{d}, [°]	1	90
P_m, [bar]	75	140
P_s, [bar]	28	55
P_o, [bar]	P_s	P_s+15
h_m, [kJ/kg]	250	340
h_s, [kJ/kg]	380	460

4.2. Key performance indicators

In this study, four Key Performance Indicators (KPIs) were considered to evaluate ejector performance for different ejector designs. These are motive and suction mass flow rates (entrainment ratio), ejector efficiency, mixture entropy generation rate, and ejector outlet flow uniformity for velocity and vapor fraction.

Mass flow rates are calculated by Fluent at the inlets and outlets of the ejector. These are reported and post-processed by the algorithm. Using the mass flow rates and boundary conditions, the ejector efficiency is calculated from the Elbel efficiency, Eq. (20) [36] using calls to the CoolProp software [28].

$$\eta_{\text{ejector}} = \frac{\dot{W}_{\text{r}}}{\dot{W}_{\text{r,max}}} = \omega \cdot \frac{h(P_{\text{out}}, s_{\text{s}}) - h_s}{h_m - h(P_{\text{out}}, s_m)} \tag{20}$$

Entropy production is found by calculating the mass-weighted average of the incoming and outgoing entropy in each section. This is done using surface definitions and an entropy look-up table implemented in ANSYS Fluent using user-defined functions. The ejector outlet flow uniformity is calculated using the Uniformity Index defined in ANSYS Fluent:

$$\gamma_a = 1 - \frac{\sum_{i=1}^{n} \left(\left| \psi_i - \overline{\psi}_a \right| \right) A_i}{2 \left| \overline{\psi}_a \right| \sum_{i=1}^{n} A_i} \tag{21}$$

where $\overline{\psi}_a$ is the averaged value of the field variable ψ over the n cells on the outlet surface, and A_i is the surface area for cell i. Here, the unformity index is calculated for the vapour fraction ϕ and the axial velocity u. These two KPIs indicate how well mixed the flows are at the outlet of the ejector.

4.3. CFD model validation

The HEM as implemented in this work has been extensively validated in previous works [17,37,38]. As previously mentioned, the prediction error of the presented model is typically considered to be within 10% for motive mass flow rate. Suction mass flow rate is less accurately predicted, and can in cases significantly deviate from experimental results. Therefore, simulation results and any optimized design should be carefully inspected and scrutinized. This also motivates further research into the modeling of R744 two-phase ejectors. The presented methodology is modular, and switching the underlying CFD model can be done with only minor modifications.

4.3.1. Mesh sensitivity study

To ensure that the mesh is sufficiently refined to describe the ejector flow and mesh independent results are achieved a mesh study was conducted. The main ejector geometry parameters are presented in Table 3. This ejector geometry is intended as an open-access geometry for simulations as sharing of this geometry is not limited by proprietary restrictions. The different ejector dimensions are illustrated in Fig. 2.

Table 3
All main ejector dimensions of the new proposed open design.

Parameter	Value
Motive Inlet diameter ($D_{\text{m-in}}$)	10.0 [mm]
Motive Throat diameter (D_{throat})	1.41 [mm]
Motive Outlet diameter ($D_{\text{m-out}}$)	1.52 [mm]
Nozzle tip thickness (t)	1.2 [mm]
Pre-mixer length (L_{mch})	4.2 [mm]
Mixer length (L_{mix})	26.0 [mm]
Mixer diameter (D_{mix})	4.0 [mm]
Diffuser diameter (D_{diff})	12.0 [mm]
Diffuser angle (α_{d})	6[°]
Motive converging angle ($\alpha_{\text{m-c}}$)	35[°]
Motive diverging angle ($\alpha_{\text{m-d}}$)	3[°]
Suction angle (α_{s})	42[°]

Previous studies with the HEM have investigated mesh independence and shown that mesh independent results can be achieved with only 9k cells for optimization studies [13]. The ejector simulations were performed with five different meshes, A, B, C, D, E that were composed of 2.2k, 8k, 26k, 60k, and 100k cells, respectively. Meshes A, B, and E were generated using an ICEM mesh refinement algorithm for coarsening and refinement of mesh C. The refinement is applied uniformly for all cells, halving/doubling the mesh size in each dimension. Mesh D was based on a smaller baseline cell size in the meshing script with a similar refinement to mesh C. These simulations were run with boundary conditions named OP1[1] close to the design point, see the footnote. The calculated mass flow rates are presented in Table 4. The motive mass flow rate tends to reduce with the mesh refinement. However, the difference between these flow rates was less than 5% for all mesh densities. The suction mass flow rate varied more than the motive MFR, and has, in general, a decreasing trend as the mesh is refined. The suction mass flow rate is less accurately predicted with mesh A, 11% difference to mesh E, while for mesh B and C the difference is less than 1%. Interestingly, mesh D produced higher suction MFR than the other meshes. This could be due to that mesh D is based on a different baseline cell size.

Based on these mesh refinement indicators mesh C was chosen for further study, as it gave reasonable accuracy, within 1% of the most refined mesh, with a low computational cost. The study shows that R744 ejector flow using the HEM can be reproduced with a coarse mesh, which agrees with previous findings by Palacz et al. [13]. Such a mesh is ideal for use in optimization algorithms where computational speed is essential.

5. Results and discussion

The presented method is flexible and can look at various combinations of features. Any computable and physical combination of geometry variables, operating condition parameters, or CFD model parameters can be used for the mapping. In addition the GPR model can be applied for the prediction of flow structures such as pressure and velocity distributions, entropy production, and flow separation. Here, the results of the methodology are presented for three use cases. Case 1; generate an operation map for off- and on-design conditions using a given ejector geometry. Case 2; design space mapping and optimization at a given operating condition. Case 3; prediction of flow structures in the ejector from CFD data. Other use cases with alternative features are presented and discussed in Section 6.

5.1. Case 1: Off-design operation mapping

Case 1 presents a method of performance mapping of a given design at various operating conditions. Only the thermodynamic features (P_m, P_s, P_o, h_m, h_s, see Table 2) are included in this part of the investigation. These features are allowed to vary as specified in Table 2. The ejector geometry used is the new ejector geometry presented in Table 3.

5.1.1. Database sampling

Model accuracy is dependent on the number of data points. To verify how accuracy is affected by the number of data points, a model convergence study is done. One can test the sensitivity to the number of data points by either removing points from the training set or by generating additional data with more points. As each database is generated with an LHC sampling method, a fair comparison cannot be

[1] OP1: P_m = 85 [bar], P_s = 33 [bar], P_o = 38 [bar], h_m = 290 [kj/kg], h_s = 432 [kj/kg]

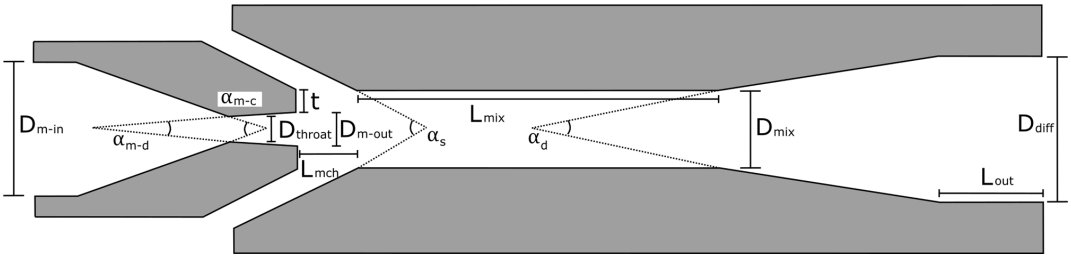

Fig. 2. Generic ejector geometry with geometry parameters. Gray color signifies solid parts.

Table 4
Mesh convergence study with different mesh sizes.

Mesh	Cells	OP1 [kg/s]	
		MFR_m	MFR_s
A	2.2k	0.0824	0.0538
B	8.0k	0.0812	0.0615
C	26k	0.0799	0.0613
D	62k	0.0795	0.0662
E	100k	0.0791	0.0609

made by simply removing data points. Therefore, three separate databases of 100, 300, 600 data points were sampled and simulated. The GPR model was trained using these three databases and the average GPR model accuracy was evaluated with different test and training sampling sizes. The mean squared error (MSE) between the GPR model prediction and the CFD data points in the test data was calculated for the different KPIs. The errors are estimated using 15% of the data as hidden test data that is left out of the model training and 85% as training data. The calculated mean square error results are shown in Fig. 3, normalized by the error with the smallest dataset.

From Fig. 3 it is found that, except for entropy, all KPIs are better predicted by increasing the database resolution. Refining the database to 600 datapoints reduced the MSE by 50–90% for the different KPIs. Interestingly, entropy production in the mixing chamber is worse resolved as the number of points is increased. This is believed to be caused by small length scales associated with the entropy production that are not resolved by the smaller data sets. Improved entropy post-processing models for entropy [39] should be implemented in further work to gain better data and insights into entropy production mechanisms in the flow.

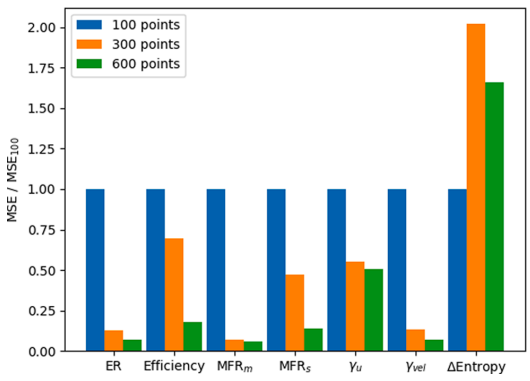

Fig. 3. Comparison of database sizes and the GPR prediction mean-square error for each KPI. The data has been non-dimensionalized by the mean square error for the 100 data point set.

Still, with only 100 data points, the algorithm can accurately calculate a performance map. The average absolute error for entrainment ratio was found to vary between 0.25 and 0.35 [–] with 100 data points, and vary between 0.06 and 0.1 [–] with 600 data points. Using a larger database could ensure even better accuracy of the GPR model, however, due to computational limitations, the study is limited to a 600 point database. The 600 data point set will be analyzed in the following sections as it gave the highest accuracy.

5.1.2. Model prediction

The GPR model can predict the ejector performance at any combination of features, however, its accuracy depends on the proximity to a nearby data point. The predictions can be used to generate a heat-map of ejector performance by varying two features and keeping the remaining constant. Such a performance mapping is presented in Fig. 4a–c in a motive condition P-h diagram using one realization of the GPR model. Here, the features for motive pressure and motive enthalpy are investigated, keeping the remaining features at constant conditions, specified in each figure caption. As shown in Fig. 4a, the model identifies a high-efficiency region near 120–140 [bar] at an enthalpy between 270 and 320 [kJ/kg] for high-pressure lifts (10 [bar]). Here, ejector break-down (no suction flow) occurs for lower motive pressure than 90 [bar]. As the pressure lift is reduced to 7 [bar], Fig. 4b, the high-efficiency region is extended to pressures between 100 and 130 [bar]. Below 100 [bar] the ejector performance quickly drops off and ejector break down occurs for pressures lower than 80 [bar]. As the pressure lift is reduced to 3 [bar], Fig. 4b, the optimum operating point moves to a smaller region closer to 90 [bar]. At low-pressure lifts, using higher pressures than 90 [bar] is not valuable in terms of ejector efficiency. The presented mapping can indicate zones that are optimal operation points for the presented ejector. Furthermore, these performance maps can be easily implemented into dynamic system simulations as a performance evaluation can be calculated within milliseconds.

5.1.3. Performance mapping - characteristic length scales

The GPR model optimizes the characteristic length scales (l in Eq. 15) for each parameter. If a feature is associated with a short characteristic length scale, the data contains more variation in that parameter. When a feature is associated with a characteristic length scale that is large compared to the feature space, then this feature is redundant to predict an output. Table 5 shows the different obtained characteristic length scales for one run of the GPR model. Characteristic length scales were limited to an upper limit of 30 standard deviations in scaled form. Based on these results, some relationships are suggested. First, the motive mass flow rate is primarily governed by the motive enthalpy (temperature) and pressure. This is reasonable as, for a chocked super-sonic flow, the upstream temperature and the upstream and downstream pressure are the primary parameters for the mass flow rate. It was expected that the outlet pressure would have a more significant impact on results, however, these results might indicate that the sampling range for outlet pressure was too small for this effect to be dominant. Second, void fraction uniformity is independent of the performance of the ejector,

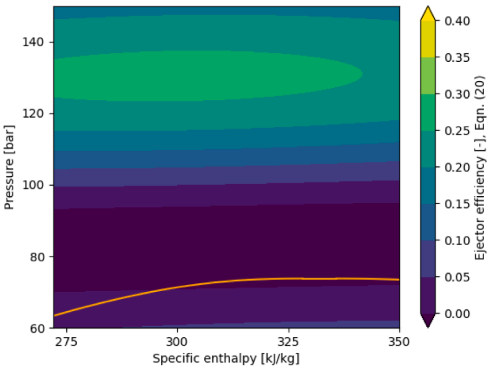

(a) Efficiency contour plot at conditions: $P_s = 35$ [bar], $P_{lift} = 10$ [bar].

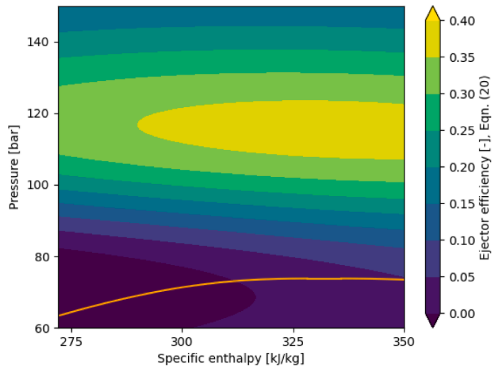

(b) Efficiency contour plot at conditions: $P_s = 38$ [bar], $P_{lift} = 7$ [bar].

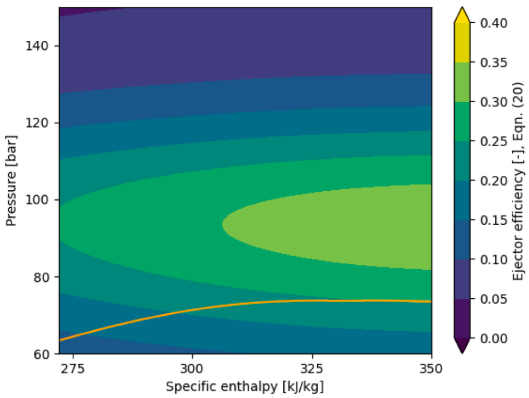

(c) Efficiency contour plot at conditions: $P_s = 42$ [bar], $P_{lift} = 3$ [bar].

Fig. 4. Efficiency (Eq. 20) map in a P-h diagram for motive conditions at different pressure lifts. Saturation line for CO_2 plotted in orange in each subfigure. Suction inlet specific enthalpy is kept constant at 430 [kJ/kg].

Table 5
Optimized characteristic length scales for different outputs. Kernel seed = 40

Output parameter	Optimized characteristic length scale for feature				
	P_m	P_o	P_s	h_m	h_s
Entrainment ratio [–]	2.17	1.65	2.05	2.71	30
Efficiency [–]	1.21	0.342	0.316	3.07	30
MFR_m [kg/s]	5.01	30	30	4.42	30
MFR_s [kg/s]	4.04	2.6	3.88	2.2	30
Velocity uni., [–]γ_u	4.21	3.31	4.28	30	30
Void frac. uni., γ_ϕ [–]	30	30	30	30	30
Entropy prod., ds_{m-d} [–]	1.65	3.17	4.35	12.8	7.63

however, this is found to be caused by the void fraction always being highly uniform at diffuser exit. Third, velocity uniformity is governed primarily by the pressures at the ejector ports and is independent of the motive and suction enthalpy. The remaining outputs (ER, efficiency, MFRs) are dependent on all variables and characteristic length scales, except on suction enthalpy. The independence of mass flow rates on suction enthalpy is believed to be due to the small differences in gas density as a function of enthalpy. This suggests that suction enthalpy can be neglected as a feature for future models as long as the ejector entrains primarily vapor.

5.1.4. Optimization of performance zones

The gradient descent optimization algorithm, see Section 3.2, was used with the GPR model to identify optimal operating regions for the ejector. As an illustration, the algorithm was tasked to optimize motive pressure and enthalpy with other conditions kept constant. A set of ten initial points were randomly sampled from the distribution between +1 and −1 standard deviation from the mean. These initial points were used in the gradient descent optimizer for ejector efficiency. By plotting a line from each starting point to its optimal value, the optimization steps can be visualized. This is shown in Fig. 5, where the optimization paths from random points in the motive P-h diagram and constant conditions P_s = 38 [bar], Plift = 7 [bar] are shown.

Fig. 5 shows that, for all initial positions, the algorithm is able to improve ejector efficiency and find a close to the optimal operating point. The algorithm converges to solutions in the range of 110–112

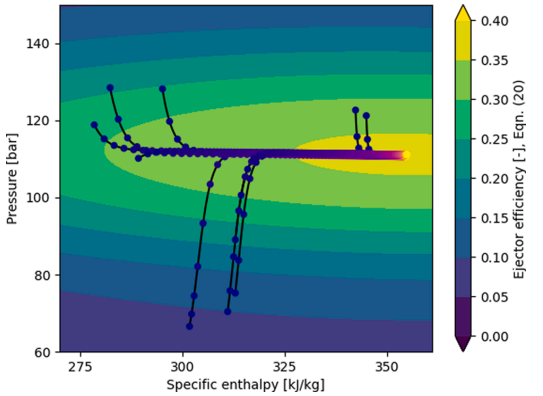

Fig. 5. Optimization paths in a P-h diagram of ejector efficiency from randomized starting positions. Operating conditions: $P_s = 38$ [bar], Plift = 7 [bar] are shown. The optimization path is colored black, and every tenth iteration it plotted with a circle colored according to the iteration number to illustrate convergence.

[bar] for motive pressure P_m and 325–370 [kJ/kg] motive enthalpy h_m with ejector efficiency of 36%. This demonstrates that the algorithm can efficiently find optimal operating conditions using the GPR surrogate model.

5.2. Case 2: Design mapping

Case 2 presents a method of design mapping and optimization of ejector geometry at a given operating condition. In this study, 5 geometric features were included and allowed to vary as presented in Table 2. The choice of geometric dimensions was based on findings from previous studies [7]. This study is limited to 5 geometric features due to the computational costs of sampling additional dimensions. The remaining geometric parameters are set according to the design in Table 3. The operating condition for design optimization is intended for heat pump use cases. With a gas-cooler temperature of 30 °C, the optimal motive pressure is calculated to approximately 85 [bar] using the correlation by Kauf [40]. Suction pressure is set according to the conditions typically found in such applications. The design point is therefore set to: $P_m = 85$ [bar], $T_m = 30[^\circ\mathrm{C}]$, $Ps = 33$ [bar], $T_s = -2[^\circ C]$, $P_{\mathrm{lift}} = 5$ [bar].

5.2.1. Database sampling

An initial database of 300 points was generated using LHC sampling. The calculation of this database took approximately 10 days of computation time on a 32 core computer. Due to the small range of positively performing ejectors ($D_{\mathrm{throat}} < D_{\mathrm{mix}} < 3D_{\mathrm{throat}}$), a second database was sampled based on the results from this first database. In this work, new limits were found manually by inspecting the dataspace, however, this procedure can in the future be automated and use an iterative approach to find the best efficiency ejector geometries.

A secondary database of 200 data points was generated with new limits chosen based on the first iteration. The limits of the first and second databases are shown in Table 6. The main reason for the resampling was that the mixing chamber diameter, being the primary factor influencing the entrainment ratio, dominated the effects of the other parameters due to its large sampling range. The mixing chamber diameter limits were therefore reduced to a range where less variation and all of the positive ER geometries were located. The calculation of this second database took approximately 5 days of computation time on a 32 core computer. The model was fitted to the data set and the accuracy was evaluated with a test set of 15% of the data points, similarly to

Table 6
First and second iteration sampling range.

Parameter	a_{min}	a_{max}
First sampling		
$D_{\mathrm{m-o}}$, [mm]	D_{throat}	1.5 D_{throat}
L_{mix}, [mm]	0	50 D_{mix}
D_{mix}, [mm]	D_{throat}	10 D_{throat}
D_{diff}, [mm]	D_{mix}	10 D_{mix}
α_{d}, [°]	1	90
Second sampling		
$D_{\mathrm{m-out}}$, [mm]	D_{throat}	2 D_{throat}
L_{mix}, [mm]	0	10 D_{mix}
D_{mix}, [mm]	D_{throat}	4 D_{throat}
D_{diff}, [mm]	D_{mix}	10 D_{mix}
α_{d}, [°]	1	90

Section 5.1.1. Based on the test data the average absolute error for entrainment ratio value was 0.07 [–]. The following results are discussed with the second iteration database.

5.2.2. Model prediction

First, each feature size is varied with the remaining features set constant according to their baseline values (Table 3). The GPR model predicted efficiency is then plotted as a function of each feature size, non dimensionalized by its maximum value, shown in Fig. 6a and b. Both figures show the ejector efficiency under single variable variations using different samples from the GPR function space. This is to illustrate that different realizations of the GPR will converge to different solutions. These results show that optimizing each of these dimensions in isolation can yield significant efficiency improvements. The mixing chamber diameter is very sensitive to optimization and shows a narrow zone of high efficiency. This trend is found in both samples of the GPR model. Similarly, the same functional relationship for mixing chamber length is found in both samples. The diffuser angle relationship is similar for both function samples, however, the optimum value is slightly different. This indicates that more data should be collected in the range of small diffuser angles. The relationship for the motive outlet diameter suggests that only this diameter has only a minor influence on performance. However, as the motive outlet diameter is increased, the ejector performance is reduced, likely due to shock-losses caused by motive flow over-expansion. The predicted performance curve with varied diffuser outlet diameter is different between the two samples, which indicates that the database contains too little information on the relationship to separate from the dominant features; D_{mix}, L_{mix}, and α_d.

Using the combined information from these two samples, the optimal motive outlet diameter from sample B and the optimal outlet diameter from sample A, the individually optimized size of each design parameter was found to be; $D^o_{\mathrm{m-out}}$ =1.78 [mm], $D^O_{\mathrm{mix}} = 3.98$ [mm], $L^O_{\mathrm{mix}} = 23.0$ [mm], $\alpha^O_d = 11.6^\circ$, $D^O_{\mathrm{diff}} = 28.1$ [mm] with a predicted efficiency of 0.42–44 (–). In comparison, the baseline design has a predicted efficiency of 0.40 [–]. The superscript *o* indicates optimum values by isolated optimization. Such a design lies remarkably close to the initially designed ejector (Table 3) in terms of mixing chamber length and diameter.

The motive outlet diameter of an ejector is designed such that the motive nozzle expansion matches the ejector mixing chamber pressure. This achieves the best efficiency as there are lower losses associated with the under- and over-expansion of the motive flow. The individually optimized motive outlet diameter is therefore expected to lie close to this point. As each data point corresponds to a CFD simulation, it is possible to inspect individual ejector data points in detail to investigate this hypothesis. A data point with a motive outlet diameter of 1.77 [mm], close to $D^o_{\mathrm{m-out}}$, is chosen from the database and the pressure

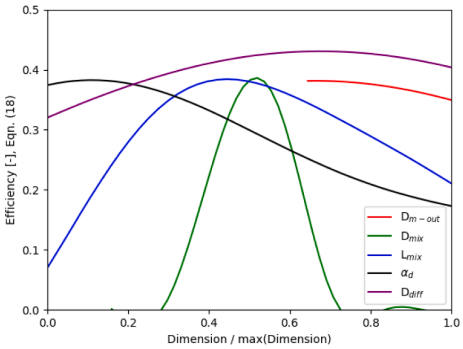

(a) Sample A. Solid line shows predicted efficiency with each dimension varied in isolation. X-axis is non-dimensionalized with the maximum value in the range. Seed 40.

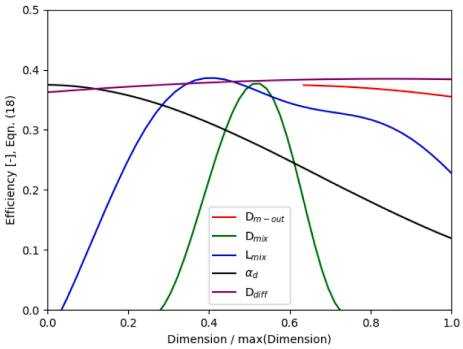

(b) Sample B. Solid line shows predicted efficiency with each dimension varied in isolation. X-axis is non-dimensionalized with the maximum value in the range. Seed 33.

Fig. 6. Plot of ejector efficiency with each dimension varied in isolation with the remaining dimensions left constant as the individual optimum values. Two different randomization seed samples for the training data sets.

profile is shown in Fig. 7. The motive expansion pressure matches the ejector mixing chamber pressure within 1 [bar], illustrating that the algorithm is able to find reasonable design parameters and demonstrating how the database of CFD results can be used to investigate design improvements.

5.2.3. Optimization of design

From previous studies [15,14], it is generally agreed that optimal ejector geometry must be found by optimizing the different parameters of the ejector geometry simultaneously. To better understand the relationships between each design parameter, a performance heat map was generated based on two geometry parameters at a time. As an example, the ejector efficiency for varying mixing diameter and lengths is shown in Fig. 8a with the remaining parameters left constant at the values obtained by single variable optimization. A high efficiency zones is identified near the previous optimal values at $D_{\text{mix}} \approx 4$ [mm] and

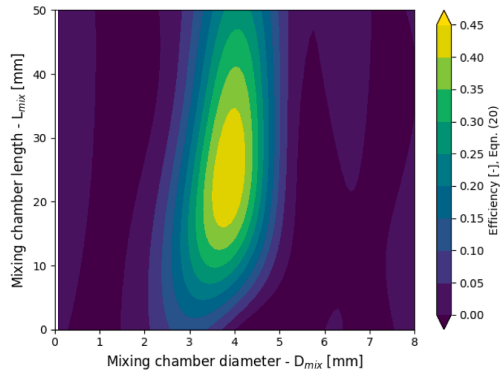

(a) Efficiency contour plot in a D_{mix}-L_{mix} design space. Other parameters kept constant at the individually optimized geometry parameters.

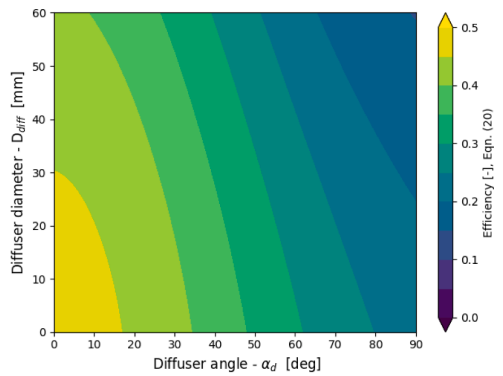

(b) Efficiency contour plot in a α_d-D_{diff} design space. Other parameters kept constant at the individually optimized geometry parameters.

Fig. 8. Efficiency plot of GPR design space prediction.

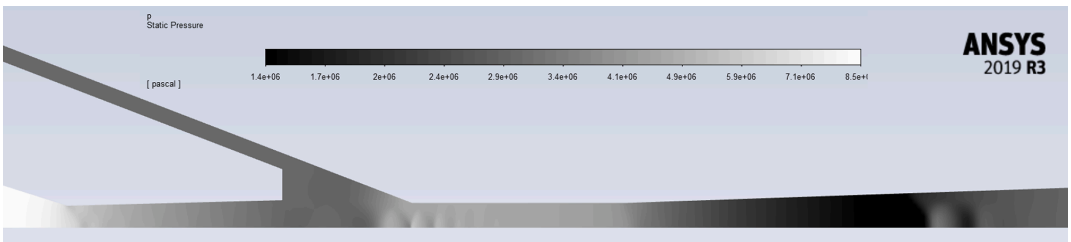

Fig. 7. Pressure distribution for datapoint #46 with dimensions: D_{m-out} =1.77 [mm], D_{mix} = 1.59 [mm], L_{mix} = 6.9 [mm], α_d = 3.9°, D_{diff} = 11.9 [mm]. The gray-color scale is log-scaled.

$L_{mix} \approx 25$ [mm]. The predicted ejector efficiency at varied diffuser geometry parameters (α_d, D_{diff}) with remaining parameters as the individual optimum values is shown in Fig. 8b. These results indicate that outlet diameters in the range of 0–20 [mm] and small diffuser diverging angles yield the highest efficiency. Further investigation with a refined database for this region of diffuser geometries is left for future work.

The designs suggested by inspection using the GPR methodology suggests designs with similar dimensions to the initial baseline design. This gives a good indication that the algorithm suggests designs that comparable to designs produced by 1D approaches [41] within a few iterations of database generation. With additional iterations of database refinement, the algorithm is believed to converge to a better, more accurate representation and a better design. A validation of the surrogate model optimized design is conducted in Section 5.2.5.

A more general approach to design optimization is to use an optimizer function on the GPR model. The gradient descent method, as described in previous sections, was used on the GPR model for design parameters. 10 initial points were sampled and optimized for maximizing ejector efficiency. The gradient descent path was constrained such that the ejector optimization algorithm would not suggest negative lengths or angles. The results are presented in Table 7. Of the 10 initial conditions, 8 ended up at the same solution with an efficiency of 43%. The remaining 2 simulations found local optimums with very poor efficiency. The optimized solution converges to a solution close to the previously mentioned individually optimal solution. To improve the design further additional sampling of the database is necessary, which is left to further work.

5.2.4. Design mapping - characteristic length scales

Similarly to Section 5.1.3, the optimized characteristic length scales associated with each geometric design parameter for the prediction of the different KPIs are investigated, shown in Table 8. Some self-evident relationships are apparent from the data. Firstly, the motive mass flow rate is not dependent on the geometry features downstream of the nozzle due to supersonic choking, and the dependency on motive outlet diameter is negligible for this range of motive outlet diameters. As the motive mass flow rate is approximately independent of the model features, the suction mass flow rate, entrainment ratio, and efficiency are closely connected. These features are primarily dependent on the mixing chamber geometry (D_{mix},L_{mix}) and the diffuser angle, which agrees with the previous experimental findings [6,7]. The outlet flow uniformity for velocity and void-fraction is, as expected, dependent only on the diffuser geometry. Lastly, the entropy production in the mixing chamber is primarily governed by the mixing chamber geometry. Further study into these parameters should be conducted in the future to better understand these relationships.

5.2.5. CFD simulation of the optimized ejector design

The CFD predictions with the optimal ejector design may not necessarily agree with the GPR performance predictions. To verify the performance of the GPR optimization, three designs with high predicted ejector efficiency were evaluated with new CFD simulations. The tested designs and the resulting predictions are shown in Table 9 and Fig. 9. The model predictions were very close to the CFD results for all three points, with less than 6% maximum deviation. Additionally, the correct trend is predicted and the best entrainment ratio is found for the optimized design. This very good agreement confirms that our novel approach is a highly useful tool for optimization studies.

Table 7
Optimized designs based on gradient descent

#	D_{m-out} [m]	D_{mix} [m]	L_{mix} [m]	α_D [°]	D_{diff} [m]	Efficiency [–]
1	0.0016	0.0039	0.024	2.4	0.028	0.43
2	0.0016	0.0039	0.024	2.4	0.028	0.43
3	0.0022	0.0059	0.038	78.2	0.004	0.01
4	0.0016	0.0039	0.024	2.4	0.028	0.43
5	0.0016	0.0039	0.024	2.4	0.028	0.43
6	0.0016	0.0039	0.024	2.4	0.028	0.43
7	0.0016	0.0039	0.024	2.4	0.028	0.43
8	0.0022	0.0058	0.000	15.4	0.037	0.02
9	0.0016	0.0039	0.024	2.4	0.028	0.43
10	0.0016	0.0039	0.024	2.4	0.028	0.43

Table 8
Optimized characteristic length scales for different outputs. Kernel seed = 8

Output parameter	Optimized characteristic length scale for feature				
	D_{m-out}	D_{mix}	L_{mix}	α_D	D_{diff}
ER [–]	9.22	1.68	1.18	5.48	30
Efficiency [–]	7.09	0.48	1.36	1.95	27.8
MFR_m [kg/s]	30	30	30	30	30
MFR_s [kg/s]	9.31	1.65	1.18	5.45	30
γ_u [–]	30	30	18.4	15.9	0.585
γ_ϕ [–]	30	30	18.4	15.9	0.585
ds_m-d [–]	30	0.13	7.03	30	30

5.3. Case 3 - Flow structures

The large databases of CFD contains additional information on the 2D flow structures that occur in the ejector. Analysis of the flow structure is in general a challenging problem due to the lack of clear distinctions of flow regimes and regions. As an example, the assumption of two distinctive motive and suction flows that exchange momentum is common in 1D models, however with detailed multidimensional CFD data such a distinction may not exist. Still, detailed knowledge of flow structures and how these vary with changing operating conditions and ejector design is highly valuable for the design process.

Case 3 presents a novel application of the GPR model, namely, to predict the internal flow structures of the ejector using the detailed CFD data. Here, the study is limited to investigating the pressure and velocity along pathlines of the motive and suction flow.

The flow structure inside the ejector is analyzed and mapped along particle pathlines inside the ejector where the curve length parameter, c, is used as a parameter for the GPR model. The velocity and pressure data along these pathlines from the CFD simulations are then used to train the GPR model. By training the GPR model with different ejector design parameters the flow structures can be analyzed as a function of the ejector design. In comparison to predicting the performance KPIs, this is a much harder problem due to the GPR model not having any knowledge of the flow physics. This tool will therefore primarily be used to gain insight into the trends of the ejector flow structures.

The pathlines of the suction and motive flow are illustrated in Fig. 10. Due to the large amount of data available in each CFD simulation, a small database with 25 CFD data points was generated. This database was uniformly sampled over the mixing chamber diameter and mixing chamber length design space in the ranges $10 < L_{mix} < 50$ [mm] and $3 < D_{mix} < 5$ [mm], respectively. The pathlines are defined from the suction and motive inlets to the ejector outlet. Along these pathlines, the different flow variables are reported and post-processed by the algorithm. As the number of data points along each pathline is in most cases several thousand, the data was reduced by averaging over increments of

Table 9
Comparison of entrainment ratio between GPR prediction and CFD model for optimized designs. $D_{m-out} = 1.77$ [mm], $D_{mix} = 3.82$ [mm], $D_{diff} = 65.1$ [mm].

Geometry	#1	#2	#3
L_{mix} [mm]	13.47	27	27
α_D [°]	15.8	15.8	5.0
ER GPR	0.601	0.714	0.742
ER CFD	0.598	0.753	0.793

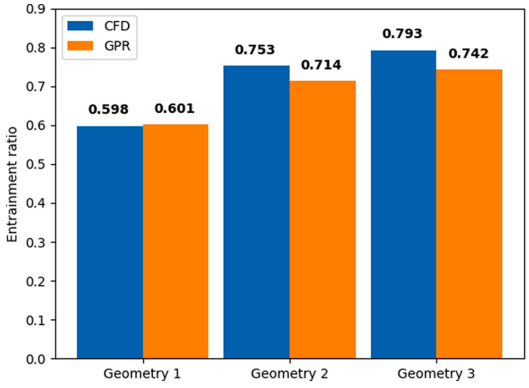

Fig. 9. Comparison of entrainment ratio predicted by the GPR model and new CFD validation points with geometries given according to Table 9.

30 steps along the pathline.

The GPR model is trained to predict the flow variable distributions along the different pathlines. The mixing chamber geometry parameters and the pathline length parameter are chosen as the model features. Fig. 11a–b shows a scatter plot of the CFD data and the predicted pressure along the central suction flow pathline. The CFD data for that geometry was hidden for the GPR predictor to verify the model accuracy when interpolating between ejector geometries. Even with the specific predicted geometry data hidden, a decent match between the CFD data and the predicted velocity and pressure distribution with a mean velocity error of 2.2 [m/s] and 0.13 [bar]. In Fig. 11a, the general pressure structures are reproduced with high accuracy. The method captures the pressure drop occurring in the mixing chamber due to a motive shock train. Still, the predicted shock strength for the smallest mixing chamber length, Fig. 11b, is not well resolved and the shock strength is overpredicted by approximately 2 [bar]. This is likely due to the short length scales and discontinuities along the path line.

A detailed insight into the effects of different design choices on the flow structure is useful for ejector design. This model can give a prediction of the changes to the local flow variables, such as velocity and pressure distributions, as a function of different design variables. An example of such an application is shown in Fig. 12a and b. Fig. 12a shows the predicted velocity along the central suction flow pathline as a function of the mixing chamber diameter for a constant mixing chamber length of 30 [mm]. The figure shows that the highest velocities are achieved with the smallest diameters due to the constricted size of the mixing chamber. For the smallest ejector diameters ($D_{\text{mix}} = 3-3.5$ [mm]), the suction MFR (ejector efficiency) is limited by the suction flow area. As the mixing chamber diameter is increased, the suction flow velocity in the ejector is reduced due to the larger flow area and the lowered mixing efficiency. At a mixing diameter of 4 [mm], the maximum ejector efficiency is reached, where the optimal compromise between mixing efficiency and flow area is found. Fig. 12b shows the predicted velocity as a function of the mixing chamber length for a mixing chamber diameter of 4 [mm]. In this data set, the shortest mixing sections were associated with the highest ejector efficiency. As the mixing chamber length is increased, the velocity of the suction flow is reduced and the high-velocity region is extended. For mixing chambers longer than 30 [mm], the predicted velocity distribution in the mixing section is flattened out. This implies that less momentum is transferred from the motive to the suction flow and that the only effect of extending the mixing section beyond 30 [mm] is increasing wall friction.

The presented methodology allows insight into design decisions on a flow structure level. The method can be used as a tool to better predict different flow structures and losses in the ejector. Still, accurately predicting sharp gradients such as shocks is a major challenge for the methodology. Therefore, to produce accurate predictions of flow structures large data sets are needed due to the larger variation of flow structures between ejector geometries and operating conditions.

5.4. Discussion

This approach to ejector mapping and optimization shows great promise both for off-design performance mapping, design mapping, and shape optimization. The algorithm is able to identify high-efficiency regions in design and operating conditions. The algorithm can identify optimized designs, and can by iteration be improved to sample appropriate ranges of data. In addition, the benefits of using CFD data for data points are used to verify ejector designs and investigate flow structures in ejectors. However, some limitations of this modeling approach should be addressed in further work, discussed below.

5.4.1. CFD model accuracy

The GPR machine learning model can only be as good as the data collected. In this study, we have assumed that the CFD results are deterministic, i.e. that the same calculation will always yield the same result. However, due to numerical errors, this cannot be guaranteed. Numerical errors due to poor convergence, poor mesh, or numerical solution errors can affect the CFD model results. This is even more significant if a larger database using data from various sources, such as numerical and experimental data collected from the literature. Ejector meshing is a significant source of numerical errors. Consistent meshing between different ejector designs is challenging due to the large variation in shape and proportions occurring within possible ejector configurations.

Furthermore, the accuracy of the underlying CFD models must be taken into account. As found in previous works [5], the motive nozzle MFR can be quite accurately predicted in the supercritical region, where

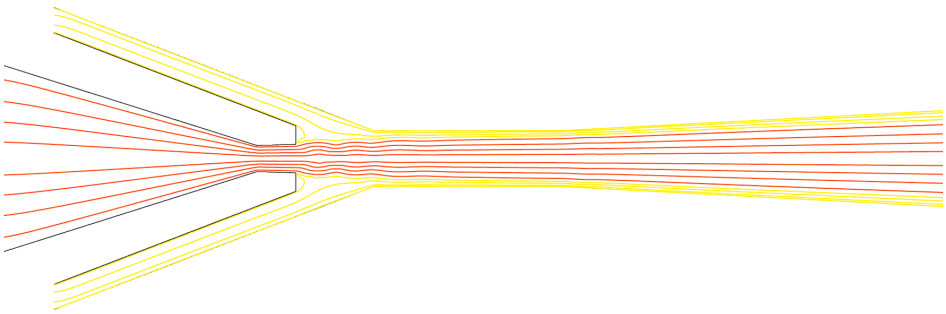

Fig. 10. Illustration of the pathlines of the suction (colored yellow) and the motive (colored red) flows.

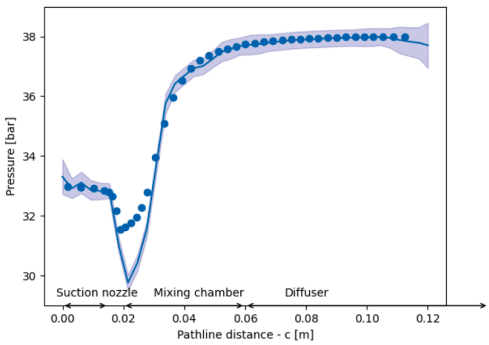

(a) Predicted pressure distribution (line plot) for mixing chamber length $L_{\text{mix}} = 0.01$ [m] along the central suction pathline with the data for the specified geometry hidden to the model.

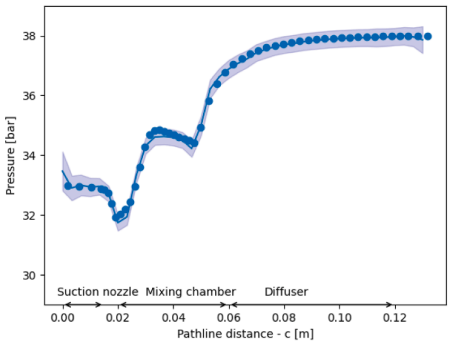

(b) Predicted pressure distribution (line plot) for mixing chamber length $L_{\text{mix}} = 0.03$ [m] along the central suction pathline with the data for the specified geometry hidden to the model.

Fig. 11. Predicted velocity distribution (line plot) along the central suction pathline for two geometries with a mixing chamber diameter of $D_{\text{mix}} = 0.004$ [m]. Verification CFD data marked with circles. The colored area correspond to the predicted velocity $+-$ 1 standard deviation.

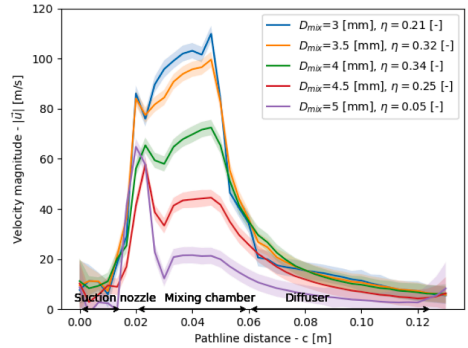

(a) Predicted velocity distribution (line plot) along the central suction pathline as a function of mixing chamber diameter. Mixing chamber length set to $L_{\text{mix}} = 30$ [mm].

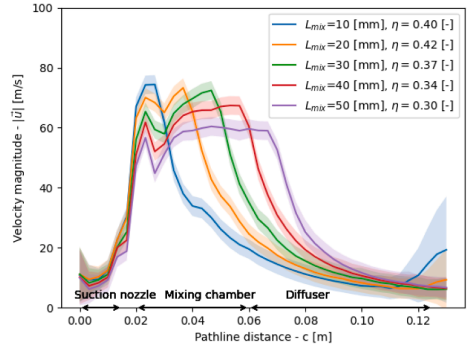

(b) Predicted velocity distribution (line plot) along the central suction pathline as a function of mixing chamber length. Mixing chamber diameter set to $D_{\text{mix}} = 4$ [mm].

Fig. 12. Predicted pressure distribution (line plot) along the central suction pathline for two geometries. Verification CFD data marked with circles. The colored area correspond to the predicted pressure +- 1 standard deviation. Approximate locations of the different ejector sections is shown on the x-axis. Ejector efficiency for each design shown in the figure legend.

this study has been primarily focused. However, the suction flow is often less accurately predicted. Up to 20% error between experimental and numerical results can be observed. This will have a significant impact on the accuracy and validity of the optimized design. Further research into suction flow prediction is necessary to fully leverage the potential of these optimization models. In this work, the motive pressure has been kept above critical to ensure that the HEM accurately represents the flow physics. However, as the motive pressure is reduced, non-equilibrium effects become dominant and must be taken into account. As there is a strong ongoing research effort on this topic, the authors fully expect that numerical methods will soon handle non-equilibrium effects with similar performance as the HEM in the supercritical region. The method developed here will be immediately able to profit from these developments. Accurate prediction of flow separation in the ejector is highly dependent on the CFD model accuracy. Wall shear stress in a turbulent multiphase flow is very complex and is highly dependent on specific CFD model choices, such as wall-mesh resolution and turbulence wall models. This makes the prediction of flow separation highly challenging and should be further investigated in future works.

5.4.2. GPR modelling

The GPR modeling approach has proven to be able to accurately reproduce CFD-generated ejector performance maps in various configurations. However, the GPR modeling method is sensitive to user errors, poor data, and outliers. It is important to be critical to the model prediction as this is a meta-model, meaning that it makes predictions based on previous model results, which can amplify errors. This work has shown that an appropriate choice of data sampling range is important for optimization, and previous knowledge should be implemented in the model at an early stage. Additionally, that the sampling range and number of data points should be chosen with care. Model accuracy is highly dependent on the number of data points. It is also key to sample such that the mean lies close to the optimal design. In this work, all features were sampled with equal density by the LHC method. This is not optimal as the different features contain different amounts of information about the different KPIs. In further work, alternative data-efficient and adaptive sampling strategies should be explored. The number of required data points scales with the number of features sampled. This study has used 5 features for each use case due to the exponentially

increasing computational costs per additional feature. The number of features and the number of data points should be chosen on a case-by-case basis. Future studies are suggested to explore feature space optimization by use of, for example, Principal Component Analysis (PCA). This could reduce the number of dimensions and the number of data points.

In this work, an iterative approach to data sampling was used based on manual inspection of the data. Further work should investigate the effect of automatically identifying high-performance regions and adaptively sample those regions. This approach can, using the GPR model, be combined with estimated uncertainty to ensure that the optimal datapoint distribution is obtained. While the generation of the 200 point database took 5 days of computation time, the method is trivially extendable to large computing clusters as the simulations of different data points are independent.

5.4.3. Flow structure analysis

A challenge that has been highlighted in the literature on response surface modeling for ejectors is the sharp gradients that occur in the design space [42]. The nonlinearities and discontinuities that occur in super-sonic ejectors are challenging to capture with simple regression methods. The GPR methodology can account for several of these structures and non-linearities, however still needs high data density in regions with large gradients for accurate predictions. The use of GPR for these predictions can be further applied to predict the 2D or 3D flow structures as well. However, as the amount of data scales rapidly with additional dimensionality, it is expected to be computationally inefficient. One of the main challenges with such an approach is the large variation in flow structures that occur inside ejectors. These structures may furthermore change abruptly with ejector design or operating conditions. Examples of such conditions are the large gradients associated with the thermodynamics near the critical point of the working fluid or the on-set of supersonic flow.

5.5. Open access tool - GPR model and data

The resulting dataset and GPR model are openly available online. The GPR prediction tool is available as Python 3.9 code based on the Scikit package [29]. The data is openly available for other researchers, and further analysis of and extensions to the databases of ejector data is encouraged. The data is organized as Comma Separated Value - files with all available geometry parameters, operating conditions, flow variables along pathlines, and KPIs. For more details regarding the use of the GPR model in Scikit, see Pedregosa et al. [29]. https://github.com/knutringstad/Ejector_GPR

6. Challenges and further work

This work has demonstrated the possibility to use machine learning on large CFD model databases for component optimization. The primary application for this algorithm is for CO_2 (R744) two-phase ejector design, but may easily be adapted for other working fluids or single-phase ejectors. In future work, the algorithm should be optimized to minimize user input and be close to fully automated. One such method would involve determining several ejector geometry parameters based on predetermined requirements. For example, the motive throat diameter can be determined to produce a given mass flow rate at a certain pressure. The motive outlet diameter can be chosen such that the motive nozzle expansion perfectly matches the mixing chamber pressure, and the outlet diameter such that the outlet velocity is below a certain value. An optimized set of ejector dimensions or a combination of dimensions, could be chosen as features and iteratively and adaptively sampled to optimize ejector operation. The current model optimizes for a single operating point, however, it is possible to optimize performance at a range of operating conditions simultaneously.

Looking forward, it is possible to consider using this approach to cover a combination of operating conditions and ejector geometry. This has the potential to optimize ejector performance and design in all possible combinations. However, this will require a large dataset. Such a dataset could be generated by combining available ejector data from experimental and numerical investigations found in the literature.

The performance maps generated in this work can be implemented into system scale dynamic simulations, similarly to the work by Haida et al. [11] for a multi-ejector module. The presented methodology can for such applications be adapted to the specific ejector geometry and operating conditions of the system, which may increase model accuracy.

Another potential application of the GPR model is to investigate CFD model error prediction, both in comparison to experimental data and in terms of mass conservation. Lastly, it is noted that this approach is generic and can be used for many other applications and components, both for optimization and performance mapping.

The use of GPR analysis in combination with CFD data shows promise as a methodology for predicting flow structures in the ejector. Future work should further explore alternative methods for analyzing the flow data. The prediction of flow separation in the ejector suction chamber and diffuser could be an important tool to avoid losses in the ejector. This could be predicted by analyzing the flow vorticity inside the different ejector sections, or by analyzing the wall shear stress. Additional analysis of mixing efficiency and momentum transfer is of interest and could be analyzed by looking into the jet boundary layer inside the ejector [43]. Another application for the GPR methodology is for the prediction of the different sources of entropy production. By analyzing the local sources of entropy production, such as viscous dissipation and heat transfer, additional insights into the relationships between entropy production and ejector design could be gained [39,44] and further analyzed using GPR. Though the GPR model struggles with capturing the strength and location of super-sonic shock distributions in the ejector, further work should be dedicated toward alternative methods for predicting shock and their related losses in the ejector. As presented in this paper, these flow structure analyses can be introduced into the GPR model either as a KPI or as a local flow variable predicted along the ejector dimensions.

A further application of the flow structure prediction tool is for CFD computation speed-up. As the general structure of several main flow variables can be predicted, the data may be used as initial conditions. This may allow CFD calculations to converge faster as the initial state is closer to the converged solution. Further work should investigate the possibility of including such a method for computational speed up.

7. Conclusions

In this work, the GPR machine learning tool for R744 two-phase ejector design has been trained using large databases of CFD data. An automated algorithm for the generation of CFD databases is presented and used to produce databases of high-quality CFD data for ejectors at various ejector operating conditions and geometries. The data is used to train a GPR model for three cases. First, a performance map of an ejector at various pressure and temperature operating conditions is presented. The model is able to reproduce CFD data for entrainment ratio with $+-0.1$ [–]. Secondly, a mapping of ejector performance factors with various ejector geometries was generated using the surrogate model with similar accuracy within an entrainment ratio of $+-0.07$ [–]. A gradient descent optimization algorithm was implemented and used to optimize ejector operation and ejector design. The final ejector design was found to have an ejector efficiency of 43%. Further improvements could be gained by increasing the number of data points in regions of high efficiency. Last, the GPR model was applied for flow structure prediction from the local CFD data using a database with varied mixing chamber geometries. The method was able to predict different pressure- and velocity structures along the suction flow pathlines within 0.13 [bar] and 2.2 [m/s]. Based on this prediction tool, the optimal combination of mixing chamber length and diameter was analyzed.

To facilitate and encourage further developments with this design method, the data and trained GPR model are made available open-access. Several suggestions for further work have been discussed, where the emphasis is put on the further development of models and methodologies to improve the ejector design process. Improvements to flow structure analysis tools, further study into the details of the machine learning models, and higher accuracy of the underlying CFD models are highlighted topics for future development. By integrating a complete methodology to encompass prediction of ejector performance and flow structures under varied operating conditions and ejector designs, the design of ejectors may in the future be designed quicker, with higher accuracy and a better understanding of design trade-offs.

Declaration of Competing Interest

The authors declare that they have no known competing financial interests or personal relationships that could have appeared to influence the work reported in this paper.

Acknowledgement

The work is part of HighEFF - Centre for an Energy Efficient and Competitive Industry for the Future, an 8-year Research Centre under the FME-scheme (Centre for Environment-friendly Energy Research, 257632). The authors gratefully acknowledge the financial support from the Research Council of Norway and user partners of HighEFF.

References

[1] (RIVM) National Institute for Public Health and the Environment, Contribution of HFCs to the greenhouse effect, 2018. https://www.rivm.nl/en/hydrofluorocarbons/contribution-of-hfcs-to-greenhouse-effect.
[2] European Commision, Regulation (EU) No 517/2014 of the European Parliament and of the Council of 16th April 2014 on fluorinated greenhouse gases and repealing Regulation (EC) No 842/2006, 2014.
[3] S. Girotto, S. Minetto, P. Neksa, Commercial refrigeration system using CO2 as the refrigerant, Int. J. Refrig. 27 (2004) 717–723, https://doi.org/10.1016/j.ijrefrig.2004.07.004.
[4] S. Elbel, N. Lawrence, Review of recent developments in advanced ejector technology, Int. J. Refrig. 62 (2016) 1–18, https://doi.org/10.1016/J.IJREFRIG.2015.10.031, https://www.sciencedirect.com/science/article/pii/S0140700715003266.
[5] K.E. Ringstad, Y. Allouche, P. Gullo, Å. Ervik, K. Banasiak, A. Hafner, A detailed review on CO2 two-phase ejector flow modeling, Therm. Sci. Eng. Prog. 20 (2020) 100647, https://doi.org/10.1016/j.tsep.2020.100647.
[6] M. Nakagawa, A. Marasigan, T. Matsukawa, A. Kurashina, Experimental investigation on the effect of mixing length on the performance of two-phase ejector for CO2 refrigeration cycle with and without heat exchanger, Int. J. Refrig. 34 (2011) 1604–1613, https://doi.org/10.1016/J.IJREFRIG.2010.07.021, https://www.sciencedirect.com/science/article/pii/S0140700710001672.
[7] K. Banasiak, A. Hafner, T. Andresen, Experimental and numerical investigation of the influence of the two-phase ejector geometry on the performance of the R744 heat pump, Int. J. Refrig. 35 (2012) 1617–1625, https://doi.org/10.1016/J.IJREFRIG.2012.04.012, https://www.sciencedirect.com/science/article/pii/S014070071200093X.
[8] J. Hu, J. Shi, Y. Liang, Z. Yang, J. Chen, Numerical and experimental investigation on nozzle parameters for R410A ejector air conditioning system, Int. J. Refrig. 40 (2014) 338–346, https://doi.org/10.1016/j.ijrefrig.2013.12.008.
[9] P. Gullo, M.R. Kærn, M. Haida, J. Smolka, S. Elbel, A review on current status of capacity control techniques for two-phase ejectors, 2020. doi:10.1016/j.ijrefrig.2020.07.014.
[10] M. Haida, J. Smolka, A. Hafner, Z. Ostrowski, M. Palacz, A.J. Nowak, K. Banasiak, System model derivation of the CO2 two-phase ejector based on the CFD-based reduced-order model, Energy 144 (2018) 941–956, https://doi.org/10.1016/j.energy.2017.12.055, https://www.sciencedirect.com/science/article/pii/S0360544217320881?via%3Dihub.
[11] M. Haida, R. Fingas, W. Szwajnoch, J. Smolka, M. Palacz, J. Bodys, A. Nowak, M. Haida, R. Fingas, W. Szwajnoch, J. Smolka, M. Palacz, J. Bodys, A.J. Nowak, An Object-Oriented R744 Two-Phase Ejector Reduced-Order Model for Dynamic Simulations, Energies 12 (2019) 1282, https://doi.org/10.3390/en12071282, https://www.mdpi.com/1996-1073/12/7/1282.
[12] M. Palacz, J. Smolka, W. Kus, A. Fic, Z. Bulinski, A.J. Nowak, K. Banasiak, A. Hafner, CFD-based shape optimisation of a CO_2 two-phase ejector mixing section, Appl. Therm. Eng. 95 (2016) 62–69, https://doi.org/10.1016/j.applthermaleng.2015.11.012, https://www.sciencedirect.com/science/article/pii/S1359431115012478.
[13] M. Palacz, J. Smolka, A.J. Nowak, K. Banasiak, A. Hafner, Shape optimisation of a two-phase ejector for CO2 refrigeration systems, Int. J. Refrig. 74 (2017) 210–221, https://doi.org/10.1016/j.ijrefrig.2016.10.013, https://www.sciencedirect.com/science/article/pii/S0140700716303425.
[14] Y. He, J. Deng, Y. Li, X. Zhang, Synergistic effect of geometric parameters on CO2 ejector based on local exergy destruction analysis, Appl. Therm. Eng. 184 (2021) 116256, https://doi.org/10.1016/j.applthermaleng.2020.116256.
[15] K. Banasiak, M. Palacz, A. Hafner, Z. Buliński, J. Smołka, A.J. Nowak, A. Fic, A CFD-based investigation of the energy performance of two-phase R744 ejectors to recover the expansion work in refrigeration systems: An irreversibility analysis, Int. J. Refrig. 40 (2014) 328–337, https://doi.org/10.1016/j.ijrefrig.2013.12.002, https://www.sciencedirect.com/science/article/pii/S0140700713003812.
[16] Y. He, J. Deng, Y. Li, L. Ma, A numerical contrast on the adjustable and fixed transcritical CO2 ejector using exergy flux distribution analysis, Energy Convers. Manage. 196 (2019) 729–738, https://doi.org/10.1016/j.enconman.2019.06.031.
[17] J. Smolka, Z. Bulinski, A. Fic, A.J. Nowak, K. Banasiak, A. Hafner, A computational model of a transcritical R744 ejector based on a homogeneous real fluid approach, Appl. Math. Model. 37 (2013) 1208–1224, https://doi.org/10.1016/j.apm.2012.03.044, https://www.sciencedirect.com/science/article/pii/S0307904X12002077.
[18] C. Lucas, H. Rusche, A. Schroeder, J. Koehler, Numerical investigation of a two-phase CO2 ejector, Int. J. Refrig. 43 (2014) 154–166, https://doi.org/10.1016/j.ijrefrig.2014.03.003, https://www.sciencedirect.com/science/article/pii/S0140700714000504.
[19] Y. Fang, S. Poncet, H. Nesreddine, Y. Bartosiewicz, An open-source density-based solver for two-phase CO2 compressible flows: verification and validation, Int. J. Refrig. (2019), https://doi.org/10.1016/j.ijrefrig.2019.05.016 https://www.sciencedirect.com/science/article/pii/S0140700719302129#bib0034.
[20] M. Haida, J. Smolka, A. Hafner, M. Palacz, K. Banasiak, A.J. Nowak, Modified homogeneous relaxation model for the R744 trans-critical flow in a two-phase ejector, Int. J. Refrig. 85 (2018) 314–333, https://doi.org/10.1016/j.ijrefrig.2017.10.010, https://www.sciencedirect.com/science/article/pii/S0140700717303948.
[21] R.B. Barta, P. Dhillon, J.E. Braun, D. Ziviani, E.A. Groll, Design and optimization strategy for ejectors applied in refrigeration cycles, Appl. Therm. Eng. 189 (2021) 116682, https://doi.org/10.1016/J.APPLTHERMALENG.2021.116682.
[22] R.B. Gramacy, Surrogates: Gaussian Process Modeling, Design and Optimization for the Applied Sciences, Chapman Hall/CRC, Boca Raton, Florida, 2020 http://bobby.gramacy.com/surrogates/.
[23] A. Maghsoodi, E. Afshari, H. Ahmadikia, Optimization of geometric parameters for design a high-performance ejector in the proton exchange membrane fuel cell system using artificial neural network and genetic algorithm, Appl. Therm. Eng. 71 (2014) 410–418, https://doi.org/10.1016/J.APPLTHERMALENG.2014.06.067.
[24] M.M. Rashidi, A. Aghagoli, R. Raoofi, Thermodynamic analysis of the ejector refrigeration cycle using the artificial neural network, Energy 129 (2017) 201–215, https://doi.org/10.1016/J.ENERGY.2017.04.089.
[25] C. Haoran, C. Wenjian, Artificial neural network modeling for variable area ratio ejector, in, in: 9th IEEE Conference on Industrial Electronics and Applications, 2014, pp. 220–225, https://doi.org/10.1109/ICIEA.2014.6931162.
[26] P. Chaurasia, K. Younis, O.S. Qadri, G. Srivastava, K. Osama, Comparison of Gaussian process regression, artificial neural network, and response surface methodology modeling approaches for predicting drying time of mosambi (Citrus limetta) peel, J. Food Process Eng 42 (2019) e12966, https://doi.org/10.1111/JFPE.12966, https://onlinelibrary.wiley.com/doi/full/10.1111/jfpe.12966.
[27] ANSYS, ANSYS fluent theory guide. Release 19.0., Canonsburg, 2018.
[28] I.H. Bell, J. Wronski, S. Quoilin, V. Lemort, Pure and Pseudo-pure Fluid Thermophysical Property Evaluation and the Open-Source Thermophysical Property Library CoolProp, Ind. Eng. Chem. Res. 53 (2014) 2498–2508.
[29] F. Pedregosa, G. Varoquaux, A. Gramfort, V. Michel, B. Thirion, O. Grisel, M. Blondel, P. Prettenhofer, R. Weiss, V. Dubourg, J. Vanderplas, A. Passos, D. Cournapeau, M. Brucher, M. Perrot, E. Duchesnay, Scikit-learn: Machine Learning in Python, J. Mach. Learn. Res. 12 (2011) 2825–2830.
[30] D.C. Liu, J. Nocedal, On the limited memory BFGS method for large scale optimization, Math. Program. 1989 45:1 45 (1989) 503–528. https://link.springer.com/article/10.1007/BF01589116. doi:10.1007/BF01589116.
[31] C.E. Rasmussen, C.K.I. Williams, Gaussian Processes for Machine Learning, Massachusetts Institute of Technology, 2006.
[32] H. Sit, C.J. Earls, Gaussian Process Regression for Estimating EM Ducting Within the Marine Atmospheric Boundary Layer, Radio Sci. 55 (2020), https://doi.org/10.1029/2019RS006890 e2019RS006890. https://agupubs.onlinelibrary.wiley.com/doi/full/10.1029/2019RS006890.
[33] Software Python Foundation, Python 3.9, 2021.
[34] M. Haida, J. Smolka, A. Hafner, M. Mastrowski, M. Palacz, K.B. Madsen, A. J. Nowak, K. Banasiak, Numerical investigation of heat transfer in a CO2 two-phase ejector, Energy 163 (2018) 682–698, https://doi.org/10.1016/j.energy.2018.08.175, https://www.sciencedirect.com/science/article/pii/S0360544218317110?via%3Dihub.
[35] B. Tang, Orthogonal Array-Based Latin Hypercubes, J. Am. Statist. Assoc. 88 (1993) 1392–1397, https://doi.org/10.1080/01621459.1993.10476423, http://www.tandfonline.com/doi/abs/10.1080/01621459.1993.10476423.
[36] S. Elbel, P. Hrnjak, Experimental validation of a prototype ejector designed to reduce throttling losses encountered in transcritical R744 system operation, Int. J. Refrig. 31 (2008) 411–422, https://doi.org/10.1016/J.IJREFRIG.2007.07.013, https://www.sciencedirect.com/science/article/pii/S0140700707001508.
[37] M. Palacz, J. Smolka, A. Fic, Z. Bulinski, A.J. Nowak, K. Banasiak, A. Hafner, Application range of the HEM approach for CO2 expansion inside two-phase

ejectors for supermarket refrigeration systems, Int. J. Refrig. 59 (2015) 251–258, https://doi.org/10.1016/j.ijrefrig.2015.07.006, https://www.sciencedirect.com/science/article/pii/S0140700715002030.

[38] M. Palacz, M. Haida, J. Smolka, A.J. Nowak, K. Banasiak, A. Hafner, HEM and HRM accuracy comparison for the simulation of CO2 expansion in two-phase ejectors for supermarket refrigeration systems, Appl. Therm. Eng. 115 (2017) 160–169, https://doi.org/10.1016/j.applthermaleng.2016.12.122, https://www.sciencedirect.com/science/article/pii/S135943111634399X.

[39] J. Sierra-Pallares, J. García Del Valle, P. García Carrascal, F. Castro Ruiz, A computational study about the types of entropy generation in three different R134a ejector mixing chambers, Int. J. Refrig. 63 (2016) 199–213, https://doi.org/10.1016/J.IJREFRIG.2015.11.007.

[40] F. Kauf, Determination of the optimum high pressure for transcritical CO2-refrigeration cycles, Int. J. Therm. Sci. 38 (1999) 325–330, https://doi.org/10.1016/S1290-0729(99)80098-2.

[41] K. Banasiak, A. Hafner, 1D Computational model of a two-phase R744 ejector for expansion work recovery, Int. J. Therm. Sci. 50 (2011) 2235–2247, https://doi.org/10.1016/j.ijthermalsci.2011.06.007, https://www.sciencedirect.com/science/article/pii/S1290072911001876.

[42] G. Grazzini, A. Milazzo, F. Mazzelli, Ejectors for efficient refrigeration: Design, applications and computational fluid dynamics, Springer International, 2018, https://doi.org/10.1007/978-3-319-75244-0. URL https://books.google.no/books?hl=no&lr=&id=Vq9SDwAAQBAJ&oi=fnd&pg=PR7&ots=Vza5cXBAC3&sig=UllOPQVfZdvUSThJ4Q4NwIvfjw8&redir_esc=y#v=onepage&q&f=false.

[43] Y. Tang, Z. Liu, Y. Li, Z. Huang, K.J. Chua, Study on fundamental link between mixing efficiency and entrainment performance of a steam ejector, Energy 215 (2021) 119128, https://doi.org/10.1016/J.ENERGY.2020.119128.

[44] F. Kock, H. Herwig, Local entropy production in turbulent shear flows: a high-Reynolds number model with wall functions, Int. J. Heat Mass Transf. 47 (2004) 2205–2215, https://doi.org/10.1016/J.IJHEATMASSTRANSFER.2003.11.025.

Paper III

Ringstad, Knut Emil; Banasiak, Krzysztof; Hafner, Armin. (2022) Swirl-Bypass Nozzle for CO_2 Two-Phase Ejectors: Numerical Design Exploration. *Energies 15, no. 18: 6765.*
DOI: https://doi.org/10.3390/en15186765

energies

MDPI

Article

Swirl-Bypass Nozzle for CO_2 Two-Phase Ejectors: Numerical Design Exploration

Knut Emil Ringstad [1,*], Krzysztof Banasiak [2], Åsmund Ervik [2] and Armin Hafner [1,*]

[1] Department of Energy and Process Engineering, Norwegian University of Science and Technology, Kolbjørn Hejes vei 1B, 7491 Trondheim, Norway
[2] SINTEF Energy Research, Kolbjørn Hejes vei 1d, 7465 Trondheim, Norway
* Correspondence: knutringstad@gmail.no (K.E.R.); armin.hafner@ntnu.no (A.H.)

Abstract: In this work, a novel ejector design concept of a swirl-bypass nozzle is proposed to improve off-design performance of CO_2 two-phase ejectors. The swirl-bypass nozzle allows part of the flow to bypass into the ejector mixing chamber to generate swirl. The design of such a device is investigated using a 3D multiphase CFD model. An extensive experimental test campaign is conducted to validate the baseline homogeneous equilibrium CFD model. The model's prediction motive mass flow rate within 2–12% error and suction mass flow rate was predicted with 3–50% error. Based on the tested ejector geometry, simulations of different ejector swirl-bypass inlets are conducted. The results show that, for the current design, total entrainment of the ejector is reduced by 2–20% with the swirl-bypass inlet. The axial position of the bypass inlet plays a primary role in the bypass inlet flow rate, and, consequently, in suction flow reduction. This is found to be due to the bypass flow blocking off the suction mass flow rate, which has a net negative impact on performance. Finally, several design improvements to improve future designs are proposed.

Keywords: computational fluid dynamics; two-phase ejector; CO_2; bypass ejector; swirl bypass

Citation: Ringstad, K.E.; Banasiak, K.; Ervik, Å.; Hafner, A. Swirl-Bypass Nozzle for CO_2 Two-Phase Ejectors: Numerical Design Exploration. *Energies* **2022**, *15*, 6765. https://doi.org/10.3390/en15186765

Academic Editor: Vasily Novozhilov

Received: 21 August 2022
Accepted: 12 September 2022
Published: 16 September 2022

1. Introduction

1.1. Literature Review

Environmentally friendly heating and cooling solutions have seen a large growth in recent years. With the ratification of the EU F-gas legislation and the Kigali amendment to the Montreal Protocol [1], increased efforts have been put toward the development of efficient and environmentally friendly cooling and heat-pumping systems. Due to the rapid transition to environmentally friendly refrigerants, much research has been put toward finding efficient system solutions with natural working fluids, such as ammonia, water, hydrocarbons, and CO_2.

A promising natural working fluid for many applications is CO_2 (R744). CO_2-based refrigeration and heat-pumping systems have been applied for many applications, such as supermarkets [2,3], heat-pump units [4–6], vehicles [7–9], light commercial refrigeration [10,11], tumble dryers [12,13], chillers [14], air-conditioners [15], and integrated systems for hotels [16]. As a refrigerant, CO_2 has several beneficial characteristics, such as favorable thermodynamic properties that allow for smaller components and efficient refrigeration cycles. Furthermore, CO_2 is non-toxic, non-flammable, and has a negligible GWP of one while being cheap and widely available [17].

However, the high operating pressure of the CO_2 transcritical cycle is associated with increased expansion losses. These losses can be partially recovered by implementing work-recovery devices such as two-phase ejectors. Ejectors work by using the expansion energy of the high-pressure flow (motive flow) and expand the flow through a super-sonic converging-diverging nozzle. The high-velocity motive flow is then mixed with a secondary flow (suction flow) and the mixture is repressurized by slowing the flow down in a diffuser.

This effectively pumps the suction flow to a higher pressure without additional work, improving system efficiency. Ejector performance is, therefore, commonly evaluated using the ratio of pumped suction mass flow rate to motive mass flow rate (Equation (1)), referred to as the entrainment ratio of the ejector.

$$\omega = \mathrm{MFR}_{\mathrm{suction}} / \mathrm{MFR}_{\mathrm{motive}} \quad (1)$$

Two-phase R744 (CO_2) ejectors are today implemented in several cooling and heat-pump applications [18–28], and can improve system COP by 10–30% [19,29].

The promising benefits of using ejector-supported R744 systems have promoted much research into ejector design and operation. Due to the complex fluid dynamics within these components, much experimental and numerical research has been devoted to better the understanding of multiphase ejectors and their design. Accurate numerical models are of high value for R744 ejector design due to several reasons, such as high sensitivity to small changes in its many design parameters, the high cost of the experimental testing of ejectors, the large differences in optimal design for different applications, and the possibility of performing low-cost exploratory investigations into their design. This has prompted research into advanced models for R744 ejectors, such as the 0D and 1D models [30–35], which have been applied for system-level calculations and ejector design. A limitation of numerical modeling using thermodynamic or 1D approaches is their inability to generally predict phenomena such as flow separation or shock-wave patterns. This problem becomes important when exploring novel ejector designs. Furthermore, new geometric ejector designs that are not within conventional ejector design space are not possible to investigate with such approaches. In recent years, emphasis has been put toward developing accurate and fast multiphase computational fluid dynamics (CFD) models for R744 ejectors, where the full 2D or 3D ejector physics are resolved, allowing for more exploratory investigations of ejector designs. Accurate CFD modeling has the added benefit of allowing detailed insights into ejector physics as all flow variables are available. However, these models are, in general, more complex and more computationally costly.

The most prominent model used in R744 two-phase ejectors modeling is the homogeneous equilibrium models (HEM) [36–44]. In general, for high-pressure and temperature motive conditions, the HEM provides good prediction accuracy at a low computational cost. However, as the motive pressure and temperature are reduced, non-equilibrium effects are no longer negligible, and delayed phase transition must be considered. Several models have been presented in the literature to model the transition to equilibrium, such as homogeneous relaxation models [40,45,46], and mixture models [47–50]. These models treat transition by considering a delayed time scale to reach equilibrium, or by modeling the phase change mechanisms directly. Non-equilibrium models have better predictive capabilities than equilibrium-based approaches for motive operating conditions in the "off-critical" region (i.e., $T_m \lesssim 30$ °C, $P_m \lesssim 75$ bar) [51]. Accurate prediction of R744 ejector flow is still an ongoing research area. Significant uncertainties are also associated with the prediction of the secondary ejector flow. This is considered a consequence of the lack of detailed understanding of the suction entrainment process, its dependency on accurate motive flow conditions, and the complexity of the multiphase turbulent mixing process in the ejector. For detailed reviews of the current status of R744 two-phase ejector modeling, see Ringstad et al. [51] and Nowak et al. [52]. Extensive experimental tests are needed to validate and verify the numerical models. Detailed experimental observations of R744 ejectors are limited, even though some work has been carried out on visualization and local measurements [53–55], additional experimental results with varied and open-access ejector geometries are needed.

A primary reason for the large interest in ejector modeling is the necessity for a detailed understanding of ejector design and its impact on ejector performance under varied operating conditions, which has been highlighted as a key focus area for ejector developments [19,51,52]. Several studies on R744 ejector design have been conducted to better understand the interdependence of different design parameters [29,44,56]. Improved

ejector-design processes have been explored using numerical CFD modeling in combination with optimization techniques. Palacz et al. [38,39] combined an evolutionary optimization algorithm with CFD modeling to optimize ejector design. Ringstad et al. [57] presented a machine-learning-based design methodology for the ejector design and performance mapping of R744 ejectors.

An efficient ejector design is highly dependent on the system operating conditions. When operated at off-design operating conditions, a passive (no active control) ejector system can dramatically reduce system COP. Nakagawa et al. [29] reported between a 34 to 82% drop in system COP for an ejector system operated in off-design conditions. Similarly, Lucas and Koehler [58] reported a 10 to 17% drop in system performance of an ejector-based system at off-design conditions. Therefore, ejector control is important for system performance. Different capacity control strategies using R744 ejectors have been presented in the literature; for a detailed review, see Gullo et al. [59]. The main technologies for this application are the multiblock ejector [60], motive swirl control [61], adjustable needle control [33,62], and pulse-width modulation [63].

Alternatively, ejector performance can be improved by active control of the suction flow. One such design is the suction-bypass design, where a controllable secondary suction inlet downstream from along the mixing section is implemented for off-design performance improvement. This inlet splits the suction flow within the ejector so that parts of the flow bypass parts of the mixing section. This allows for the suction flow to enter the ejector in a low-pressure zone under off-design conditions. The bypass concept improves ejector performance by reducing entropy production in supersonic shocks and allows for more optimal suction inflow conditions. In such designs, the entrainment ratio is defined by the total mass flow rate pumped by the recovered work from the motive flow, Equation (2):

$$\omega = (\mathrm{MFR}_{\mathrm{suction}} + \mathrm{MFR}_{\mathrm{bypass}})/\mathrm{MFR}_{\mathrm{motive}} \quad (2)$$

The goal of such a design is to increase the total pumped mass flow beyond what can be achieved with only the suction port. The bypass concept for ejectors has been investigated with various working fluids, with steam [64,65], methane [66,67], air [68,69], and R744 [70,71]. Tang et al. [65] investigated the bypass concept for steam ejectors using numerical CFD calculations. The study identified several low-pressure zones that could be utilized, and close to a 4% improvement in entrainment ratio was obtained by implementing the bypass nozzle. The bypass concept was implemented for pressure regulation in the steam ejector [65], and findings indicate an increase in entrainment ratio of up to 26% using this strategy. Chen et al. [68] presented a CFD investigation into the bypass ejector concept for air ejectors, finding that up to a 10% increased entrainment ratio could be generated. Later, Chen et al. [69] presented additional numerical results with different geometries for the bypass inlet. They found that significant improvements by up to 32.8% in entrainment ratio could be made by optimization of the bypass geometry parameters. Chen et al. [66] investigated an ejector study with methane as the working fluid where an ejector with an adjustable needle and bypass inlet was implemented, achieving up to 74.5% improved entrainment. Chen et al. [67] followed this with a detailed investigation of the methane ejector with two bypass inlets. With one bypass inlet, up to a 34.8% improvement was obtained in comparison to without a bypass. By the implementation of two bypass ports, a larger improvement of up to 48.9% was achieved. While the findings with single-phase ejectors are valuable for comparison, much of the knowledge is not directly transferable to two-phase ejectors such as those predominantly implemented in R744 cycles.

The bypass concept for R744 two-phase ejectors was first proposed and explored numerically by Bodys et al. [70]. They explored different bypass geometries using a 2D CFD model. The exploration was performed with six bypass locations in the ejector diffuser and with two bypass inlet angles at different pressure lift conditions. Their findings were that the bypass inlet could improve suction mass flow rate at low-pressure lifts by up to 37%. Furthermore, they found that the optimal location for the bypass inlet was at a distance of 40% of the mixing chamber into the diffuser. Recently, Bodys et al. [71] followed up this

study with an experimental investigation of a bypass suction inlet. In this work, the authors proved the applicability of the suction-bypass concept for ejector efficiency improvement and proposed a control strategy for such solutions. The resulting efficiency improvement was as high as 37% at low-pressure lifts when the bypass inlet was introduced. Furthermore, a full 3D CFD investigation was conducted to gain a better understanding of the ejector flow physics. The authors mention the potential for introducing a swirl component to the model for further improvements of the bypass concept.

The concept of adding the swirl component to the motive and suction flow at the ejector inlets has been proposed in previous works to intensify the mixing process in the mixing section of the ejector [72,73]. The idea is that the surface area of the interface between the suction and motive flow is increased and more momentum is transferred. Additionally, the centrifugal force can encourage faster spreading and, therefore, mixing of the central flow core. Bodys et al. [73] investigated the effects of the swirl-flow component at the ejector motive and suction inlets of a two-phase R744 ejector. They concluded that some improvements could be gained in the entrainment ratio by the implementation of a motive inlet swirl component. However, the suction flow swirl component only limited the suction flow rate through the suction nozzle and had a negative impact on the entrainment ratio. In the mentioned study, as the swirl component was added before the suction inlet, the impact of the swirl component in the mixing chamber was reduced.

1.2. Swirl-Bypass Concept

To the best of the authors' knowledge, the concept of ejector improvement through combined bypass flow and swirl generation has not been considered. In this paper, such a solution is presented and discussed in terms of its design and flow characteristics. The novel swirl-bypass concept is presented in this paper to potentially cover two applications: (A) improving entrainment ratio at off-design operating conditions and (B) serving as an additive motive-capacity control technique. These applications are illustrated in Figure 1A,B. In this work, concept (A) is investigated.

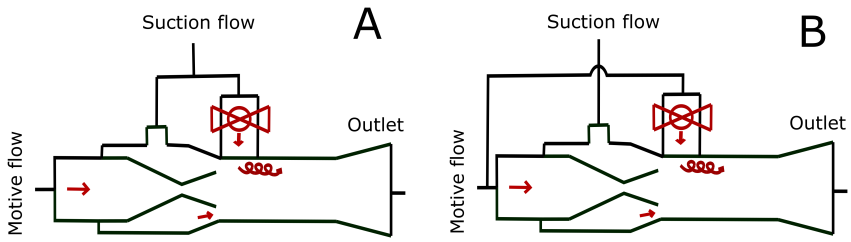

Figure 1. Illustration of the two swirl-bypass concepts (**A**,**B**). Concept (**A**) is a suction swirl bypass ejector. Concept (**B**) is a motive swirl bypass ejector.

The novel idea is to add an additional angled inlet to the ejector downstream of the motive nozzle to generate swirl flow. At off-design conditions, the inlet can be used to bypass a part of the suction flow, similar to the standard bypass inlet, and the flow can be used to generate swirl. The swirl-inducing suction flow could then potentially improve mixing efficiency, indirectly and directly improving the entrainment ratio. This corresponds to concept (A).

Alternatively, the swirl-bypass inlet can be used to control the motive mass flow rate. Similar to the motive swirl control mechanism presented by Zhu and Elbel [61], the high-pressure motive flow can be split into two streams. One stream enters the motive nozzle normally, while, unlike the motive swirl control discussed by Zhu and Elbel [61], the second stream enters the swirl-bypass entrance inside the ejector mixing chamber. The second motive flow is then used to generate swirling flow and can be controlled by a valve upstream of the bypass inlet, corresponding with concept B. Such a design allows for the

control of the motive flow not only to reduce the motive flow below the choked design value but also to increase the motive mass flow by bypassing the motive nozzle to generate swirl. This concept will perform better than a parallel expansion valve as long as the swirl flow has any positive impact on the flow.

1.3. Knowledge Gap

In this work, the novel concept of a swirl-inducing bypass inlet is explored numerically using 3D CFD simulation. As limited comparable ejector designs are available, the design space of such a bypass inlet will be tested with varied bypass geometries. Different inclination angles and locations of the bypass chamber are explored. The flow structure and its implications on ejector operation and design are discussed in terms of swirl and mixing. The results indicate that the design of this type of ejector is complex, and must be considered in conjunction with the rest of the ejector design. This study will, in this way, enable future designs of a swirl-bypass inlet and several design considerations and suggestions are presented. Limited knowledge regarding the influence of swirl on two-phase ejectors is available; however, the potential of utilizing swirl in ejectors has been highlighted by several authors in the literature [61,71]. This article further fills this knowledge gap by supplying detailed simulation results and analysis of the influence and decay of swirl in the ejector. Furthermore, the baseline HEM CFD model without a bypass is validated against new experimental results with an ejector geometry designed for high entrainment at low-pressure lift.

2. CFD Model

2.1. Multiphase Model

The CFD model used in this work is a homogeneous equilibrium model (HEM) based on the formulation by Smolka et al. [36]. The HEM assumes that both phases are at full mechanical, thermal, and thermodynamic equilibrium; hence, the flow can be described using a single velocity- ($\vec{u}$), temperature- (T), and pressure-field (P). The HEM is, therefore, classified as a pseudo-fluid or single-fluid approach where a single set of transport equations, Equations (3)–(5), are solved. Here, the energy equation, Equation (5), is reformulated to an equivalent enthalpy formulation.

$$\frac{\partial}{\partial t}\rho_{\text{mix}} + \nabla \cdot (\rho \vec{u}) = 0, \tag{3}$$

$$\frac{\partial}{\partial t}\rho_{\text{mix}}\vec{u} + \nabla \cdot (\rho \vec{u}\vec{u}) = -\nabla \cdot p + \nabla \cdot \tau_{\text{eff}}, \tag{4}$$

$$\frac{\partial}{\partial t}\rho_{\text{mix}} h_{\text{mix}} + \nabla \cdot (\rho \vec{u} h_{\text{mix}}) = \nabla \cdot (\Gamma_{\text{eff}} \nabla h_{\text{mix}}) + \dot{S}_{h1} + \dot{S}_{h2} + \dot{S}_{h3} \tag{5}$$

Here, the subscript *mix* indicates the pseudo-fluid mixture properties. ρ, p, h, q refer to the density, pressure, enthalpy, and heat flux, respectively. The effective stress tensor $\tau_{ij,\text{eff}}$ is the laminar (Newtonian) and turbulent stress tensors combined, $\tau_{\text{eff}} = \tau_{\text{laminar}} + \tau_{\text{turb}}$. In this equation, h is the specific enthalpy, and Γ_{eff} is the effective diffusion coefficient. The terms $\dot{S}_{h1,2,3}$ describe the mechanical energy, the irreversible dissipation of the kinetic energy variations, and the dissipation of the turbulent kinetic energy, respectively, explained in detail in the work by Smolka et al. [36].

The enthalpy and pressure can then be used to uniquely identify the thermodynamic equilibrium state, and, from this, the thermodynamic properties can be calculated. Properties are typically divided into thermophysical (Equation (6)) and transport (Equation (7)) properties.

$$\begin{bmatrix} \rho \\ c_p \\ \alpha \\ T \\ s \end{bmatrix} = f(p,h), \tag{6}$$

$$\begin{bmatrix} \mu \\ \lambda \end{bmatrix} = g(p, h), \tag{7}$$

where $\rho, \alpha, \mu, \lambda, c_p, s$ are the pseudo-fluid density, vapor volume fraction, kinematic viscosity, thermal conductivity, heat capacity, and entropy, respectively. Mixture properties are evaluated using mass- and volume-weighted averages.

The properties of liquid and gas are evaluated by the pressure and enthalpy, interpolated from a look-up table. The CoolProp library [74] for R744 is based on the Span–Wagner equation of state, which is considered the most accurate equation of state (EoS) for CO_2 and is widely used for R744 ejector simulations [51]. Here, CoolProp is used to generate the look-up tables that are imported in Fluent using UDFs.

The HEM model for R744 two-phase ejectors is considered accurate for motive flow inlet conditions at supercritical pressure and temperatures, referred to as "near-critical" conditions [51]. In the present study, the operating conditions will primarily concern high pressure and temperature operating conditions, where the assumption of equilibrium flow is considered fair [46]. Compared to other approaches presented in the literature, the HEM model is preferable in robustness and stability. Numerical stability is critical for modeling the complex geometry considered in this work. The HEM model has been extensively validated for R744 two-phase ejectors [51] in terms of mass flow rate predictions. Still, the prediction uncertainty of local variables, such as pressures and velocities, is not well-understood due to the lacking experimental validation data. Due to the high accuracy in the considered domain and superior stability characteristics, the HEM model is chosen for this work.

2.2. Turbulence Model

Turbulence modeling is a key feature of accurate CFD predictions. The mixing process inside the ejector is, to a large extent, governed by the turbulent viscosity, ν_t, predicted by the turbulence model. For R744 two-phase ejectors, it is common to use pseudo-fluid two-equation turbulence models, such as the $k-\epsilon$ and $k-\omega$ models. The turbulent viscosity, ν_t, can then be calculated based on two turbulence parameters. The models involve solving the set of transport equations for these turbulent properties. As studied by Bodys et al. [50], different turbulence models can yield significantly different predictions of turbulent flow characteristics. An initial study was conducted to compare the $k-\epsilon$ and $k-\omega$ models for the swirl bypass inlet geometry, discussed in Section 4.4. Due to the complexity of the geometry and sharp gradients near the bypass inlet, a fully wall-resolved simulation with turbulent mesh resolution of $y^+ \approx 1$ was not achievable and unstable simulations would occur. Instead, the mesh was resolved to $y^+ \approx 30+$. In conclusion, the $k-\omega$ SST model is used due to its better accuracy.

2.3. Numerical Approach

The CFD problem is solved using a 3D steady-state pressure-based coupled algorithm in ANSYS Fluent 2020 R2. The numerical schemes used were the second-order upwind scheme for the momentum, density, enthalpy (UDS), and turbulence transport equations. Second-order schemes were chosen to reduce the influence of numerical viscosity, while higher order discretizations were disregarded due to numerical stability concerns near the swirl bypass inlet. Higher order accuracy will improve gradient estimation, which has an impact on shock resolution. The pressure was calculated using the PRESTO! scheme, which is the preferred pressure discretization for high swirl flows [75]. Gradients were evaluated with the least-square cell gradient calculation, which is associated with comparable or higher accuracy than the Green Gauss node- and cell-based approaches, respectively, for regions of high mesh non-orthogonality [75]. This is primarily a concern in the vicinity of the swirl-bypass inlet, as the baseline mesh has otherwise high orthogonal quality. The boundary conditions were specified as pressure inlets and outlets. Constant pressure and enthalpy were specified at the inlets. These boundary conditions are standard for CFD modeling of two-phase R744 ejectors [51], and ensure that the modeling problem is well-

posed. These boundary conditions are set according to the experimentally measured values; thus, measurement uncertainty limits the accuracy of the model prediction. The turbulence boundary conditions were set to 5% turbulence intensity and a turbulent viscosity ratio of 5. The performance impact of turbulent boundary conditions is commonly found to be negligible [50] due to the turbulence generated in the ejector typically being more significant than the inlet turbulence.

2.4. Calculation of Ejector Parameters

Different ejector parameters will be investigated in this study to better understand the ejector flow structure. To evaluate the effects on ejector mixing-layer thickness, the vorticity thickness, δ_w, is used [76]:

$$\delta_w(\theta) = \Delta U_\infty / \left(\frac{\partial u_x}{\partial r} \right)_{\max} \tag{8}$$

The calculation is based on defining the thickness by the largest gradient in the mixing layer compared to the velocity difference across the boundary. The velocity difference, ΔU_∞, is calculated from:

$$\Delta U_\infty = U_{\text{motive}} - U_{\text{suction}}, \tag{9}$$

where U_{motive} is calculated based on the maximum velocity of the motive flow, and U_{suction} is calculated based on the velocity in the section between the upper boundary layer and the motive core. The characteristic velocity was, for this region, calculated based on the velocity at $r_s = 0.9 \cdot R_{\text{wall}}$.

3. Swirl Injection Geometry

The swirl-bypass inlet is an additional inlet entering the mixing chamber of the ejector. As opposed to the standard bypass inlet, the novel swirl-bypass nozzle is angled with a tangential component to the ejector. The effect of such a design is investigated in detail in this study. Several studies have shown that positive efficiency effects can be gained by increasing mixing by the use of swirl flow. To the best of the author's knowledge, the bypass injection for swirl generation in ejectors has not yet been explored in the literature. For this design, a compromise has to be made between moving the swirl-bypass inlet downstream for better off-design performance or upstream in the mixing chamber for optimal mixing performance. This is studied further in this work.

Different bypass swirl designs are possible, such as implementing a swirl chamber where the swirl is generated before being sucked into the ejector. However, in this work, a design where the bypass channel is directly inserted tangentially into the mixing chamber is explored.

The swirl-bypass port is illustrated with the main parameters shown in Figure 2. These parameters are: the relative bypass location measured from the nozzle exit position, $x_b = (x_{\text{bypass inlet}} - x_{\text{motive outlet}})/D_{\text{mix}}$; the bypass inlet width W and length L; the bypass tangential angle α_t and the bypass inclination angle α_i. The tangential angle, α_t, is the angle formed in the cross-sectional plane of the mixing chamber (y–z—cross section in Figure 2) between the center line of the bypass inlet and the radial vector from the mixing-chamber center at their intersecting point. This angle can vary between 0° and 90°, where 0° corresponds to a bypass with no tangential component and 90° corresponds to a fully tangential inlet. The bypass inclination angle is the angle between the mixing chamber centerline and the bypass inlet in the axial direction. In the suction nozzle, the suction flow is slightly expanded through a converging channel. This converts a part of the suction pressure into velocity. Similarly, a compression ratio, $CR = A_{\text{in}}/A_{\text{out}}$, is used to correct the bypass-inlet area. This area must also be corrected for the larger area on the cylindrical mixing chamber surface. The area correction is then added to the inlet of the suction bypass nozzle. Due to the tangential angle of bypass entrance, the problem is inherently three dimensional and will, in this study, be investigated with 3D CFD modeling. Here, the integration of suction and bypass ports is not considered and is left for future studies.

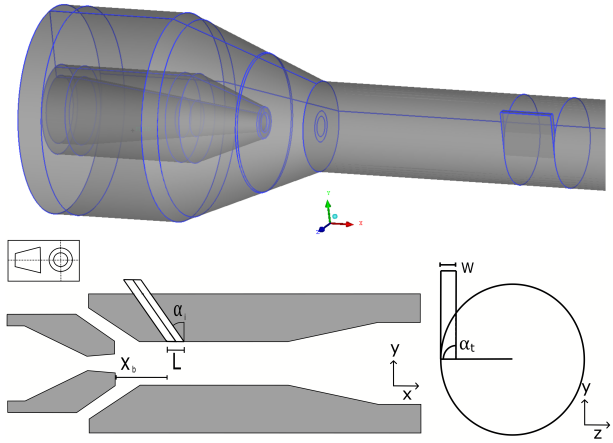

Figure 2. Generic ejector geometry with geometry parameters. Gray color signifies solid parts.

The bypass inlet dimension was defined with a length $L = D_{mix/2}$ and a width $W = D_{mix}(1 - cos(30°))/2$, such that 30° of the mixing-chamber circumference would be open. These numbers were chosen based on an initial calculation, where it was found that a larger width would limit the swirl production as a significant amount of flow would be angled toward the ejector center line with a minimal tangential component. The ejector geometry that this inlet is tested with is the geometry presented in Table 1 and was experimentally tested and numerically validated in this article. This was chosen to have a fair model validation for the baseline geometry and to compare any performance improvement or reduction with an already optimized design. However, it is noted that performance improvements are believed to be better for an ejector designed for higher pressure lift and lower entrainment ratio, discussed further in Section 6.

Table 1. Main dimensions of the ejector geometry with dimensions as defined in Ringstad et al. [57].

Parameter	D_{throat}	L_{mch}	L_{mix}	D_{mix}	D_{out}	α_{diff}	$\alpha_{m\text{-}conv}$	$\alpha_{suction}$
Value	0.85 mm	3 mm	34 mm	3.1 mm	10 mm	5°	30°	38°

4. Model Validation

The HEM has been previously extensively studied for two-phase R744 ejectors [36,46,77]. In general, the accuracy is considered to be within 5% for motive mass flow rate and 10–20% for suction mass flow rate [51] when near super-critical motive conditions are considered. Further validation and mesh independence verification are conducted with new experimental data in the following sections.

4.1. Experimental Test Campaign

To validate the 3D HEM model results, an experimental test campaign was set up at the NTNU/SINTEF Energy Research laboratory in Trondheim-Norway. The experimental rig is an R744 system with one base-load compressor and two parallel compressors, two R744 gas-coolers for heat rejection to a glycol- and a water loop, two evaporators, and an expansion device test section where a novel ejector design is installed. The detailed system description can be found in the work by Banasiak et al. [78]. The system is equipped with pressure-, temperature-, and mass-flow sensors, shown in Table 2.

Table 2. Characteristics of the measuring devices.

Parameter	Device	Accuracy
P	Cerabar PMP71	±0.25% of span
ΔP	Deltabar PMD75	±0.25% of span
T	PT 1000	±0.15 K
MFR	Rheonik RHM 08 Coriolis mass flow meter	±0.1% of reading

The system has been installed with a novel R744 two-phase ejector designed for low-pressure lift and high entrainment ratio intended for heat pump conditions. The main ejector-shape design parameters are listed in Table 1. These ejector dimensions were based on a design optimization using an advanced 1D ejector model [79]. The ejector was produced in stainless steel with a provided wall-roughness estimate of Ra0.8. To evaluate ejector performance additional pressure, temperature and mass-flow rate sensors were installed as displayed in Figure 3. The full range of experimental test points is shown in Table A1 in the Appendix A.

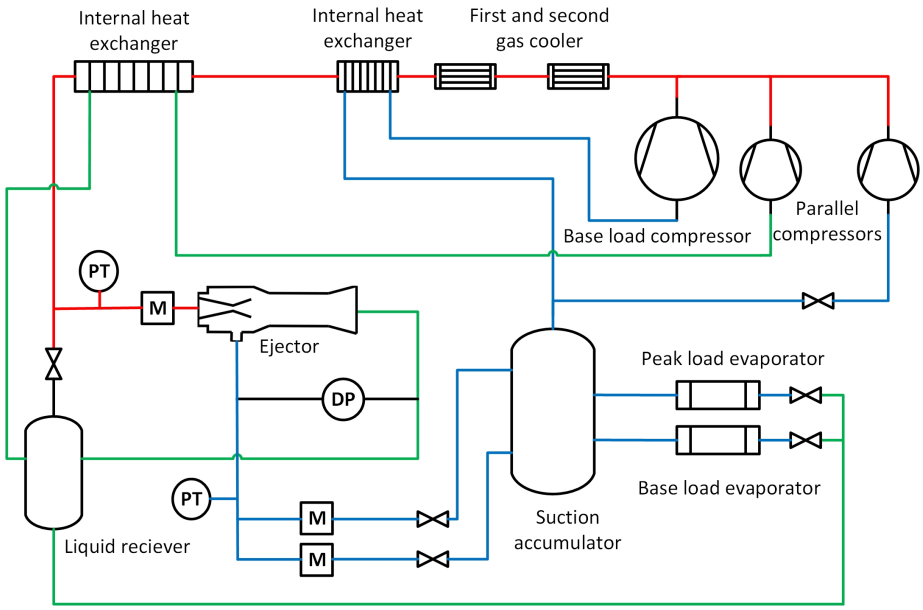

Figure 3. Simplified illustration of the system layout with new ejector and sensors installed. PT—pressure/temperature sensor, DP—differential pressure sensor, M—mass flow meter.

4.2. Comparison with Experimental Results

Four data points will be used for validation of the CFD model corresponding to different motive conditions at 90 bar, 80 bar, 75 bar, and 83 bar and pressure lifts of 2.1 bar, 3.6 bar, 1.5 bar, and 2.5 bar, respectively. These cases will be referred to as cases I-IV and correspond to the experimental data points 49, 59, 62, and 79 in Table A1, respectively. Case I is a measurement at a higher operating pressure and intermediate pressure lift, case II is a measurement at an intermediate operating pressure and high-pressure lift, case III is a measurement at low operating pressure and low-pressure lift, and case IV is a measurement at an intermediate operating pressure and intermediate pressure lift.

The experimental results and the calculated CFD results at those operating conditions are shown in Table 3. Here, the subscripts m, s and o refer to motive, suction and outlet

conditions, respectively. The experimental measurements were calculated from a time series where close to a steady state was achieved. The standard deviation over the measurement period is, therefore, calculated for the mass flow rates and are shown along with the experimental validation data.

Table 3. Comparison of experimental and CFD results at different operating conditions. δ = MFR_{CFD} − MFR_{Exp}. The MFR measurements are shown with the standard deviation over the experimental measurement period. Subscript *exp* refers to an experimentally obtained value.

	P_m [bar]	T_m [°C]	P_s [bar]	T_s [°C]	P_o [bar]	$MFR_{m,exp}$ [g/s]	δ_m [g/s]	$MFR_{s,exp}$ [g/s]	δ_s [g/s]
I	90.3	29.2	34.2	7.9	36.3	33.9 ± 0.2	−0.9	44.0 ± 0.5	+1.2
II	79.9	29.3	31.9	14.6	35.6	26.0 ± 0.5	−1.5	6.74 ± 0.05	+2.15
III	74.6	24.3	34.3	8.6	35.7	29.3 ± 1.2	−3.6	36.6 ± 1.9	+5.0
IV	82.8	34.5	34.3	9.1	37.0	21.6 ± 0.2	−1.1	26.3 ± 0.7	+13.4

The results from the simulations compared to the experimental data are shown in Table 3. As found previously in the literature [51], a good agreement between experimental measurements and computed solution for the motive MFR is found for the high motive pressure operating conditions, with less than 3%, 6% and 6% difference in predicted MFR for cases I, II, and IV, respectively. As the pressure and temperature are reduced, the motive MFR is underpredicted by −12% by the model in comparison to experimental results, shown in Figure 4. This is in agreement with previous findings with the HEM and is in the literature attributed to non-equilibrium phase change [46].

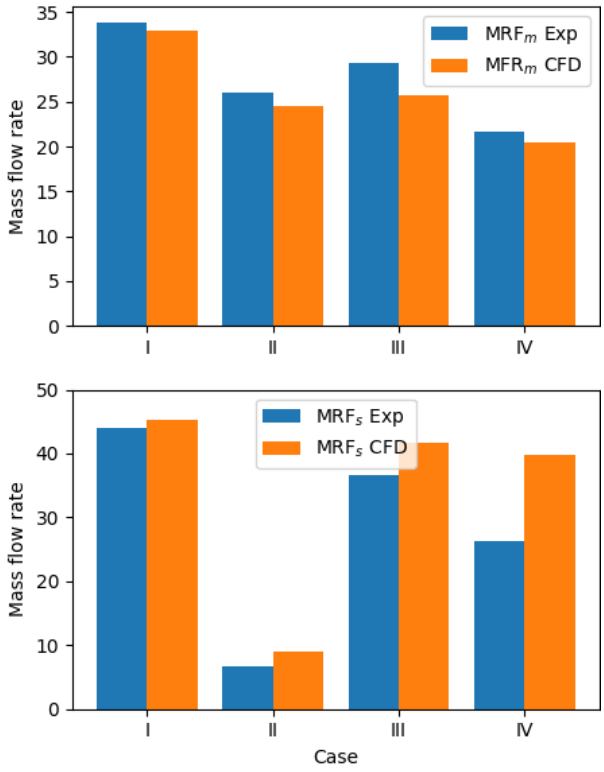

Figure 4. Comparison of experimental and numerical results in terms of motive (**upper**) and suction (**lower**) mass flow rate prediction.

The suction MFR prediction is, in comparison, more challenging to accurately reproduce and the accuracy is, in general, lower than for the motive MFR. Here, the suction MFR is over-predicted by 3%, 31%, 14%, and 51% for cases I, II, III, and IV, respectively. The prediction is thought to be better for the high-pressure cases (I, II) due to the better prediction of the motive flow structure. For the lower pressure case (III), the motive flow structure is less accurately reproduced locally in the ejector, which reduces the prediction accuracy of the mixing process and, therefore, the suction MFR. The suction MFR prediction error is the largest for case IV. Accurate prediction of the suction flow is a common challenge in modeling R744 ejectors, and errors up to 100% are not uncommon. These errors are typically attributed to turbulence modeling; however, currently, there exists no consensus on this [51].

4.3. Mesh Independence Study

A mesh study was conducted to assure that the 3D physics effects are well-presented by the mesh. The four validation points, I, II, III, and IV are calculated using meshes with varied mesh resolutions. Using the ANSYS ICEM software, a 3D-structured mesh was generated with high orthogonal quality and low skewness in the main dimensions. The meshes were generated based on a high-quality in-house meshing algorithm for ejectors, implemented into the ejector CFD automation toolset presented by the author in previous openly available work [57]. This will allow for machine-learning-based optimization of the ejector bypass inlet in future works. An example of the meshes generated is shown in Figure 5. Here, the impact of mesh resolution on the motive flow shock train and the performance parameters is analyzed.

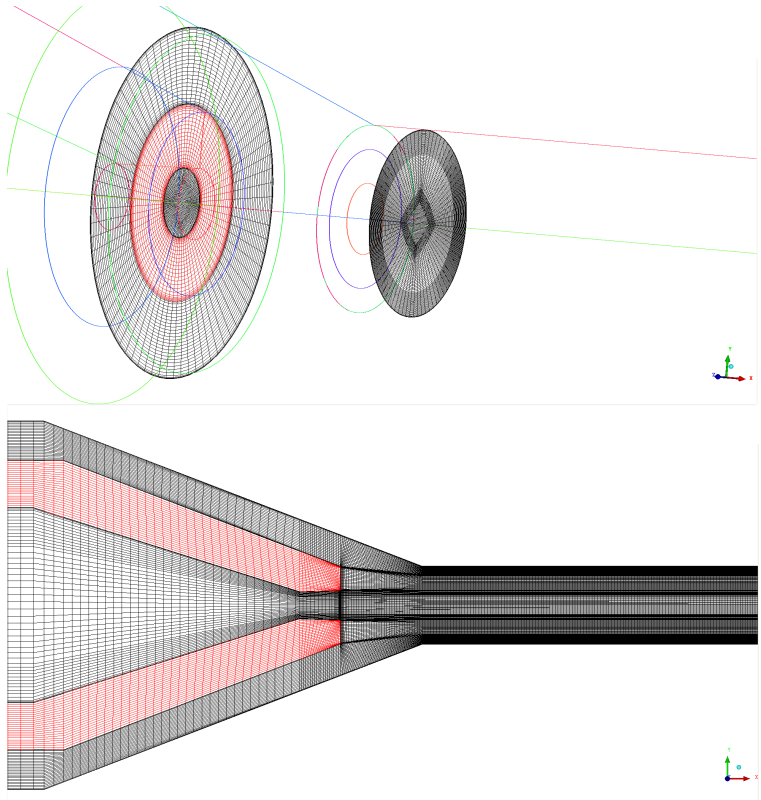

Figure 5. Generic ejector geometry with geometry parameters. The red color signifies solid parts.

Different meshes are compared and referred to as meshes A–E. The meshes A, B, and C were generated with 700,000, 1,000,000, and 2,000,000 cells, respectively. Two additional meshes, D and E, were generated with higher resolution in the premixing chamber and along the ejector walls, respectively. The cell counts for these meshes were 1,400,000 cells for mesh D and 2,500,000 cells for mesh E.

4.3.1. Flow-Rate Prediction

The mesh independence of the mass flow rate prediction must be verified. The motive and suction MFR predicted at different resolutions of mesh quality for the different cases are shown in Table 4. For all cases, the motive mass flow rate prediction is nearly independent of the mesh resolution, and only a 1% overprediction error is found between the coarsest and finest meshes. This is in agreement with previous findings with the HEM [51] and is ascribed to the choked motive flow in the ejector. For all cases, the suction MFR is reduced by increased mesh resolution until reaching around 2000k cells. For case I, the difference between the coarsest and finest mesh in suction MFR prediction is 6%. For cases II and IV the refinement has a large impact on the suction MFR as the mesh is refined to 2,500,000; cells. For mesh E (2,500,000) the accuracy of the suction MFR is, for cases I, II, and III, close to the experimentally obtained data points, and this mesh is concluded to be sufficiently refined for further computation.

Table 4. Mesh convergence study with different mesh sizes.

Mesh	Case	Cells	MFR_m [kg/s]	MFR_s [kg/s]
A	I	700,000	0.0333	0.0473
B	I	1,000,000	0.0331	0.0468
D	I	1,400,000	0.0330	0.0448
E	I	2,500,000	0.0330	0.0452
A	II	700,000	0.0245	0.0105
B	II	1,000,000	0.0245	0.0101
E	II	2,500,000	0.0245	0.0089
A	III	700,000	0.0257	0.0417
B	III	1,000,000	0.0257	0.0417
C	III	2,000,000	0.0257	0.0416
D	IV	1,400,000	0.0205	0.0396
E	IV	2,500,000	0.0206	0.0397

4.3.2. Shock Resolution

The results with meshes A, B, C, and E are compared for the resolution of the motive flow shock train. The pressure distribution along the center ejector axis for case I is shown in Figure 6. Meshes A, B, and C underestimate the shock strength in comparison to mesh E. A more resolved mesh in this region lowers the minimum pressure reached in the shock.

Figure 7 shows the Mach number distribution in the ejector for case IV for two mesh resolutions (1,400,000 and 2,500,000) corresponding to mesh D and E. The Mach number lines for Mach 1 are illustrated with a red contour line. In the figure, it is clear that mesh refinement to 2,500,000 cells improves the detailed resolution of the shock train. The results with mesh E show that the high-velocity core is extended by refining the mesh. This is attributed to the reduction in numerical viscosity from mesh refinement. The difference in predicted mass flow rates is very small, so the effect of this additional resolution does not significantly affect the entrainment of the secondary flow.

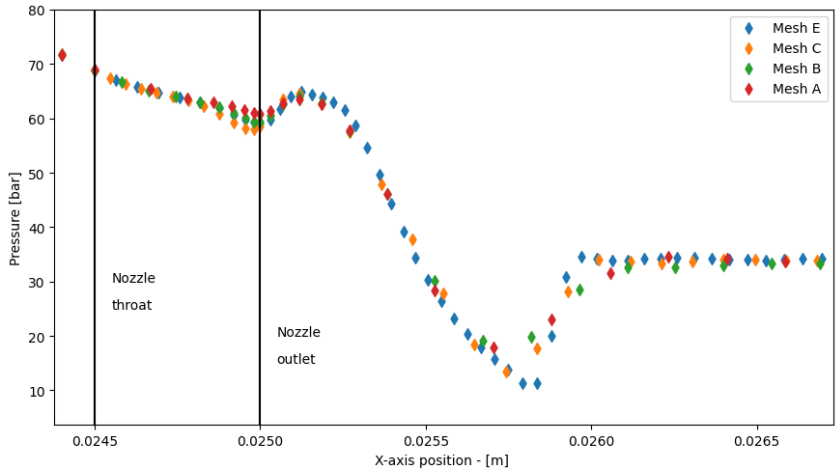

Figure 6. Pressure distribution for case I along the x-axis for meshes A, B, C, and E.

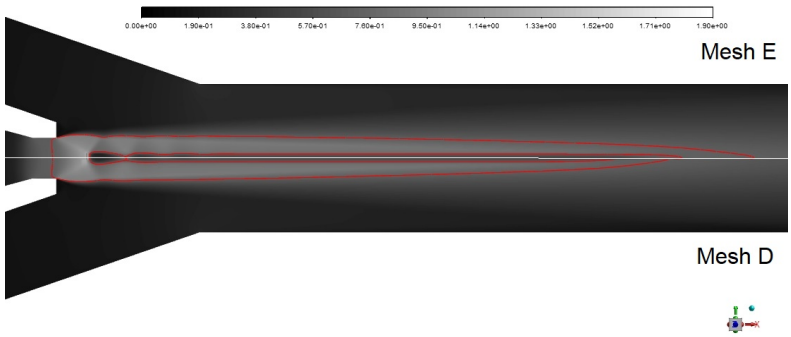

Figure 7. Mach number distribution for meshes E (**top**) and D (**bottom**) for case IV. Red line illustrates Mach 1.

In total, it was decided to use Mesh E with 2,500,000 cells for the following calculations.

4.4. Comparison of Turbulence Models

The choice of turbulence model was based on an initial comparison of the $k-\epsilon$ realizable model and the $k-\omega$ SST model models. A calculation using mesh D for experimental test case I with the two turbulence models was conducted and the results are shown in Table 5.

Table 5. Comparison of turbulence the $k-\omega$ SST and $k-\epsilon$ realizable models for Case I with mesh D.

Turbulence Model	MFR_m [kg/s]	MFR_s [kg/s]
$k-\omega$ SST	0.0330	0.0448
$k-\epsilon$ realizable	0.0330	0.0273
Experimental	0.0339	0.0440

Both models predict the same motive MFR as this is primarily governed by supersonic choking. For prediction of the suction MFR, it is found that the $k-\omega$ model predicts the experimentally measured MFR accurately with an over-prediction error of about 2%. The $k-\epsilon$ model, on the other hand, severely under-predicts the suction MFR with an

error of approximately −38%. This difference in predictive ability could be influenced by many parameters, such as mesh resolution, geometry, and model parameters. In addition, these turbulence models are not tuned for multiphase flows, so these findings are not generalizable outside two-phase R744 ejectors. Still, the findings agree with the detailed turbulence model study of Bodys et al. [50], where the $k-\omega$ model predictions were, overall, more accurate and generally over-predicted the suction MFR, and the $k-\epsilon$ realizable model predictions were overall less accurate and generally under-predicted the suction MFR. Based on these calculations, the authors decided to continue using the $k-\omega$ SST model.

4.5. Bypass Inlet

To verify the importance of meshing and simulating the bypass inlet section, simulations with the bypass inlet section geometrically resolved were compared to simulations with the bypass specified as a boundary on the ejector wall. Introducing the bypass entrance poses a meshing challenge due to the high gradients and large cell skewness near the interception of the mixing chamber and the bypass inlet. Still, simulating the entrance was numerically preferable to specifying the boundary conditions on the ejector wall, as it yielded numerically stable results. Meshing and solution of the bypass entrance region add computational cost to the simulations; however, it also improves the accuracy of the model as a more physically reasonable boundary condition could be specified at the start of the bypass inlet. Furthermore, this removes the need for specifying boundary conditions with specified swirl and axial components, which introduces additional model uncertainties as these components are determined by the bypass inlet geometry.

5. Results

In this work, the swirl-bypass concept is explored by investigating the influence of its main geometry parameters, and their influence on the ejector flow field. First, different swirl-bypass ejector geometries are investigated and discussed regarding optimal design. Secondly, the flow structure and swirl characteristics are explored and analyzed in detail. The simulations are conducted with operating conditions corresponding to case IV and case I. The simulations are set up with boundary conditions for the suction and bypass inlet at the same pressure. The overall performance of the ejector is, therefore, calculated with the total entrainment of the ejector, Equation (2).

In general, the simulations with the bypass inlet showed that gas suction could be achieved; however, the swirl flow would significantly reduce the suction mass flow rate, with a net negative impact on entrainment. This is found in all configurations of geometric design and operating conditions.

The CFD simulations were computed on the NTNU IDUN computing cluster [80]. The cluster has more than 70 nodes and 90 GPUs. Each node contains two Intel Xeon E5-2630 v2 CPUs, at least 128 GB of main memory, and is connected to an Infiniband network. Storage is provided by two storage arrays and a Lustre parallel-distributed file system. Computation time using one 20-core node for a single data point was 1–2 weeks depending on the specific geometry.

5.1. Bypass Inlet Design

A study of the different geometric parameters is conducted. The results are compared to a baseline simulation without a bypass inlet. Due to the large computational cost of each simulation, the study is limited to investigating the swirl-bypass position, the swirl inclination- and tangential angle, and the pressure lift at these two operating conditions. The results are shown in Table 6.

Table 6. Parameter study of the different geometric features of the bypass inlet on bypass performance. Simulations are identified by the simulation ID Sim, where the prefix N indicates no-bypass. The column named Diff is defined as the difference in percentage between the total entrainment (bypass and suction) compared to the same operating condition without bypass.

Case	Sim	x_b [-]	α_i [°]	α_t [°]	P_{lift} [bar]	MFR_s [kg/s]	MFR_b [kg/s]	Diff [%]
Case IV	1	2	0	90	2.5	0.0295	0.0016	−21.3
	2	4	0	90	2.5	0.0321	0.0015	−15.0
	3	7	0	90	2.5	0.0375	0.0006	−3.6
	4	10	0	90	2.5	0.0385	0.0003	−1.8
	5	4	20	90	2.5	0.0324	0.0015	−14.2
	6	4	45	90	2.5	0.0328	0.0012	−13.9
	7	4	0	40	2.5	0.0303	0.0027	−16.5
	8	4	0	60	2.5	0.0308	0.0025	−15.7
	9	4	45	90	2	0.0395	0.0019	−20.0
	10	10	0	90	1	0.0454	0.0025	−14.0
Case I	11	2	0	90	2	0.0328	0.0021	−22.8
	12	4	0	60	2	0.0320	0.0039	−20.6
	13	4	0	90	2	0.0335	0.0021	−21.3
	14	4	20	90	2	0.0340	0.0020	−20.5
	15	7	0	90	2	0.0357	0.0015	−17.7
	16	4	20	90	1	0.0378	0.0024	−18.8
	17	4	20	90	0.5	0.0426	oscillating	
No bypass								
Case IV	N1	-	-	-	2.5	0.039514	-	
	N2	-	-	-	2	0.051762	-	
	N3	-	-	-	1	0.055674	-	
Case I	N4	-	-	-	2	0.045234	-	
	N5	-	-	-	1	0.049482	-	
	N6	-	-	-	0.5	oscillating	-	

5.1.1. Bypass Position, x_b

The first main parameter for a bypass inlet design is the downstream location of the bypass inlet. The bypass locations are defined along the mixing section in increments of mixing chamber diameters. The bypass inlet position was varied between $2 \times D_{\text{mix}}$ and $10 \times D_{\text{mix}}$.

The influence of bypass inlet location is visualized in Figure 8. The figure shows that the choice of inlet bypass position has a major impact on the total pumped flow rate and total entrainment ratio, Equation (2). For a bypass location close to the ejector motive nozzle, the suction effect is more significant, producing a relatively larger bypass flow rate, approximately 1.6 g/s, and 2.1 g/s, for case IV and case IV, respectively. In comparison, the suction nozzle produces 29.5 g/s and 32.8 g/s, for case IV and case IV, respectively. As the bypass port is moved downstream in the mixing chamber, the bypass flow quickly drops to nearly zero. On the other hand, the entrained suction flow increases as the bypass inlet is moved toward the end of the mixing chamber. This is attributed to the bypass flow blocking and disturbing the flow path of the suction flow entering the mixing chamber. Compared to the ejector without a bypass inlet, the effect of the bypass is to reduce the total suction flow as the total flow rate accounted for by the suction nozzle is approximately 10 times larger than the bypass nozzle. This is seen for both operating conditions and all configurations of the bypass port.

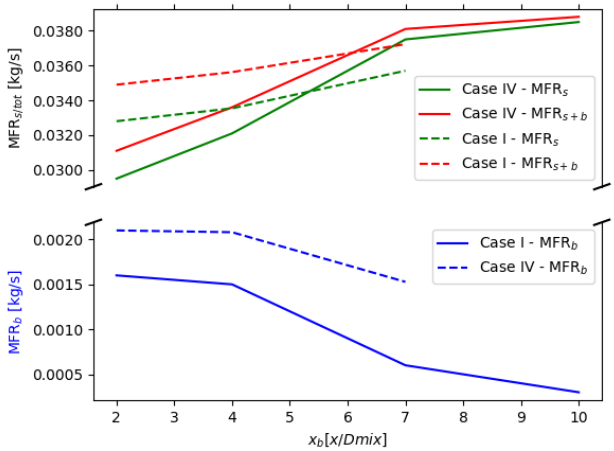

Figure 8. Plot of bypass (blue) and suction (green) mass flow rate as a function of bypass inlet position. The total pumped flow rate is shown in red.

This blockage effect is illustrated in Figure 9. Just after the bypass inlet, colored in blue, the axial velocity through the ejector is reduced to small or even locally negative values. This forces the suction flow that would pass through this area to deviate its flow path, which drastically reduces suction flow. Additionally, the path taken by the suction flow around the bypass flow creates a vortex, illustrated in Figure 10, that disturbs the main motive flow and is moved off-center.

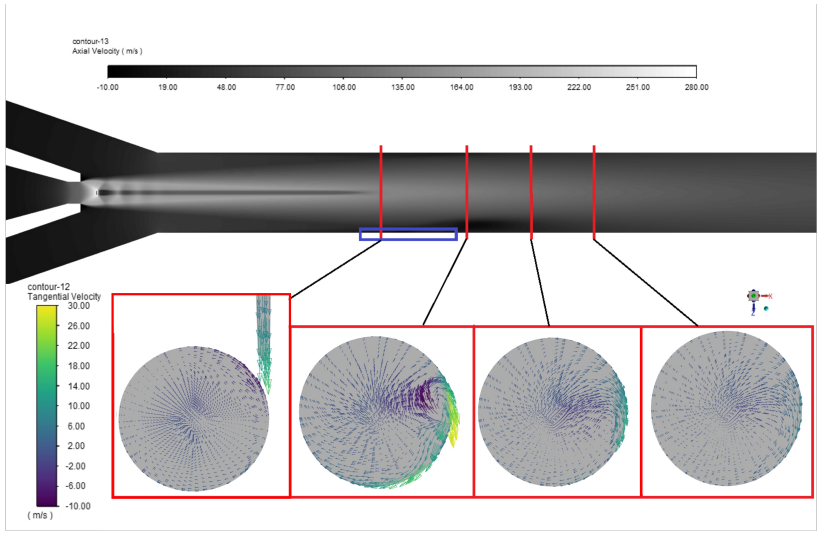

Figure 9. **Top**: Contour plot of the axial velocity in gray. The bypass inlet is colored blue. **Bottom**: Cross-sectional vector plots of the tangential velocity shown for locations along the axial direction after the bypass inlet.

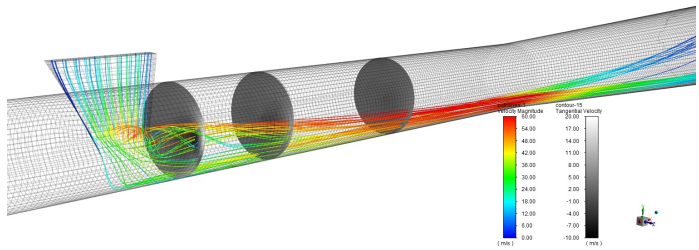

Figure 10. Flowpath illustration of the flow coming from the bypass inlet. Different cross-sectional contour plots of the tangential velocity are shown for locations along the axial direction after the bypass inlet.

5.1.2. Flow Inclination Angle, α_i, and Flow Tangential Angle, α_t

The effect of the flow inclination and tangential angles are evaluated by varying these parameters for the bypass geometry at bypass position $x_b = 4$. The inclination angle is varied between 0° to 45°. The variation in this parameter has only a minor effect on the suction and bypass flow rates. Increasing the flow inclination angle to 20° has a positive impact on the suction flow, increasing it by approximately 1–2% for cases IV and I, and had only a minor negative impact of 4% on the bypass flow for case IV and a negligible impact for case I. Further increasing the inclination angle to 45° further increases the suction mass flow rate by approximately 1%. However, this reduces the bypass flow rate by approximately the same amount. This is in agreement with the findings of Bodys et al. [70], where the impact of the bypass inlet angle was found to be negligible.

Varying the tangential angle of the bypass inlet has a significant impact on both suction and bypass flow. Reducing this angle directs the bypass flow more directly toward the central flow inside the mixing chamber. The central low pressure is, therefore, able to pump more bypass flow into the ejector. However, this comes at the cost of further blocking and disturbing the main suction flow. By decreasing the tangential angle to 60°, the bypass flow rate would increase by 85% for case IV and 66% for case I. Further decreasing this angle to 40° from 60° increased the flow rate by a further 8%. Similarly to the bypass position, the increase in bypass flow rate reduces the suction flow rate. By reducing the tangential bypass angle, the swirl component of the bypass velocity is reduced as the inlet direction is changed from tangential to radial.

5.1.3. Pressure Lift

The effect of varying pressure lift depends on the bypass geometry. For the bypass entrance near the end of the mixing chamber ($x_b = 10$, simulation 4 and 10) the bypass is significantly increased by 730% when the pressure lift is reduced from $P_{\text{lift}} = 2.5$ bar to $P_{\text{lift}} = 1$ bar. While for a bypass entrance close to the start of the mixing chamber ($x_b = 4$, simulation 14 and 16), the influence of the pressure lift on bypass flow rate is smaller, producing only an increase by 20%. Consequently, when the bypass flow is increased at a lower pressure lift, the swirl blockage effect is increased and overall performance is reduced in comparison to the ejector design without a bypass. This is seen for the simulations with a bypass inlet near the end of the ejector mixing chamber, where the difference in total entrainment between an ejector with (simulation 4 and 10) and without (simulation N3) bypass is increased from −1.6% to −14%. However, for bypass inlets near the start of the ejector mixing chamber, this difference is reduced from −20.5% to −18.8%. This increase in performance could be attributed to the higher bypass performance of the bypass inlet for lower pressure lifts. It is noted that the ejector configuration with an inlet further toward the end of the mixing chamber at a low pressure lift corresponds most closely with the conventional bypass ejector design, for instance, discussed by Bodys et al. [70], where the bypass is introduced in the ejector diffuser. However, this configuration is believed to gain less value from increased mixing by introducing a swirl component as the remaining

distance to exploit swirl mixing is shorter. Figure 11 shows the pressure distribution along the mixing-chamber center line. It can be seen that, for higher pressure lift, a significant increase in pressure of approximately 2 bar is seen along the mixing chamber, while only increasing by 0.1 bar in the low-pressure lift case. This implies that the position of the bypass flow rate is more sensitive to the bypass port position for high-pressure-lift operating conditions than for low-pressure lifts. This is important to design for when considering an ejector that will operate at varied pressure lifts.

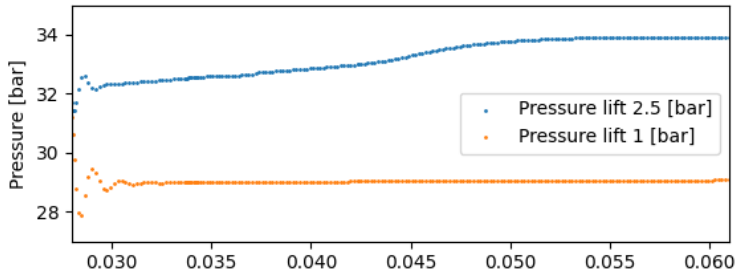

Figure 11. Pressure variation along the mixing-chamber center line for simulations N4 and N5.

5.2. Flow Structure of Swirl Mixing

Plotting the axial velocity distribution (x-direction in figures) along the radial direction at different axial positions in the mixing chamber for simulation N1, the barrel shock flow structure is seen, see Figure 12. The flow structure is symmetric around the ejector center axis. This structure is dampened and smoothed out as the flow moves toward the end of the mixing chamber. At approximately $x_b = 4$, the velocity profile reaches the classical parabolic shape with one velocity maxima along the flow center. These profiles are then used to analyze the boundary layer thickness along the mixing chamber in an ejector without a bypass inlet according to Equation (8), shown in Figure 13. The mixing layer thickness starts very thin with a thickness below 0.1 mm due to the two high-velocity peaks of the barrel shock. As the velocities are decreased, the mixing layer increases to a maximum of 0.9 mm at x_b 8 [-], near halfway through the mixing chamber. The mixing layer then decreases further down the mixing chamber as the velocities are largely evened out.

Referring to the direction towards the bypass entrance (negative z-direction) as angle $\theta_{bp} = 0$, the velocity profiles for the different directions in a swirl-bypass flow is shown in Figure 14 and 15 for simulation 5. Comparing this to the flow structure of the mixing layer without a swirl bypass, it is clear that symmetry is lost. There is a clear low-velocity zone right after the bypass entrance with close to negative axial velocity values, which, as the flow follows the swirl direction path, creates a high-velocity zone on the opposite side of the mixing chamber (θ_{bp} = 180°).

Figure 16 shows the mixing-layer thickness for different directions of velocity profiles calculated based on Equation (8). The mixing-layer thickness has a similar profile to the result without bypass. The figure shows that the mixing layer is for all angles increasing up until a maximum near $x_b = 6$, with a local minimum near $x_b = 4$, the location of the bypass inlet. Near the bypass inlet ($x_b = 4$), as the flow enters and reaches $\theta_{bp} = 90$–$180°$, a low-velocity zone is produced. This low-velocity zone increases the velocity difference between the flow core and the wall, which makes the mixing-layer thickness smaller. The flow that would go through this zone is instead diverted to the region on the opposite side of the bypass inlet, $\theta_{bp} = 270°$, which produces a corresponding high-velocity zone. This high-velocity zone in the suction flow region evens out the flow profile causing the wider mixing layer. As the flow develops down the mixing chamber, these high and low-velocity regions are shifted with the swirling of the flow. Eventually, the high and low flow regions are inverted and the mixing thickness is largest for angle $\theta_{bp} = 90°$ and smallest for the angle $\theta_{bp} = 270°$. The non-symmetric swirl structure then continues further into the diffuser.

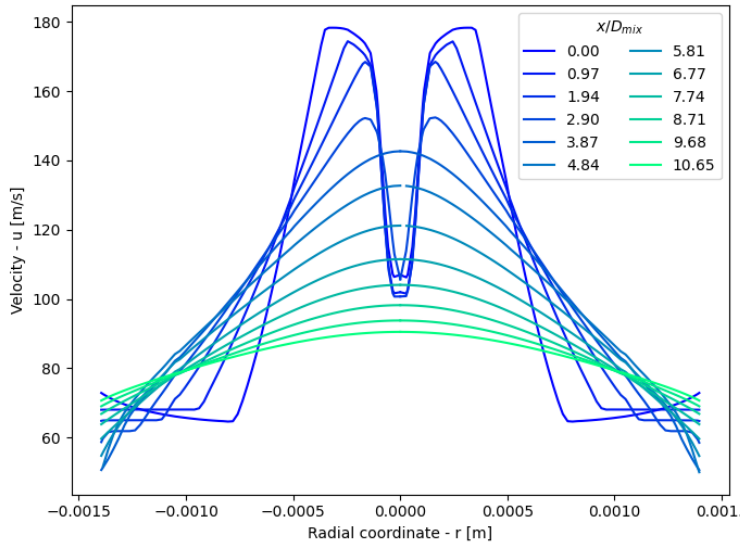

Figure 12. Velocity plot in the y-direction for the ejector without a bypass inlet. The flow is symmetric around the center line in this flow.

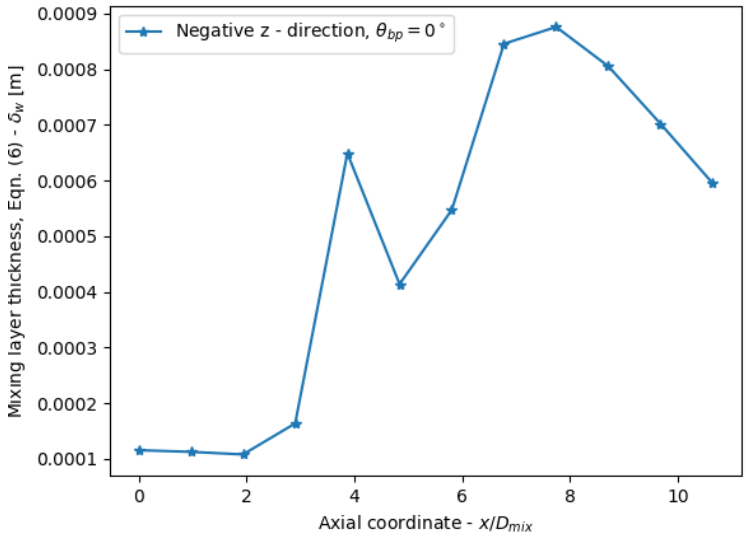

Figure 13. Mixing layer thickness along the mixing-chamber center line without a bypass inlet.

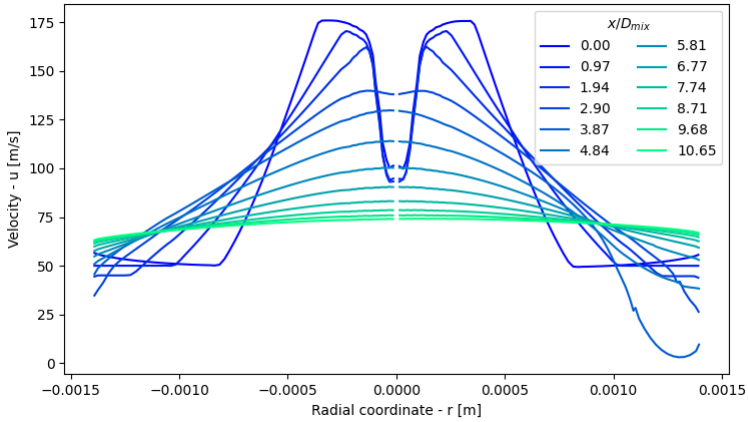

Figure 14. Velocity plot in the z-direction. Positive r direction is in the direction towards the bypass inlet, $\theta_{bp} = 0°$.

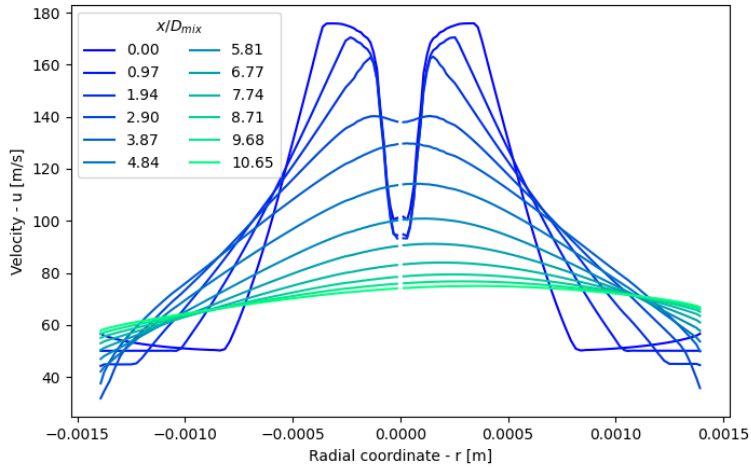

Figure 15. Velocity plot in the y direction. Positive r direction is in the direction furthest offset from the flow path of the bypass inlet, $\theta_{bp} = 270°$.

It is observed that, both for the swirl bypass and the standard ejector geometry, Figures 13 and 16, the mixing-layer thickness is evolving along the mixing chamber. Compared to theoretical estimates of this spreading rate of the mixing layer of a jet [81,82], the spreading rate of the mixing layer in the ejector varies significantly over the ejector mixing chamber. In this figure, no region of steady mixing-thickness growth is available for comparison. This is due to the barrel-shock structure in this ejector, which makes comparison challenging.

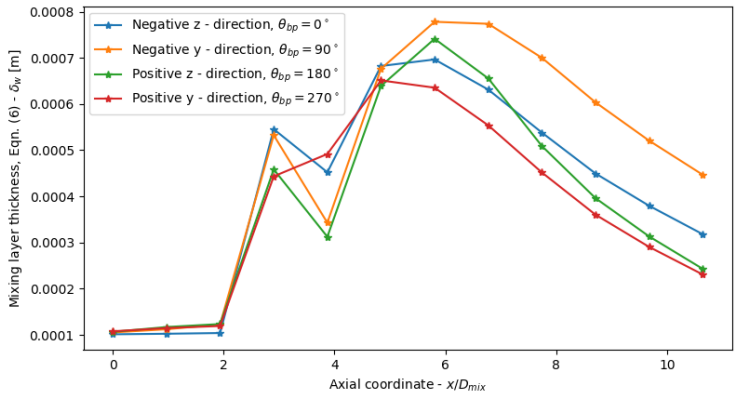

Figure 16. Plot of the mixing-layer thickness for an ejector with a bypass inlet calculated towards the wall in different radial directions plotted along the mixing-chamber center line.

Figures 17 and 18 show the development of the tangential velocity along the different orthogonal radial directions. Figure 17 clearly shows a spike of positive tangential flow near the wall at the starting location of the bypass inlet (positive radial direction). Towards the center, the flow travels in the opposite direction, setting up a vortex that dies out further downstream in the mixing chamber. On the opposing side, the flow tangential-flow direction has evened out over the cross section. In the y direction, Figure 18 shows that, right before the bypass entrance, a significant increase in tangential velocity occurs in the opposing direction to the bypass induced flow. These tangential flows in both positive and negative y directions are both moving away from the bypass inlet and towards the other side of the ejector mixing chamber. This is believed to be caused by the space taken up by the bypass flow displacing the suction flow. Downstream from the bypass inlet, the tangential velocity profile from the bypass flow is established.

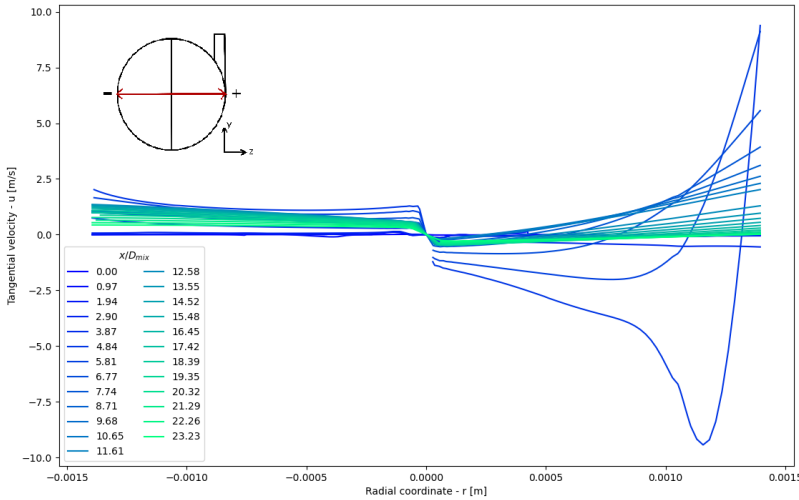

Figure 17. Tangential velocity plot in the z direction. Positive r direction is in the direction towards the bypass inlet, $\theta_{bp} = 0^\circ$.

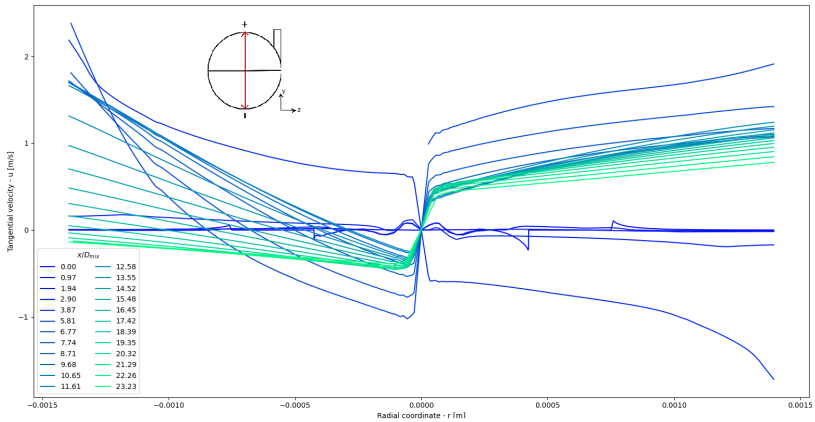

Figure 18. Tangential velocity plot in the y direction. Positive r direction is in the direction furthest offset from the flow path of the bypass inlet, $\theta_{bp} = 270°$.

5.3. Discussion

In this work, the bypass-swirl-generation inlet has been numerically investigated with CFD. The applied HEM CFD model was validated with new experimental results with a new ejector geometry. The results show the highest accuracy for high pressure and temperature motive operating conditions where predictions for motive mass flow rate are within an error 6%, which agree with previous findings in the literature with similar HEM approaches [51]. The validation work presented in this article has highlighted that significant differences are still observed between CFD modeling and measurements. This is especially true for the suction flow, where between 3 and 50% prediction error is observed. This is believed to be due to the local prediction accuracy of motive flow, the lack of accurate turbulence models that account for two-phase effects, and the lack of appropriate multiphase models for this application. In general, the numerical models are limited for high accuracy prediction of the swirl-bypass and suction flow rate. These will depend on the accurate prediction of local flow variables such as pressure and velocities, especially in the vicinity of the bypass inlet. As of yet, very limited local experimental validation data is available for R744 ejectors, primarily due to the small size, high pressures, high velocities, and multiphase flow inside the device. Still, comparison between different models can give valuable insight into the impact of different ejector design variables.

An ejector-bypass concept intended to generate swirl in the ejector mixing chamber is tested for various geometric configurations. The results show that the key impact of the swirl-bypass inlet for this specific ejector geometry is to disturb the suction flow, creating a non-symmetric mixing that reduces ejector performance. This effect is dominant regardless of the bypass angles and position. The main cause of the decrease in performance is attributed to the blocking effect of the bypass flow, limiting the available flow area of the suction flow, the turbulent energy loss induced by the non-optimal collision between these two flows, the lack of swirl component velocity recovery at the outlet, and non-symmetric effects induced by the swirl inlet. Another significant feature of the bypass swirl flow is the non-symmetric flow structure caused by having only one bypass inlet. The non-symmetry caused significant disruption to the flow path of the suction and motive flow that carried on into the diffuser. Based on these simulations, it is found that 3D effects, such as induced non-symmetric flow, are highly important to accurately predict ejector performance with swirl, and that, in general, 2D flow solutions are inadequate for designing such devices.

5.4. Open Access

To promote open access to research into environmentally sustainable solutions with ejectors, the research produced will be made available openly. The ejector geometry, code

for the generation of high-quality ejector swirl bypass mesh in ANSYS ICEM, experimental data, and velocity and mixing layer calculations are available at: https://github.com/knutringstad/Swirl_bypass_ejector (accessed on 10 September 2022).

6. Further Work and Future Design Considerations

Based on the results of this study, several improvements and suggestions for future study of swirl bypass ejectors have been found. The primary reason for the poor performance of the presented ejector is the blockage effect that is caused by the bypass flow obstructing the path of the suction flow. Increasing the diameter of the ejector mixing chamber is believed to allow for the bypass flow to flow primarily in the outer section of the mixing chamber, near the wall. This would reduce the swirl component's radial extension into the suction flow, which, in turn, will reduce the efficiency of the swirl mixing. However, the bigger mixing chamber would allow the suction flow to be less disturbed by the bypass inlet, improving the suction flow rate. Secondly, varying the size and shape of the bypass opening could reduce the impact of the suction flow blocking. Reducing the size of the opening will increase the velocity of the flow from the bypass inlet. This could be applied to intensify mixing while potentially reducing the blocked area of the suction flow. Optimization of the shape of the opening is also of interest; however, for simplicity of component manufacturing rectangular or circular openings are preferred.

Another significant feature of the bypass swirl flow is the non-symmetric flow structure caused by having only one bypass inlet. The non-symmetry caused significant disruption to the flow path of the suction and motive flow that carried on into the diffuser. By increasing the bypass inlet velocity (reducing bypass port flow area) the flow would reach further around the perimeter of the mixing chamber. This could reduce non-symmetry as the bypass flow is more evenly distributed around the mixing chamber axial direction. Another potential design improvement would be to introduce multiple inlets that were offset from each other. Such a solution would reduce non-symmetric effects that push the flow off center. This solution will, however, require additional study to find a good design in terms of manufacturability and port connections.

In this study, the swirl-velocity component is quickly smoothed out by viscosity as the flow progresses through the ejector. However, this effect may be significant for an ejector that produces a larger swirl component. In that case, the diffuser needs to be designed for swirl-component recovery.

Future studies should investigate using a holistic approach to device design. This work has only considered the swirl-bypass inlet as an addition to an already high-performance ejector design. It is, therefore, difficult to gain the largest benefit from the swirl mixing without integrating the bypass port with the other ejector design parameters. This integration could be considered by the use of optimization techniques such as those used in the authors' previous work [57]. The intended application of the swirl bypass inlet is to generate a swirl flow that increases the mixing of motive and suction flow. Each ejector is designed to have this occur inside the mixing chamber. When the pressure lift is lower than design conditions, a higher potential for work recovery is present; however, the mixing chamber will be under-dimensioned for the entrainment ratio. Here, the potential for ejector performance improvement by swirl mixing is the largest. In this work, an ejector designed for already low-pressure lifts was used, so limited improvements could be gained. Future studies should investigate the optimal ranges of swirl mixing operation and these should be integrated into the ejector design. This work has not considered the integration of the bypass and suction port, which should, in general, be designed practically and compactly with limited flow losses. The swirl-bypass concept can also be combined with other ejector concepts. Combining a swirl-bypass and a diffuser-bypass concept could potentially improve ejector entrainment by improving the performance of the ejector under different off-design conditions. Combining motive-inlet swirl and bypass-swirl generation can potentially generate synergistic effects if optimized appropriately to generate additional swirl

flow. Advanced ejector design concepts, especially in combination, require appropriate control strategies for optimal performance, which need to be explored in future work.

The authors also highlight the potential of the second application of a swirl-bypass inlet, referred to in this paper as concept (B), for motive flow control. Such a device has not yet been explored and is left for further work. Most of the design suggestions mentioned are also applicable to such a design. The bypass-design considerations regarding positioning of the bypass inlet for the optimal flow rate are then not applicable, as these are primarily decided by the motive pressure.

7. Conclusions

In this work, a novel swirl-bypass ejector design concept is explored using a high-fidelity 3D CFD model. To verify model accuracy, the multiphase CFD model is validated against new experimental data collected at a range of operating conditions with a novel ejector design. A comparison of experimental and simulation data showed good agreement (within a 6% prediction error) for the motive flow rate prediction for high operating pressures, and poorer agreement (within a 12% prediction error) for lower operating conditions, as is often seen in the literature. The ejector swirl bypass concept performed poorly with a single inlet port. The simulations showed that the generated mixing effect of the swirl flow was minimal in comparison with the reduced efficiency due to the effect of the bypass flow blocking the suction flow area. The reduction in performance of the total entrained flow ranged from -2% to -20%, depending primarily on bypass position. This effect persisted for all different configurations of the bypass port; however, it was lower for bypass positions toward the end of the mixing chamber where less bypass flow rate is produced. The bypass flow rate was found to be highly sensitive to pressure lift for inlets near the end of the mixing chamber, and less sensitive when positioned closer to the motive nozzle. The bypass flow also introduces a non-symmetric effect that pushes the primary and secondary flow out of the ejector center line. This is believed to be causing large losses due to the onset of recirculation zones in the diffuser. The mixing-layer thickness was analyzed with and without the swirl bypass and the off-center motive flow was found to cause the mixing layer between motive and suction flow to be thicker and thinner on either side of the ejector mixing chamber. Lastly, different possibilities for improvements to this concept are suggested that could bring up the efficiency of this ejector design concept. These design improvements include:

- Increase in mixing-chamber diameter.
- Reduction in bypass inlet size.
- Optimization of bypass inlet opening shape.
- Adding additional bypass inlets with a constant offset.

Additionally, several directions for future research have been presented that can potentially improve future generations of the swirl-bypass ejector design:

- Combined design optimization of ejector and swirl bypass inlet.
- Identification of optimal operating ranges.
- Designing for simple and low-cost manufacturing.
- Exploration of the combination of different ejector concepts.
- Definition of appropriate control strategies.

Author Contributions: Conceptualization, K.E.R., A.H., Å.E. and K.B.; methodology, K.E.R., Å.E.; software, K.E.R. and Å.E.; validation, K.E.R. and K.B.; formal analysis, K.E.R.; investigation, K.E.R., A.H., Å.E. and K.B.; resources, K.E.R., A.H., Å.E. and K.B.; data curation, K.E.R. and K.B.; writing—original draft preparation, K.E.R., A.H., Å.E. and K.B.; writing—review and editing, K.E.R., A.H., Å.E. and K.B.; visualization, K.E.R.; supervision, A.H., Å.E. and K.B.; project administration, A.H.; funding acquisition, A.H. All authors have read and agreed to the published version of the manuscript.

Funding: This publication was funded by HighEFF—Centre for an Energy Efficient and Competitive Industry for the Future, an 8-year Research Centre under the FME-scheme (Centre for Environment-friendly Energy Research, 257632). The authors gratefully acknowledge the financial support from the Research Council of Norway and user partners of HighEFF. The authors acknowledge the European Union's Horizon 2020 research and innovation program, 'TRI-HP project' (grant number 814888), for providing the tested ejector and for use of the experimental test rig at NTNU/SINTEF energy research laboratory in Trondheim-Norway.

Institutional Review Board Statement: Not applicable.

Informed Consent Statement: Not applicable.

Data Availability Statement: The data and analysis scripts are available at: https://github.com/knutringstad/Swirl_bypass_ejector (accessed on 10 September 2022).

Conflicts of Interest: The authors declare no conflict of interest.

Appendix A

Table A1. Experimental test data at different pressure and temperature operating conditions at the ejector outlet, suction inlet and motive inlet. The datapoints used in the paper (49, 59, 62, 79) are bolded and marked with an '*'-symbol.

#	P_m [bar]	T_m [°C]	P_m [bar]	T_s [°C]	ΔP [bar]	P_o [bar]	MFR_m [kg/s]	MFR_s [kg/s]
1	79.7	24.7	34.5	14.6	1.5	36.0	0.0322	0.0414
2	79.8	24.1	34.5	9.6	1.9	36.4	0.0331	0.0337
3	80.4	23.1	31.5	9.8	3.9	35.5	0.0346	0.0062
4	85.0	24.2	34.5	13.2	1.6	36.2	0.0361	0.0431
5	84.9	24.4	33.7	11.6	2.0	35.7	0.0357	0.0371
6	85.2	23.7	30.8	9.6	4.3	35.1	0.0368	0.0073
7	89.9	23.8	34.3	10.1	1.7	36.0	0.0390	0.0450
8	90.2	23.9	33.6	9.2	2.0	35.6	0.0391	0.0410
9	90.0	23.4	30.6	8.1	4.6	35.2	0.0395	0.0086
10	94.9	24.4	34.4	9.6	1.8	36.2	0.0409	0.0476
11	95.2	23.5	32.7	8.3	2.8	35.4	0.0418	0.0345
12	95.1	24.1	30.2	7.5	5.2	35.4	0.0414	0.0070
13	65.0	12.0	34.4	12.1	1.2	35.5	0.0315	0.0258
14	69.7	11.5	34.4	11.0	1.0	35.4	0.0342	0.0327
15	74.9	11.9	34.4	9.4	1.0	35.4	0.0367	0.0374
16	65.2	11.9	33.6	13.2	1.9	35.5	0.0319	0.0142
17	70.1	11.7	32.8	9.6	2.4	35.2	0.0348	0.0145
18	74.8	11.9	33.0	8.3	2.1	35.1	0.0370	0.0220
19	64.9	11.9	33.0	16.0	2.5	35.4	0.0321	0.0079
20	70.1	11.9	32.2	9.4	3.0	35.2	0.0352	0.0073
21	75.1	11.9	31.4	8.3	3.7	35.0	0.0379	0.0058
22	65.0	14.5	34.2	13.7	1.3	35.5	0.0311	0.0237
23	69.6	15.4	34.5	11.1	1.1	35.6	0.0331	0.0320
24	74.5	13.5	34.5	10.9	1.1	35.5	0.0361	0.0370
25	64.7	14.6	33.5	13.7	2.0	35.5	0.0312	0.0124
26	70.3	14.8	33.5	11.9	2.1	35.5	0.0340	0.0180
27	74.9	14.4	33.0	9.7	2.1	35.1	0.0365	0.0228
28	64.9	15.3	32.9	14.2	2.6	35.5	0.0315	0.0062
29	69.7	14.8	32.9	14.1	2.8	35.7	0.0339	0.0083
30	75.4	14.6	31.6	9.7	3.5	35.1	0.0373	0.0073
31	70.3	19.1	33.9	10.3	1.6	35.5	0.0324	0.0264
32	74.7	20.3	34.0	12.5	1.2	35.2	0.0340	0.0380
33	80.0	20.0	34.5	10.1	1.2	35.8	0.0369	0.0426

Table A1. *Cont.*

#	P_m [bar]	T_m [°C]	P_m [bar]	T_s [°C]	ΔP [bar]	P_o [bar]	MFR_m [kg/s]	MFR_s [kg/s]
34	85.0	19.3	34.4	9.4	1.2	35.6	0.0394	0.0430
35	90.0	19.2	34.1	7.5	1.3	35.5	0.0415	0.0442
36	94.9	19.5	33.9	7.4	1.5	35.4	0.0434	0.0452
37	69.9	19.3	33.5	11.3	2.0	35.5	0.0320	0.0193
38	75.3	19.0	32.9	11.2	2.3	35.2	0.0354	0.0205
39	80.0	19.2	33.8	9.9	1.9	35.7	0.0373	0.0305
40	85.1	18.8	33.1	8.0	2.2	35.3	0.0398	0.0296
41	89.8	19.3	33.5	6.7	2.0	35.4	0.0415	0.0364
42	94.9	19.7	32.9	7.6	2.4	35.3	0.0435	0.0351
43	70.0	18.6	32.7	16.0	2.8	35.5	0.0328	0.0086
44	75.1	18.4	31.8	11.1	3.5	35.3	0.0360	0.0067
45	79.9	18.8	31.6	11.4	3.9	35.5	0.0380	0.0071
46	84.9	19.2	30.5	6.9	4.4	34.8	0.0404	0.0071
47	89.8	19.4	30.6	8.5	4.8	35.4	0.0423	0.0072
48	95.1	19.1	29.5	6.7	5.4	34.9	0.0447	0.0060
49 *	90.3	29.2	34.2	7.9	2.0	36.3	0.0339	0.0440
50	95.1	28.3	33.8	6.9	2.0	35.8	0.0377	0.0476
51	90.2	29.0	32.4	7.0	3.2	35.6	0.0340	0.0249
52	95.0	28.1	32.5	6.6	3.1	35.6	0.0378	0.0310
53	90.3	29.2	30.8	7.0	4.6	35.5	0.0338	0.0063
54	95.4	27.5	30.3	6.4	5.0	35.3	0.0384	0.0078
55	79.7	28.6	34.4	8.0	1.9	36.3	0.0270	0.0343
56	84.7	30.1	34.5	8.0	2.1	36.6	0.0290	0.0370
57	80.0	29.5	34.8	8.7	2.1	36.9	0.0259	0.0308
58	84.8	28.8	32.4	7.9	3.1	35.5	0.0306	0.0198
59 *	79.9	29.3	31.9	14.6	3.7	35.6	0.0260	0.0067
60	85.1	28.2	30.8	7.0	4.1	34.9	0.0315	0.0076
61	71.2	24.4	34.2	8.8	1.4	35.7	0.0262	0.0336
62 *	74.6	24.3	34.3	8.6	1.5	35.7	0.0293	0.0366
63	69.9	24.6	33.4	9.3	2.2	35.6	0.0247	0.0161
64	75.3	23.7	33.5	8.4	2.1	35.6	0.0305	0.0257
65	69.7	23.4	32.1	9.9	2.9	35.0	0.0266	0.0068
66	74.7	24.4	32.2	13.2	3.3	35.4	0.0291	0.0070
67	72.8	15.2	34.1	11.8	1.3	35.4	0.0350	0.0310
68	73.2	14.7	33.3	11.1	2.0	35.3	0.0355	0.0223
69	72.9	14.8	31.4	10.7	3.5	34.9	0.0363	0.0055
70	80.0	14.8	34.3	9.2	1.1	35.4	0.0384	0.0414
71	79.9	14.1	33.0	8.3	2.2	35.2	0.0388	0.0260
72	80.2	14.1	31.2	8.6	4.1	35.3	0.0397	0.0061
73	80.0	13.9	32.4	8.2	2.9	35.3	0.0391	0.0173
74	85.1	14.6	34.3	10.6	1.2	35.5	0.0407	0.0440
75	84.9	15.1	33.4	9.7	1.9	35.3	0.0406	0.0338
76	85.0	14.2	30.4	8.2	4.6	34.9	0.0420	0.0061
77	79.9	23.7	32.5	8.0	2.8	35.4	0.0335	0.0184
78	84.8	23.9	32.2	7.4	3.1	35.3	0.0364	0.0195
79 *	82.8	34.5	34.3	9.1	2.7	37.0	0.0216	0.0263
80	83.1	34.6	32.4	8.5	3.5	35.9	0.0217	0.0122
81	82.8	34.6	31.7	9.6	3.9	35.6	0.0217	0.0053
82	86.3	34.3	34.4	9.1	2.3	36.7	0.0244	0.0332
83	85.7	34.7	33.4	8.2	3.0	36.4	0.0235	0.0225
84	85.9	33.8	31.3	7.9	4.1	35.3	0.0248	0.0077
85	64.9	19.8	33.9	11.7	1.6	35.5	0.0281	0.0193

Table A1. *Cont.*

#	P_m [bar]	T_m [°C]	P_m [bar]	T_s [°C]	ΔP [bar]	P_o [bar]	MFR_m [kg/s]	MFR_s [kg/s]
86	65.2	19.5	33.5	11.9	2.0	35.5	0.0286	0.0128
87	65.2	19.3	32.6	12.9	2.7	35.3	0.0291	0.0049
88	94.9	19.6	32.2	6.8	3.2	35.4	0.0438	0.0257
89	95.0	19.0	30.9	6.2	4.3	35.2	0.0443	0.0146
90	90.7	18.8	32.1	6.8	3.5	35.5	0.0424	0.0199
91	85.5	19.1	32.1	7.1	3.2	35.3	0.0402	0.0186
92	80.1	18.1	32.2	7.3	3.1	35.2	0.0382	0.0147
93	94.9	13.0	34.2	8.1	1.4	35.6	0.0450	0.0480
94	95.0	12.9	33.0	7.2	2.2	35.2	0.0454	0.0374
95	94.8	12.6	31.9	6.3	3.3	35.1	0.0457	0.0255
96	94.9	12.4	29.4	5.4	5.4	34.7	0.0466	0.0073
97	89.9	12.6	34.2	8.9	1.2	35.4	0.0432	0.0466
98	89.9	12.7	33.1	8.3	2.1	35.2	0.0434	0.0355
99	90.1	12.6	32.1	7.1	3.1	35.2	0.0437	0.0242
100	89.9	12.6	30.5	6.6	4.6	35.1	0.0442	0.0097
101	85.0	12.0	34.3	10.2	1.1	35.5	0.0412	0.0441
102	84.9	12.2	33.0	9.0	2.1	35.1	0.0415	0.0311
103	84.8	12.5	31.9	8.2	3.3	35.1	0.0417	0.0175
104	84.9	12.5	30.5	8.1	4.6	35.0	0.0423	0.0065
105	80.0	12.9	34.1	11.7	1.5	35.6	0.0389	0.0347
106	80.0	12.5	33.4	11.0	2.0	35.4	0.0392	0.0282
107	80.0	12.4	32.2	10.1	3.2	35.3	0.0396	0.0149
108	80.0	11.9	31.0	9.7	4.1	35.1	0.0402	0.0063
109	89.9	12.6	34.2	8.9	1.2	35.4	0.0432	0.0466
110	89.9	12.7	33.1	8.3	2.1	35.2	0.0434	0.0355
111	90.1	12.6	32.1	7.1	3.1	35.2	0.0437	0.0242
112	89.9	12.6	30.5	6.6	4.6	35.1	0.0442	0.0097
113	94.9	13.0	34.2	8.1	1.4	35.6	0.0450	0.0480
114	95.0	12.9	33.0	7.2	2.2	35.2	0.0454	0.0374
115	94.8	12.6	31.9	6.3	3.3	35.1	0.0457	0.0255
116	94.9	12.4	29.4	5.4	5.4	34.7	0.0466	0.0073
117	89.9	14.5	34.0	13.1	1.4	35.4	0.0426	0.0431
118	90.2	14.9	33.1	11.9	2.2	35.3	0.0428	0.0338
119	90.2	14.8	32.1	10.6	3.2	35.3	0.0431	0.0219
120	89.8	14.6	30.1	9.3	5.0	35.0	0.0438	0.0064
121	94.6	14.9	34.1	11.2	1.4	35.6	0.0444	0.0469
122	94.8	14.6	32.7	9.5	2.6	35.2	0.0448	0.0333
123	95.3	14.4	31.7	8.2	3.6	35.2	0.0453	0.0227
124	95.1	14.4	29.8	7.1	5.1	35.0	0.0459	0.0088
125	90.5	33.8	34.4	9.7	2.6	37.0	0.0286	0.0344
126	90.4	33.6	32.5	7.7	3.3	35.8	0.0286	0.0229
127	90.0	33.7	30.9	6.9	4.4	35.3	0.0282	0.0081
128	95.0	33.8	34.1	9.4	2.7	36.8	0.0318	0.0378
129	94.9	34.7	33.1	8.9	3.6	36.7	0.0306	0.0243
130	94.8	33.2	30.8	7.6	4.5	35.3	0.0321	0.0118

References

1. European Commision. Regulation (EU) No 517/2014 of the European Parliament and of the Council of 16th April 2014 on Fluorinated Greenhouse Gases and Repealing Regulation (EC) No 842/2006. *Off. J. Eur. Union* **2014**, *150*, 195–230.
2. Gullo, P.; Hafner, A.; Banasiak, K. Transcritical R744 refrigeration systems for supermarket applications: Current status and future perspectives. *Int. J. Refrig.* **2018**, *93*, 269–310. [CrossRef]
3. Karampour, M.; Sawalha, S. Energy efficiency evaluation of integrated CO_2 trans-critical system in supermarkets: A field measurements and modelling analysis. *Int. J. Refrig.* **2017**, *82*, 470–486. [CrossRef]
4. Rony, R.; Yang, H.; Krishnan, S.; Song, J.; Rony, R.U.; Yang, H.; Krishnan, S.; Song, J. Recent Advances in Transcritical CO_2 (R744) Heat Pump System: A Review. *Energies* **2019**, *12*, 457. [CrossRef]
5. Austin, B.T.; Sumathy, K. Transcritical carbon dioxide heat pump systems: A review. *Renew. Sustain. Energy Rev.* **2011**, *15*, 4013–4029. [CrossRef]

6. Jin, Z.; Eikevik, T.M.; Nekså, P.; Hafner, A. Investigation on CO_2 hybrid ground-coupled heat pumping system under warm climate. *Int. J. Refrig.* **2016**, *62*, 145–152. [CrossRef]
7. Yang, J.; Yu, B.; Chen, J. Improved genetic algorithm-based prediction of a CO_2 micro-channel gas-cooler against experimental data in automobile air conditioning system. *Int. J. Refrig.* **2019**, *106*, 517–525. [CrossRef]
8. Luger, C.; Rieberer, R. Multi-objective design optimization of a rail HVAC CO_2 cycle. *Int. J. Refrig.* **2018**, *92*, 133–142. [CrossRef]
9. Ozcana, H.G.; Gunerhanb, H.; Hepbaslia, A.; Yaldirakc, H. Environmental Impact and Performance Comparison of Refrigerants (R744 and R134a) in a Mobile Air Conditioning System Used for Cooling Buses. *Int. J. Eng. Technol.* **2014**, *7*, 233–241. [CrossRef]
10. de Carvalho, B.Y.K.; Melo, C.; Pereira, R.H. An experimental study on the use of variable capacity two-stage compressors in transcritical carbon dioxide light commercial refrigerating systems. *Int. J. Refrig.* **2019**, *106*, 604–615. [CrossRef]
11. Mastrullo, R.; Mauro, A.W.; Perrone, A. A model and simulations to investigate the effects of compressor and fans speeds on the performance of CO_2 light commercial refrigerators. *Appl. Therm. Eng.* **2015**, *84*, 158–169. [CrossRef]
12. Sian, R.A.; Wang, C.C. Comparative study for CO_2 and R-134a heat pump tumble dryer—A rational approach. *Int. J. Refrig.* **2019**, *106*, 474–491. [CrossRef]
13. Mancini, F.; Minetto, S.; Fornasieri, E. Thermodynamic analysis and experimental investigation of a CO_2 household heat pump dryer. *Int. J. Refrig.* **2011**, *34*, 851–858. [CrossRef]
14. Purohit, N.; Sharma, V.; Fricke, B.; Gupta, D.K.; Dasgupta, M.S. Parametric analysis and optimization of CO_2 trans-critical cycle for chiller application in a warm climate. *Appl. Therm. Eng.* **2019**, *150*, 706–719. [CrossRef]
15. Dai, B.; Zhao, X.; Liu, S.; Yang, Q.; Zhong, D.; Hao, Y.; Hao, Y. Energetic, exergetic and exergoeconomic assessment of transcritical CO_2 reversible system combined with dedicated mechanical subcooling (DMS) for residential heating and cooling. *Energy Convers. Manag.* **2020**, *209*, 112594. [CrossRef]
16. Smitt, S.; Tolstorebrov, I.; Gullo, P.; Pardiñas, A.; Hafner, A. Energy use and retrofitting potential of heat pumps in cold climate hotels. *J. Clean. Prod.* **2021**, *298*, 126799. [CrossRef]
17. Kim, M.H.; Pettersen, J.; Bullard, C.W. Fundamental process and system design issues in CO_2 vapor compression systems. *Prog. Energy Combust. Sci.* **2004**, *30*, 119–174. [CrossRef]
18. Gullo, P.; Hafner, A.; Banasiak, K.; Minetto, S.; Kriezi, E.; Gullo, P.; Hafner, A.; Banasiak, K.; Minetto, S.; Kriezi, E.E. Multi-Ejector Concept: A Comprehensive Review on its Latest Technological Developments. *Energies* **2019**, *12*, 406. [CrossRef]
19. Elbel, S.; Lawrence, N. Review of recent developments in advanced ejector technology. *Int. J. Refrig.* **2016**, *62*, 1–18. [CrossRef]
20. Chen, J.; Jarall, S.; Havtun, H.; Palm, B. A review on versatile ejector applications in refrigeration systems. *Renew. Sustain. Energy Rev.* **2015**, *49*, 67–90. [CrossRef]
21. Sumeru, K.; Nasution, H.; Ani, F.N. A review on two-phase ejector as an expansion device in vapor compression refrigeration cycle. *Renew. Sustain. Energy Rev.* **2012**, *16*, 4927–4937. [CrossRef]
22. Sarkar, J. Ejector enhanced vapor compression refrigeration and heat pump systems - A review. *Renew. Sustain. Energy Rev.* **2012**, *16*, 6647–6659. [CrossRef]
23. Besagni, G.; Mereu, R.; Inzoli, F. Ejector refrigeration: A comprehensive review. *Renew. Sustain. Energy Rev.* **2016**, *53*, 373–407. [CrossRef]
24. Tashtoush, B.M.; Al-Nimr, M.A.; Khasawneh, M.A. A comprehensive review of ejector design, performance, and applications. *Appl. Energy* **2019**, *240*, 138–172. [CrossRef]
25. Aidoun, Z.; Ameur, K.; Falsafioon, M.; Badache, M.; Aidoun, Z.; Ameur, K.; Falsafioon, M.; Badache, M. Current Advances in Ejector Modeling, Experimentation and Applications for Refrigeration and Heat Pumps. Part 2: Two-Phase Ejectors. *Inventions* **2019**, *4*, 16. [CrossRef]
26. Elbel, S. Historical and present developments of ejector refrigeration systems with emphasis on transcritical carbon dioxide air-conditioning. *Int. J. Refrig.* **2011**, *34*, 1545–1561. [CrossRef]
27. Besagni, G. Ejectors on the cutting edge: The past, the present and the perspective. *Energy* **2019**, *170*, 998–1003. [CrossRef]
28. Bodys, J.; Palacz, M.; Haida, M.; Smolka, J.; Nowak, A.J.; Banasiak, K.; Hafner, A. Full-scale multi-ejector module for a carbon dioxide supermarket refrigeration system: Numerical study of performance evaluation. *Energy Convers. Manag.* **2017**, *138*, 312–326. [CrossRef]
29. Nakagawa, M.; Marasigan, A.; Matsukawa, T.; Kurashina, A. Experimental investigation on the effect of mixing length on the performance of two-phase ejector for CO_2 refrigeration cycle with and without heat exchanger. *Int. J. Refrig.* **2011**, *34*, 1604–1613. [CrossRef]
30. Zhu, J.; Elbel, S. Application of Vortex Control to an Automotive Transcritical R744 Ejector Cycle. *SAE Tech. Pap. Ser.* **2018**, *1*, 1–6. [CrossRef]
31. Zheng, L.; Deng, J.; Zhang, Z. Dynamic simulation of an improved transcritical CO_2 ejector expansion refrigeration cycle. *Energy Convers. Manag.* **2016**, *114*, 278–289. [CrossRef]
32. Liu, F.; Groll, E.A. Study of ejector efficiencies in refrigeration cycles. *Appl. Therm. Eng.* **2013**, *52*, 360–370. [CrossRef]
33. Elbel, S.; Hrnjak, P. Experimental validation of a prototype ejector designed to reduce throttling losses encountered in transcritical R744 system operation. *Int. J. Refrig.* **2008**, *31*, 411–422. [CrossRef]
34. Taslimi Taleghani, S.; Sorin, M.; Poncet, S.; Nesreddine, H. Performance investigation of a two-phase transcritical CO_2 ejector heat pump system. *Energy Convers. Manag.* **2019**, *185*, 442–454. [CrossRef]

35. Taslimi Taleghani, S.; Sorin, M.; Poncet, S. Modeling of two-phase transcritical CO_2 ejectors for on-design and off-design conditions. *Int. J. Refrig.* **2018**, *87*, 91–105. [CrossRef]
36. Smolka, J.; Bulinski, Z.; Fic, A.; Nowak, A.J.; Banasiak, K.; Hafner, A. A computational model of a transcritical R744 ejector based on a homogeneous real fluid approach. *Appl. Math. Model.* **2013**, *37*, 1208–1224. [CrossRef]
37. Lucas, C.; Rusche, H.; Schroeder, A.; Koehler, J. Numerical investigation of a two-phase CO_2 ejector. *Int. J. Refrig.* **2014**, *43*, 154–166. [CrossRef]
38. Palacz, M.; Smolka, J.; Kus, W.; Fic, A.; Bulinski, Z.; Nowak, A.J.; Banasiak, K.; Hafner, A. CFD-based shape optimisation of a CO_2 two-phase ejector mixing section. *Appl. Therm. Eng.* **2016**, *95*, 62–69. [CrossRef]
39. Palacz, M.; Smolka, J.; Nowak, A.J.; Banasiak, K.; Hafner, A. Shape optimisation of a two-phase ejector for CO_2 refrigeration systems. *Int. J. Refrig.* **2017**, *74*, 210–221. [CrossRef]
40. Haida, M.; Smolka, J.; Hafner, A.; Ostrowski, Z.; Palacz, M.; Madsen, K.B.; Försterling, S.; Nowak, A.J.; Banasiak, K. Performance mapping of the R744 ejectors for refrigeration and air conditioning supermarket application: A hybrid reduced-order model. *Energy* **2018**, *153*, 933–948. [CrossRef]
41. Fang, Y.; Poncet, S.; Nesreddine, H.; Bartosiewicz, Y. An open-source density-based solver for two-phase CO_2 compressible flows: Verification and validation. *Int. J. Refrig.* **2019**, *106*, 526–538. [CrossRef]
42. Haida, M.; Fingas, R.; Szwajnoch, W.; Smolka, J.; Palacz, M.; Bodys, J.; Nowak, A.; Haida, M.; Fingas, R.; Szwajnoch, W.; et al. An Object-Oriented R744 Two-Phase Ejector Reduced-Order Model for Dynamic Simulations. *Energies* **2019**, *12*, 1282. [CrossRef]
43. He, Y.; Deng, J.; Li, Y.; Ma, L. A numerical contrast on the adjustable and fixed transcritical CO_2 ejector using exergy flux distribution analysis. *Energy Convers. Manag.* **2019**, *196*, 729–738. [CrossRef]
44. He, Y.; Deng, J.; Li, Y.; Zhang, X. Synergistic effect of geometric parameters on CO_2 ejector based on local exergy destruction analysis. *Appl. Therm. Eng.* **2021**, *184*, 116256. [CrossRef]
45. Colarossi, M.; Trask, N.; Schmidt, D.P.; Bergander, M.J. Multidimensional modeling of condensing two-phase ejector flow. *Int. J. Refrig.* **2012**, *35*, 290–299. [CrossRef]
46. Palacz, M.; Haida, M.; Smolka, J.; Nowak, A.J.; Banasiak, K.; Hafner, A. HEM and HRM accuracy comparison for the simulation of CO_2 expansion in two-phase ejectors for supermarket refrigeration systems. *Appl. Therm. Eng.* **2017**, *115*, 160–169. [CrossRef]
47. Bodys, J.; Smolka, J.; Palacz, M.; Haida, M.; Banasiak, K. Non-equilibrium approach for the simulation of CO_2 expansion in two-phase ejector driven by subcritical motive pressure. *Int. J. Refrig.* **2020**, *114*, 32–46. [CrossRef]
48. Giacomelli, F.; Mazzelli, F.; Milazzo, A. A novel CFD approach for the computation of R744 flashing nozzles in compressible and metastable conditions. *Energy* **2018**, *162*, 1092–1105. [CrossRef]
49. Giacomelli, F.; Mazzelli, F.; Banasiak, K.; Hafner, A.; Milazzo, A. Experimental and computational analysis of a R744 flashing ejector. *Int. J. Refrig.* **2019**, *107*, 326–343. [CrossRef]
50. Bodys, J.; Smolka, J.; Palacz, M.; Haida, M.; Banasiak, K.; Nowak, A.J. Effect of turbulence models and cavitation intensity on the motive and suction nozzle mass flow rate prediction during a non-equilibrium expansion process in the CO_2 ejector. *Appl. Therm. Eng.* **2022**, *201*, 117743. [CrossRef]
51. Ringstad, K.E.; Allouche, Y.; Gullo, P.; Ervik, Å.; Banasiak, K.; Hafner, A. A detailed review on CO_2 two-phase ejector flow modeling. *Therm. Sci. Eng. Prog.* **2020**, *20*, 100647. [CrossRef]
52. Nowak, A.J.; Palacz, M.; Smolka, J.; Banasiak, K.; Bulinski, Z.; Fic, A.; Hafner, A. CFD simulations of transport phenomena during transcritical flow of real fluid (CO_2) within ejector. *Int. J. Numer. Methods Heat Fluid Flow* **2016**, *26*, 805–817. [CrossRef]
53. Zhu, Y.; Wang, Z.; Yang, Y.; Jiang, P.X. Flow visualization of supersonic two-phase transcritical flow of CO_2 in an ejector of a refrigeration system. *Int. J. Refrig.* **2017**, *74*, 352–359. [CrossRef]
54. Bodys, J.; Palacz, M.; Haida, M.; Smolka, J.; Dziurowicz, D.; Majchrzyk, M.; Nowak, A.J. Experimental investigation of R744 transcritical flow and mixing in the two-phase ejector. *J. Physics: Conf. Ser.* **2022**, *2177*, 012044. [CrossRef]
55. Palacz, M.; Bodys, J.; Haida, M.; Smolka, J.; Nowak, A.J. Two-phase flow visualisation in the R744 vapour ejector for refrigeration systems. *Appl. Therm. Eng.* **2022**, *210*, 118322. [CrossRef]
56. Banasiak, K.; Hafner, A.; Andresen, T. Experimental and numerical investigation of the influence of the two-phase ejector geometry on the performance of the R744 heat pump. *Int. J. Refrig.* **2012**, *35*, 1617–1625. [CrossRef]
57. Ringstad, K.E.; Banasiak, K.; Ervik, Å.; Hafner, A. Machine learning and CFD for mapping and optimization of CO_2 ejectors. *Appl. Therm. Eng.* **2021**, *199*, 117604. [CrossRef]
58. Lucas, C.; Koehler, J. Experimental investigation of the COP improvement of a refrigeration cycle by use of an ejector. *Int. J. Refrig.* **2012**, *35*, 1595–1603. [CrossRef]
59. Gullo, P.; Kærn, M.R.; Haida, M.; Smolka, J.; Elbel, S. A Review on Current Status of Capacity Control Techniques for Two-Phase Ejectors. *Int. J. Refrig.* **2020**, *119*, 64–79. [CrossRef]
60. Hafner, A.; Försterling, S.; Banasiak, K. Multi-ejector concept for R-744 supermarket refrigeration. *Int. J. Refrig.* **2014**, *43*, 1–13. [CrossRef]
61. Zhu, J.; Elbel, S. Experimental investigation of a novel expansion device control mechanism: Vortex control of initially subcooled flashing R134a flow expanded through convergent-divergent nozzles. *Int. J. Refrig.* **2018**, *85*, 167–183. [CrossRef]
62. Liu, F.; Groll, E.A.; Li, D. Investigation on performance of variable geometry ejectors for CO_2 refrigeration cycles. *Energy* **2012**, *45*, 829–839. [CrossRef]

63. Gullo, P.; Birkelund, M.; Kriezi, E.E.; Ryhl Kærn, M. Novel flow modulation method for R744 two-phase ejectors—Proof of concept, optimization and first experimental results. *Energy Convers. Manag.* **2021**, *237*, 114082. [CrossRef]
64. Tang, Y.; Liu, Z.; Li, Y.; Shi, C.; Wu, H. Performance improvement of steam ejectors under designed parameters with auxiliary entrainment and structure optimization for high energy efficiency. *Energy Convers. Manag.* **2017**, *153*, 12–21. [CrossRef]
65. Tang, Y.; Li, Y.; Liu, Z.; Wu, H.; Fu, W. A novel steam ejector with auxiliary entrainment for energy conservation and performance optimization. *Energy Convers. Manag.* **2017**, *148*, 210–221. [CrossRef]
66. Chen, W.; Huang, C.; Chong, D.; Yan, J.J. Numerical assessment of ejector performance enhancement by means of combined adjustable-geometry and bypass methods. *Appl. Therm. Eng.* **2019**, *149*, 950–959. [CrossRef]
67. Chen, W.; Fan, J.; Huang, C.; Liu, S.; Chong, D.; Yan, J.J. Numerical assessment of ejector performance enhancement by means of two-bypass inlets. *Appl. Therm. Eng.* **2020**, *171*, 115086. [CrossRef]
68. Chen, W.; Chen, H.; Shi, C.; Xue, K.; Chong, D.T.; Yan, J.J. Impact of operational and geometrical factors on ejector performance with a bypass. *Appl. Therm. Eng.* **2016**, *99*, 476–484. [CrossRef]
69. Chen, W.; Chen, H.; Shi, C.; Xue, K.; Chong, D.; Yan, J. A novel ejector with a bypass to enhance the performance. *Appl. Therm. Eng.* **2016**, *93*, 939–946. [CrossRef]
70. Bodys, J.; Smolka, J.; Banasiak, K.; Palacz, M.; Haida, M.; Nowak, A.J. Performance improvement of the R744 two-phase ejector with an implemented suction nozzle bypass. *Int. J. Refrig.* **2018**, *90*, 216–228. [CrossRef]
71. Bodys, J.; Smolka, J.; Palacz, M.; Haida, M.; Banasiak, K.; Nowak, A.J. Experimental and numerical study on the R744 ejector with a suction nozzle bypass. *Appl. Therm. Eng.* **2021**, *194*, 117015. [CrossRef]
72. Park, I.S. Numerical investigation of entraining performance and operational robustness of thermal vapor compressor having swirled motive steam inflow. *Desalination* **2010**, *257*, 206–211. [CrossRef]
73. Bodys, J.; Smolka, J.; Palacz, M.; Haida, M.; Banasiak, K.; Nowak, A.J.; Hafner, A. Performance of fixed geometry ejectors with a swirl motion installed in a multi-ejector module of a CO_2 refrigeration system. *Energy* **2016**, *117*, 620–631. [CrossRef]
74. Bell, I.H.; Wronski, J.; Quoilin, S.; Lemort, V. Pure and Pseudo-pure Fluid Thermophysical Property Evaluation and the Open-Source Thermophysical Property Library CoolProp. *Ind. Eng. Chem. Res.* **2014**, *53*, 2498–2508. [CrossRef] [PubMed]
75. ANSYS. ANSYS Fluent Theory Guide. Release 19.0. Canonsburg. 2018. Available online: https://www.ansys.com/academic/terms-and-conditions (accessed on 10 September 2022).
76. Gatski, T.B.; Bonnet, J.P. *Compressibility, Turbulence and High Speed Flow*; Elsevier Ltd.: Amsterdam, The Netherlands, 2013. [CrossRef]
77. Palacz, M.; Smolka, J.; Fic, A.; Bulinski, Z.; Nowak, A.J.; Banasiak, K.; Hafner, A. Application range of the HEM approach for CO_2 expansion inside two-phase ejectors for supermarket refrigeration systems. *Int. J. Refrig.* **2015**, *59*, 251–258. [CrossRef]
78. Banasiak, K.; Hafner, A.; Kriezi, E.E.; Madsen, K.B.; Birkelund, M.; Fredslund, K.; Olsson, R. Development and performance mapping of a multi-ejector expansion work recovery pack for R744 vapour compression units. *Int. J. Refrig.* **2015**, *57*, 265–276. [CrossRef]
79. Banasiak, K.; Hafner, A. 1D Computational model of a two-phase R744 ejector for expansion work recovery. *Int. J. Therm. Sci.* **2011**, *50*, 2235–2247. [CrossRef]
80. Sjalander, M.; Jahre, M.; Tufte, G.; Reissmann, N. {EPIC}: An Energy-Efficient, High-Performance {GPGPU} Computing Research Infrastructure. *arXiv* **2019**, arXiv:1912.05848.
81. Brown, G.L.; Roshko, A. On density effects and large structure in turbulent mixing layers. *J. Fluid Mech.* **1974**, *64*, 775–816. [CrossRef]
82. Papamoschou, D.; Roshko, A. The compressible turbulent shear layer: An experimental study. *J. Fluid Mech.* **1988**, *197*, 453–477. [CrossRef]

Conference Papers

Investigation of CFD models for ammonia ejector design

Knut RINGSTAD[(a)], Yosr ALLOUCHE[(a)], Armin HAFNER[(a)]

[(a)] Norwegian University of Science and Technology,
Kolbjørn Hejes vei 1B, 7491 Trondheim, Norway,
knut.e.ringstad@ntnu.no , yosr.allouche@ntnu.no , armin.hafner@ntnu.no

ABSTRACT

In this work the flow structures inside a transonic- single phase ammonia ejector is investigated using CFD. The efficiency of ammonia (R717) vapor compression cycles can be improved by including an ejector component in the system. A good understanding of the flow phenomena inside the ejector is required for proper design of these components. In the present work a 2D axisymmetric CFD model using ANSYS Fluent software is used to investigate the flow characteristics of the ejector. The model uses a steady-state coupled pressure-based solver together with the k-omega SST turbulence model. A mesh refinement study has been done to investigate grid independency. Results indicate that the model can predict the correct trends of ejector operation, however, fails to accurately reproduce the experimental results. The results suggest that a more advanced multiphase models may be required to accurately model super-sonic ammonia ejectors.

Keywords: R717, Ejector, Computational Fluid Dynamics, Numerical Modelling, Transonic, Turbulence

1. INTRODUCTION

The introduction of the EU F-Gas Regulation 517/2014 (European commission, 2014) has brought about much interest for environmentally friendly and natural working fluids. Therefore, a promising candidate for industrial scale refrigeration is the ammonia ejector refrigeration system (ERS). Ammonia boasts low cost, high performance and favourable thermodynamic properties (Besagni et al, 2016). However, as a refrigerant ammonia has seen less frequent use than other natural working fluids. This is due to the high safety requirement due to toxicity and flammability of ammonia.

ERS provide a good alternative to compressor driven systems in terms of energy consumption. However, the ejector cycle efficiency is highly dependent on the ejector design. It is therefore of interest to have accurate models to rapidly investigate different designs. Still, the complexity of the flow inside the ejector requires advanced models to capture the physics accurately. Therefore, computational fluid dynamics (CFD) as a modelling tool has been extensively used for this application. Over the last decade, CFD simulations have been used for a variety of ejector applications and working fluids (Allouche et al., 2014, Croquer et al., 2016, Besagni and Inzoli, 2017). Two important aspects of single-phase CFD modelling of ejectors that have been extensively discussed in the literature are the dimensionality of the problem (2D or 3D flow) and the treatment of turbulence.

Many CFD investigations of ejectors have used 2D geometries (Croquer et al., 2016, Allouche et al., 2014), a simplification that significantly reduces computational requirements. Early simulations with 3D geometries (Pianthong et al, 2007, Sriveerakul et al, 2007) indicated that a 2D geometry sufficiently described the flow physics due to the high velocities in the ejector. This was however later contended by Mazzelli et al. (2015), who concluded that 3D effects are important for accurate description of flow at off-design conditions. Turbulence models for ejectors have been investigated by many research groups, and for many working fluids. However, no agreement about a preferred turbulence model has been found. Bartosiewicz et al. (2006) performed a CFD study with different RANS turbulence models looking into shock- boundary-layer interaction. Their conclusion was that k-epsilon RNG and k-omega standard model is best suited for shock capturing. Later, a comparison of the k-omega SST and the k-epsilon standard models was done by Hemidi et al. (2009) for an air-ejector. Their study indicated that the k-epsilon showed better agreement for on design conditions, and k-omega performed better at off-design conditions. The work by Mazzelli et al (2015) showed that, for an air-ejector, the k-omega SST model showed best global results. This was further supported in Besagni and Inzoli (2017), where the local and global flow features were investigated. Croquer et al. (2016) investigated ejector flow with R134a, their results indicate that k-epsilon model showed better agreement with experimental results for global flow features such as entrainment ratio, however the k-omega SST model was

still preferred due to better resolution of the local features. They also investigated the effects of different equations of state, comparing the ideal gas law with the Redlich-Kwong-Soave (RKS) and REFPROP 7 real gas databases (Lemmon et al., 2002). They concluded that the ideal gas model highly overpredicted the entrainment ratio compared to the real gas database equations.

Limited research on ammonia ejectors is available due to the aforementioned safety requirements. Especially experimental literature on ejector driven ammonia vapor compression systems is sparse. Sankarlal and Mani (2006, 2007) did experimental investigations of ejector refrigeration systems with ammonia. They investigated ejector entrainment ratio and COP with different condenser temperatures and different ejector geometries. Banasiak and Hafner (2013) used this data to verify their 1D model and to investigate different ejector geometries. Other zero- and one-dimensional models have been presented for ammonia ERS (Kornhauser, 1990, Kairouani, 2009, Banasiak et al., 2015). To the author's knowledge little CFD research has been done on ammonia ejectors. The work by Riffat et al (1996) was an early attempt at CFD modelling ejector flow for different working fluids, including ammonia. However, due to the technical limitations at the time, these simulations had to be considered with many simplifying assumptions and at a low resolution.

The present work contributes by doing a CFD investigation of the flow structures inside a transonic-single phase ammonia ejector. The numerical models and setup are discussed in Section 2.1. Further, in Section 2.2, the results are compared with previous work and a grid refinement study is discussed. In Section 3 the results are shown and compared with experimental results. The effect of different model assumptions is also discussed here. The conclusions are stated in Section 4.

2. MODEL AND RESULTS

2.1. Numerical modelling

The model is set up using the ANSYS Fluent v19.2 software framework. Simulations of the ejector were done with ammonia vapor as the working fluid, as to be comparable with the experimental work of Sankarlal and Mani (2006) and the 1D model of Banasiak and Hafner (2013).

2.1.1. Computational mesh

The computational mesh was generated using the ICEM CFD v.19.1 meshing framework. This software is based on a multiblock approach and is well suited to generation of structured grids. The ejector geometry as defined in Sankarlal and Mani (2006) is considered, cf. figure 1. Due to the symmetric geometry the domain was treated as 2D axisymmetric.

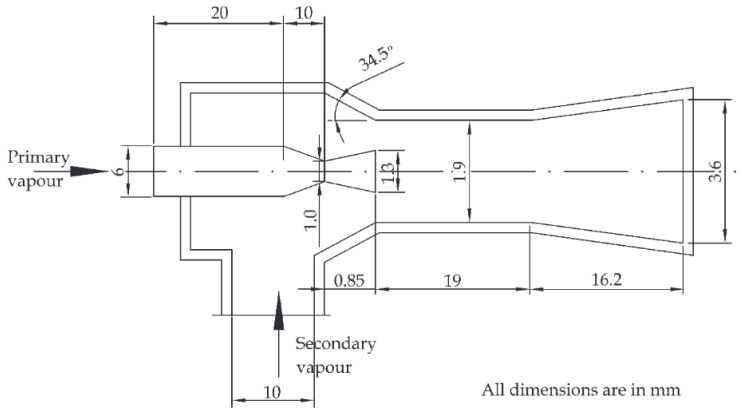

Figure 1: Geometry as defined in Sankarlal and Mani (2006), lengths are not to scale with illustration dimensions

Previous works (Pianthong et al., 2007, Sriveerakul et al., 2007) concluded that three dimensional effects are negligible for on-design conditions. Due to the computational requirements investigation of 3D effects has been left for future work. The generated mesh is 2D axisymmetric with quad cells in the whole domain. The investigated meshes were made with 50k and 200k cells. The obtained mesh showed good skewness- (below 0.3) and orthogonal quality (above 0.8). Grid independence was evaluated with two grid sizes, cf. section 2.2.1, as well as low quality autogenerated tetra mesh made with the ANSYS Meshing software.

2.1.2. Numerical solution

The equations of compressible fluid flow were solved in ANSYS Fluent using a steady state pressure-based coupled solver. Ammonia vapor is considered as a single-phase working fluid. The ammonia vapor will enter the two-phase dome in the ejector, however these two-phase effects are neglected due to modelling complexity. The validity of a single-phase simplification is investigated below in Section 3.

The ideal gas- and the real gas Redlich-Kwong-Soave (RKS) equations of state were considered and coupled with the flow solver. In the work of Croquer et al (2016), the RKS and Peng-Robinson real gas solvers yielded results closer to the experimentally observed entrainment ratio compared to ideal gas law for simulations with R134a as the working fluid. The same is observed in these simulations, cf. Table 2. Advective schemes for all variables were discretized with the second order upwind method. The pressure was discretized with the second order scheme. The least squares approach is used to evaluate gradients. Turbulence is modelled with the k-omega SST model. The near wall turbulence is treated with automatic blending function wall treatment in the k-omega models. The blending function yields results that are less sensitive to the mesh y+ value in the near wall region. Still, a low y+ value (y+<10) was observed along the domain walls. A wall resolved mesh with y+ of order 1 was tested but did not yield stable solutions.

2.1.3. Initial- and boundary conditions

The solution was initialized with the full-multigrid initiation tool with 5 multigrid levels. To improve stability, the ideal gas equation of state was used for the first 1000 iterations for the high-resolution mesh. As in Banasiak and Hafner (2013), the flow is in this work assumed to be saturated vapor at the generator and evaporator outlets, corresponding to the motive and suction inlet of the ejector, respectively. The pressure boundary conditions are defined as the saturated vapor pressure at the inlet and outlet temperatures defined in Sankarlal and Mani (2006), cf. Table 1.

Table 1. Pressure and temperature boundary conditions, three outlet conditions are evaluated here referred to as case A ($T_{condenser}$ =30°C), B ($T_{condenser}$ =33°C) and C ($T_{condenser}$ =36°C), respectively.

Boundary	*Temperature [K]*	*Pressure[bar]*
Motive inlet	*344*	*33.9*
Suction inlet	*283*	*6.2*
Outlet	*303, 306, 309*	*11.6, 12.7, 13.9*

The outlet temperature is defined only for back-flow conditions and is otherwise treated as a zero gradient Neumann boundary condition for temperature. A turbulence intensity of 5% and a turbulent viscosity ratio of 10 was specified at all inlets and outlets. These effects of these boundary conditions have been found to be negligible compared to the production of turbulence in the ejector (Croquer et al, 2016).

2.1.4. Convergence

The computations were done on a 2xAMD Epyc 24-core processor computer with 2.0 GHz clock speed. On 20 parallel cores the computations took approximately 2 hours to reach the specified convergence criterion for the 200k cell mesh. Convergence was evaluated based on reduction in scaled residuals by a factor of 1e-6 for all variables.

2.2. Verification and Validation

2.2.1. Grid refinement study

To ensure a mesh independent solution three grid resolutions were tested with the ideal gas and k-omega SST models. The entrainment ration ER was chosen as the performance indicator. An additional poorer mesh was autogenerated with ANSYS Meshing for comparison. The converged entrainment ratios and the motive- and suction mass flow rate are presented in Table 2 with the number of iterations to converge.

Table 2. Summary of grid refinement study results for the entrainment ratio and number of iterations to convergence. Outlet pressure as defined for case A, T_c = 30°C. Simulations were run with k-omega SST turbulence model and ideal gas law.

Grid	*Equation of state*	*Motive mass flow rate* [kg/s]	*Suction mass flow rate* [kg/s]	*Entrainment ratio, ER*	*Iterations*
200k cells	*Real gas RKS*	*0.00465*	*0.00126*	*0.272*	*6k*
	Ideal gas law	*0.00417*	*0.00126*	*0.303*	*6k*
50k cells	*Real gas RKS*	*0.00481*	*0.00118*	*0.246*	*1.2k*
	Ideal gas law	*0.00431*	*0.00119*	*0.276*	*1.2k*
80k cells[a)]	*Real gas RKS*	*0.00475*	*0.00122*	*0.258*	*2k*
	Ideal gas law	*0.00426*	*0.00123*	*0.289*	*2k*

a) Low quality mesh autogenerated mesh, did not converge beyond scaled residuals 1e-3

The mesh refinement yielded a large spread in entrainment ratio and motive mass-flow results. Further grid studies are required to improve upon the results. The high density (200k) mesh gave larger discrepancy compared to the experimental results for both the RKS and ideal gas law cases. This could be due to additional physics introduced in the high density mesh. For example, near wall turbulent structures could be erroneously predicted by a mismatch between near wall treatment and mesh refinement. The general trend observed is that the ideal gas equation of state underpredicts the motive mass-flow compared to RKS, and therefore over predicts the ER. This was also previously noted by Croquer et al. (2016). The medium density (50k) mesh was used for the rest of the study as it yielded results closest to experimental value of ER=0.2129.

2.2.2. Comparison with previous results

The results of the simulations are compared to the results of Sankarlal and Mani (2006) and Banasiak and Hafner (2013), shown in Table 3. The model by Banasiak and Hafner (2013) was based on their previous model for two-phase CO_2 ejectors (Banasiak and Hafner, 2013). This 1D model is able to model two-phase non-equilibrium effects. Two-phase effects are not considered by the present CFD model and could explain the large deviations from the experimental and 1D results.

Table 3. Comparison of entrainment ratio at different condenser temperatures in previous works. 50k cells grid, k-omega turbulence model, RKS.

$T_{condenser}$, °C	*30*	*33*	*36*
Study	*Entrainment ratio*		
Experimental- Sankarlal and Mani (2006)	*0.2129*	*0.1751*	*0.1431*
1D model – Banasiak and Hafner (2013)	*0.2130*	*0.1800*	*0.1280*
Present work	*0.246*	*0.244*	*0.112*
Present work, error	*15%*	*40%*	*-22%*

3. RESULTS AND DISCUSSION

The aim of this work is to investigate the capabilities of CFD modelling for ammonia ejectors. The effect of condenser temperature and the flow structures inside the ejector are presented below. Furthermore, the potential sources of error will be critically investigated.

Three modes are commonly used to classify ejector operation: double chocked, single chocked and ejector-failure (Allouche et al., 2014). These regions are commonly presented in the literature with an ejector characteristic curve, showing the entrainment ratio as a function of the pressure or temperature. The characteristic shape of ejector performance for a single phase ejector reproduce the three modes of operation mentioned above. In the double choked region the entrainment ratio is constant up to a certain condenser pressure (temperature). Beyond this pressure, in the single choked region, the entrainment ratio decreases linearly down to zero. At zero entrainment ratio the ejector is no longer functional. The present CFD results indicate such a trend (Figure 2), as the entrainment remains constant between condenser temperature 30 to 33. This trend is, however, not seen in the experimental or 1D model results. This suggests that some underlying assumption may be wrong.

One potential source of error is numerical inaccuracies. These discrepancies should be reduced with mesh refinement. However, as shown in Section 2.2.1, grid refinement did not improve the errors and mesh independency could not be shown. Further investigation into mesh and numerical solution methods is required.

Another potential cause for the discrepancies between the CFD model and the experimental results is the assumption of single phase flow. The difference in results between different equations of state emphasizes the impact of the thermodynamic models. As the ejector flow exists partially inside the two-phase dome, multi-phase effects may be non-negligible. Furthermore, the rapid depressurization in the motive nozzle may induce a non-equilibrium phase transfer referred to as flashing. Flashing ejectors has been studied extensively for water, and has been shown to have a large impact on model performance (Liao and Lucas, 2017). To further investigate the errors connected to the two-phase assumption further numerical work is required. Furthermore, experimental values for the mass flow rate in the suction and motive stream are needed to accurately verify and validate further CFD work.

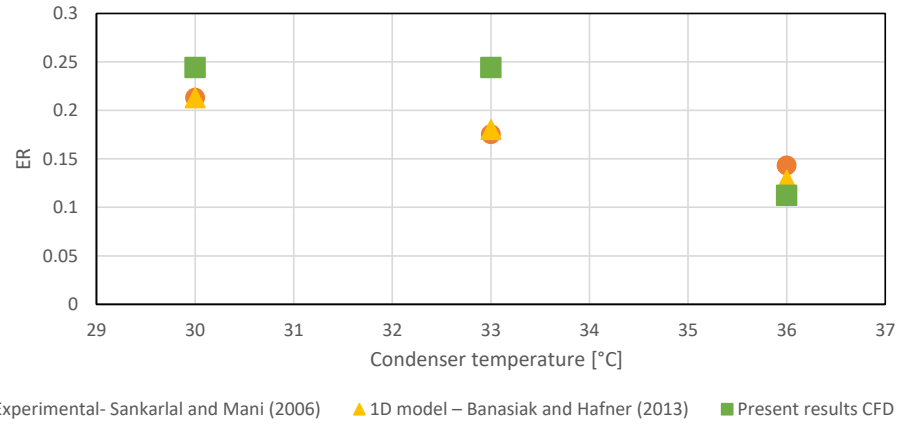

Figure 2: Ejector characteristic curve. Entrainment ratio (ER) vs condenser temperature T_c

The velocity and pressure distribution along the centreline for the 1D model and CFD model are shown in Figure 3 and Figure 4, respectively. The center line velocity shows a similar trend in the 1D and CFD model results. Both models yield a maximum velocity at the nozzle throat. However, in Banasiak the velocity quickly levels out to a constant value in the mixing section. The present CFD results show that this velocity reduction happens through a series of shocks and level off at a higher velocity than the 1D model. Similarly, the CFD results show that the expansion process in the diffuser happens through a shock train, which is not apparent in the 1D model results. Still, these difference may be attributed to the single phase assumption.

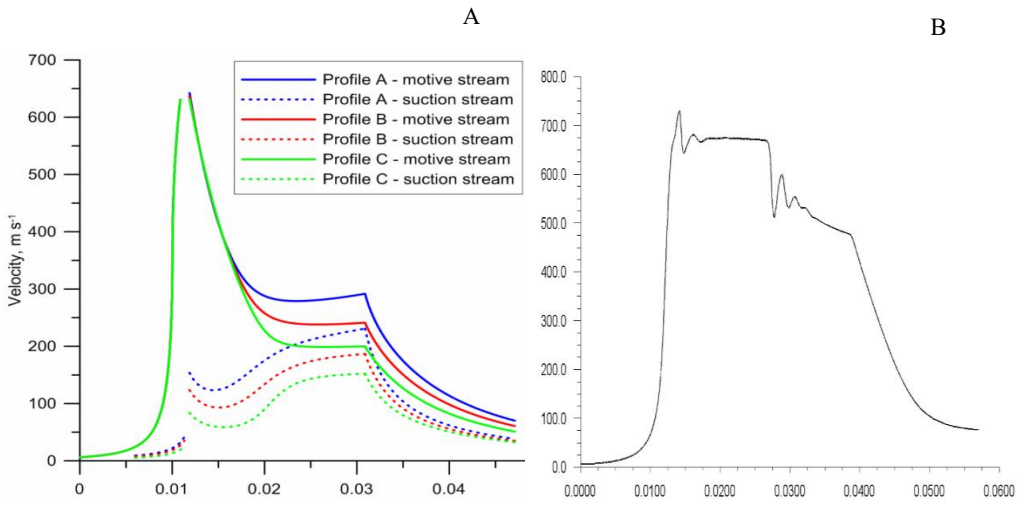

Figure 3: Velocity distribution along centreline. A: Banasiak and Hafner (2013), B: Present work

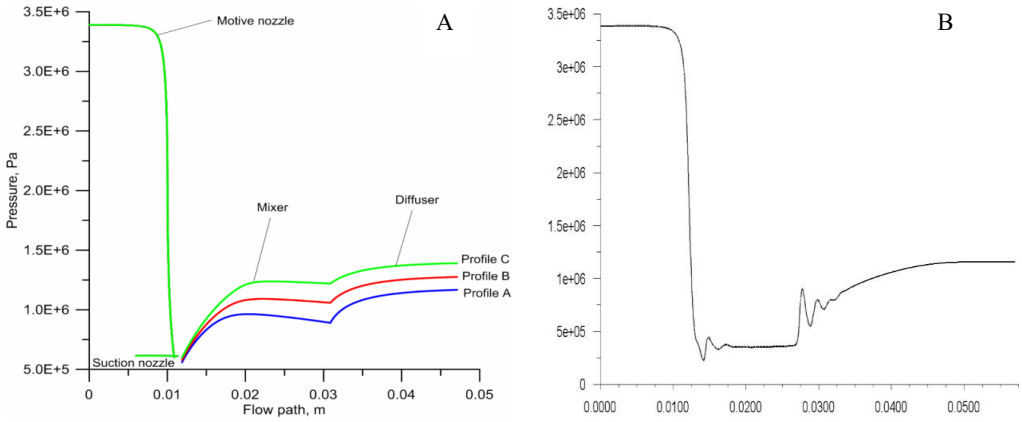

Figure 4: Pressure distribution along centreline. A: Banasiak and Hafner (2013), B: Present work

4. CONCLUSIONS

Accurate modelling of ejectors can improve efficiency of ejector refrigeration system. In the present work, a CFD model of a super-sonic ejector with ammonia (R717) has been presented. The model results show high dependency on the different meshes and equation of state. The CFD model can predict the different regions commonly observed in ejector operation, however experimental data is not well predicted. The model inaccuracies are difficult to attribute to a single modelling aspect. However, the single-phase assumption as well as numerical errors are thought to be the main contributors to the observed discrepancies. The limited experimental results make validation and model improvement challenging. Further experimental investigations with accurate measurements of both motive and suction mass-flow rates is necessary to improve the accuracy of the CFD models.

ACKNOWLEDGEMENTS

The work is part of HighEFF - Centre for an Energy Efficient and Competitive Industry for the Future, an 8-year Research Centre under the FME-scheme (Centre for Environment-friendly Energy Research, 257632/E20). The authors gratefully acknowledge the financial support from the Research Council of Norway and user partners of HighEFF.

NOMENCLATURE

CFD	Computational fluid dynamics	*ER*	Entrainment ratio
ERS	Ejector refrigeration system	*RANS*	Reynolds Averaged Navier Stokes
RKS	Redlich-Kwong-Soave		

REFERENCES

Allouche, Y., Bouden, C., Varga, S., 2014. A CFD analysis of the flow structure inside a steam ejector to identify the suitable experimental operating conditions for a solar-driven refrigeration system. International Journal of Refrigeration 39, 186–195

Banasiak, K., Hafner, A., 2011. 1D Computational model of a two-phase R744 ejector for expansion work recovery. International Journal of Thermal Sciences, 50(11), 2235-2247.

Banasiak, K., Hafner, A., 2013, Influence of ejector performance on the overall efficiency on ammonia ejector refrigeration cycle, Proceedings of the 5th IIR Conference: Ammonia Refrigeration Technology, Ohrid

Banasiak, K., Hafner, A., Steiner, A., 2015, COP improvement of two-stage ammonia heat pumps by use of ejector, Proceedings of the 6th IIR Conference: Ammonia Refrigeration Technology, Ohrid

Bartosiewicz, Y., Aidoun, Z., Mercadier, Y., 2006, Numerical assessment of ejector operation for refrigeration applications based on CFD, Applied Thermal Engineering,Volume 26, Issues 5–6, Pages 604-612

Besagni, G., Inzoli, F., 2017. Computational fluid-dynamics modeling of supersonic ejectors: Screening of turbulence modeling approaches., Applied Thermal Engineering 117, 122–144

Besagni, G., Mereu, R., Inzoli, F., 2016. Ejector refrigeration: A comprehensive review., Renewable and Sustainable Energy Reviews 53, 373 – 407.

Croquer, S, Poncet, S., Aidoun, Z., 2016, Turbulence modeling of a single-phase R134a supersonic ejector. Part 1: Numerical benchmark, International Journal of Refrigeration, Volume 61, Pages 140-152

Elbel, S., Lawrence, N., 2016, Review of recent developments in advanced ejector technology, International Journal of Refrigeration, Volume 62, Pages 1-18

European Commission, 2014. Regulation (EU) No 517/2014 of the European Parliament and of the Council of 16th April 2014 on fluorinated greenhouse gases and repealing Regulation (EC), No 842/2006. Brussels, Belgium.

Hemidi, A., Henry, F., Leclaire, S., Seynhaeve, J., Bartosiewicz, Y., 2009, CFD analysis of a supersonic air ejector. Part II: Relation between global operation and local flow features, Applied Thermal Engineering, Volume 29, Issues 14–15, Pages 2990-2998

Kairouani, L., Elakhdar, M., Nehdi, E., Bouaziz, N., 2009. Use of ejectors in a multi-evaporator refrigeration system for performance enhancement. International Journal of Refrigeration 32 (6), 1173–1185.

Kornhauser, A., The Use of an Ejector as a Refrigerant Expander, 1990, International Refrigeration and Air Conditioning Conference, Paper 82.

Lemmon, E., Huber, M., McLinden, M., 2002, NIST reference fluid thermodynamic and transport properties—REFPROP. NIST standard reference database, 23, v7.

Liao, Y., Lucas, D., 2017. Computational modelling of flash boiling flows: A literature survey. Int. J. Heat Mass Transfer 111, 246–265.

Mazzelli, F., Little, A., Garimella, S., Bartosiewicz, Y., 2015, Computational and experimental analysis of supersonic air ejector: Turbulence modeling and assessment of 3D effects, International Journal of Heat and Fluid Flow, Volume 56, 305-316

Pianthong, K., Seehanam, W., Behnia, M., Sriveerakul, T., Aphornratana, S., 2007, Investigation and improvement of ejector refrigeration system using computational fluid dynamics technique, Energy Conversion and Management, Volume 48, Issue 9, Pages 2556-2564

Sankarlal T., Mani A., 2006, Experimental studies on an ammonia ejector refrigeration system, Int. Communications in Heat and Mass Transfer, 33: 224–230.

Sankarlal T., Mani, A., 2007, Experimental investigations on ejector refrigeration system with ammonia, Renewable Energy, 32: 1403–1413.

Sriveerakul, T., Aphornratana, S., Chunnanond, K., 2007, Performance prediction of steam ejector using computational fluid dynamics: Part 1. Validation of the CFD results,International Journal of Thermal Sciences,Volume 46, Issue 8, Pages 812-822

Manuscript ID: 1870
DOI: 10.18462/iir.icr.2019.1870

CO_2 ejector modelling using CFD: current status

Knut RINGSTAD[(a)], Yosr ALLOUCHE[(a)], Paride GULLO[(a)], Krzysztof BANASIAK[(b)], Armin HAFNER[(a)]

[(a)] Norwegian University of Science and Technology, Kolbjørn Hejes vei 1B, 7491 Trondheim, Norway,
[(b)] SINTEF Energy, Kolbjørn Hejes vei 1d, 7465 Trondheim, Norway
knut.e.ringstad@ntnu.no, armin.hafner@ntnu.no

ABSTRACT

This paper presents the current status of CFD modelling applied to CO_2 two-phase ejectors for refrigeration applications. Previous reviews on CO_2 ejector technology have provided detailed analysis and thorough discussion about the optimal design and performance parameters. However, there is still a lack of information about CFD modelling of CO_2 ejectors, mainly when it comes to the accuracy of the two-phase ejector models. The ultimate goal of this paper is to provide a complete overview about CFD modelling of two-phase CO_2 ejectors for refrigeration applications, as mainly analytical approaches were previously discussed. The fundamental background for the research work carried out within CO_2 two-phase modelling using CFD is presented through this review. Moreover, it highlights the main challenges that are still needed to be overcome mainly related to turbulence modelling, fluid properties and 3D-effects in multi-phase flows.
Keywords: CFD, Expansion Work Recovery, Multi-Phase Flow, R744, Trans-Critical Refrigeration System, Two-Phase Ejector.

1. INTRODUCTION

The entry into force of the EU F-Gas Regulation 517/2014 (European commission, 2014) has led CO_2 (R744) to take centre stage as the most promising refrigerant for many applications. Also, despite its low critical temperature, nowadays trans-critical R744 vapour-compression systems offer great energy efficiencies even at high cooling medium temperatures. This result can be achieved by recovering part of the available expansion work with the aid of two-phase ejectors. As an example, it was found that commercial R744 refrigeration units consume up to 25% less electricity than the solutions relying on man-made working fluids in warm climates (Gullo et al., 2018). Furthermore, ejector-equipped CO_2 vapour-compression systems are expected to attain similar energy benefits to those experienced in supermarkets in other applications too (Hafner et al., 2014). However, the potential improvements in performance offered by an ejector are highly sensitive to its four characteristic dimensions, i.e. suction nozzle, motive nozzle, mixing chamber and diffuser. Therefore, methods for efficient and accurate design of ejectors has gained interest from industry and academia. A promising tool for enhancing ejector performance is the advanced computational fluid dynamics (CFD). CFD offers insights into the complex flow in the ejector device and has already been applied to single-phase ejector with satisfactory results (Grazzini et al., 2018). An overview of R744 two-phase ejector CFD models was presented by Nowak et al. (2016) and also discussed by Elbel and Lawrence (2016). These investigations revealed that currently state of the art CFD models can quite accurately predict certain flow parameters in R744 two-phase ejectors. However, the comparison with the limited experimental results uncovers significant errors, especially at off-design conditions. In addition, the limitations and advantages of different models as well as recent developments and challenges in flash models for R744 have not lately been described. Therefore, the aim of this paper is to bridge the aforementioned knowledge gaps by carrying out a comprehensive review on the developments of CFD models for R744 two-phase ejectors. Special attention has been given to two-phase flashing models, as this has been the discussion focus in recent literature.

2. EVALUATION OF CURRENT STATUS

CO_2 two-phase ejectors were primarily designed and investigated mainly based on experimental studies (Elbel and Lawrence, 2016). The experimental work by Nakagawa et al. (2011) revealed improvements in Coefficient of Performance (COP) of up to 26% compared to systems without ejectors. However, design of ejectors can be carried out more efficiently with models, as the time and resource costs of experimental studies heavily outweigh those of models. Furthermore, accurate models can give insights into the flow physics that can allow for improved and new designs. Still, unobtrusive experimental results for the validation of these models is lacking due to the difficulty involved. While much progress has been made on R744 ejector modelling, the treatment of multiphase flows is not well understood and many simplifying assumptions have been considered. Several theoretical frameworks have been presented for such models The development started with one dimensional models with the homogeneous equilibrium model (Liu and Groll, 2012), which was later furthered with more advanced non-equilibrium approaches (Banasiak and Hafner, 2011; Brown et al., 2013). While able to capture much of the flow physics, 3D effects were found to be non-negligible (Smolka et al., 2013). These limitations ushered in a much research in the multidimensional CFD models. The paper is organized as follows, the homogeneous equilibrium model, homogeneous relaxation model and the mixture models are presented in Subsection 2.1-2.3. Some applications of these models are described in Subsection 2.4, further model reduction is discussed in Subsection 2.5. The advantages and limitations of the aforementioned models are summarized in Section 3. Finally, main conclusions are given in Section 4.

2.1. Homogeneous Equilibrium Model

The high accuracy and relative simplicity of the homogeneous equilibrium model (HEM), where two-phase pure CO_2 mixture is modelled as a pseudo-single-phase fluid, has been demonstrated for one-dimensional models (Elbel and Lawrence, 2016). The HEM approach assumes instantaneous thermodynamic and mechanical equilibrium between liquid and vapour. With these assumptions both phases are described with a single velocity-($\vec{u}$), temperature- (T) and pressure-field (P). Smolka et al. (2013) implemented such a homogeneous equilibrium model (HEM) into a 3D CFD model using ANSYS Fluent (ANSYS, 2019) to capture two-phase effects in R744 ejectors. They used an enthalpy formulation (Equation 1) in the Energy equation, treating enthalpy, instead of temperature, as the transported variable in the energy equation. The energy equation is then re-written into:

$$\nabla \cdot (\rho \vec{u} h) = \nabla \cdot (\Gamma_{eff} \nabla h) + \dot{S}_{h1} + \dot{S}_{h2} + \dot{S}_{h3} \qquad \text{Eq. (1)}$$

The source terms $\dot{S}_{h1-3}$ describe the mechanical energy, the irreversible dissipation of the kinetic energy variations and the dissipation of the turbulent kinetic energy (Smolka et al., 2013), respectively. Under the equilibrium assumption the pressure and enthalpy uniquely define the thermodynamic state in the two-phase dome:

$$\rho, \mu, k, c_p = f(P, h) \qquad \text{Eq. (2)}$$

The two-phase equilibrium properties were in Smolka et al. (2013) found using the REFPROP library (Lemmon et al., 2013), and implemented into Fluent using user-defined functions (UDFs). Experimental results performed at the SINTEF Energy Research laboratory in Trondheim (Norway) were presented and used to validate the model. Their findings indicate that 3D effects are non-negligible as was commonly assumed in previous simulations (Colarossi et al., 2012). The HEM approach produced results that could accurately describe the global parameters (e.g. mass flow rate) for conditions near the critical point. A maximum deviation of about 12% for the mass flow rate was computed. A similar approach to the work by Smolka et al. (2013) was proposed by Lucas et al. (2014). A 3D CFD model using the HEM approach was implemented in the open source CFD framework OpenFOAM (Weller et al, 1998), using the TEMO-media library. The results were compared with the experimental data collected by Lucas et al. (2013). The comparison showed 20% and 10% discrepancy in pressure recovery when operating with and without suction flow, respectively. They concluded that this error difference was due to the model's inaccurate description of mixing losses. Further studies with the HEM were implemented by Giacomelli et al. (2016, 2018a).

In these works, the HEM was implemented with look-up tables generated from the REFPROP library for speed of sound and density.
Palacz et al. (2015) evaluated the application range of the HEM approach for R744 ejectors within typical supermarket refrigeration operational conditions. Here, a multi-ejector block was investigated with experimental validation for 24 different running modes. Their findings indicate that the HEM approach can produce accurate results when the operating conditions are close to or above the critical pressure of CO_2. However, as the motive pressure and temperature is decreased the accuracy of the HEM approach is dramatically lowered when compared to their experimental results. These significant errors were attributed to the non-equilibrium effects at operating conditions away from the critical point. These effects are discussed in the next paragraph.
The limitations of the HEM have previously been discussed in the literature (Wallis, 1980, Liao and Lucas, 2017). In general, states further away from the critical point have a wider meta-stable region. This translates to slower meta-stable transition and larger significance for non-equilibrium effects. Further limitations concerning the homogeneous approaches is discussed in Section 3.

2.2. Homogeneous Relaxation Model

Palacz et al. (2015) concluded that non-equilibrium models are necessary to properly model a R744 ejector for the whole range of common supermarket operating conditions. Bilicki and Kestin (1990) introduced the homogeneous relaxation model, a relaxed version of the HEM. The homogeneous relaxation model (HRM) assumes, similarly to the HEM approach, a single pseudo fluid representing the mixture of the two-phases. However, meta-stability effects are treated by applying a relaxed vapour quality transport equation (Eq. 3).
This relaxation delays the onset of phase change in the meta-stable region. Downar-Zapolski et al. (1996) defined a relation for the relaxation time, θ, formulated in Eq. 4. The parameters of Eq. 4 are the mixture void fraction defined in Eq. 5, and φ is a non-dimensionalized pressure parameter. This latter parameter was defined for supercritical parameters in Angielczyk et al. (2010) stated in Eq. 6. The exponents a and b were empirically fit for CO_2 in Angielczyk et al. (2010). Among the first works with CFD simulations of R744 ejectors using the HRM is the model used by Colarossi et al. (2012). In this work, the HRM was implemented in a 2D CFD model using the OpenFOAM framework. As a starting point, they used the empirical relations for the relaxation factor for flashing water (Downar-Zapolski et al., 1996). Colarossi et al. (2012) compared the resulting pressure recovery from their simulations with the experimental results in Nakagawa et al. (2011). The comparison showed up to 50% deviation, with an average error of 18.6%. They concluded that the non-equilibrium effects were negligible, this was however evaluated near the critical point of R744.

$$\frac{Dx}{Dt} = \frac{\bar{x} - x}{\theta} \qquad \text{Eq. (3)}$$

$$\theta = \theta_0 \alpha^a \varphi^b \qquad \text{Eq. (4)}$$

$$\alpha = \frac{\rho_{sl} - \rho}{\rho_{sl} - \rho_{sv}} \qquad \text{Eq. (5)}$$

$$\varphi = \left| \frac{P_{sat}(s_{motive}) - P}{P_{crit} - P_{sat}(s_{motive})} \right| \qquad \text{Eq. (6)}$$

The results by Palacz et al. (2015) were contrasted with those obtained by Palacz et al. (2017a), which were based on the HRM approach relying on the constant relaxation time for CO_2 presented by Angielczyk et al. (2010). The comparison revealed that the HRM was able to improve model prediction compared to HEM when the operating regime is far away from the critical point. However, at supercritical inlet conditions the HEM approach would perform better than their HRM. Overall, the authors found that their current HRM only improved model accuracy by up to 5% compared to the HEM. This improvement was found unsatisfactory which prompted further investigation into the choice of relaxation time.

The conclusions from Palacz et al. (2017a) were that a constant relaxation time is not appropriate when a large range of operating conditions is considered. Much investigation went into the different parameters of equation (4) in the study by Haida et al. (2018d). The effect of the different parameters θ_0, *a* and *b* on the nozzle expansion process was discussed. In the mentioned study an optimization algorithm was used to find optimal relaxation time parameters for different operational ranges. The authors divided the motive nozzle pressure into a high, medium and low pressure range. In each pressure range the RT-parameters that minimized the mass flow rate error were found. The modified HRM showed improved results with below 15% error for the mass flow are for the extended operating range.

2.3. Mixture Models

The physical mechanisms of phase change are only indirectly treated by the HEM and HRM, as the two-phase properties are determined based on equilibrium states. An alternative approach to evaluate the phase fractions is using mixture models. Similar to the homogeneous approaches, an averaged mass, momentum and energy equation are solved with the single pseudo fluid approach (Eqs. 7-9). However, an additional equation governing the transport of the phase fraction is included, Eq. 10. Here, additional submodels for the phase mass transfer mechanisms (Λ) allow for more accurate estimates of the phase fraction (α). The state of each phase is then evaluated separately and thermodynamic properties are found by volume and mass averaging from the vapour and liquid properties. This contrasts the HEM and HRM, where the phase fraction and other fluid properties are evaluated based on the equilibrium state in the two phase region (Eq. 2).

$$\frac{\partial \rho_m}{\partial t} + \frac{\partial}{\partial x_j}\left(\rho_m u_{m,j}\right) = 0 \qquad \text{Eq. (7)}$$

$$\frac{\partial \rho_m u_{m,i}}{\partial t} + \frac{\partial}{\partial x_j}\left(\rho_m u_{m,j} u_{m,i} + P\delta_{ij} - \tau_{ij,eff}\right) = 0 \qquad \text{Eq. (8)}$$

$$\frac{\partial \rho_m E_m}{\partial t} + \frac{\partial}{\partial x_j}\left(\rho_m u_{m,j} h_m - q_{j,eff} + u_{m,i}\tau_{ij,eff}\right) = 0 \qquad \text{Eq. (9)}$$

$$\frac{\partial \rho_k \alpha_k}{\partial t} + \frac{\partial}{\partial x_j}\left(\rho_k u_j \alpha_k\right) = \Lambda_e - \Lambda_c \qquad \text{Eq. (10)}$$

the subscript *k* is the phase index, summing over the N number of phases. To the best of the authors' knowledge, the first use of a mixture model for the R744 ejector was presented in Yazdani et al. (2012). In the mentioned paper, a non-equilibrium mixture model was implemented into a 3D CFD model in ANSYS Fluent. Yazdani et al. (2012) found the thermodynamic properties using the REFPROP libraries for supercritical fluid and subcooled fluid. States inside the saturation region were interpolated from the saturation lines in the REFPROP library. Mass transfer was considered through condensation and evaporation mechanisms, where meta-stability was treated by introducing a time delay analogous to the relaxation time of the HRM. The model of Yazdani et al. (2012) also included additional terms for velocity slip between the phases in Equation 8.
Recently, Giacomelli et al. (2018b) implemented a mixture model in ANSYS Fluent to simulate supersonic nozzle flow. In this model the compressibility of both the liquid and gas phase was considered with user-defined real gas models. Here, the two-phases were treated computationally as two interacting fluids of different species, allowing their better description. The model uses look-up tables based on the NIST REFPROP library to define the properties of both phases. Furthermore, the presented method is applicable for a wide range of multiphase and compressible flows.

2.4. Applications

The presented CFD models have been extensively used for investigations of designs and concepts. The CFD model by Smolka et al. (2013) was used to investigate irreversibility in the ejector in

Banasiak et al. (2014). The entropy increase in different sections of the ejector was evaluated with different ejector geometries. The analysis shows that the mixing section is one of the most significant contributors to entropy generation due to the complex shock- and turbulent structures. Furthermore, the authors argue that geometric optimization should focus on the interactions between different geometric parameters, as individual optimization of these parameters in isolation yields suboptimal results. Entropy generation in ejectors was further investigated by Sierra-Pallares (2016), where a direct method was applied to investigate entropy generation in three R134a ejectors. The authors novel approach involved solving the differential equations of entropy transport, identifying four mechanisms of entropy generation. Their investigation revealed that the primary contributor is the turbulent viscous dissipation produced in the shock train and nozzle exit shear layer.
Later, this model was applied for the investigation of an optimized shape of R744 two-phase ejectors by Palacz et al. (2016). The optimization tool was developed with the *ejectorPL* software. This is a script that automates most of the CFD workflow in the pre- and post-processing, and feeds the resulting model into the optimization algorithm. The optimization was done using both a genetic algorithm and an evolutionary algorithm for six geometrical parameters to maximize the ejector efficiency. The results show that these methodologies can effectively be used for shape optimization when the operating conditions are within the CFD model's range of validity. The shape investigations were furthered in Palacz et al. (2017b) with 3 more geometric parameters and for two additional ejector geometries than in Palacz et al. (2016). Here the genetic algorithm was applied. This procedure improved the ejector efficiencies by 6% in a robust and efficient way. A comparative study of the controllable needle ejector (Liu et al., 2012) and the fixed geometry ejector (as used in the multi-ejector block concept formulated by Hafner et al., 2014) was done by Smolka et al. (2016). The previously mentioned model using the HEM approach was used. The simulation results showed high and predictable ejector efficiency for the fixed-geometry setup for all investigated operating conditions. On the one hand, the controllable-geometry case was able to outperform the fixed-geometry case for certain needle positions. On the other hand, it was shown that these positions were difficult to evaluate, and gave less predictable efficiency. Simulations of ejector operation of three different ejectors in a multi-ejector block were presented by Bodys et al. (2016). The investigation focuses on the use of swirl-motion generator on ejector performance. The authors suggest that improvements to the mass entrainment ratio could be achieved at very high motive inlet rotational speeds. Furthermore, a full-scale 3D CFD investigation of the multi-ejector block was carried out by Bodys et al. (2017). The authors demonstrated the stable operation of the multi-ejector based refrigeration unit and indicated the possibility of shape optimization for pressure loss reduction.
The HRM model presented by Palacz et al. (2017a) was implemented together with a heat transfer model (coupled with the CFD solver) for the ejector walls by Haida et al. (2018a). An extensive sensitivity analysis of the mesh was also performed. The experimental and numerical investigation demonstrated high accuracy of the model, being capable of reproducing the wall temperature distribution within ± 5K. The accuracy of different turbulence models for the prediction of near wall temperature distribution as well as of mass entrainment ratio was presented. Four turbulence models were compared: (i) k−ε Realizable model, (ii) k−ω SST model, (iii) Transition SST model and (iv) Reynold stress model. The comparison showed that choice of turbulence models had a significant effect on the results. The Transition SST turbulence model yielded the most accurate prediction of mass entrainment ratio and wall temperature distribution. Furthermore, the investigation showed that the effect of ambient temperature and non-adiabatic boundary conditions on the ejector outer wall was negligible. However, the non-adiabatic boundary conditions on the inner ejector wall had a significant impact on the flow parameters. This implies that the use of non-adiabatic ejector wall boundary conditions may be important to capture the correct flow physics. The authors also suggest that the use of materials with low thermal conductivity may improve ejector performance.

2.5. Model Reduction

The large computational time expense of CFD models are, in general, prohibitive for large scale optimization procedures. Computational tools such as *ejectorPL*, that can quickly generate CFD models are important for rapid investigation of potential improvements. Therefore, reducing the model size while maintaining the high accuracy of the CFD models have recently been discussed. The authors would like to point to two methods that have recently been applied for the reduction of ejector CFD models, reduced order modelling and lumped parameter modelling. Reduced order models attempts to find an optimal basis for a model by looking at previous results. These results are typically outputs from a high accuracy CFD model or an experimental investigation. The

investigations by Haida et al. (2018b, 2018c) brought to light that the reduced order model ensures high accuracy results (i.e. within 10% mass flow rate error) for a R744 ejector over most of the investigated conditions.
Besagni (2019) presented a thorough discussion on the current and future state of ejector modelling. Here, emphasis was put on the lumped parameter approach. The integration of CFD models with lumped parameter models was previously described by the mentioned author. While not yet applied to R744 systems, this should be considered for future investigations. Still, research into more accurate CFD models will continue to be important as these directly impact the quality of these reduced models.

3. DISCUSSION

A summary of the different two-phase methods described in this paper is presented in Table 1. The HEM approach has the advantage of simplicity and stability, and can yield accurate results for supercritical conditions. It is well suited for initial designs and optimizations, however has limited accuracy for subcritical conditions. The HRM has been developed to overcome the main limitations of the HEM, while retaining much of the benefits of the HEM. The HRM considers meta-stable effects, and using variable relaxation times can yield accurate results for sub- and supercritical conditions. The mixture model is a more advanced model that solves an additional conservation equation for the phase fraction, however this requires further sub-modelling for closure of the equations. Here, separate evaluation of the liquid and gas states gives a more accurate average value for the fluid transport properties. Both the HRM and the mixture model have parameters of non-equilibrium that needs to be tuned, based on substantial experimental effort. This may help generate results with higher reliability, however requires detailed knowledge of the flow conditions.
All discussed models for the R744 ejector treat the two-phase flow as a single phase fluid with some notion of average transport properties. This assumption is severely limiting as all information about phase interfaces are lost, furthermore transport properties such as an averaged fluid viscosity and speed of sound are not well defined. Some discussion on the current modelling of these properties can be found in Awad and Muzychka (2008). However, due to the lack of experimental, tuning an accurate two-fluid model is beyond the current state of the art.

Table 1. Summary of two-phase models used for R744 ejector CFD modelling

Model	Advantages	Challenges and limitations
Homogeneous Equilibrium model Smolka et al. (2013), Lucas et al. (2014), Giacomelli et al. (2016)	-Simplicity and stability, -Accurate at supercritical conditions, -Extensively tested in literature	-Does not consider meta-stability (underestimates flashing flows)
Homogeneous Relaxation model Colarossi et al. (2012), Palacz et al. (2017a), Haida et al. (2018a)	-Considers meta-stability, -Extended with variable relaxation time for subcritical conditions	-Empirically based parameters for relaxation time, -Requires tuning of parameters
Mixture model Yazdani et al. (2012), Giacomelli et al. (2018b)	-Considers meta-stability, -Can more accurately evaluate the phase fractions by mass transfer modelling -Highly accurate results for motive flows	-Increased complexity, -Requires tuning of model parameters, -Less profound literature database on R744 ejectors

All mentioned methods are based on a pseudo-fluid approach. While more advanced two-phase models have been proposed and utilised in the literature for flashing water (Liao and Lucas, 2017), this has not yet been feasible for R744 ejectors. Mainly, this is due to the small dimensions of the

R744 ejectors, which limit experimental investigations. Many other research questions remain unanswered and is beyond the scope of this review. One of the toughest challenges is proper understanding of turbulent effects. While model tests have been performed with different Reynolds Averaged Navier-Stokes models, little is known about the two-phase effects on turbulence. Furthermore, the effects of wall heat transfer (Haida et al., 2018a) and wall surface roughness (Brezgin et al., 2017) have been shown to have an effect on the flow. Also, it has never been quantitatively estimated how much the presence of lubricants dissolved/mixed with R744 could influence first the fluid properties and second the validation procedures performed in all the reported papers. Other aspects of modelling including mesh design, solvers, 3D-effects, shock-capturing and computational requirements should be further addressed. Lastly, the interactions between the aforementioned factors may be important, and understanding if we are tuning the correct physical phenomenon with the available experimental results remains a major challenge.

4. CONCLUSIONS

The transition to more environmentally friendly refrigeration systems has brought about a great interest in ejector-equipped CO_2 systems for several applications and operating in any climate context. Much due to the size of this component accurate CFD models have been used to improve its design. The HEM approach has been the most prominently used model, and has been applied for design applications. Due to inherent limitations of the equilibrium assumption, the HRM and mixture models have been implemented into commercial CFD software. These models include meta-stability effects, which have been found to be important for R744 refrigeration applications. These methods have been applied for investigations of heat transfer, swirl generation, entropy generation and controllable geometries. Furthermore, methods for reducing computational cost of these models have recently been discussed. While the currently available models are able to reproduce experimental results with satisfactory accuracy, further research into turbulence, multiphase effects and shock structures may improve model accuracy and enable improved design procedures for R744 ejectors. Further discussion on the different aspects in CFD modelling of R744 ejectors will be presented in future review work.

ACKNOWLEDGEMENTS

The work is part of HighEFF - Centre for an Energy Efficient and Competitive Industry for the Future, an 8-year Research Centre under the FME-scheme (Centre for Environment-friendly Energy Research, 257632/E20). The authors gratefully acknowledge the financial support from the Research Council of Norway and user partners of HighEFF.

NOMENCLATURE

CFD	Computational fluid dynamics	*COP*	Coefficient of Performance
HEM	Homogeneous equilibrium model	*HRM*	Homogeneous relaxation model
UDF	User defined function		
a,b	Dimensionless exponents	c_p	Heat capacity ($kJ \cdot kg^{-1} \cdot K^{-1}$)
E	Total energy ($kg \cdot s^{-2} m^{-1}$)	*h*	Specific enthalpy ($kJ \cdot kg^{-1}$)
k	Thermal conductivity ($kJ \cdot s^{-1} \cdot m^{-2} K^{-1}$)	*P*	Pressure (bar)
s	Specific entropy ($kJ \cdot kg^{-1} \cdot K^{-1}$)	*S*	Enthalpy source term
T	Temperature (K)	*u*	Velocity (ms^{-1})
x	Vapour quality		
	Greek letters		
α	Phase fraction	Γ	Diffusion coefficient
θ	Relaxation time	Λ	Mass transfer coefficient
μ	Dynamic viscosity ($kg \cdot m^{-1}\ s^{-1}$)	ρ	Density ($kg \cdot m^{-3}$)
τ	Shear stress	φ	Non-dimensionalized pressure parameter
	Subscripts		
c	Condensation	*crit*	Critical condition

e	Evaporation	*eff*	Effective
k	Phase index	*m*	Mixture property
motive	Motive nozzle condition	*sat*	Saturated
sv	Saturated vapour	*sl*	Saturated liquid

REFERENCES

Angielczyk, W., Bartosiewicz, Y., Butrymowicz, D., Seynhaeve, J.-M., 2010. 1-D Modeling of Supersonic Carbon Dioxide Two-Phase Flow Through Ejector Motive Nozzle, Int. Refrig. Air Cond. Conf, 1-8

ANSYS® Fluent, 2019. Latest Release 19.2

Awad, M.M., Muzychka, Y.S., 2008. Effective property models for homogeneous two-phase flows, Exp. Therm Fluid Sci. 33 (1), 106-113

Banasiak, K, Hafner, A., 2011, 1D Computational model of a two-phase R744 ejector for expansion work recovery, Int. J. Therm. Sci. 50(11), 2235-2247

Banasiak, K., Hafner, A., Kriezi, E.E., Madsen, K.B., Birkelund, M., Fredslund, K., Olsson, R., 2015. Development and performance mapping of a multi-ejector expansion work recovery pack for R744 vapor compression units. Int. J. Refrig 57, 265–276.

Banasiak, K., Palacz, M., Hafner, A., Bulinski, Z., Smołka, J., Nowak, A.J., Fic, A., 2014. A CFD-based investigation of the energy performance of two-phase R744 ejectors to recover the expansion work in refrigeration systems: An irreversibility analysis. Int. J. Refrig 40, 328–337.

Besagni, G., 2019. Ejectors on the cutting edge: the past, the present and the perspective. Energy 170, 998-1003.

Bilicki, Z., Kestin, J., 1990. Physical Aspects of the Relaxation Model in Two-Phase Flow. Proc Math Phys Eng Sc 428 (1875), 379–397.

Bodys, J., Palacz, M., Haida, M., Smolka, J., Nowak, A.J., Banasiak, K., Hafner, A., 2017. Full-scale multi-ejector module for a carbon dioxide supermarket refrigeration system: Numerical study of performance evaluation. Energy Convers. Manage. 138, 312–326.

Bodys, J., Smolka, J., Palacz, M., Haida, M., Banasiak, K., Nowak, A.J., Hafner, A., 2016. Performance of fixed geometry ejectors with a swirl motion installed in a multi-ejector module of a CO_2 refrigeration system. Energy 117, 620–631.

Brezgin, D. V., Aronson, K. E., Mazzelli, F., & Milazzo, A. (2017). The surface roughness effect on the performance of supersonic ejectors. Thermophys. Aeromech., 24(4), 553-561.

Brown, S., Martynov, S., Mahgerefteh, H., Proust, C., 2013. A homogeneous relaxation flow model for the full bore rupture of dense phase CO_2 pipelines. Int. J. Greenhouse Gas Control 17, 349–356.

Colarossi, M., Trask, N., Schmidt, D.P., Bergander, M.J., 2012. Multidimensional modeling of condensing two-phase ejector flow. Int. J. Refrig 35 (2), 290–299.

Downar-Zapolski, P. Bilicki, Z. Bolle, L., Franco, J., 1996. The non-equilibrium relaxation model for one-dimensional flashing liquid flow. Int. J. Multiphase Flow 22 (3), 473–483.

Elbel, S., Lawrence, N., 2016. Review of recent developments in advanced ejector technology. Int. J. Refrig 62, 1–18.

European Commission, 2014. Regulation (EU) No 517/2014 of the European Parliament and of the Council of 16th April 2014 on fluorinated greenhouse gases and repealing Regulation (EC), No 842/2006. Brussels, Belgium.

Giacomelli, F., Mazzelli, F., Milazzo, A., 2018b. A novel CFD approach for the computation of R744 flashing nozzles in compressible and metastable conditions. Energy 162, 1092–1105.

Giacomelli, F., Banasiak, K., Hafner, A., 2018a. Experimental and Numerical Investigation on an Ejector for CO_2 Vapor Compression Systems, 13th IIR Gustav Lorentzen Conference, IIR, 1179-1187

Giacomelli, F., Mazzelli, F., Milazzo, A., 2016. Evaporation in supersonic CO_2 ejectors: analysis of theoretical and numerical models. 9th International Conference on Multiphase Flow, ICMF, 22-27

Gullo, P., Hafner, A., Banasiak, K., 2018. Transcritical R744 refrigeration systems for supermarket applications: Current status and future perspectives. Int. J. Refrig 93, 269-310,

Grazzini, G., Milazzo, A., Mazzelli, F., 2018. Ejectors for efficient refrigeration: Design, applications and computational fluid dynamics. Springer International Publishing.

Hafner, A., Forsterling, S., Banasiak, K., 2014. Multi-ejector concept for R-744 supermarket refrigeration. Int. J. Refrig 43, 1–13.

Haida, M., Smolka, J., Hafner, A., Palacz, M., Banasiak, K., Nowak, A. J., 2018d. Modified homogeneous relaxation model for the R744 trans-critical flow in a two-phase ejector. Int. J. Refrig 85, 314–333.

Haida, M., Smolka, J., Hafner, A., Ostrowski, Z., Palacz, M., Nowak, A.J., Banasiak, K., 2018c. System model derivation of the CO_2 two-phase ejector based on the CFD-based reduced-order model. Energy 144, 941–956.

Haida, M., Smolka, J., Hafner, A., Ostrowski, Z., Palacz, M., Madsen, K.B., Forsterling, S., Nowak, A.J., Banasiak, K., 2018b. Performance mapping of the R744 ejectors for refrigeration and air conditioning supermarket application: A hybrid reduced-order model. Energy 153, 933–948.

Haida, M., Smolka, J., Hafner, A., Mastrowski, M., Palacz, M., Madsen, K.B., Nowak, A.J., Banasiak, K., 2018a. Numerical investigation of heat transfer in a CO_2 two-phase ejector. Energy 163, 682–698.

Lemmon E.W., Huber M.L., McLinden M.O., 2013, Nist standard reference database 23: reference fluid thermodynamic and transport properties - refprop, National Institute of Standards and Technology, Standard Reference Data Program.

Liao, Y., Lucas, D., 2017. Computational modelling of flash boiling flows: A literature survey. Int. J. Heat Mass Transfer 111, 246–265.

Liu, F., Li, Y., Groll, E. A., 2012. Performance enhancement of CO_2 air conditioner with a controllable ejector. Int. J. Refrig 35 (6), 1604–1616.

Lucas, C., Rusche, H., Schroeder, A., Koehler, J., 2014. Numerical investigation of a two-phase CO_2 ejector. Int. J. Refrig 43, 154–166.

Lucas, C., Koehler, J., Schroeder, A., Tischendorf, C., 2013. Experimentally validated CO_2 ejector operation characteristic used in a numerical investigation of ejector cycle. Int. J. Refrig 36(3), 881–891.

Nakagawa, M., Marasigan, A., Matsukawa, T., Kurashina, A., 2011. Experimental investigation on the effect of mixing length on the performance of two-phase ejector for CO_2 refrigeration cycle with and without heat exchanger. Int. J. Refrig 34 (7), 1604–1613.

Nowak, A.J., Palacz, M., Smolka, J., Banasiak, K., Bulinski, Z., Fic, A., Hafner, A., 2016. CFD simulations of transport phenomena during transcritical flow of real fluid (CO_2) within ejector. Int. J. Numer. Method H. 26(3/4), 805–817.

Palacz, M., Smolka, J., Nowak, A.J., Banasiak, K., Hafner, A., 2017b. Shape optimization of a two-phase ejector for CO_2 refrigeration systems. Int. J. Refrig 74, 212–223.

Palacz, M., Haida, M., Smolka, J., Nowak, A. J., Banasiak, K., Hafner, A., 2017a. HEM and HRM accuracy comparison for the simulation of CO_2 expansion in two phase ejectors for supermarket refrigeration systems. Appl. Therm. Eng. 115, 160–169.

Palacz, M., Smolka, J., Kus, W., Fic, A., Bulinski, Z., Nowak, A.J., Banasiak, K., Hafner, A., 2016. CFD-based shape optimization of a CO_2 two-phase ejector mixing section. Appl. Therm. Eng. 95, 62–69.

Palacz, M., Smolka, J., Fic, A., Bulinski, Z., Nowak, A. J., Banasiak, K., Hafner, A., 2015. Application range of the HEM approach for CO_2 expansion inside two-phase ejectors for supermarket refrigeration systems. International Journal of Refrigeration 59, 251–258.

Sierra-Pallares, J., García del Valle, J., García Carrascal, P., Castro Ruiz, F., 2016. A computational study about the types of entropy generation in three different R134a ejector mixing chambers, Int. J. Refrig 63, 199-213

Smolka, J., Palacz, M., Bodys, J., Banasiak, K., Fic, A., Bulinski, Z., Nowak, A.J., Hafner, A., 2016. Performance comparison of fixed- and controllable-geometry ejectors in a CO_2 refrigeration system. Int. J. Refrig 65, 172–182.

Smolka, J., Bulinski, Z., Fic, A., Nowak, A.J., Banasiak, K., Hafner, A., 2013. A computational model of a transcritical R744 ejector based on a homogeneous real fluid approach. Appl. Math. Modell. 37 (3), 1208–1224.

Wallis, G. B., 1980. Critical two-phase flow. Int. J. Multiphase Flow 6 (1-2), 97–112.

Weller, H.G., Tabor, G., Jasak, H., Fureby, C., 1998. A tensorial approach to computational continuum mechanics using object-oriented techniques. Comput. Phys. 12 (6), 620.

Yazdani, M., Alahyari, A. A., Radcliff, T. D., 2012. Numerical modeling of two-phase supersonic ejectors for work-recovery applications. Int. J. Heat Mass Transfer 55 (21-22), 5744–5753.

PAPER ID: 0380
DOI: 10.18462/iir.compr.2020.0380

COMPARATIVE STUDY OF R744 EJECTOR CFD MODELS

Knut E Ringstad[(a)], Armin Hafner[(a)]

[(a)] Norwegian University of Science and Technology,
Kolbjørn Hejes vei 1B, 7491 Trondheim, Norway
knut.e.ringstad@ntnu.no

ABSTRACT

This work presents a comparative study of four different R744 ejector CFD models at a wide range of operating conditions. The models compared are the homogeneous equilibrium model, the UDRGM mixture model, a homogeneous relaxation model and a Eulerian two-fluid model. The results are also compared to experimental data available in the literature. The models are tested for high and low operating pressures, and the effects of non-equilibrium are discussed. The results are discussed and recommendations for model developments are suggested.

Keywords: Refrigeration, Carbon Dioxide, Compressors, COP, Evaporators, Energy Efficiency

1. INTRODUCTION

In recent years, the HVAC&R industry is turning away from high global warming potential gases (GWP) refrigerants, such as the hydroflourocarbon (HFCs) gases, and increasingly toward natural and environmentally friendly refrigerants. One of the primary candidates for many HVAC&R applications is using R744 (CO_2) as a refrigerant. R744 boasts high system efficiency, low refrigerant cost, non-toxicity, non-flammability, aswell as negligible GWP. Many technologies for R744 systems have been developed over the last decades, especially for high ambient temperature applications. Of these technologies, special interest has been devoted to two-phase ejectors. A two-phase R744 ejectors is a work recovery device that uses the throttling losses inherent in the process to recompress a secondary flow to a higher pressure. Still, the design process for of these devices is not yet developed due to the complex nature of the flow. Therefore, design and modelling tools using computational fluid dynamics (CFD) has been a focal point of research over the last decade.

Several models have been presented in the literature, all with different benefits and drawbacks. The most commonly employed model is the Homogeneous Equilibrium Model (HEM) (Smolka et al., 2013, Palacz et al., 2015). This approach assumes full equilibrium in momentum, temperature and pressure between the phases. This approach is simple, yet efficient for modelling many ejector functions. However, it was later found that this approach loses accuracy when operating conditions at below critical pressure are considered (Palacz et al., 2017). This is illustrated in Figure 1., where motive nozzle mass flow rate accuracy is visually presented in a P-h diagram. Several novel models that account for this thermodynamic non-equilibrium has since then been presented. A homogeneous relaxation model (HRM) was proposed by Palacz et al. (2017). This approach was later extended with variable relaxation scales to achieve better accuracy at a wide range of operating conditions (Haida et al., 2018). Later Giacomelli et al. (2018,2019) presented a mixture model, which uses sub-models for evaporation and condensation to account for the relaxation process to equilibrium conditions. This approach showed better accuracy than previous approaches, however this came at the cost of very high computational costs. Recently, (Bodys et al., 2020) presented a mixture model for very low pressure conditions. Recently, Ringstad and Hafner (2020), proposed using a more complex two-fluid CFD model. This approach is still under development as is dependent on many more sub-model parameters than previous models. While many of these advances has improved the modelling capabilities for R744 two-phase ejectors, siginificant errors are still observed when comparing with experiments.

This paper will present a comparison of a HEM, a HRM, a mixture model by Giacomelli et al. (2018) and a Eulerian-Eulerian (two-fluid) non-equilibrium model. For more details on R744 ejector models, see the detailed

review of the state of the art R744 ejector models (Ringstad et al., 2019, 2020), previously presented by the authors.

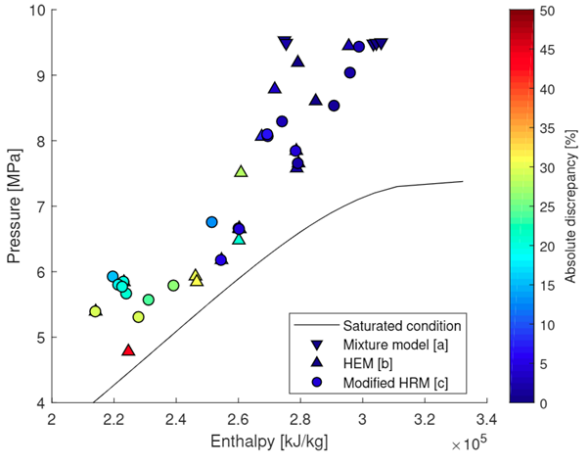

Figure 1: Summary of CFD model accuracy for motive nozzle mass flow rate (Ringstad et al., 2020)

2. MULTIPHASE MODELS

In this paper three multiphase models are presented, three pseudo-fluid models; (a) a homogeneous equilibrium model (HEM) based on the formulation by Smolka et al. (2013), (b) a mixture model based on the multi-species user-defined real-gas model (Giacomelli et al., 2019), (c) a homogeneous equilibrium model (HEM) based on the formulation by Haida et al., 2018, and (d) a two-fluid eulerian-eulerian model (Ringstad and Hafner, 2020). All models were implemented into ANSYS Fluent 19.2 through user defined functions, described in further detail below.

2.1. Homogeneous Equilibrium Model

Assuming equilibrium between the phases, i.e. equilibrium in pressure, velocity, temperature and chemical potential, a set of 2D transport equations for mass (Eq. 1), momentum (Eq. 2) and energy can be defined for a mixture of two phases. This model is referred to as the Homogeneous Equilibrium Model.

$$\frac{\partial \rho_m}{\partial t} + \frac{\partial}{\partial x_j}\left[\rho_m u_{mj}\right] = 0, \qquad \text{Eq. (1)}$$

$$\frac{\partial}{\partial t}(\rho_m u_{mi}) + \frac{\partial}{\partial x_j}\left[\rho u_{mi} u_{mj} + p_m \delta_{ij} - \tau_{mij}\right] = 0, \qquad \text{Eq. (2)}$$

Smolka et al. (2013) reformulated the energy equation into an enthalpy formulation in the form Eq. (3) which is introduced into ANSYS Fluent through a user-defined-scalar.

$$\nabla \cdot (\rho \vec{u} h) = \nabla \cdot (k_{\text{eff}} \nabla h) + \dot{S}_{h1} + \dot{S}_{h2} + \dot{S}_{h3}, \qquad \text{Eq. (3)}$$

Here, h is the specific enthalpy, $\vec{u}$ is the velocity vector, k_{eff} the effective diffusion coefficient, and the source terms $\dot{S}_{h1,2,3}$ describe the mechanical energy, the irreversible dissipation of the kinetic energy variations and the dissipation of the turbulent kinetic energy, respectively (Smolka et al., 2013). At homogeneous equilibrium, the enthalpy and pressure uniquely define a thermodynamic state in the two-phase dome:

$$\rho, \mu, k, \alpha, T, q = f(p, h), \qquad \text{Eq. (4)}$$

By assuming homogeneous equilibrium, the void-fraction is defined by the thermodynamic state as all phase change mechanisms are assumed to be instantaneous. A look-up table (100x100) was generated for the real fluid properties of R744 using the REFPROP (Lemmon et al., 2007) thermodynamic library calculated based on the Span-Wagner equation of state. The mixture viscosity and thermal conductivity based were found by a volume weighted average.

2.2. Homogeneous Relaxation Model

The mixture model is similar to the HEM based on the mixture averaged continuity, momentum and energy equations, Eqns. (1)- (3), also referred to as a pseudo-fluid approach. In the mixture model, thermodynamic non-equilibrium can be introduced by considering an additional equation for the transport of vapour fraction, Eqn. (5).

$$\frac{\partial}{\partial \mathrm{t}}(\rho_k \alpha_k) + \frac{\partial}{\partial \mathrm{x_j}}\left(\alpha_\mathrm{k}\rho_\mathrm{k}\mathrm{u_j}\right) = \Gamma, \qquad \text{Eq. (5)}$$

where Γ is a forcing term that describes the phase change mechanisms, and the offset from thermodynamic equilibrium. Previously, two formulations for the vapour fraction have been used for R744 ejector CFD models, the homogeneous relaxation models (Palacz et al., 2017, Haida et al., 2018), and the Mixture model (Giacomelli et al., 2019, Yazdani et al., 2012). The HRM treats the transition toward equilibrium as a relaxation process, governed by a relaxation time scale, θ, described in Eq. (6):

$$\Gamma_r = -\rho \frac{\beta - \beta_{eq}}{\theta} \qquad \text{Eq. (6)}$$

Here, β is the local flow quality and is the flow quality at equilibrium. The relaxation time has previously been studied by (Downar-Zapolski et al., 1996, Angielczyk et al, 2010, Haida et al., 2018). A relation for the relaxation time scale was found:

$$\theta = \theta_0 \alpha^a \phi^b \qquad \text{Eq. (7)}$$

Where, θ_0 is a scaling constant, α is the mixture void fraction, φ is a pressure parameters, and *a* and *b* are scaling parameters. The parameters *a* and *b* were investigated by Haida et al. (2018) and an optimized set was found, which is used in this work. The properties were defined as for the HEM, however the density was formulated using meta-stable liquid density from the REFPROP thermodynamic library, see the work by Palacz et al., 2017.

2.3. Mixure Model

Alternatively, the mixture model introduces non-equilibrium effects by directly modelling the phase change mechanisms between two phases. This is done by modelling the evaporation and condensation of the fluid with two terms, $\Gamma = \Gamma_c + \Gamma_e$. In this work, the Lee model is used to model phase change, Eqns. (6) and (7), similarly to previous works with this model (Giacomelli et al., 2018, 2019).

$$\Gamma_e = \sigma_e \alpha_l \rho_l \frac{T - T_{sat}}{T_{sat}}, \qquad \text{Eq. (7)}$$

$$\Gamma_c = \sigma_c \alpha_v \rho_v \frac{T - T_{sat}}{T_{sat}}, \qquad \text{Eq. (8)}$$

Numerical investigations of the R744 ejector using the mixture model (Giacomelli et al., 2018) found the evaporation and condensation constants that best fit experimental results were σ_e=100000 and σ_c= 0.1. These values were used for these simulations.

The two-phase mixture properties are defined by a mass or volume-based averaging of the two compressible phases. The phases are both evaluated by pressure and temperature, interpolated from a look-up table (152x126) based on the REFPROP thermodynamic library. The properties allow for meta-stable conditions of both liquid and

gas phase. The RERPROP library for R744 is based on the Span-Wagner equation of state, which is considered the most accurate EoS for CO_2 and is widely used for R744 ejector simulations.

2.4. Two fluid model

A two-fluid model solves one set of transport equation for each phase, q, with surrounding phases, p, Eqns. (8-10). The pressure, P_m is assumed equal for both phases.

$$\frac{\partial}{\partial t}(\alpha_q \rho_q) + \frac{\partial}{\partial x_j}\left[\alpha_q \rho_q u_{qj}\right] = 0, \qquad \text{Eq. (9)}$$

$$\frac{\partial}{\partial t}\left(\alpha_q \rho_q u_{qi}\right) + \frac{\partial}{\partial x_j}\left[\alpha_q \rho_q u_{qi} u_{qj} - \tau_{qij}\right] + R_{pq,i} + \left(\dot{m}_{pq} v_{pq,i} - \dot{m}_{qp} v_{qp,i}\right) + \alpha_q \frac{\partial P_m}{\partial x_j}\delta_{ij} - F_{dispersed,i} = 0, \qquad \text{Eq. (10)}$$

$$\frac{\partial}{\partial t}\left(\alpha_q \rho_q h_q\right) + \frac{\partial}{\partial x_j}\left[\rho_q u_{qj} h_q + q_{qj} - u_{qi} T_{qij}\right] + Q_{pq} + h_{pq}\left(\dot{m}_{pq} - \dot{m}_{qp}\right) + \alpha_q \frac{\partial p_m}{\partial t} = 0, \qquad \text{Eq. (11)}$$

To successfully implement this model into ANSYS Fluent, some limitations of the software had to be overcome using *user-defined functions* (UDFs). Firstly, Fluent only allows for relations for specific heat as a function of temperature, $c_p = f(T)$. This was overcome by calculating a separate temperature field for the superheat of the liquid that includes superheat beyond the saturation temperature. Secondly, the interphasial enthalpy (the latent heat), h_{qp} must be defined as a single constant, here referred to as h_F. This issue was solved by introducing an additional source term to the liquid and gas energy-equations using a variable latent heat function and setting h_F to zero. For more details, see Ringstad and Hafner (2020).

The model includes several closure models, which allow adaptability and more advanced phase-coupling mechanisms than the simple pseudo fluid model. In this model the following closure models are used:

(a) Phase change: Lee model, see Eq. 7. and 8.

(b) Equation of state: Span-Wagner with non-equilibrium states, see Section 2.2.

(c) Momentum interaction: Schiller Neumann, see (ANSYS Fluent theory guide, 2019).

3. NUMERICAL MODEL SETUP

A numerical model was set up such that it could be compared to the experimental work by Palacz et al., 2017. The ejector geometry is described in Table 1.

Table1. Ejector dimensions

Dimension	EJ-2 (Palacz et al., 2017)
Inlet diameter, mm	3.80
Throat diameter, mm	1.41
Outlet diameter, mm	1.58
Converging angle	30.0°
Diverging angle	2.0°

A mesh convergence study was conducted with three 2D meshes, A, B, and C, with 6k, 25k and 100k cells, respectively. The ANSYS ICEM meshing software was used to generate structured meshes with high orthogonality

and low skewness, as in the previous work (Ringstad and Hafner, 2020). The mesh study indicated that mesh B was of high enough quality to properly describe the flow physics. For this study 3D effects are neglected due to computational limitations.

Four experimental cases presented by Palacz et al., 2017 are simulated. The experimentally messured conditions in these experiments are presented in Table 2. These values were used to calculate the boundary conditions of the simulations. A set of four points were chosen to get a selection of super critical, critical, and sub-critical operating conditions.

Table 2. Experimental conditions for R744 ejector operation (Palacz et al., 2017).

	P_{motive} [bar]	T_{motive} [C]	$P_{suction}$ [bar]	$T_{suction}$ [C]	P_{out} [bar]
1	53.93	6.33	27.3	5.7	34.23
9	66.51	22.41	28.21	2.21	34.85
14	75.79	28.07	28.17	2.58	36.80
18	94.46	35.28	27.21	2.60	32.85

The pressure-based implicit formulation in ANSYS Fluent was used in the calculations. This is the only option that is compatible with multiphase models in ANSYS Fluent. While it is generally agreed that density-based formulations performed better for highly compressible flows, pressure-based solvers have successfully been used for super sonic flows. The PRESTO! scheme was used for pressure and the second order upwind scheme was used for all other variables in the computations. The calculations with the HEM and HRM were done using a steady solver, which is a common assumption for R744 ejector flows. The mixture- and Eulerian model were run until steady state with a transient solver, to improve solver stability.

4. RESULTS AND DISCUSSION

4.1. Convergence

The simulations were run on 8 cores at 3.0 GHz clock frequency. The convergence criterion was based on steady residuals for all flow variables, as well as a steady solution for mass flow rates.

The HEM showed, in most cases, good stability and quite fast convergence, only somewhat dependent on initial and boundary conditions. The average case with 25k mesh-size would take approximately 70k iterations within 30-120 minutes. Some cases would not converge fully to the previously specified convergence criterion. This is likely due to the assumption of equilibrium not being fulfilled for those cases.

The HRM, similarly to the HEM shows good stability as long as appropriate formulations for the meta-stable density is used. It was found that using best fit functions for the data points provided better convergence and stability than using look-up table interpolation. The HRM would not converge as well for very low pressure conditions (Case #1). For this region it is suggested to converge, by first running with an HEM model or to use the mixture model presented by Bodys et al (2020). %. The HRM had some convergence issues, especially with second–order schemes. This may be due to numerical stiffness or implementation errors. When second-order schemes were applied to the vapour fraction transport equation became unstable.

The mixture model by Giacomelli (2019) showed very slow convergence rates and unstable behaviour, as previously reported by (Giacomelli et al., 2018, 2019). Depending on initial and boundary conditions, the simulations did not indicate convergence after 10 million iterations for the tested cases. The simulations indicated oscillating and diverging outlet flow rates, which would not satisfy mass conservation. The simulations were therefore stopped, as running until convergence could take up to several hundreds or thusands of CPU hours (Giacomelli et al., 2019). As the simulations did not converge, the simulations results are not used in further comparison.

The two-fluid model showed quite good convergence rates and would in most cases converge to a steady solution within 20-100k iterations, depending on the time-step size. The model showed stable convergence when appropriate initial conditions and phase change coefficients were chosen. However, finding these initial conditions was in certain cases challenging. Still, the model was found to be more stable than expected based on model complexity.

4.2. Comparison with previous results

The results of the simulations as well as the experimentally obtained values from Palacz et al (2015) are presented in Table 5.

Table 5: Comparison of numerical and experimental results;
The notation * indicates no suction flow, - indicates unstable simulation, ** indicates oscillating flow
TFM results from Ringstad and Hafner (2020).

	Experimental (kg/s)		HEM (%)		HRM (%)		TFM (%)	
case	m_m	m_s	Err_m	Err_s	Err_m	Err_s	Err_m	Err_s
1	0.099	0.0297	26.8	-3.0	-	-	-15.1	*
9	0.072	0.0137	17.5	-7.4	-9.8	-38.0	-8.5	-38.3
14	0.089	0.0249	28.2	42.6	-19.1	**	-13.6	-9.6
18	0.084	0.0353	0.3	1.1	-	-	13.6	-47.3

HEM shows that for decreaseing motive pressure the model accuracy drops. Additional test was conducted for the HEM at operating conditions near case 14, where much better accuracy was found, ie. motive MFR errors smaller than 7%. The results using the TFM results found in previous numerical results Ringstad and Hafner (2020). The accuracy is much below the HEM accuracy. Further work is suggested on this model to improve model accuracy.

5. CONCLUSION

All the discussed models (HEM, UDRGM Mixture, HRM, TFM) have previously shown to be able to predict R744 ejector flow with reasonable accuracy. In this work, it was found that the UDRGM mixture model is highly sensitive to initial conditions, is relatively unstable and has a high computational cost. This characteristic makes the UDRGM mixture model unreliable as a tool for optimization and rapid design. In comparison, the HEM, HRM and TFM can produce converged results within much shorter simulation time. Still, the more accurate thermodynamic library of the UDRGM shows in general a higher accuracy than other model in previous works. This motives research into efficiently implementing such a library in other models, such as the TFM.

The simulation results for the HEM are similar to those conducted in previous works, showing that the HEM can produce reasonable accuracy for super-critical operating conditions, but suffer at lower operating pressures. This implementation of the HRM showed poor convergence properties and would in general perform poorer than the HEM. However, previous versions of the HEM (Haida et al., 2018) have shown good convergence properties.The mixture model has been shown in previous studies to have very good accuracy (Giacomelli et al. 2019), however it was in this study found that the convergence rate of the model is too high for practical simulation. In comparison, the TFM produced results with lower accuracy, especially in the super-critical case. However, the TFM produced better results for lower operating conditions. The TFM can also be further improved by tuning the phase change parameters. The ability to add additional closure models to the TFM is its benefit as more physics can be incorporated into the simulations. This will bring the physical realism and model accuracy up with more research. Improving these submodels will however require extensive research into different flow phenomenons such as non-equilibrium thermodynamics, phase change modelling, two phase turbulence, and bubble break-up and coalescence, which is suggested as further work.

ACKNOWLEDGEMENTS

The work is part of HighEFF - Centre for an Energy Efficient and Competitive Industry for the Future, an 8-year Research Centre under the FME-scheme (Centre for Environment-friendly Energy Research, 257632/E20). The authors gratefully acknowledge the financial support from the Research Council of Norway and user partners of HighEFF.

NOMENCLATURE

cp	Specific Heat (kJ/kg)	q	Heat transfer (kW)	Γ	Phase change term (kg/s)
h	Specific enthalpy (kJ/kg)	R	Momentum interaction term (N/s)	μ	Viscosity (m^2/s)
k	Thermal conductivity (kW/K)	*T*	temperature (K)	ρ	Density (kg/m^3)
m	Mass transfer (kg/s)	*u*	Velocity (m/s)	σ	Phase change coeficiente (-)
P	pressure (Pa)	*α*	Volume fraction (m^3/m^3)	τ	Stress tensor (N/m^2)

REFERENCES

Angielczyk, W., Bartosiewicz, Y., Butrymowicz, D, Seynhaeve, 2010, J.-M., 1-D modeling of supersonic carbon dioxide two-phase flow through ejector motive nozzle, International Refrigeration and Air Conditioning Conference 1-8

Ansys® Fluent, Release 19.1, ANSYS Fluent theory guide, 2019, ANSYS, Inc.

Bodys, J., Smolka, J., Palacz, M., Haida, M., Banasiak, K., 2020, Non-equilibrium approach for the simulation of CO2 expansion in two-phase ejector driven by subcritical motive pressure, International Journal of Refrigeration 114 32-46, doi: 10.1016/j.ijrefrig.2020.02.015.

Brennen, C. E., 2005 Fundamentals of multiphase flow, Cambridge UniversityPress, Cambridge,. doi:10.1017/CBO9780511807169.

Downar-Zapolski, P., Bilicki, Z, Bolle, L., Franco, J., 1996, The non-equilibrium relaxation model for one-dimensional flashing liquid flow, International Journal of Multiphase Flow 22 473–483.doi:10.1016/0301-9322(95)00078-X.

Giacomelli, F. Mazzelli, F., Milazzo, A., 2018, A novel CFD approach for the computation of R744 flashing nozzles in compressible and metastable conditions, Energy 162 ,1092–1105 (nov 2018). doi: 10.1016/j.energy.2018.08.050.

Giacomelli, F., Mazzelli, F., Banasiak, K., Hafner, A., Milazzo, A., 2019, Experimental and computational analysis of a R744 flashing ejector, International Journal of Refrigeration 107, 326-343, 10.1016/j.ijrefrig.2019.08.007

Haida, M., Smolka, J., Hafner, A., Palacz, M., Banasiak, K., Nowak, A., 2018, Modified homogeneous relaxation model for the R744 trans-critical flow in a two-phase ejector, International Journal of Refrigeration 85,314-333,10.1016/j.ijrefrig.2017.10.010.

Kim, M. H., Pettersen, J., Bullard, C. W.,, 2004 Fundamental process and system design issues in CO2 vapor compression systems, Progress in Energy and Combustion Science 30 (2) 119–174 (jan 2004). doi: 10.1016/J.PECS.2003.09.002.

Lemmon, E. W., Bell, I. H. Huber, M. L. McLinden, M. O., NIST Standard Reference Database 23: Reference Fluid Thermodynamic and Transport Properties-REFPROP, Version 9.0, National Institute of Standards and Technology (2018). doi: http://dx.doi.org/10.18434/T4JS3C

Palacz, M. Haida, M., Smolka, J., Nowak, A. J., Banasiak, K., Hafner, A., 2017, HEM and HRM accuracy comparison for the simulation of CO2expansion in two-phase ejectors for supermarket refrigeration systems, Applied Thermal Engineering 115 160–169 (mar 2017).doi:10.1016/j.applthermaleng.2016.12.122.

Palacz, M., Smolka, J., Fic, A., Bulinski, Z., Nowak, A. J., Banasiak, K., Hafner, A., 2015, Application range of the HEM approach for CO2 expansion inside two-phase ejectors for supermarket refrigeration systems, International Journal of Refrigeration 59 251–258 (nov 2015). doi: 10.1016/j.ijrefrig.2015.07.006.

Ringstad, K. E., Allouche, Y., Gullo, P., Banasiak, K., Hafner, A., 2019, CO2 ejector modelling using CFD: current status., in: 25th IIR International Congress of Refrigeration Proceedings.

Ringstad, K. E., Hafner, A., 2020, Two-fluid CFD model for R744 two-phase ejectors, in: 14th Gustav Lorentzen Conference Proceedings, Kyoto,

Ringstad, K. E., Allouche, Y., Gullo, P., Ervik, Å., Banasiak, K., Hafner, A., 2020, A detailed review on R744 two-phase ejector modeling, Thermal Science and Engineering Progress 20, doi: 10.1016/j.tsep.2020.100647.

Smolka, J., Bulinski, Z., Fic, A., Nowak, A. J., Banasiak, K., Hafner, A., 2013, A computational model of a transcritical R744 ejector based on a homogeneous real fluid approach, Applied Mathematical Modelling 37 (3) 1208–1224 (feb 2013). doi: 10.1016/j.apm.2012.03.044.

Yazdani, M., Alahyari, A. A., Radcliff, T. D., 2012, Numerical modeling of two-phase supersonic ejectors for work-recovery applications, International Journal of Heat and Mass Transfer 55 (21-22) 5744–5753 (oct2012). doi: 10.1016/j.ijheatmasstransfer.2012.05.071

PAPER ID: 1147
DOI: 10.18462/iir.gl.2020.1147

TWO-FLUID CFD MODEL FOR R744 TWO-PHASE EJECTORS

Knut E Ringstad[(a)], Armin Hafner[(a)]

[(a)] Norwegian University of Science and Technology,
Kolbjørn Hejes vei 1B, 7491 Trondheim, Norway
knut.e.ringstad@ntnu.no

ABSTRACT

This paper presents early results from a novel two-fluid Eulerian-Eulerian multiphase model for R744 two-phase ejectors, which to the authors knowledge has not previously been presented in literature. As opposed to previous R744 ejector models, this formulation includes non-equilibrium states for temperature, momentum, and chemical potential. The model is implemented into ANSYS Fluent using user-defined-functions and is able to achieve converged results faster than previous non-equilibrium formulations. Results are compared with experimental results. The mesh and model parameters are studied for their impact on accuracy.

Keywords: Refrigeration, Carbon Dioxide, Compressors, COP, Evaporators, Energy Efficiency

1. INTRODUCTION

The current global warming crisis will require a large-scale response, calling for significant technological shifts in industries, worldwide. Responding to this, modern HVAC system are moving away from high global warming potential gases (GWP) refrigerants, such as the hydroflourocarbon (HFCs) gases. Instead, developing refrigeration technologies based on natural environmentally friendly refrigerants has been an important focus point of current research. Of the natural refrigerants, R744 (CO_2) has stood out due to its favourable thermo-physical properties (Kim et al. 2004), negligible GWP, non-flammability, non-toxicity and low cost. A critical enabling technology for R744 refrigeration systems is the two-phase ejector. A two-phase R744 ejectors is a work recovery device that allows for efficient R744 refrigeration, even in warm climates. However, improper design and control of two-phase ejectors can be detrimental for the system efficiency. Consequentially, much research has been devoted to developing advanced flow models for R744 ejector flow.

The model that has seen most use is the Homogeneous Equilibrium Model (HEM) (Smolka et al., 2013, Palacz et al., 2015). However, this model assumes full equilibrium between the phases. Palacz suggested that this model has a limited range of applicability and has significant errors at low pressure motive conditions that are often observed in R744 ejector system operation. Palacz suggested that at these low-pressure working conditions non-equilibrium effects are non-negligible, inciting research into non-equilibrium models. To account for these effects, a homogeneous relaxation model was presented (Palacz et al., 2017). Still, the HRM experiences significant errors at sub-critical motive pressures. An alternative approach was suggested by Giacomelli et al. (2018, 2019), where a mixture model was used to model a converging diverging nozzle (Giacomelli et al., 2018), and a R744 ejector (Giacomelli et al., 2019). The results showed good results for predicting the motive mass flow rate, however the computational cost of this model was found to be very high. In general, all models are still not able to accurately and reliably predict the suction nozzle mass flow rate accurately. This is likely because of the complexity of the driving mechanisms of the suction flow. To model these effects more advanced modelling tools are necessary. A model framework which enables more accurate modelling of these effects are the two-fluid models. These models are more complex as they involve a much larger set of coupling equations and more equations. For more details on R744 ejector models, see the detailed review of the state of the art R744 ejector models (Ringstad et al., 2019), previously presented by the authors.

2. MULTIPHASE MODELS

Multiphase models can be classified according to the number of equations solved. In general, the models are classified into two groups, pseudo-fluid models and two-fluid models (Eulerian-Eulerian). The pseudo-fluid models use an averaged set of equations for the mixture of the two phases. This reduces the number of equations to one set of transport equations, however, is based on several simplifying assumptions. On the other hand, two-fluid models use one set of equations for each phase. This model is therefore more physically realistic, however is dependent on several closure models. These closure models must be better understood to fully utilize the potential benefits of such a two-fluid model. In this paper a novel two-fluid eulerian-eulerian model for R744 ejectors is presented. To the authors knowledge this is the first full two-fluid model for R744 ejectors presented in the available literature. The model was implemented into ANSYS Fluent 19.2 through user defined functions, described in further detail below.

2.1. Two fluid model

The two-fluid model solves one set of transport equation for each phase, q, with surrounding phases, p, Eqns. (1-4). The pressure, P_m is assumed equal for both phases.

$$\frac{\partial}{\partial t}(\alpha_q \rho_q) + \frac{\partial}{\partial x_j}\left[\alpha_q \rho_q u_{qj}\right] = 0, \quad \text{Eq. (1)}$$

$$\frac{\partial}{\partial t}\left(\alpha_q \rho_q u_{qi}\right) + \frac{\partial}{\partial x_j}\left[\alpha_q \rho_q u_{qi} u_{qj} - T_{qij}\right] + R_{pq,i} + \left(\dot{m}_{pq} v_{pq,i} - \dot{m}_{qp} v_{qp,i}\right) + \alpha_q \frac{\partial P_m}{\partial x_j}\delta_{ij} - F_{dispersed,i} = 0, \quad \text{Eq. (2)}$$

$$\frac{\partial}{\partial t}\left(\alpha_q \rho_q h_q\right) + \frac{\partial}{\partial x_j}\left[\rho_q u_{qj} h_q + q_{qj} - u_{qi} T_{qij}\right] + Q_{pq} + h_{pq}\left(\dot{m}_{pq} - \dot{m}_{qp}\right) + \alpha_q \frac{\partial p_m}{\partial t} = 0, \quad \text{Eq. (3)}$$

$$\frac{\partial}{\partial t}(\alpha_q) + \frac{\partial}{\partial x_j}\left[\alpha_q u_{qj}\right] = 0, \quad \text{Eq. (4)}$$

In these equations Einstein summation notation has been used for the directions with subscripts i and j. ρ, u, h, α are, respectively, the density, velocity, enthalpy, and phase volume fraction of the liquid or gas. The phase strain tensor is defined as $T_{qij} = \alpha_q \mu'_q\left(\frac{\delta u_i}{\delta x_j} + \frac{\delta u_j}{\delta x_i}\right)$, where the phase viscosity is includes the contribution from turbulence. The heat flux in each phase, q, and interphasial heat transfer Q_{pq}, need special treatment, discussed below. Several phase interaction terms are included in this model. $R_{pq,i}$ is the momentum interaction term. Phase change models for the interphasial mass transfer, $\dot{m}_{pq}$ is discussed in below. Phase change will also introduce additional transfer of energy, H_{pq} and momentum, V_{pq}, which are the latent heat and drift velocity.

In this work, the Lee model is used to model phase change, Eqns. (5) and (6), similarly to previous works with this model (Giacomelli et al., 2018, 2019).

$$\dot{m}_{pq} = \sigma_e \alpha_l \rho_l \frac{T - T_{sat}}{T_{sat}}, \quad \text{Eq. (5)}$$

$$\dot{m}_{qp} = \sigma_c \alpha_v \rho_v \frac{T - T_{sat}}{T_{sat}}, \quad \text{Eq. (6)}$$

Numerical investigations of the R744 ejector using the mixture model (Giacomelli et al., 2018) found the evaporation and condensation constants that best fit experimental results were σ_e=100000 and σ_c= 0.1. A study on the effects of these two coefficients in presented in this work.

The two-phase mixture properties are defined by a mass or volume-based averaging of the two compressible phases. The phases are both evaluated by pressure and temperature, interpolated from a look-up table (152x126) based on the REFPROP thermodynamic library. The properties allow for meta-stable conditions of both liquid and gas phase. The RERPROP library for R744 is based on the Span-Wagner equation of state, which is considered the most accurate EoS for CO_2 and is widely used for R744 ejector simulations. The thermodynamic look-up tables are based on the work by Giacomelli et al., (2018), however only considers density, viscosity and speed of sound.

To successfully implement this model into ANSYS Fluent, some limitations of the software had to be overcome using *user-defined functions* (UDFs). Firstly, Fluent only allows for relations for specific heat as a function of temperature, $c_p = f(T)$. Secondly, the interphasial enthalpy (the latent heat), h_{qp} must be defined as a single constant, here referred to as h_F. To correct for the issue of specific heat, a separate temperature field, T', is calculated using UDFs. The temperature field is calculated using a REFPROP look-up table in the liquid and gas regions up to the saturation point, such that $T'=f(P, h)$. Beyond the saturation point the non-equilibrium temperature is estimated by:

$$T'_{\text{superheated}} = T_{\text{saturated}} + \frac{h - h_{\text{sat}}}{c_p} \qquad \text{Eq. (7)}$$

Thus, the temperature field is independent of the specific heat defined in Fluent. To address the second issue, an additional source term, S_{pq}, is added to the enthalpy equation, Eq. (8), such that it would compensate for the constant value used in Fluent, with a latent heat that is a function of pressure, $h_{qp}(P)$.

$$\dot{S}_{pq} = \left[\dot{m}_{pq} - \dot{m}_{qp}\right]\left(h_{pq}(P) - h_{\text{F}}\right) \qquad \text{Eq. (8)}$$

Due to the change of temperature field, the interphasial heat transport models are not valid. Therefore, the inter-phasial heat exchange is assumed to be zero, $Q_{\text{pq}} = 0$. Furthermore, heat conduction is assumed negligible. These limitations are planned to be adressed in further work.

The model includes several closure models, which allow adaptability and more advanced phase-coupling mechanisms than the simple pseudo fluid model. In this model the following closure models are used:

(a) Momentum interaction: Schiller Neumann, see (ANSYS Fluent theory guide, 2019).

(b) Turbulence model for turbulent viscosity: Mixture formulation of k-epsilon realizable model

(c) Dispersion forces are neglected in this study.

Further testing and study of these closure models is necessary, however is left for future work.

3. NUMERICAL MODEL SETUP

The simulations were made to best reproduce the experimental results presented by (Palacz et al., 2017). Several 2D axi-symmetric structured meshes with N=6k, 25k and 100k cells were generated using the ANSYS ICEM meshing framework. The generated meshes were of high orthogonal quality with low skewness. The meshes were generated based on the dimensions used in the experimental and numerical investigations of Palacz et al., 2015. The boundary conditions for pressures and temperatures used are presented in Table 1, corresponding to the experimental conditions presented by Palacz et al. (2017). A set of four points were chosen to get a selection of super critical, critical, and sub-critical operating conditions due to the computational time constraint.

Table 1. Experimental conditions for R744 ejector operation (Palacz et al., 2017).

	P_{motive} [bar]	T_{motive} [C]	$P_{suction}$ [bar]	$T_{suction}$ [C]	P_{out} [bar]
1	53.93	6.33	27.3	5.7	34.23
9	66.51	22.41	28.21	2.21	34.85
14	75.79	28.07	28.17	2.58	36.80
18	94.46	35.28	27.21	2.60	32.85

The pressure-based implicit formulation in ANSYS Fluent was used in the calculations. This is the only option that is compatible with multiphase models in ANSYS Fluent. While it is generally agreed that density-based formulations performed better for highly compressible flows, pressure-based solvers have successfully been used for super sonic flows. The PRESTO! scheme was used for pressure and the second order upwind scheme was used for all other variables in the computations. The TFM model was run until steady state with a transient solver, to improve solver stability. The ejector simulations were performed with three different meshes, A, B, C, with 6k, 25k, and 100k cells, respectively. Table 2 shows the suction and motive massflow rates calculated using the different mesh resolutions for case 18.

Table 2. Experimental conditions for R744 ejector operation (Palacz et al., 2017). *Oscillating inlet flow

	Case	mfr (kg/s)	Mesh		
			A	B	C
TFM (σ_e =5.0E+5)	18	M_m	0.0954	0.0954*	0.0961*
		M_s	0.0186	0.0207	0.0107

The two-fluid model achieves similar results for all meshes in terms of motive mass flow rate. However, mesh refinement introduces some oscillations to the motive flow. This was found to be caused by oscillations in the nozzle pressure-field. These oscillations might be caused by numerical errors or might be a physical phenomenon. The suction mass flow rate does not seem to be converged for this case. Prediction of the suction mass flow rate is in general very sensitive to the flow in the ejector. Due to the oscillations for finer meshes and faster computation time, mesh A was chosen for the TFM. However, it is expected that this will lower the TFM accuracy. The oscillating behaviors is believed to be caused by the thermodynamic properties and will be studied in further work.

4. RESULTS AND DISCUSSION

The phase change parameters are highly significant for the motive nozzle flow solution and the predicted mass flow rate. Therefore, a study on the evaporation coefficient σ_e was conducted to find the most appropriate coefficient with the Lee model. The results are shown in Table 3.

Table 3. Comparison motive mass flow rate with different evaporation phase change coefficient, Sigma e. Bolded text indicates solution used for comparison with experiments. (a) Oscillating outlet flow (b) Overheated gas (c) Unrealistic shock solution

M_m (kg/s)		Sigma e			
	Experiment	1E4	1E5	5E5	1E6
1	0.099	0.0850 (b)	**0.0841**	0.081 (a)	0.080 (a)
9	0.072	0.0851 (b)	**0.0659**	0.063 (a)	0.060 (a)

14	0.089	0.0954 (b)	**0.769**	0.068	0.067 (a)
18	0.084	0.112 (c)	0.102	**0.095**	0.094 (a)

The trend indicates that as σ_e is increased the motive mass flow rate is decreased, which is also seen in previous work (Palacz et al., 2017), where the HRM gives lower predicted mass flow rates than the HEM. Increase in σ_e is equivalent to bringing the thermodynamic state faster to equilibrium. Thus, it is expected that for super-critical flashing (case 18) the coefficient should be very high. Indeed, the trend indicates that even further increase in σ_e would be nessecary to achieve the experimentally observed motive mass flow rate. However, as σ_e was increased beyond 1.0E+5, the outlet mass flow rate would give oscillating results, noted in Table 3 with (a). This is believed to be caused by an oscillating mass transfer between the phases driven by the high coefficient. For low-pressure motive conditions (case 1) the simulations suggest that a lower mass transfer coefficient than 1E4 should be implemented. However, for very low values of σ_e, the delayed phase change will transfer too much energy into the gaseous phase, giving unrealistically high overheating of the gas beyond saturation. In total, these results motivate investigation into a more physically realistic mass-transfer model, which is left for further work.

Table 4: Comparison of numerical and experimental results; TFM with best coefficient from Table 4. The notation * indicates no suction flow.

	Experimental (kg/s)		TFM (%)	
case	m_m	m_s	Err_m	Err_s
1	0.099	0.0297	-15.1	*
9	0.072	0.0137	-8.5	-38.3
14	0.089	0.0249	-13.6	-9.6
18	0.084	0.0353	13.6	-47.3

The resulting mass flow rates with the TFM (with best match σ_e found in Table 3) are presented in Table 4. The TFM performed poorer than the HEM (Palacz et al., 2017). However, the TFM results were produced with a lower resolution mesh and without tuning for optimal coefficients. The TFM does however keep motive mass flow rate accuracy within 15% for all operating conditions, which can be improved by further tuning of the phase change coefficients. The suction mass flow rate is not well predicted by the TFM. This is expected as no emphasis has been put on turbulence or momentum interaction modeling in this work. Accounting for these effects is left for further work. Extensive research into appropriate closure models for this problem is nessecary to achieve realistic suction mass flow rate predictions. However, the potential to improve this prediction using advanced closure models is also the benefit of the TFM.

5. CONCLUSION

A novel two-fluid model (TFM) that accounts for thermal, velocity and thermodynamic non-equilibrium is presented in this work. A work-around that enables non-constant latent heat and pressure dependent specific heat in ANSYS Fluent is presented. The effects of phase change coefficients on model mass flow rate prediction is found to be significant. Still, further research is nessecary to improve model accuracy. The TFM produced results with lower accuracy than previous models. However, the TFM can also be further improved by tuning the phase change parameters. The ability to add additional closure models to the TFM is a benefit as more physics can be incorporated into the simulations. This will bring the models physical realism and accuracy up with more research. Improving these submodels will however require extensive research into different flow phenomenons such as non-equilibrium thermodynamics, phase change modelling, two phase turbulence, and bubble break-up and coalescence, which is suggested as further work.

ACKNOWLEDGEMENTS

The work is part of HighEFF - Centre for an Energy Efficient and Competitive Industry for the Future, an 8-year Research Centre under the FME-scheme (Centre for Environment-friendly Energy Research, 257632/E20). The authors gratefully acknowledge the financial support from the Research Council of Norway and user partners of HighEFF.

NOMENCLATURE

cp	Specific Heat (kJ/kg)	q	Heat transfer (kW)	Γ	Phase change term (kg/s)
h	Specific enthalpy (kJ/kg)	R	Momentum interaction term (N/s)	μ	Viscosity (m^2/s)
k	Thermal conductivity (kW/K)	*T*	temperature (K)	ρ	Density (kg/m^3)
m	Mass transfer (kg/s)	*u*	Velocity (m/s)	σ	Phase change coeficiente (-)
P	pressure (Pa)	*α*	Volume fraction (m^3/m^3)	τ	Stress tensor (N/m^2)

REFERENCES

Ansys® Fluent, Release 19.1, ANSYS Fluent theory guide, 2019, ANSYS, Inc.

Giacomelli, F. Mazzelli, F., Milazzo, A., A novel CFD approach for the computation of R744 flashing nozzles in compressible and metastable conditions, Energy 162 (2018) 1092–1105 (nov 2018). doi: 10.1016/j.energy.2018.08.050.

Giacomelli, F. Mazzelli, F., Banasiak, K., Hafner, A. Milazzo, A., Experimental and Computational Analysis of a R744 Flashing Ejector, Accepted for publication: International Journal of Refrigeration (2019)

Kim, M. H., Pettersen, J., Bullard, C. W., Fundamental process and system design issues in CO2 vapor compression systems, Progress in Energy and Combustion Science 30 (2) (2004) 119–174 (jan 2004). doi: 10.1016/J.PECS.2003.09.002.

Lemmon, E. W., Bell, I. H. Huber, M. L. McLinden, M. O., NIST Standard Reference Database 23: Reference Fluid Thermodynamic and Transport Properties-REFPROP, Version 9.0, National Institute of Standards and Technology (2018). doi: http://dx.doi.org/10.18434/T4JS3C

Palacz, M. Haida, M., Smolka, J., Nowak, A. J., Banasiak, K., Hafner, A., HEM and HRM accuracy comparison for the simulation of CO2expansion in two-phase ejectors for supermarket refrigeration systems, Applied Thermal Engineering 115 (2017) 160–169 (mar 2017).doi:10.1016/j.applthermaleng.2016.12.122.

Palacz, M., Smolka, J., Fic, A., Bulinski, Z., Nowak, A. J., Banasiak, K., Hafner, A., Application range of the HEM approach for CO2 expansion inside two-phase ejectors for supermarket refrigeration systems, International Journal of Refrigeration 59 (2015) 251–258 (nov 2015). doi: 10.1016/j.ijrefrig.2015.07.006.

Ringstad, K. E., Allouche, Y., Gullo, P., Banasiak, K., Hafner, A., CO2 ejector modelling using CFD: current status., in: 25th IIR International Congress of Refrigeration Proceedings., 2019 (2019).

Smolka, J., Bulinski, Z., Fic, A., Nowak, A. J., Banasiak, K., Hafner, A., A computational model of a transcritical R744 ejector based on a homogeneous real fluid approach, Applied Mathematical Modelling 37 (3) (2013) 1208–1224 (feb 2013). doi: 10.1016/j.apm.2012.03.044.

CFD-based design algorithm for CO2 ejectors

Knut RINGSTAD[(a)], Krzysztof BANASIAK[(b)], Armin HAFNER[(a)]

[(a)] Norwegian University of Science and Technology,
Kolbjørn Hejes vei 1B, 7491 Trondheim, Norway
[(b)] SINTEF Energy, Kolbjørn Hejes vei 1d, 7465 Trondheim, Norway
knut.e.ringstad@ntnu.no

ABSTRACT

In this work, a novel CFD-database generation algorithm for CO2 ejectors are presented. The algorithm is explained and its details discussed. A case for CFD database generation is then performed based on an ejector design for an industry client. The ejector design is investigated with different design parameters around the suggested design. Design improvements are suggested based on the numerical results, and a final design is suggested. The final design had a high ejector efficiency of simulated to be 46% at the design point, and the ejector performance is evaluated and discussed for off-design conditions.

Keywords: R744, Ejector, Computational Fluid Dynamics, Numerical Modelling, Ejector design

1. INTRODUCTION

The transition to more environmentally friendly solutions is accelerating. In the HVAC industry, a lot of research has been focused on natural and environmentally friendly working fluids. Of the natural refrigerants, CO2 systems is considered to be a highly efficient and cost-effective solution for many applications.

CO2 systems can in many situations be significantly improved by the introduction of ejector solutions. Ejectors are work-recovery devices that by utilizing the expansion of a high pressure 'motive' to pump a secondary 'suction' flow from a low pressure. The ratio of entrained suction flow to motive flow is referred to as the entrainment ratio (ER), see Eq. (1):

$$ER = \frac{\dot{m}_s}{\dot{m}_m} \quad \text{Eq. (1)}$$

The efficiency of the ejector can then be defined by ratio of actual to maximum theoretical recovered work, defined in Eq. (2), described in detail by Elbel and Lawrence (2016):

$$\eta_{ejector} = ER\frac{h_{s,iso}-h_s}{h_m-h_{m,iso}} \quad \text{Eq. (2)}$$

Increasing use of ejector solutions has encouraged more research into ejector design and modelling. In recent years, emphasis has been put on the development of advanced CFD models for the prediction of CO2 ejector performance (Giacomelli et al. 2019, Bodys et al. 2020, He et al. 2019). For a detailed review of CO2 ejector model development, see Ringstad et al. 2020.

CFD based algorithms for ejector design have been presented in previous works (Palacz et al 2016, Palacz et al 2017). Palacz et al. (2016-2017) presented a shape optimization algorithm based on the EjectorPL algorithm. In these works, a genetic optimization algorithm was used to look for design improvements for 6 geometry shape parameters, namely; mixing chamber diameter, mixing chamber length, motive nozzle, premixing chamber length, motive nozzle converging and diverging angle, and motive nozzle outlet diameter. Recently, He et al. (2021) investigated the covariation between 3 geometric shape parameters and the exergy production of the flow. Their study found that the syngeristic effects of several ejector parameters must be considered simultaneously to identify design improvements. Similar findings were reported by Banasiak et al. (2014).

In this work, the homogeneous equilibrium two-phase ejector CFD model is implemented into a fully automated algorithm for generation of CFD databases. The CFD database is then used to design an ejector for an industry client for application in a new heat-pump system. The design is investigated for off-design conditions.

2. MULTIPHASE MODEL

In this work, a homogeneous equilibrium model (HEM) is used for calculation of two-phase flow of CO2 in the ejector. The model is implemented in ANSYS v.19.3 with user-defined-functions for fluid properties and enthalpy transport.

The HEM is based on an enthalpy-formulation implemented developed by Smolka et al. (2013). The model assumes thermodynamic, thermal and mechanical equilibrium between the phases. The averaged set of equations for the liquid and vapor phase are then presented as, Eq. 1-3:

$$\frac{\partial \rho_m}{\partial t} + \frac{\partial}{\partial x_j}\left[\rho_m u_{mj}\right] = 0, \quad \text{Eq. (3)}$$

$$\frac{\partial}{\partial t}(\rho_m u_{mi}) + \frac{\partial}{\partial x_j}\left[\rho u_{mi} u_{mj} + p_m \delta_{ij} - \tau_{mij}\right] = 0, \quad \text{Eq. (4)}$$

$$\nabla \cdot (\rho \vec{u} h) = \nabla \cdot (k_{\text{eff}} \nabla h) + \dot{S}_{h1} + \dot{S}_{h2} + \dot{S}_{h3}, \quad \text{Eq. (5)}$$

Here, h is the specific enthalpy, $\vec{u}$ is the velocity vector, k_{eff} the effective diffusion coefficient, and the source terms $\dot{S}_{h1,2,3}$ describe the mechanical energy, the irreversible dissipation of the kinetic energy variations and the dissipation of the turbulent kinetic energy, respectively (Smolka et al., 2013). The thermodynamic state is then uniquely defined at homogeneous equilibrium by the pressure and enthalpy:

At homogeneous equilibrium, the enthalpy and pressure uniquely define a thermodynamic state in the two-phase dome (Eq. 6):

$$\rho, \mu, k, \alpha, T, q, c = f(p, h) \quad \text{Eq. (6)}$$

In addition, the k-epsilon Realizable turbulence model with scalable wall functions is used as the turbulence model.

3. DATABASE GENERATION TOOL

3.1. Database layout

The database is organized in cases for ease of use. A case contains a collection of results, meshes, post-processing and algorithm settings. The settings can be changed for each ejector design to user specifications, such as changing CFD settings, meshing settings, and sampling algorithm settings.

3.1.1. Parameters and database sampling

Each case will contain a separate database of model parameters. The model parameters are changeable and more parameters can be added depending on case requirements. The parameters contain the CFD model parameter, boundary condition and shape parameters that decide the ejector design and operating condition. The database also contains several outputs, such as predicted mass flow rates and other performance indicators.

Each parameter can be defined as a feature; a feature is a parameter that is sampled in the database. The remaining parameters are kept at the predefined baseline conditions. The sampling can be done via linear sampling between two values, which can use a space filling or a latin hypercube design to sample the feature-space. For the ejector design algorithm, a list of 16 geometry parameters and 5 boundary condition values are used for a calculation. In this work, the studied features will be motive nozzle throat diameter, Dt, the motive nozzle outlet diameter, Dmo, and the mixing chamber length, Lmix and diameter, Dmix.

3.1.2. Properties

For these calculations a look-up table for CO2 is used in the HEM model generated using the CoolPack library. However, the algorithm can easily be interchanged with other working fluids.

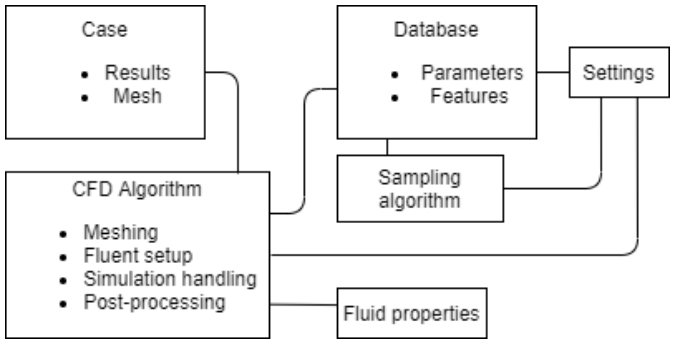

Figure 1: Database layout

3.2. Numerical solver and setup

The numerical solver is a Pressure-based Coupled solver for 2D axisymmetric flow. The second order upwind discretization schemes are used for momentum, k, epsilon, and enthalpy transport variables and the PRESTO scheme for pressure. A steady solver was used with a CFL number that was stepped up from 0.3 to 0.5 during simulation.

Inlets are defined as pressure inlets with constant value Dirichlet boundary conditions. The ejector outlet is defined as a pressure outlet, with a Neumann zero gradient boundary condition for enthalpy. A turbulence intensity of 5% and a turbulent viscosity ratio of 10 was specified at all inlets and outlets. A wall roughness of 2 micrometers, adiabatic and no-slip boundary conditions are applied to the ejector walls. The pressure and enthalpy boundary conditions at motive inlet, suction inlet and outlet were defined based on inputs from the database.

3.3. Grid generation algorithm

The meshes were generated using ANSYS ICEM with an automated script for geometry setup using RPL files. The script uses the 16 inputs from the database to generate the geometry. The geometry is then meshed automatically based on the specified meshing settings. The generated meshes are of high orthogonal quality and refined in regions of large flow variation. The script is capable of 2D and 3D meshes, however due to computational load the 2D meshes are used in this work. Several numerical mesh study have been conducted for similar ejectors using the HEM model (Smolka et al. 2013). In general, these works have found that approximately 20-40k cells is adequate to reproduce ejector flow. Different meshes were also tested in this work and negligible difference was found between the X cell mesh and Y cell mesh.

3.4. Convergence

The computations were done on a 2xAMD Epyc 24-core processor computer with 2.0 GHz clock speed. On 8 parallel cores the computations took approximately 2-4 hours to reach the specified convergence criterion for the 70k cell mesh. The script is also capable of running on a remote cluster for computational speed up, however this capability was not used in this work.

3.5. Graphical User Interface

To simplify ejector design experience a graphical user interface (GUI) was implemented. The GUI allows the user to select the parameter starting values and see how the selection affects the ejector geometry design. This allows for better understanding and speed in the ejector design process.

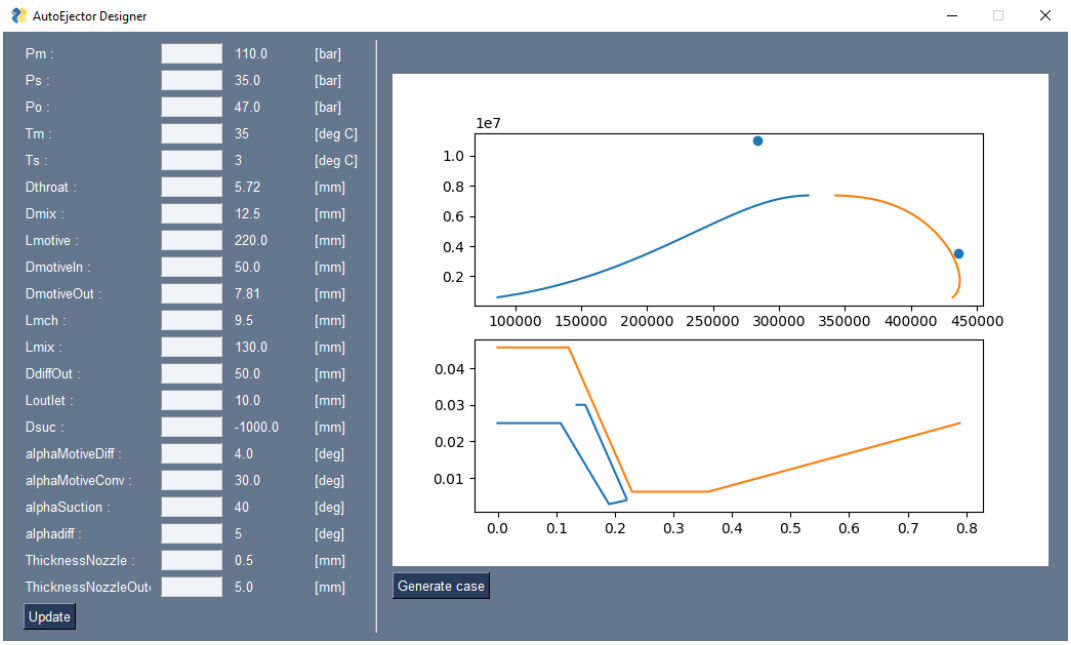

Figure 2: Graphical user interface

3.6. Autoejector design methodology

The database algorithm AutoEjector is employed for rapid CFD based ejector design. The design case is an ejector for heat pump applications that will be scaled up from a smaller design. The design process is done in three stages:

(i) Motive nozzle design matching at design point

(ii) Mixing chamber optimization

(iii) Off-design performance mapping

The initial step is required to tune the mass flow rate of the ejector. The ejector motive nozzle throat diameter is increased until the specified mass flow rate is reached. Using a set motive nozzle converging and diverging angle, the motive nozzle geometry is then defined by the motive outlet diameter, Dmo. The motive outlet diameter is then increased until pressure matching with the mixing chamber pressure.

The second step is to design an efficient mixing chamber. The mixing chamber diameter and length are investigated with a large database of varied mixing lengths and diameters. The optimal design is then judged based on these results. Other parameters were not judged in this methodology. However, the eventual goal is to combine this tool with machine learning to optimize entire ejector geometry in this step.

The last step is to evaluate the ejector at off design conditions. This is done by sampling the ejector performance at different pressure lifts and motive pressure conditions. Also this step is planned to be automated with a machine learning algorithm for performance mapping.

4. RESULTS AND DISCUSSION

4.1. Design investigation

The design specifications by the industry client was an ejector with motive mass flow rate of 2.5 kg/s at the design point: motive pressure 110 bar, motive temperature 37° C, suction pressure 35 bar, suction temperature 5°C superheat, pressure lift 12 bar.

The design investigation was carried out according to the predefined design methodology. This was done by generating one database for each design stage, i.e. one for motive throat and outlet diameter, one for mixing section diameter and length, and one for varied pressure lift.

Table 1. Motive nozzle throat diameter design

Design parameter	*Value [mm]*	*Motive MFR [kg/s]*
Dthroat	5.72	1.53
	6	1.69
	6.5	1.98
	7	2.29
	7.5	2.64
	7.12	2.37
	7.24	2.45
	7.36	2.54

Table 2 shows the predicted motive mass flow rates with varied motive nozzle throat diameter. As the HEM will in cases under predict the motive mass flow rate, the design value was set to 7.3 mm, giving a motive mass flow rate of 2.48 kg/s.

The motive nozzle outlet diameter is the parameter that decides the motive nozzle flow expansion and must be tuned for the design point flow. The results are shown in Table 3. An outlet diameter of Dmo=9.7 mm was chosen and the expansion profile was verified to be close to ideal for the design point.

Table 2. Motive nozzle outlet diameter design

Design parameter	*Value [mm]*	Jet flow
Dmo	9.0	Under expanded
	9.2	Under expanded
	9.5	Slightly underexpanded
	10.5	Slightly over expanded
	12.0	Severly over expanded
	13.0	Severly over expanded

In the second design stage, the mixing chamber will be optimized to maximize suction flow. For proprietary reasons the full ejector geometry will be presented in non-dimensional form, as a ratio between the design parameter and the final design parameter. The mixing chamber diameter was calculated based on the ratio of Dmix/Dthroat and neighbouring datapoints were sampled. The results are shown in Table 3.

Table 3. Mixing chamber diameter design, L/L_final = 0.76

Design	*Dmix / Dmix_final*	*Suction MFR [kg/s]*
I	0.91	0.91
II	0.94	1.01
III	0.97	1.11
IV	1	1.17
V	1.06	1.14
VI	1.17	0.81

Based on these results the mixing diameters with the highest suction mass flow rate (III, IV, V) were further tested by co-variation of Lmix and Dmix. The results are shown in Table 4. The mixing length had a minor effect on suction mass flow rate. The final design was chosen based on the best performance of the resulting geometries.

Table 4. Mixing chamber length and diameter design

Dmix / Dmix_final	*Lmix / Lmix_final*	*Suction MFR [kg/s]*
0.97	1	0.993
0.97	1.06	1.013
0.97	1.17	1.010
1	1	1.195
1	1.06	1.191
1	1.17	1.186
1	1.2	1.171
1.06	1	1.184
1.06	1.06	1.177
1.06	1.17	1.166
1.06	1.27	1.097

With the optimized design at design point the ejector efficiency was calculated to be 46%.

4.2. Off-design performance

Lastly, the ejector performance is tested at different pressure lifts, shown in Table 5. The results indicate that the ejector design is able to operate at pressure lifts up to 17-18 bar. The maximum efficiency of the ejector is at the design point of 12 bar, and the efficiency quickly drops off beyond 14 bar of pressure lift.

Table 5. Off- design performance at varied pressure lifts

Pressure lift (bar)	Motive mass flow rate kg/s	Suction mass flow rate kg/s	Ejector efficiency (-) Eqn. (2)
8	2.482	1.260	0.30
10	2.482	1.258	0.39
12	2.482	1.195	0.46
14	2.482	0.898	0.42
16	2.482	0.403	0.22
18	2.482	-0.084	-0.05

Figure 3 shows the velocity in the mixing chamber distribution for the different pressure lifts. The flow clearly transitions from a long shock train to a short core with high velocity flow as the pressure lift increases. It also illustrates the suction flow going from super-sonic chocked flow to sub-sonic flow for higher pressure lifts.

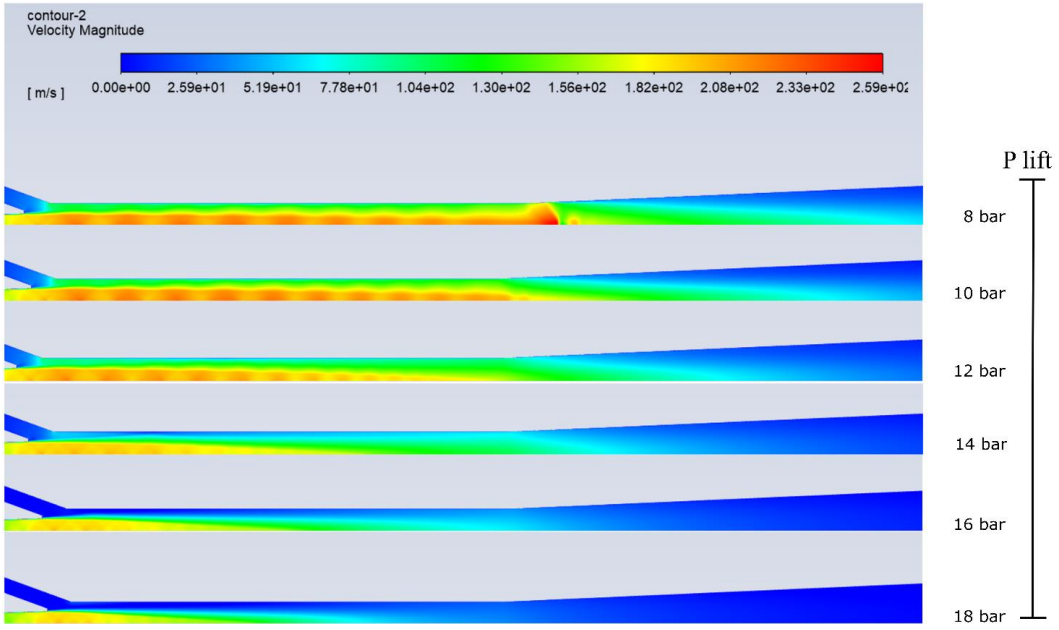

Figure 3: Velocity distribution in mixer and diffuser at different pressure lifts

The full 2D or 3D flow distribution, as shown in Figure 3, gives an exceptional tool for flow investigation that is not available for simpler 0D or 1D approaches. As an example, these models are able to identify flow vortexes that hinder suction flow, or in detail describe the mixing process in various parts of the ejector. Since CFD modelling is based on fewer assumptions than alternative 0D or 1D approaches, it can also be applied to a wider range of geometries and flows, that are outside the scope of the simpler approaches. The cost of using CFD in comparison to other approaches is the computational cost, as calculating a single operating point can take hours in comparison to minutes with lower dimensional approaches.

4.3. Discussion

The CFD-based database design algorithm shows great promise for rapid testing of different geometries and operating conditions. Automatic meshing and CFD setup reduced design time dramatically and reduces the probability of setup or meshing errors. The design methodology presented shows that this approach can identify efficient ejector designs, and is an ideal candidate of automation. A fully automated design algorithm based on this approach is left for further work.

Another potential application for this database design tool is to generate data samples for a machine learning algorithm. This work is under way, and could potentially identify more optimal designs by using advanced optimization methods on ejector design data.

5. CONCLUSIONS

An automated approach for generation of CFD databases of ejectors is presented. This approach can generate CFD data for a generic ejector geometries and at a wide range of operating conditions. The layout and structure of the program is explained and discussed and the algorithm is used for an ejector design case for an industry partner. The algorithm was able to drastically speed up the design process and gave an efficient final design.

The benefits of using CFD models is discussed and the ejector operation at off-design pressure lifts are investigated.

ACKNOWLEDGEMENTS

The work is part of HighEFF - Centre for an Energy Efficient and Competitive Industry for the Future, an 8-year Research Centre under the FME-scheme (Centre for Environment-friendly Energy Research, 257632/E20). The authors gratefully acknowledge the financial support from the Research Council of Norway and user partners of HighEFF.

NOMENCLATURE

CFD	Computational fluid dynamics	*ER*	Entrainment ratio
HEM	Homogeneous Equilibrium Model		

REFERENCES

Banasiak, K., Hafner, A., 2011. 1D Computational model of a two-phase R744 ejector for expansion work recovery. International Journal of Thermal Sciences, 50(11), 2235-2247.

Banasiak, K., Palacz, M., Hafner, A., Buliński, Z., Smołka, J., Nowak, A. J., Fic, A., 2014, A CFD-based investigation of the energy performance of two-phase R744 ejectors to recover the expansion work in refrigeration systems: An irreversibility analysis, International Journal of Refrigeration 40, 328–337. URL:https://www.sciencedirect.com/science/article/pii/S0140700713003812.DOI: 10.1016/j.ijrefrig.2013.12.002.

Elbel, S., Lawrence, N., 2016, Review of recent developments in advanced ejector technology, International Journal of Refrigeration, 62, pp. 1-18, 10.1016/j.ijrefrig.2015.10.031 URL: https://www.sciencedirect.com/science/article/pii/S0140700715003266

He, Y., Deng, J., Li, Y.,Zhang, X., 2021. Synergistic effect of geometric parameters on CO2 ejector based on local exergy destruction analysis,Applied Thermal Engineering,Volume 184,116256, ISSN 1359-4311, DOI: https://doi.org/10.1016/j.applthermaleng.2020.116256.

He, Y., Deng, J., Li, Y., Ma, L., 2019, A numerical contrast on the adjustable and fixed transcritical CO2 ejector using exergy flux distribution analysis,Energy Conversion and Management,Volume 196, Pages 729-738,ISSN 0196-8904, https://doi.org/10.1016/j.enconman.2019.06.031.

Palacz, M., Smolka, J., Kus, W., Fic, A., Bulinski, Z., Nowak, A. J., Banasiak, K., Hafner, A., 2016, CFD-based shape optimisation of a CO2 two-phase ejector mixing section, Applied Thermal Engineering 95 62–69. URL: https://www.sciencedirect.com/science/article/pii/S1359431115012478. DOI: 10.1016/j.applthermaleng.2015.11.012.

Palacz, M., Smolka, J, Nowak, A. J., Banasiak, K., Hafner, A., 2017, Shape optimisation of a two-phase ejector for CO2 refrigeration systems, International Journal of Refrigeration 74 210–221. URL: https://www.sciencedirect.com/science/article/pii/S0140700716303425. DOI: 10.1016/j.ijrefrig.2016.10.013.

Ringstad, K. E. Allouche, Y., Gullo, P., Ervik, Å., Banasiak, K., Hafner, A., A detailed review on CO2 two-phase ejector flow modeling, Thermal Science and Engineering Progress, Volume 20,2020,100647, ISSN 2451-9049, https://doi.org/10.1016/j.tsep.2020.100647.

Smolka, J., Bulinski, Z., Fic, A., Nowak, A. J., Banasiak, K., Hafner, A, A computational model of a transcritical R744 ejector based on a homogeneous real fluid approach, Applied Mathematical Modelling 37 (2013) 1208–1224. DOI: 10.1016/j.apm.2012.03.044.

EjectorDesigner software documentation

Ringstad, Knut Emil,2021

EjectorDesigner

Technical Documentation EjectorDesigner

Version 1.0.1

Knut Emil Ringstad

September 8, 2021

Contents

1 Introduction

The EjectorDesigner software is an OpenAccess software for ejector design and performance mapping. The software is based on automatic generation of large CFD databases using ANSYS Fluent []. The data is analysed using the Gaussian Process Regression code from the SciKit learn packages. Due to propriatary restrictions, the multiphase HEM model can not be shared. However, it can be replaced with minor alterations to the code. The scripts are written in Python [], using the following packages:

- Pandas - For structuring and analysing larger databases
- Numpy - For matrix and vector operations
- OS - For directory tree organizing
- Matplotlib - For plotting
- CoolProp [] - For refrigerant property evaluations
- SciKit Learn GPR [] - For machine learning predictor and other useful tools
- Threading - Used for running multiple instances of Fluent simultaneously

For details on the models or design tool, see the authors thesis and journal publication (open access):
citation
URL: Not yet published
citation
URL: Not yet published

2 Brief overview

The code is structured based on the creation of a *working case* (WR). This *working case* contains the settings that will be applied, the database, the CFD results, and CFD meshes. These are organized into their corresponding folders in each cases tree structure, see the the directory structure below.

To generate a new case, the *makeCase()* -function is available in the *main.py* script. The case settings for the case can then be set, discussed further in Section 4. When running the main program, the settings files are based on the files in the folder </*CurrentSettings*>. When a new case is loaded (*loadCase()*- function in *main.py*), the *working case*'s settings are put into the in the </*CurrentSettings*> folder.

After the settings have been specified, the *MakeDatabase()*- function can be run in *main.py* to generate a uncalculated database, ie. without any results. To fill the database with results, the *UpdateDatabase()*- function can be run in *main.py* to start the calculations. After the calculations are done, the database can be found in the *working case* tree structure under </*Results*>.

To analyse the database results, the pandas dataframes can be used directly or the data analysis tools can be used. The data analysis tools includes the GPR prediction tool. To use this copy the database into the </*DataAnalysis*>- folder and run the wanted analysis scripts.

```
EjectorGPR/
 Cases/
   your_case_name/
     Meshes_and_cases/
     Results/
       Database_and_results
     PreviousResults/
     Settings/
       settings_files
 CFDinterface/
   CFD_pre_and_post_code
 Sampling/
   sampling_code
 DatabaseInterface/
   database_interface_code
 CurrentSettings/
   settings_files
 main.py
 CFD_calculation_tools
-------------------------
 DataAnalysis/
```

3 User example

3.1 Generating a database

This example will illustrate how to generate a database with 5 ejector geometries features and N=200 samples (Lmix, α, Dmo, Dout, Dmix). The design point is set to: P_m = 85 [bar], T_m = 30[°C], Ps = 33 [bar], T_s = -2[°C], P_{lift} = 5 [bar]. The analysis of the database with the GPR tool is also presented. To start a case named 'Example_Case' is generated with the command:

```
#in main
MakeCase('Example_Case_Dmix_Lmix')
```

This generates the folder </*Example_Case*> in the folder </*Cases*>. In this folder, the following changes are made to the settings (see Section 4 for more information about the settings):

- The geometry parameters in *BaselineConditions* are changed to correspond with the ejector geometry presented in the Article [], restated in Table 1.
- The operating conditions in *BaselineConditions* are changed to match the design point.
- The settings in *SamplingSettings* are changed as shown below.
- If a different Fluent-case name is used than *EjectorSolver.cas* this needs to be specified in *CFDSettings*.
- Choose the number of cores you want to use for your CFD calculation in *CFDSettings*, according to your RAM and core count. These are chosen by defining the variables : <NumberParallel> and <NumberCoresPerParallel>, and will use NumberParallel$\times$NumberCoresPerParallel cores on your computer.

Loading this case (notice that the </*CurrentSettings*> folder is updated), the database can be generated by running:

```
#in main
LoadCase('Example_Case_Dmix_Lmix')
makeDatabase()
```

This produces the uncomputed pre-database, *TestPointMatrix.csv*, in the </*Results*> subfolder of the *working case*.

The results from this database can be calculated by running:

```
#in main
updateDatabase()
```

The program will start running and the computations will start on your local computer. If the program is stopped during calculation, it can easily be restarted by running this command again. As the program is running, the database file *Default_database.csv* (name chosen in settings), found in the *</Results>* subfolder, will be filled with data from the post processing of all completed calculations.

When all the calculations are completed, the *Default_database.csv* can be analysed, shown in the following sections.

```
#in SamplingSettings
samplingBool=true
NumberOfSamples = 200
samplingMode = 'LinearLatinHyperCube'
featureDict = {
"Pm":0,
"Ps":0,
"Po":0,
"hm":0,
"hs":0,
"LintletConst":0,
"DmotiveIn":0,
"DmotiveOut":1,
"Dthroat":0,
"alphaMotiveDiff":0,
"alphaMotiveConv":0,
"Lmch":0,
"alphaSuction":0,
"Lsuction":0,
"Dmix":1,
"Lmix":1,
"alphadiff":1,
"DdiffOut":1,
"Loutlet":0,
"Dsuc":0,
"ThicknessNozzle":0,
"ThicknessNozzleOuter":0,
}
```

```
#in SamplingSettings
SamplingMinDict = {
    "DmotiveOut":0.00141+0.00003,
    "Dmix":0.00141+0.00003,
    "Lmix":0.001,
    "alphadiff":0.1,
    "DdiffOut":1e-3,
}

SamplingMaxDict = {
    "DmotiveOut":20e-3,
    "Dmix":0.00141 * 10,
    "Lmix":0.004*50,
    "alphadiff":90,
    "DdiffOut":20e-3,
}
```

Table 1: Available features and their parameter sampling range for LHC-sampling algorithm.

Parameter	a_{min}	a_{max}
$D_{m\text{-}out}$, [mm]	D_{throat}	1.5 D_{throat}
L_{mix}, [mm]	0	50 D_{mix}
D_{mix}, [mm]	D_{throat}	10 D_{throat}
D_{diff}, [mm]	D_{mix}	10 D_{mix}
α_d, [°]	1	90

3.2 Data analysis

To analyse the database, several tools are available. The database can be loaded into a Pandas dataframe to gather information about the simulations. For more information about the Pandas dataframes see the Pandas documentation. To analyse the data using GPR machine learning, the data (*Default_database.csv*) is copied into the </*DataAnalysis*> folder. This example shows how the GPR function is used for plotting heat maps of design variables. For more details on usage of the SciKit Learn GPR model and the SciKit learn toolset, see [**?**]. The primary options are set as:

```
# in GPR_function_design
trainBool=True
displayBool=True
optimizeBool=False
csvname='Default\_database.csv'
df = pd.read_csv(csvname)
features = ["DmotiveOut", "Dmix", "Lmix", "alphadiff", "DdiffOut"]
output = ["eff"]
seed = 2
```

The *trainBool* boolean variable is set to true the first time you run a model. It toggles wether the GPR model is trained using the *csvname* file as the database. It can be set to false if you do not want to retrain the GPR model, but use the previously stored GPR model.
The *trainBool* boolean variable toggles if you wish the heat maps to be plotted.
The *optimizeBool* boolean variable toggles if you wish the optimization using gradient descent to be used on the GPR response-surface mapping.
The *features* list must contain the names of the variables that you chose as features to be sampled in the database.
The *output* varible is the output you wish to predict using GPR. Here, the ejector efficiency, *"eff"*, is used, however it can be exchanged for entrainment ratio, *"ER"* other KPI's.

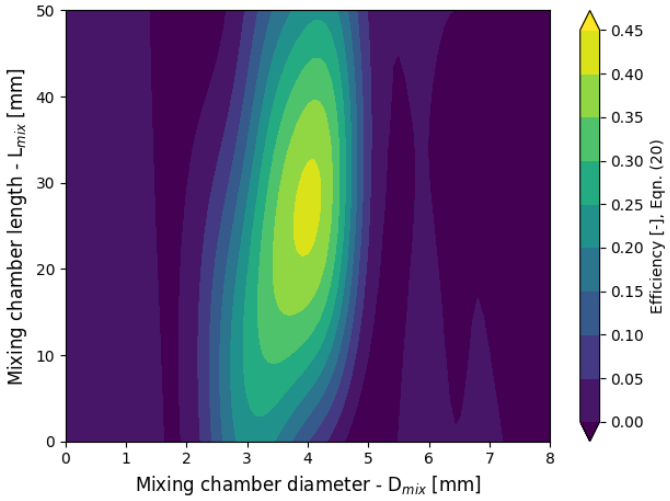

Figure 1: Output heat map from GPR model trained on the database.

The *seed* vaiable is used in randomization, and can be changed to see how different GPR realizations look like.

Running the program produces the following outputs:

```
Training GPR model
Model trained
Avg abs error: 0.031275220
Avg square error: 0.002739662
0.104**2 * RBF(length_scale=[4.01, 0.361, 1.54, 1.71, 300])
+ WhiteKernel(noise_level=0.000183)
```

Where the last line is the optimized kernel that was trained, and the output plot is shown as Figure 1.

4 Settings

The settings in the *working case* folder is organized into different files for different applications.

- The BaselineConditions settings are the settings where the geometry and operating condition variables are set. If a feature is sampled, these values are ignored.

- The CaseSettings file includes the names and locations of the folder locations for that *working case*. This is setup automatically if the *MakeCase()*- function is used.
- The CFDSettings file includes the numerical CFD calculation parameters (relaxation parameters, CFL numbers). In addition the calculation parallelization core counts are set here, see Section 3.1.
- The DatabaseSettings includes the names of the different variables and outputs in the database. Does not need to be changed for ejector calculations.
- The MeshingSettings includes the *ManualMesh* toggle boolean variables for manual meshing, where instead of the standard mesh names, the *MeshName* variable is used. The meshing algorithm includes different meshing strategies, set with *meshingMode*. If *meshingMode* is set to "Const_mix_number" a constant number of cells across the mixing section will be generated by the meshing script. This constant number of cells is set with the variable *Ncells_mix*.
- The SamplingSettings file has the settings for the database sampling. Database sampling is turned off or on with the *SamplingBool* variable. If the database is sampling, the number of samples used in the database is set by the variable *NumberOfSamples*. The sampling only applies to features specified for sampling. These features are chosen by setting the *featureDict* dictionary. If a feature is assosiated with a 1, then that feature is sampled. Otherwise, if it is a 0, then that feature is not sampled. The features are then sampled between a minimum value and a maximum value. These values are specified for each variable in the *SamplingMinDict* and *SamplingMaxDict* dictionaries. For now, only the "LinearLatinHyperCube" choice is availalbe for the *samplingMode*. The latin hypercube approach samples the feature space very efficiently, with low overlap.

ISBN 978-82-326-7064-2 (printed ver.)
ISBN 978-82-326-7063-5 (electronic ver.)
ISSN 1503-8181 (printed ver.)
ISSN 2703-8084 (online ver.)

NTNU

Norwegian University of
Science and Technology